

The University of Nottingham

UNITED KINGDOM · CHINA · MALAYSIA

Nuclearity, Structure and Properties of Tiara-like Complexes

Thesis submitted to the University of Nottingham for the degree of Doctor of Philosophy

Harry James Martin, MSci

May 2018

Declaration

Except where specific reference is made to other sources, the work presented in this thesis is the original work of the author. It has not been submitted, in whole or in part, for any other degrees.

Signed:

Date:

Abstract

The work in this thesis principally describes the synthesis and formation of a series of tiara-like complexes, a class of cyclic transition metal complexes of varying sizes. Despite the numerous examples of this class of complex within the scientific literature, little to no control over the size of the reported molecules is reported. This work aims to attain some degree of selectivity over the nuclearity of the synthesised complexes by two methods; firstly, the modification of reaction conditions with a focus on the choice of solvent used for the synthesis and the second method involving a modification of the structure of the ligand used.

Five tiara-like complexes have been synthesised and characterised. The first of these, Pd NAC (**1**), gives only a single, six-membered product when the reaction is performed using THF as the solvent. When protic alcohols are used instead of THF, additional complexes of different sizes are seen within the MALDI mass spectrum. Replacement of the amide group of the ligand with an ester to remove the possibility of hydrogen-bonding shows the synthesis of six-membered and eight-membered rings when the complex is synthesised in THF. Electrolysis of a DMF solution of **1** results in accumulation of charge accompanied by a change of colour from yellow to red-brown; TEM imaging of the solution shows the presence of Pd nanoparticles.

The second tiara synthesised, Pd ETG (**2**), gives a larger eight-membered ring which results from the relocation of the carbonyl moiety relative to **1**. This complex was shown to be able to host two molecules of methyl iodide, as evidenced by the single crystal structure; this is the first and only example of a tiara-like complex able to encapsulate two molecules of solvent simultaneously.

The same ligand, methyl 3-mercaptopropionate (MMP) was used to synthesise both nickel-

and palladium-containing tiara-like complexes. The two isomers are compared in detail by NMR and crystallography; the palladium complex crystallises into a higher symmetry *R*-3 space group when compared to *P*-1 for the nickel complex. Mixed Pd/Pt tiara-like complexes were examined; it was observed that modification of the starting ratio of the metal precursors gave a corresponding shift in the ratio of the mixed products observed in the mass spectra.

Acknowledgements

I will be eternally grateful to my supervisor Professor Neil Champness, firstly for allowing me this opportunity to work within his research group, but largely for everything that he has done for me after that- for all the support, advice and just general chats and conversation- it has been a huge pleasure to work with you. I would also like to thank Maggie Mallory here- you've been an invaluable help over the past few years along with being a generally wonderfully supportive and friendly person. The School of Chemistry won't be the same without you.

This work would not have been possible without the help of the skilled staff within the School of Chemistry. To Dr Mick Cooper and Ben Pointer-Gleadhill for all your help with the mass spectrometry; Dr Shaz Aslan, Kev Butler and Dr Adrienne Davies for assisting me with NMR; Dr Stephen Davies for your help with the electrochemistry; Dr Will Lewis and Dr Connie Pfeiffer for the help with my crystal structures (especially that really difficult one!), and Dr Graham Rance and Dr Mike Fay for the DLS and TEM respectively.

A huge thank you to everyone I've worked with in B52 over the past 4 years. The B52 post-docs: Dr Lixu Yang, Dr Dan Fonseca-Segura and Dr Nic Pearce (plus Connie again) for the help and advice with my reactions. All of my fellow PhD students: Ben, Tim, Sarah, Sam, Harry, Charlie, Phil, Charlotte, Hawazen, Arjun- you've all been excellent lab partners. A big thank you to Valentina and Naomi for all your help during the six months or so we worked together. Our project might not have worked out how we wanted but it was fun working together!

My last two lab companions who never left my side- my fume hood 4 and my bleach bucket. You did your jobs well and I know everyone else in the lab is grateful for keeping the smells

away.

To Ellie, for turning my world upside down, for introducing me to so many new things and for being there when I needed the most help- I cannot thank you enough for everything. You were once my lab partner and now you're my partner in everything we do.

Finally, for those who've helped me the most. I would never have gotten this far without the love and support of my family. Mum and Dad, Grandma, Kayleigh, Sarah and Amy- your love and support means everything to me. My amazing parents- you originally kindled my interest in science and your constant encouragement got me to where I am now. My wonderful sisters- each of you has worked incredibly hard and you're all so successful in what you're following, you've really pushed me to do the same with my work. This is dedicated to each of you.

List of Abbreviations

1D	One Dimensional
2D	Two Dimensional
ACE	Acetone
AcOH	Acetic acid
atet	2-aminoethanethiol
ATR	Attenuated Total Reflection
CIF	Crystallographic Information File
CFSE	Crystal Field Stabilisation Energy
COSY	Correlation Spectroscopy
CV	Cyclic Voltammetry
Da	Daltons
DCC	N,N-dicyclohexylcarbodiimide
DCTB	Trans-2-[3-(4-tert-butylphenyl)-2-methyl-2-propenylidene]-malononitrile
DFT	Density Functional Theory
DLS	Dynamic Light Scattering
DMAP	Dimethylaminopyridine
DMF	Dimethylformamide
DMSO	Dimethylsulfoxide
DNA	Deoxyribonucleic Acid
DOSY	Diffusion Ordered Spectroscopy
EDT	1,2-ethanedithiol
EDX	Energy-Dispersive X-ray
EI	Electron Impact
EMA	Ethyl mercaptamide
E_p^a	Peak anodic potential
E_p^c	Peak cathodic potential
eq	Equivalents
ESI	Electrospray Ionisation
etet	2-ethylthioethanethiolate
ETG	Ethyl thioglycolate
EtOH	Ethanol
Fc	Ferrocene
Fc^+	Ferrocenium
FID	Free Induction Decay
FT	Fourier Transform
GPC	Gel Permeation Chromatography
HMDSO	Hexamethyldisiloxane
IR	Infra-red
IUPAC	International Union of Pure and Applied Chemistry
LMCT	Ligand-to-Metal Charge Transfer
MACie	Mechanism, Annotation and Classification in Enzymes
MALDI	Matrix Assisted Laser Desorption Ionisation
MEA	2-mercaptoethyl acetate
MeOH	Methanol

MMP	Methyl 3-mercaptopropionate
MS	Mass Spectrometry
mtet	2-methylthioethanethiolate
MTG	Methyl thioglycolate
MW	Molecular Weight
m/z	Mass / Charge ratio
NAC	*N*-acetylcysteamine
NHC	*N*-heterocyclic carbenes
NMR	Nuclear Magnetic Resonance
N,*N*- DIEA	*N*, *N*-diisopropylethylamine
NOE	Nuclear Overhauser Effect
NOESY	Nuclear Overhauser Effect Spectroscopy
n-PrOH	n-Propanol
ORTEP	Oak Ridge Thermal Ellipsoid Program
PDT	1,3-propanedithiol
PET	Phenylethylthiolate
pTLC	Preparative Thin-Layer Chromatography
pyet	2-(2-mercaptoethyl)pyridine
ROESY	Rotating frame Overhauser Effect Spectroscopy
RVC	Reticulated Vitreous Carbon
SCE	Saturated Calomel Electrode
SEC	Size-Exclusion Chromatography
SEM	Scanning Electron Microscope
S*i*Pe	isopentylthiol
SiPr	isopropylthiol
SMM	Single Molecule Magnets
S*t*Bu	tertbutylthiol
TEM	Transmission Electron Microscopy
TFA	Trifluoroacetic acid
THF	Tetrahydrofuran
TLC	Thin Layer Chromatography
TOCSY	Total Correlation Spectroscopy
ToF	Time of Flight
UV	Ultraviolet
Vis	Visible
vs	Versus
VT	Variable Temperature
XRD	X-ray Diffraction

Contents

Title Page....i
Declaration....ii
Abstract....iii
Acknowledgements....v
List of Abbreviations....vii
Contents....ix
Chapter 1: Macrocycles, Supramolecular Chemistry and Tiara-like Complexes....1
1.1 Macrocycles and Supramolecular Chemistry....2
1.1.1 Macrocycles and Metallacrowns....2
1.1.2 Supramolecular Chemistry....12
1.2 Metal Thiolates....18
1.2.1 Metal-Sulfur Bonds....18
1.2.2 Tiara-like Complexes....21
1.3 Thesis Outline....25
1.4 References....27
Chapter 2: Synthesis and Formation of Tiara-like Complexes....31
2.1 Introduction....32
2.1.1 Tiara Nuclearity....32
2.1.2 Hydrogen Bonding....38
2.1.3 Purification of Tiara-like Complexes....41
2.2 Results and Discussion....44
2.2.1 Formation of a New Series of Tiara-like Complexes....44
2.2.2 Synthesis of Pd NAC....45
2.2.3 Synthesis of Pd ETG....61
2.2.4 Synthesis of Pd MEA....71
2.2.5 Separation of Tiara-like Complexes....78
2.2.6 Synthesis of Pd EMA....80
2.2.7 Synthesis of Pd MMP....92
2.3 Conclusions....101
2.4 Experimental....103
2.5 References....111
Chapter 3: Properties and Applications of Tiara-like Complexes....113
3.1 Introduction....114

3.1.1 Catalytic Properties of Palladium....114
3.1.2 Metal Nanoparticles....118
3.1.3 Tiaras as Molecular Hosts for Small Guest Molecules....121
3.2 Results and Discussion....127
3.2.1 NMR Spectroscopy....127
3.2.2 IR and UV/vis Spectroscopy....144
3.2.3 Electrochemistry, DLS and TEM....150
3.2.4 Inclusion Complexes and Hirshfeld Surfaces....165
3.3 Conclusions....177
3.4 Experimental....179
3.5 References....182
Chapter 4: Heteronuclear and Non-Palladium Tiara-like Complexes....185
4.1 Introduction....186
4.1.1 Metalloproteins and Metalloenzymes....186
4.1.2 Mixed Ligand Tiaras....190
4.2 Results and Discussion....193
4.2.1 A Nickel Analog Tiara-like Complex....193
4.2.2 Pd/Pt Heteronuclear Tiara-like Complexes....200
4.3 Conclusions....211
4.4 Experimental....213
4.5 References....216
Chapter 5: Conclusions and Future Work....218
5.1 Conclusions....219
5.1.1 General Summary of Thesis....219
5.1.2 Future Work....223
5.2 References....225
Appendices....226
Appendix I: Standard Stench Protocols....227
Appendix II: Analytical Techniques....229
A2.1 Introduction....229
A2.2 Techniques....229
A2.2.1 2-Dimensional Nuclear Magnetic Resonance Spectroscopy....229
A2.2.2 Electrochemistry....235
A2.2.3 Hirshfeld Surface Analysis....237
A2.2.4 Infra-red Spectroscopy....241

A2.2.5 Size-Exclusion Chromatography....242
A2.2.6 Transmission Electron Microscopy....245
A2.2.7 Energy-Dispersive X-ray Spectroscopy....246
A2.2.8 UV/Visible Spectroscopy....247
A2.2.9 X-ray Diffraction....248
A2.3 References....251

Chapter 1

Macrocycles, Supramolecular Chemistry and Tiara-like Complexes

1.1 Macrocycles and Supramolecular Chemistry

1.1.1 Macrocycles and Metallacrowns

1.1.1.1 Crown Ethers

Cyclic molecules have long been of interest to chemists. Combining pleasing aesthetics with unique properties, they are particularly sought-after by many research groups, due to in part their difficulty to synthesise. Beginning with the discovery of the class of molecules now known as crown ethers in 1967 by Charles J. Pedersen,[1,2] this field of work would eventually be recognised with the Nobel Prize in Chemistry in the year 1987 to Pedersen, along with Donald J. Cram and Jean Marie-Lehn[3] *"for their development and use of molecules with structure-specific interactions of high selectivity". Figure 1.1* illustrates the structure of 18-crown-6, a well-studied crown ether.

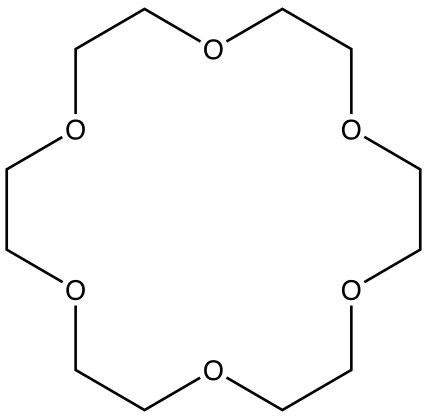
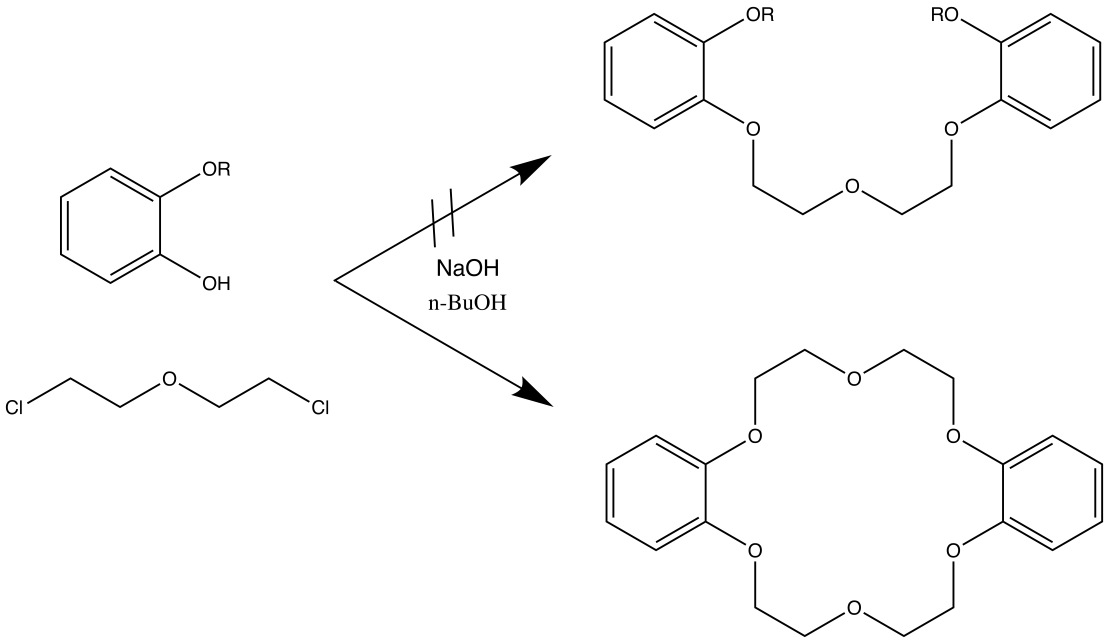


Figure 1.1: Chemical structure of 18-crown-6, a common crown ether.

The original synthesis of a crown ether was serendipitously reported due to the presence of an impurity in a reaction designed to afford a different product.[4] A small amount of unprotected catechol present in the reaction mixture formed the macrocyclic product 2,3,11,12-dibenzo- 1,4,7,10,13,16-hexaoxacyclooctadeca-2,11-diene; this is shown in *Scheme 1.1*. Due to its cumbersome name it is usually referred to as dibenzo-18-crown-6. This naming

convention is true for other members of the class of crown ethers, wherein the first number refers to the total number of atoms within the macrocyclic ring and the second number refers to the number of oxygen atoms specifically.



Scheme 1.1: Original, serendipitous, synthesis of a crown ether. The intended product is located top-right, the obtained crown ether, dibenzo-18-crown-6, is located below.

It was noticed that while the unknown compound was only sparingly soluble in methanol, its solubility was greatly increased in the presence of sodium ions, such that the compound freely dissolved in solutions of sodium hydroxide in methanol. This lead to the discovery that the compound was complexing sodium ions within the cavity, the first reported stable neutral complexing agent of sodium or potassium ions.[5] Further, it was found that yields of up to 45% could be achieved when the reaction was performed using sodium or potassium hydroxide, considerable for the synthesis of an 18-membered organic ring.[6] However, yields were much lower when either lithium or tetramethylammonium hydroxides were utilised, which are not complexed well by the crown ether. It was concluded that the formation of the product is templated by sodium and potassium cations (see *Figure 1.2*), with the polyether

'wrapping' around the positive charge during the formation.[4] The 'crown' designation comes from the image of the polyether coiled around the cation, much like a crown sat upon the head of a person; both may be removed easily.

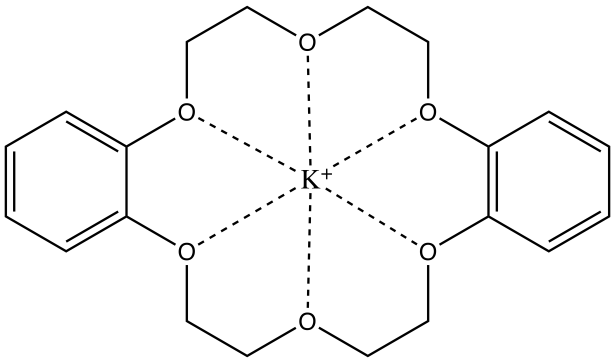


Figure 1.2: Binding of K^+ within the crown ether macrocycle; interactions between the cation and the crown ether oxygen atoms are shown by dashed lines.

It was found that the most stable complexes contained a higher number of oxygen atoms, provided that they were separated by at least two carbon units and symmetrically distributed.[2,4] They have been shown to complex a wide variety of metal ions,[7] including Li^+, Na^+, K^+, Rb^+, Cs^+, NH_4^+, RNH_3^+, Ag^+, Au^+, Ca^{2+}, Sr^{2+}, Ba^{2+}, Ra^{2+}, Zn^{2+}, Cd^{2+}, Hg^+, Hg^{2+}, La^{3+}, Tl^+, Ce^{3+}, and Pb^{2+}; isolable transition metal complexes are relatively few, though some have been published.[8] The size of the crown ether has been found to determine selectivity for particular metal ions; smaller crowns such as dibenzo-12-crown-4 have a higher affinity for lithium cations,[2] which dibenzo-18-crown-6 and 18-crown-6 do not bind well. The structure of a small crown ether, dibenzo-14-crown-4, is shown in Figure 1.3 for comparison with 18-crown-6.

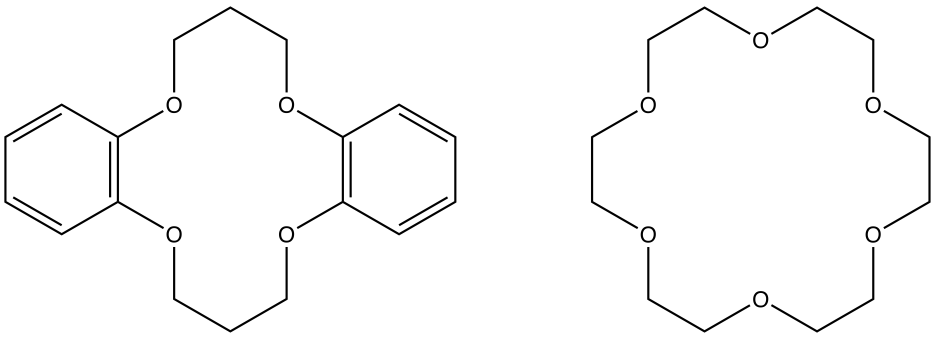


Figure 1.3: Structures of dibenzo-14-crown-4 (left) and 18-crown-6 (right). The former possesses a higher affinity for Li^+ than the latter.

1.1.1.2 Cryptands and Spherands

This work was followed up quickly in 1969 with the publication of the cryptands, similar molecules that combined amine functionality into the polyethers,[9,10] the structure of the archetypical cryptand is given in *Figure 1.4*. Discovered by the chemist Jean-Marie Lehn; his PhD student Jean-Pierre Sauvage, a co-author of the paper, would also eventually be awarded the 2016 Nobel Prize "*for the design and synthesis of molecular machines*".[11]

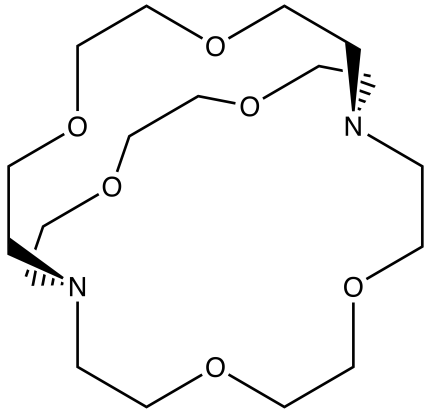


Figure 1.4: Chemical structure of [2.2.2]cryptand.

The cryptands are similar to the crown ethers but contain tertiary amine functionality in the form of two nitrogen caps; the valency of the nitrogen allows for an additional 'strand' to complex metal cations. Cryptands are able to bind guests more strongly than crown ethers of comparable size, giving rise to the "cryptate effect".[12]

Spherands, in contrast, were not reported until 1979 by Donald J. Cram, who would become the third recipient of the 1987 Nobel Prize in Chemistry;[13-15] the structure of the first published spherand is shown in *Figure 1.5*. They are far stronger complexing agents than either crown ethers or cryptands due to their design in that they are 'preorganised' towards guest encapsulation.[15,16] The central methoxy groups have been enforced into adopting positions corresponding to octahedral geometry with respect to a central guest. This removes the need for the host to organise itself during complexation, decreasing the free energy cost of guest binding;[15] in effect this entropic cost is 'paid' during the initial synthesis of the spherand rather than during the guest binding. Further to this, the close proximity of the electron lone pairs of the methoxy groups creates electrostatic repulsion which is relieved on the binding of a positively charged guest. These postulations were evidenced by crystal structures of spherands on the inclusion and exclusion of Li^+; no significant changes in the conformation were observed with the exception of the pseudo-ortho O···O distance; which decreased from 2.92 Å to 2.78 Å (expected distance 2.8 Å) showing a release of bond angle strain.[15]

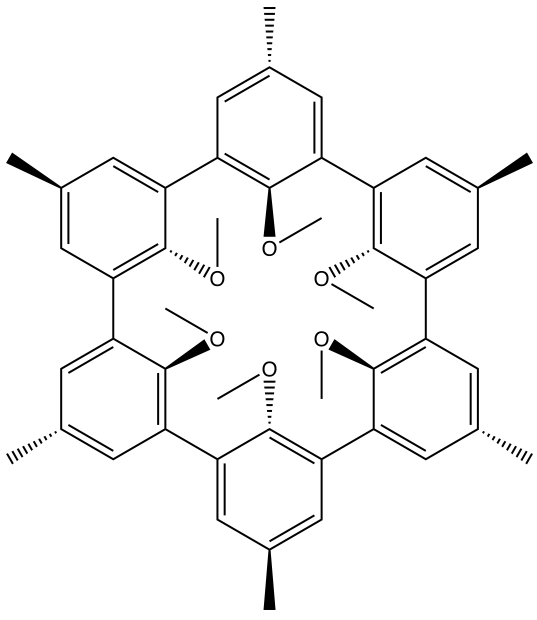


Figure 1.5: Structure of the first published spherand.

The spherands also showed a marked selectivity towards Li^+ and Na^+ cationic guests, attempted complexation of K^+, Mg^{2+} and Ca^{2+} indicated little to no binding by NMR spectroscopy or other techniques;[15,17] an early example of molecular recognition.

1.1.1.3 Metallacrowns

Metallacrowns, as their name suggests, may be regarded as the inorganic equivalent to the crown ethers, incorporating several transition metal atoms within the crown. They are generally composed of an $[M\text{-}N\text{-}O\text{-}]_n$ core and follow a similar naming convention as the crown ethers, where each metallacrown is given a designation of X-MC-Y, where X is the total number of atoms within the ring and the Y is the number of oxygen donor atoms.

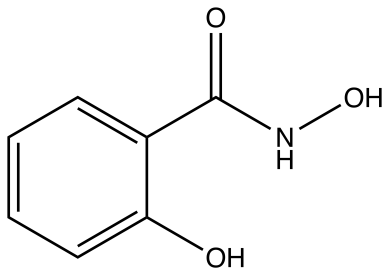


Figure 1.6: The chemical structure of salicylhydroxamic acid, a commonly used ligand for the formation of metallacrowns complexes.

The first report of such a compound was published in 1988 by Lah and Pecoraro[18] as a structural analog of the organic ring 12-crown-4, with the structure of $(Mn^{II}[Mn^{III}(salicylhydroximate)]_4(acetate)_2(DMF)_6).2DMF$, formed by the reaction of Mn(II) acetate with 1 eq. of salicylhydroxamic acid (see *Figure 1.6*) in DMF. Four Mn(III) atoms lie in the ring of the crown coordinated by the salicylhydroximate carbonyl oxygens, phenolate oxygens, nitrogen atoms and two DMF molecules each, while the last Mn(II) is located within the centre of the complex coordinated by the hydroxylimine oxygens and two acetate molecules, making the complex mixed valence.

The complex has comparable properties to that of 12-crown-4. The bite distance and cavity size for the latter are 2.79 Å and 0.6 Å respectively,[19] whereas for the new metallacrown analog the same factors were observed to be 2.67 Å and 0.5 Å.[18]

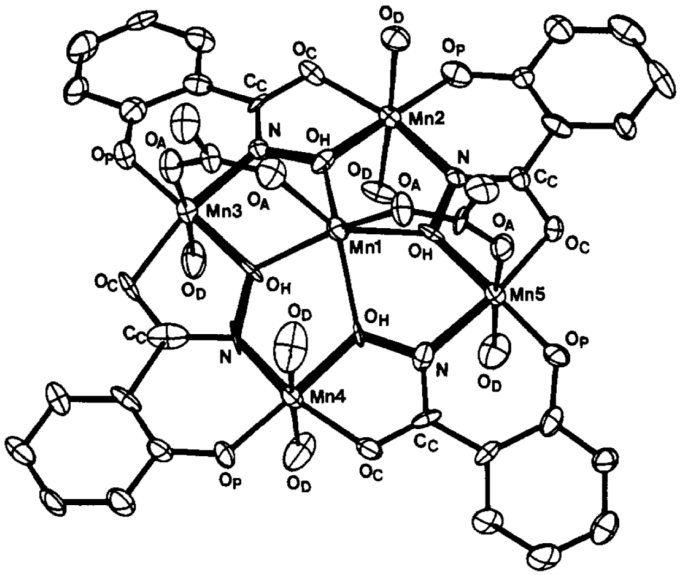


Figure 1.7: Structure of $\{Mn^{II}[Mn^{III}(salicylhydroximate]_4(acetate)_2(DMF)_6\}$, the first published metallacrown.[18] Thermal ellipsoids are shown at 30% probability. Oxygen labelling is as follows: O_A = acetate oxygen, O_C = carbonyl oxygen, O_H = hydroxylimine oxygen, O_P = phenolate oxygen, O_D = DMF oxygen.

While it was initially expected that the cavity would be of a greater size due to the increased Mn-N (1.93 Å - 1.99 Å, average 1.97 Å) and Mn-O (1.83 Å - 1.88 Å, average 1.87 Å) bond distances over the C-C (1.50 Å) and C-O (1.42 Å) bond distances, the bonding angles of the octahedral Mn(III) are much shorter than its crown ether analog. The bond angles of the crown ether[20] range from 108° to 113°, while the average Mn-N-O, N-O-Mn and O-Mn-N angles[19] are (respectively) 119°, 116° and 88°. Thus, the cavity size for the metallacrown is reduced relative to the crown ether, a comparison is illustrated in *Figure 1.8*.

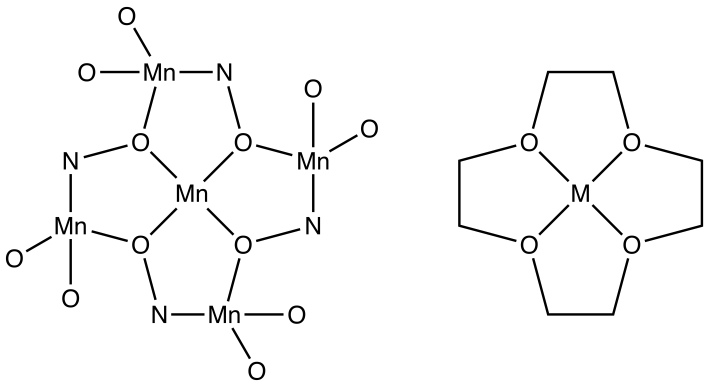


Figure 1.8: Inner crown core of $\{Mn^{II}[Mn^{III}(salicylhydroximate]_4(acetate)_2(DMF)_6\}$ (left) and 12-crown-4 (right).

Also published in the year 1989 were the metallacrowns $Fe^{III}[Fe^{III}$(salicylhydroximato)(MeOH)(acetate)$]_3$[21] and [VO(salicylhydroximato)(MeOH)$]_3$[22], both of which are analogues of 9-crown-3. The former was shown to bind a central Fe(III) whereas the latter had an empty cavity; it is suspected that the vanadyl oxygen atoms block complexation of anions capable of stabilising a captured cation.[23]

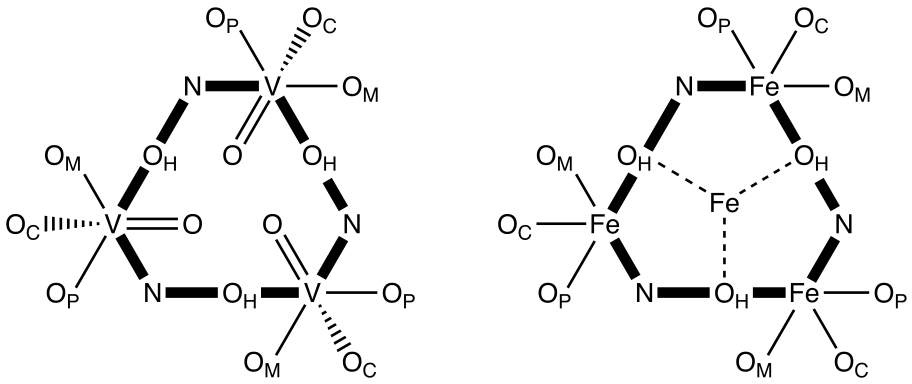
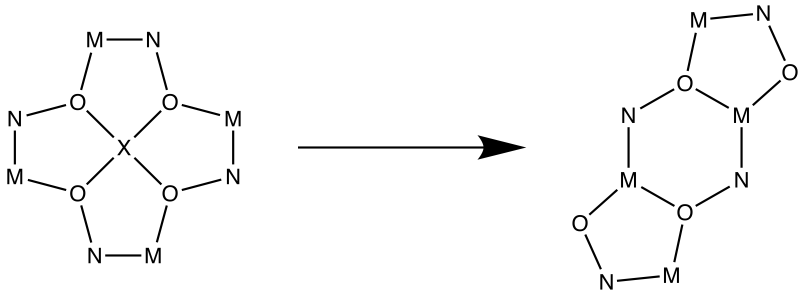


Figure 1.9: Chemical structures of the 9-V-3 and 9-Fe-3 cores. The metallacrown rings are highlighted and two acetate molecules have been omitted from the 9-Fe-3 structure for clarity. Oxygen labelling is as follows: O_M = methanol oxygen, O_C = carbonyl oxygen, O_P = phenolate oxygen, O_H = hydroxylimine oxygen.

The structures of the three complexes, 9-V-3, 9-Fe-3 and 12-Mn-4 are all of similar composition, being formed by the reaction of a simple transition metal precursor $VO(acac)_2$, $FeSO_4$ and Mn(II) acetate respectively) with 1 equivalent of salicylhydroxamic acid. In the

formation of 9-V-3, 3 equivalents of $NaOCH_3$ or NaOH were added; for 9-Fe-3, 3 equivalents of NaOAc were used instead; both reactions were performed using methanol as the solvent. For 12-Mn-4, no additional reagents were added and DMF was used as the solvent. However, from this alone it is unclear as to why the latter should form the larger 12-membered macrocycle. Analysis of the bonding of the manganese centres suggests that the cations undergo Jahn-Teller distortion;[18,21] adoption of a larger 12-Mn-4 crown ring allows the distortion to be oriented perpendicular to the core. *Figure 1.9* illustrates that the axial positions in the 9-MC-3 metallacrowns are occupied by ring oxygen atoms, whereas the 12-MC-4 axial positions are occupied solely by DMF ligands.

The 9-V-3 metallacrown may be classified as a "vacant metallacrown", a label which includes all crowns lacking a central guest.[24,25] Since their discovery, the field of metallacrowns has expanded to include other sub-classes such as "collapsed metallacrowns", which possess a deflated core causing, or following, expulsion of the central guest,[24,26,27] the collapse of a metallacrown is shown in *Scheme 1.2*.



Scheme 1.2: Collapse of a 12-MC-4 metallacrown.

"Inverse metallacrowns", comparatively, are metallacrowns formed by the reversal of the linkage in the ligand such that the metal atoms, rather than the oxygen atoms, face the interior of the cavity.[24,28] This allows the complex to coordinate anionic rather than cationic guests.

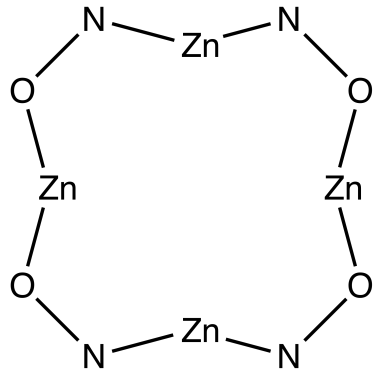


Figure 1.10: Simplified structure of *inv*$(OH)_2$[12-$MC_{Zn2+N(pro)}$-4]. Note the reversed [M-O-N-M-N-O-] configuration.

Metallacrowns have diverse properties beyond simple guest inclusion, they have been shown to catalyse organic reactions such as the oxidation of hydrocarbons[29] and cyclopropanation of alkenes, recognise specific molecules,[31-33] and possess interesting magnetic properties, including some that function as single molecule magnets (SMMs).[24, 34-37]

1.1.2 Supramolecular Chemistry

1.1.2.1 Catenanes

Supramolecular Chemistry has been described as "chemistry beyond the molecule" and "the chemistry of the intermolecular bond" by the chemist Jean-Marie Lehn[38] within his Nobel Lecture on 'Scope and Perspectives on Molecules, Supermolecules and Molecular Devices'. Unlike traditional chemistry, where the study of the covalent bond or collection thereof to form large and elaborate single molecules is principle, supramolecular chemistry refers to the study of non-covalent interactions to form intricate arrays of self-assembled structures. Such non-covalent interactions include, but are not limited to, hydrogen bonding, charge, dipole and electrostatic interactions, π-π stacking and van der Waals forces to generate association between two or more discrete molecules.[39]

Beginning with the discovery of Pedersen's crown ethers and Lehn's own cryptands, a new field of chemistry was quickly developed into a flourishing area of research that continues to gather momentum, as evidenced by the awarding of the 2016 Nobel Prize in Chemistry to Jean-Pierre Sauvage, James Fraser Stoddart and Ben L. Feringa *"for the design and synthesis of molecular machines".*[11]

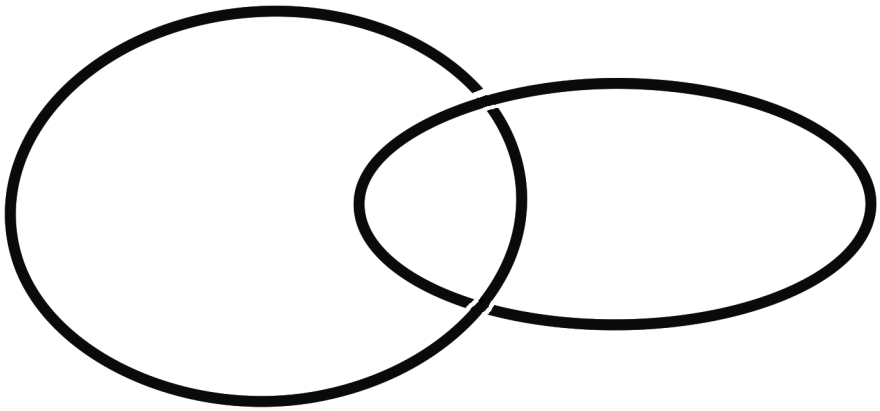
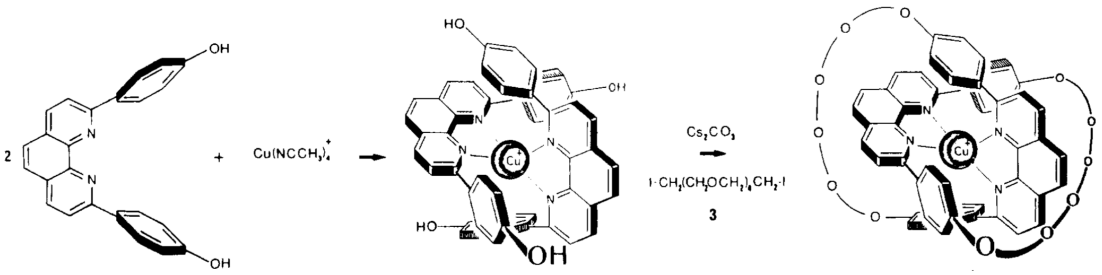


Figure 1.11: Simplified structure of a [2]catenane. The two molecules are shown as rings, interlocked but not attached.

One of the simplest forms of an interlocked supramolecular system, shown in *Figure 1.11*, is that of a catenane,[40] from the Latin *catena*, meaning 'chain'. A catenane is comprised of two or interlocking ring-shaped molecules, such that each is threaded through another and all are inseparable without disruption or destruction of a covalent bond, although none are covalently linked to each other. The components are sometimes referred to as being joined by a "mechanical bond"[41] due to the nature of the linkage between them. These assemblies are denoted as [n]catenane, where n is the number of individual components that make up the entire structure.[42] While these structures have been known since the 1960s, their synthesis was based on statistical methods, relying on the chance arrangement of molecules in solution to form around one another and the yields were correspondingly low.[40-45] In 1984, Sauvage published a new approach, illustrated in *Scheme 1.3*, in which the assembly of the catenane was templated by metal coordination.[46-48]



Scheme 1.3: Synthesis of a [2]catenane templated by Cu(I). Demetallation was subsequently accomplished by treatment with tetramethylammonium cyanide.[46]

The tetrahedral coordination of two phenol-substituted phenanthroline molecules by a copper(I) salt followed by condensation of the hydroxyl groups to polyethers gave the resultant interlocked catenane in 19% overall yield, a marked increase over the <0.1-5% previously reported for catenanes.[46] Upon demetallation of the copper by addition of cyanide salts to the metallacatenate, the two rings are free to rotate, but are inseparable. Interestingly, it was shown crystallographically that while the phenanthroline ring systems are in proximity while coordinated to the copper centre, on complexation the rings rotate to distance the two

phenanthrolines (see *Figure 1.12*).[47]

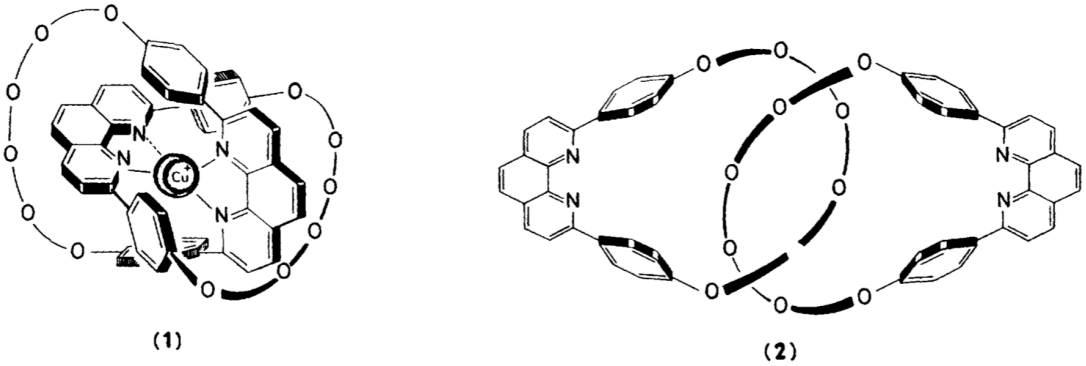


Figure 1.12: Rearrangement of the catenane on complexation (left) and decomplexation (right).[47]

As crown ethers would eventually lead to the development of metallacrowns, neither are catenanes limited to being comprised of solely organic components. The creation of inorganic catenanes containing metal atoms within the rings followed shortly after the templated synthesis of organic catenanes with the reporting of a gold(I) [2]catenane (see *Figure 1.13*) in 1995.[49]

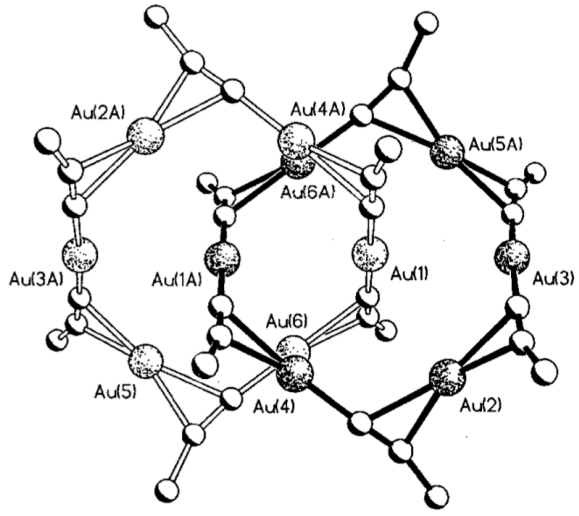


Figure 1.13: Crystallographic structure of the reported gold(I) [2]catenane.[49]

Two hexanuclear Au^{I} rings coordinated linearly by tertbutyl acetylene were found to be interlocked when formed from the addition of the ligand to a solution of $[Au(NH_3)_2]BF_4$; the

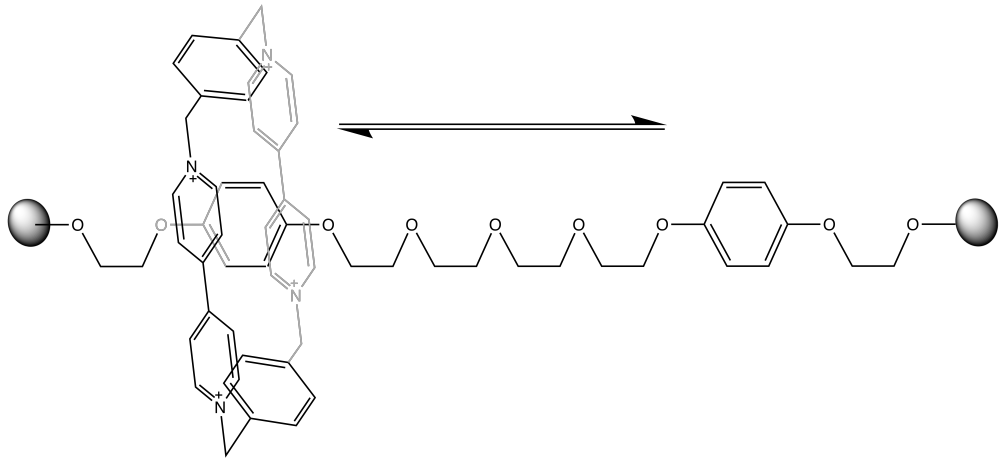
[2]complex was obtained in 65% yield- an impressive feat for a supramolecular assembly. The inter-ring Au…Au distances were found to be between 3.215(2) Å and 3.351(2) Å in distance, within the range of close stabilising contacts. This known propensity of gold to form weak favourable interactions, known as aurophilicity,[50] was thought to be the driving force behind the formation of the interlinked product.

1.1.2.2 Rotaxanes and Molecular Machines

A similar class of supramolecules was developed around the same time known as 'rotaxanes' (from *rota* + *axle*) that consist of a ring-shaped molecule threaded around a central 'rod' molecule. The ring is prevented from disassociation by bulky 'stoppers' on the terminal ends of the rod. Alternatively these stoppers may be absent and the ring held in place by strong intramolecular interactions; such an assembly is termed a 'pseudorotaxane'.[41] Like catenanes, the number of components within the system is indicated by [n], thus a [2]rotaxane designation refers to a single macrocycle around the rod and a [3]rotaxane would normally mean two macrocycles to a single rod.

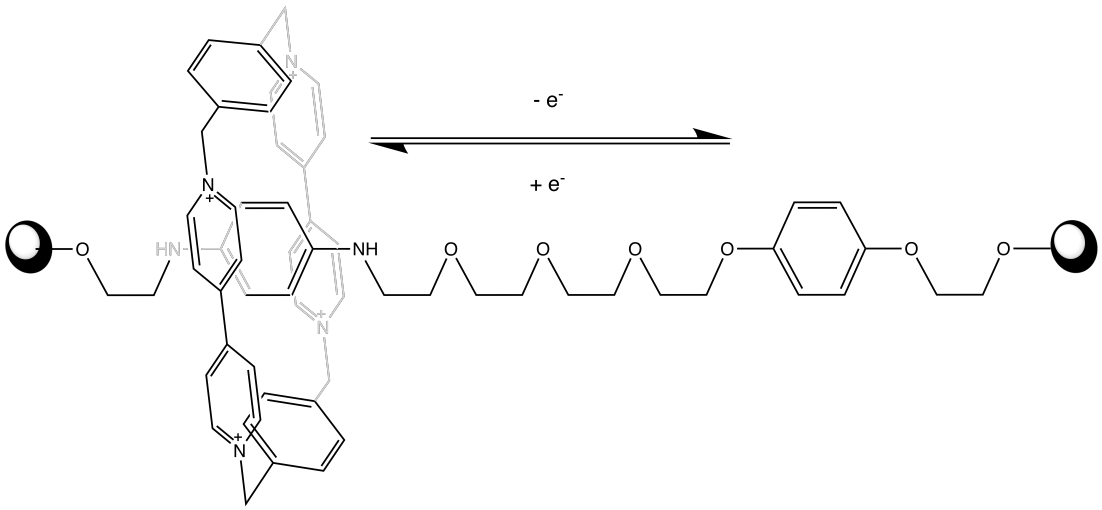
Similarly to catenanes, early synthetic approaches to rotaxanes similarly relied on statistical chance of the components being in proximity during formation and becoming interlocked.[51] Rotaxanes are generally prepared by either 'slipping', in which the assembled components are simply heated together to push the macrocycle over the stoppers of the rod,[52] 'capping', in which the macrocycle is introduced around the rod by intramolecular interactions and the stopper groups attached afterwards preventing disassociation,[53,54] or by 'clipping' wherein the macrocycle is formed by closure of a chain species around the rod which acts as a template; [55-59] this approach has also been utilised to synthesise [3]catenanes. It was this approach, pioneered by J. Fraser Stoddart, that lead to yields of rotaxanes high enough to make their synthesis truly viable.

These advances in the development of rotaxanes would shortly lead to the creation of the first molecular shuttle, consisting of a paraquat-based [2]rotaxane,[60] the structure of which is given in *Scheme 1.4*.



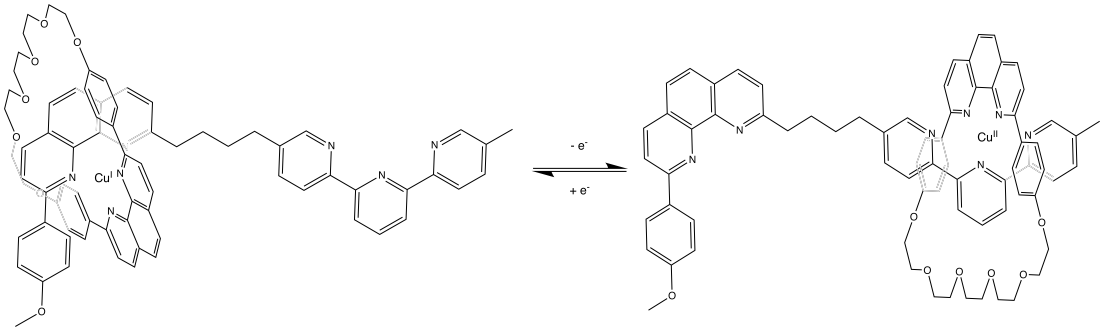
Scheme 1.4: A molecular shuttle able to relocate between two "stations" on the rotaxane rod.

The paraquat macrocycle is electron deficient and therefore forms favourable interactions with the electron rich hydroquinol "stations" on the rod. As the macrocycle is not covalently linked with the rod, it is free to shuttle back and forth between the two identical hydroquinol rings; the energy barrier to this shuttling was estimated as $\Delta G \approx 13$kcal mol^{-1}.[60] At room temperature in solution the shuttling is too rapid to be observable by NMR spectroscopy, however cooling of the solution to -50°C allowed the 'occupied' and 'unoccupied' hydroquinol rings to be resolved, with the former being located upfield of the latter.



Scheme 1.5: Stoddart's electrochemical molecular switch. On reduction of the system, the macrocycle relocates to the station shown here on the right. Oxidation reverses this process such that the macrocycle returns to the original station.

This principle of synthesising "stations" into the rotaxanes would shortly lead to asymmetrisation of the rod such that the movement of the macrocycle could be controlled by external stimuli. Both Stoddart's[61] and Sauvage's[62] research groups independently developed electrochemically switchable rotaxanes, shown in *Scheme 1.5* and *Scheme 1.6* respectively.



Scheme 1.6: Sauvage's electrochemical molecular switch

In the years since the reporting of the first molecular switches, vastly more complicated machines have been reported by these groups, among others. Molecular muscles,[63,64] elevators,[65] motors,[66-75] pumps,[75,76] and nanocars[77-79] have all been synthesised and published; and the field only continues to expand with each passing year.

1.2 Metal Thiolates

1.2.1 Metal-Sulfur Bonds

The tendency of sulfur to form metal-ligand complexes has been well-known for many years. In the year 1834 the compound ethyl thiol, the sulfur-containing analog of ethanol, was synthesised by the Danish chemist William Christopher Zeise who named the substance "mercaptan", shortened from the Latin "corpus mercurium captan", translated as "mercury capturing substance".[80] This name resulted from the tendency of the compound to react strongly with mercury oxide. The name has continued in use and is often used for chemicals containing the thiol group as a prefix, such as in the chemical mercaptopyridine (see *Figure 1.14*).

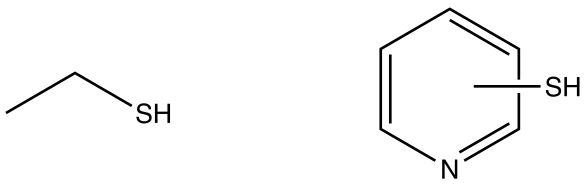


Figure 1.14: Structures of left: ethyl mercaptan (ethyl thiol, ethanthiol), right: mercaptopyridine (*x*-pyridinethiol, *x* = 2,3,4)

The affinity for the thiol group for metal ions is well-studied and thought to arise from a combination of two factors; the first being the weaker strength of the S-H bond (363 $kJmol^{-1}$) relative to the O-H bond (459 $kJmol^{-1}$).[81] The thiol proton is more acidic than the alcohol proton, with a pK_a of 10.3 for PhSH when compared to 18.0 for PhOH,[82] resulting in the greater nucleophilicity of the RS^- species. The lower electronegativity of sulfur (2.58) compared to oxygen (3.44) results in the increased availability of the electron lone pairs for donation to metal centres. Further to this, sulfur is a softer Lewis base than oxygen, as defined by Pearson's Hard-Soft Acid-Base Theory,[83] leading to stronger interactions with softer Lewis acids, such as the late transition metals, particularly those of the second and third row. This

may explain the well-known affinity of sulfur for gold and mercury. The other electron lone pairs of the sulfur atom are well-placed to interact with the metal centres via additional π-bonding interactions. A strong tendency of thiolate ligands is to bridge multiple metal centres via donation of a sulfur lone pair from a 3p orbital; so predominant is this occurence, examples of monodentate thiolates are relatively few and often require steric hindrance or alternate form of stabilisation to be formed.

Of the mononuclear, monodentate metal-thiolate compounds, a small number of complexes with the general formula $[M^{II}(SPh)_4]^{2-}$ where M = Mn, Fe, Co, Ni, Zn, Cd have been prepared.[84,85] These complexes possess distorted tetrahedral geometry and are reasonably air-sensitive. The related and less air-stable complex $[Fe^{III}(SPh)_4]^-$ (see *Figure 1.15*) has also been synthesised[86]; this complex undergoes substitution reactions to give complexes of the formula $[Fe^{III}(SR)_4]^-$ where R = CH_2CH_3, CH_2Ph, CH_2CH_2Ph, and $C(CH_3)_3$). These complexes are prone to reduction at the metal centre with corresponding oxidation of the thiolate to the disulfide.[86,87]

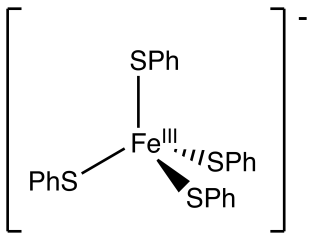


Figure 1.15: Structure of $[Fe^{III}(SPh)_4]^-$. The symmetry is distorted from T_d to approximately D_{2d}.

The vast majority of reported metal-sulfur complexes contain thiolate ligands in a μ_2-bridging configuration due to the ability of sulfur to donate one of its 3p lone pairs of electrons. This often results in polynuclear cage-like complexes; a commonly adopted shape is the adamantane-like complex (see *Figure 1.16*) in the representative structures $[M^{II}_4(SPh)_{10}]^{2-}$ where M = Fe, Co, Zn, Cd.[88] These compounds are labile and interconversion between metal

ions occurs when the complexes were mixed in solution to give rise to $[M^{II}_{n}M'^{II}_{4-n}(SPh)_{10}]^{2-}$ complexes.

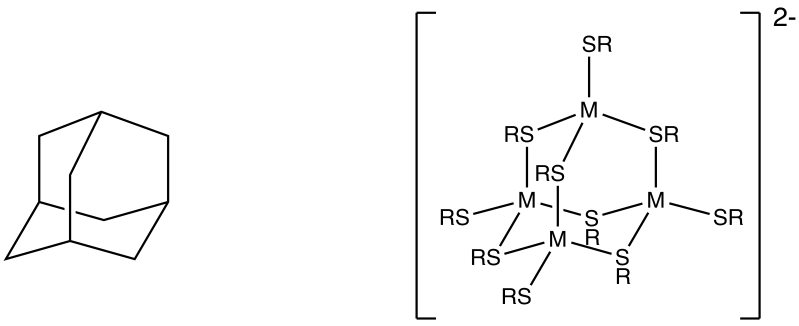
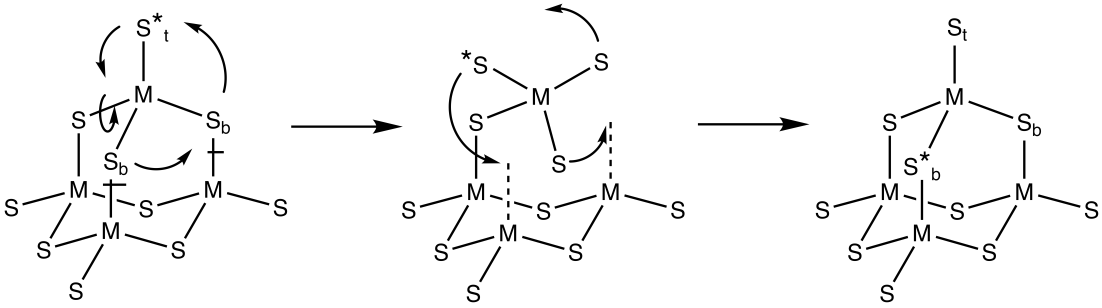


Figure 1.16: Structures of adamantane (left) and $[M^{II}_{4}(SPh)_{10}]^{2-}$ where M = Fe, Co, Zn, Cd.

These exchange reactions were evidenced by ^{1}H NMR. In addition, the homonuclear complexes are fluxional, with interconversion between the terminal and bridging thiolates. These resonances coalesce when the sample is examined at an elevated temperature, with full coalescence at 305K for $[Fe^{II}_{4}(SPh)_{10}]^{2-}$. The process of interconversion is illustrated below in *Scheme 1.7*.



Scheme 1.7: Fluxionality of thiolate ligands, phenyl attachments omitted for clarity. Terminology is as follows: S_b = bridging thiolate, S_t = terminal thiolate.

These complexes are useful models of many metal-containing enzyme active sites, as many metalloenzymes contain cysteine bound transition metal atoms for structure or catalytic activity. For a review of metalloenzymes in greater detail, refer to *Chapter 4.1*.

1.2.2 Tiara-like Complexes

1.2.2.1 The Square Planar Geometry

Due to this propensity of thiolate ligands to bridge metal centres, the resultant complexes often have a high degree of nuclearity. Most transition metals prefer to adopt tetrahedral or octahedral geometries leading to the cage-like structures adopted above. The main exceptions to this rule are the metals of Group 10 in their second oxidation state: nickel, palladium and platinum. Due to their d^8 electronic configuration, these metals often prefer to adopt square planar shapes to place their electrons in lower energy d orbitals (see *Figure 1.17*).

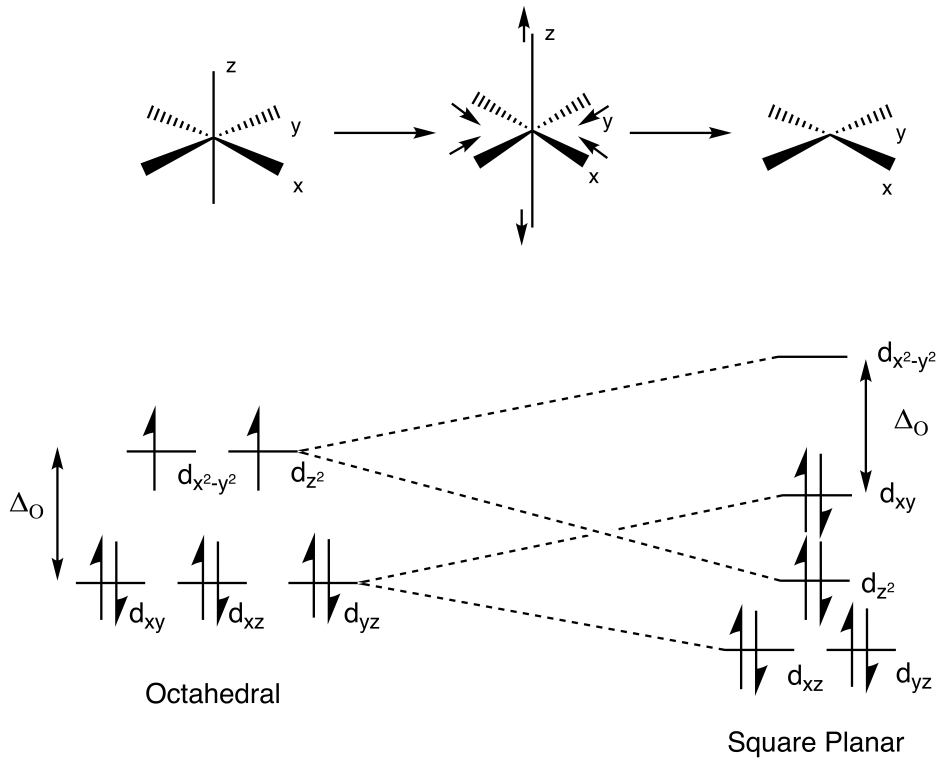


Figure 1.17: CFSE (Crystal Field Stabilisation Energy) diagram of octahedral and square planar geometries.

The square planar geometry is derived from the octahedral system by a hypothetical elongation of the axial ligands in the z plane, lowering the repulsive electron-electron interactions and also therefore the energy of the orbitals with presence in the z-dimension,

d_{xy}, d_{yz}, d_{z^2}. Correspondingly, the ligands in the x and y planes contract, raising the energy of these orbitals, d_{xy} and $d_{x^2-y^2}$. The overall result is a net lowering of the energy of the complex, with a lowering of the coordination number from 6 to 4. These complexes are often examples of compounds that violate the 18-electron rule by being stable $16e^-$ complexes. The metal ions that commonly adopt this geometry are the aforementioned Group 10 metals Ni^{II}, Pd^{II} and Pt^{II}, particularly the latter two. However Rh^{I}, Ir^{I} and Au^{III} also possess a d^8 electron configuration and are therefore commonly found in this geometry. Due to their coordinative unsaturation, square planar complexes often show strong catalytic capabilities, such as Wilkinson's catalyst, $[Rh(PPH_3)_3Cl]$ (see *Figure 1.18*), utilised in the hydrogenation of alkenes. [89]

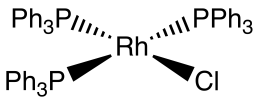


Figure 1.18: Structure of Wilkinson's catalyst, $[Rh(PPh_3)_3Cl]$.

For further information on transition metal catalysis, refer to *Chapter 3.1.1*.

1.2.2.2 Tiara-like Complexes

Tiara-like or toroidal complexes are a family of Group 10 transition metal-thiolate complexes, identified by a polynuclear $[M(\mu_2\text{-}SR)_2]_n$ structure, where M = Ni, Pd, Pt and R = any alkyl or aryl group and $n \geq 4$. The metal atoms are arranged in a plane, with the thiolate sulfurs bridging the metal centres above and below this plane. This forms a chain or ribbon of $[M(SR)_2]$ subunits which enclose to form a ring geometry. The general structure of these complexes is shown in *Figure 1.19*.

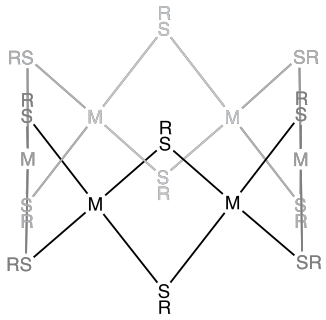


Figure 1.19: General structure of a hexanuclear (n = 6) tiara-like complex. M = Ni, Pd, Pt and R = alkyl, aryl.

The synthesis of these complexes can be achieved in one step by combination of a thiol ligand with a suitable metal salt in basic solution and stirring under ambient conditions for several hours. Precipitation of the resulting complex followed by washing and drying generally affords the desired complex in yields of between 60-90%. It has been observed that the yield has some concentration-dependence; in one report the lowering of the concentration of palladium chloride as the starting material from 0.25M to 0.04M reduced the yield from 90% to 67%.[90] In addition to this conventional synthesis, formation of tiara-like complexes has also been achieved by solvothermal synthesis.[91-93]

While Group 10 sulfides were originally thought of as insoluble polymeric species,[94] they have recently become more definitively characterised as these sulfur-bridged metallacrowns that represent an analagous structure to the -[M-N-O]- manganese metallacrowns pioneered by Pecoraro; it has been suggested that tiara-like complexes should follow the standard metallacrown designations, in this case a hexanuclear tiara would be denoted as 12-MC-6, where 12 is the number of linked atoms within the crown and 6 is the number of metal centres. It is important to note however that the number of atoms within the crown ring is actually 18 due to the doublecrown nature of the complex.

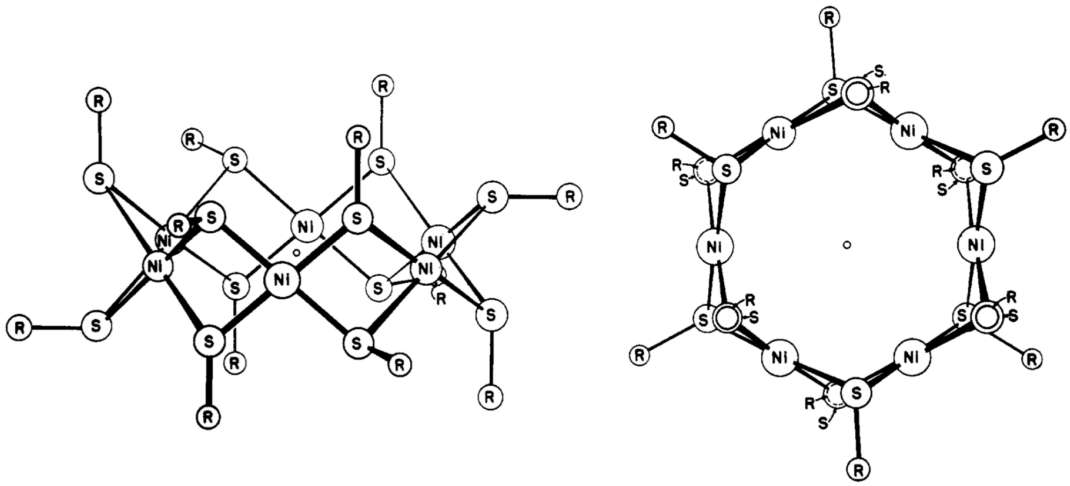


Figure 1.20: Structure of the first reported tiara-like complex $[Ni(SCH_2CH_3)_2]_6$. R = CH_2CH_3. Ligand groups omitted for clarity.[95]

The first reported synthesis of a tiara-like complex was published in 1965, formed by the reaction of nickel(II) chloride with bis(ethylthio)dimethyltin.[95] Recrystallisation of the obtained product from hexane allowed the elucidation of the structure by single crystal x-ray diffraction (XRD), revealing the novel doublecrown structure. Unlike previous insoluble metal sulfides, the newly discovered compound, in the form of a purple-black crystalline powder, was found to be soluble in organic solvents. A related compound, palladium n-propyl mercaptide, had already been reported the previous year with one proposed structure being the tiara doublecrown.[96] This was confirmed a few years later in 1968 when the tiara crown was revealed by x-ray diffraction.[97] The crystallographic structure is shown in *Figure 1.21*.

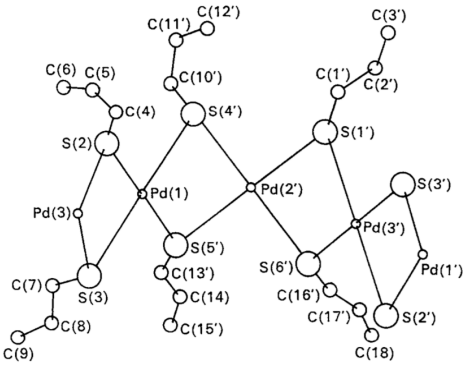


Figure 1.21: The crystal structure of palladium n-propyl mercaptide, determined by x-ray diffraction. The asymmetric unit of the complex is shown with the remainder of the ring generated by symmetry methods.[97]

1.3 Thesis Outline

The principle aims of this work have been to develop a foundation on which tiara-like complexes, as cyclic molecules, may be incorporated into supramolecular structures such as catenanes and rotaxanes. Supramolecular chemistry is still accelerating in application and interest but the inclusion of inorganic components is not yet widespread, aside from the use of metal atoms to template the formation of the assemblies. Metal complexes offer diverse properties that are often not matched by their organic counterparts, such as reversible binding, along with unique magnetic, catalytic and electronic properties. Hybrid organic-inorganic complexes are therefore attractive targets to synthesise as they combine useful properties of both those areas of chemistry. Some novel molecules of this composition have already been synthesised.[98,99]

However, it was quickly noted that the most common size of tiara-like complex, hexanuclear, would be insufficient for these supramolecular assemblies. There are no documented reports of any hexanuclear tiaras acting as molecular hosts for a small guest compound due to the small volume of the central void. The number of reported complexes with a greater size than hexanuclear is unfortunately very few when compared to the 6-membered tiaras. Further to this, there are essentially no dedicated studies investigating the factors that contribute to the formation of a larger ring, as virtually all differently sized tiara rings have been formed by chance rather than intentionally designed to possess a greater nuclearity.

The object of this work has therefore been to firstly understand some of these factors that result in the formation of a larger nuclearity than 6, and secondly develop a method towards reliably synthesising larger nuclearity complexes. This is initially discussed within *Chapter 2*, where the historical reports of different nuclearity tiaras are introduced, along with an examination of the proposed reasoning behind the acquisition of the unusually (non-

hexanuclear) sized ring. This is continued further in the Results section where a simple method to alter the composition of a tiara-like complex is introduced.

The complexes synthesised in *Chapter 2* are then examined in greater detail in the rest of the thesis, including a study of the inclusion properties of one of the complexes reported. As mentioned previously, the impetus behind utilising inorganic components stems from their unique electronic and catalytic properties, and these are also examined in detail in *Chapter 3*. The fourth chapter then deals with other modifications to the tiara core, including the replacement of the metal and the incorporation of two different metals, as few studies have dealt with the change in properties of a single tiara complex solely by altering the choice of metal within the crown.

This work aims to investigate some of the lesser-studied areas around tiara-like complexes. It is hoped that this thesis will serve as a foundation towards those attempting to combine the unique structure and diverse properties of tiaras into supramolecular assemblies.

1.4 References

1. C. J. Pedersen, *J. Am. Chem. Soc.*, 1967, **89** (10), 2495-2496.
2. C. J. Pedersen, *J. Am. Chem. Soc.*, 1967, **89** (26), 7017-7036.
3. "The Nobel Prize in Chemistry 1987". Nobelprize.org. Nobel Media AB 2014. Web. 8 Mar 2018. <http://www.nobelprize.org/nobel_prizes/chemistry/laureates/1987/>.
4. C. J. Pedersen, *Angew. Chem. Int. Ed. Engl.*, 1988, **27**, 1021-1027.
5. C. J. Pedersen, *Aldrichimica Acta*, 1971, **4**, 1.
6. C. J. Pedersen, *Org. Synth.*, 1972, **52**, 66.
7. C. J. Pedersen and H. K. Frensdorff, *Angew. Chem. Int. Ed. Engl.*, 1972, **11**, 16-25.
8. A. C. L. Su and J. F. Weiher, *Inorg. Chem.*, 1968, **7** (1), 176-177.
9. B. Dietrich, J.-M. Lehn and J.-P. Sauvage, *Tetrahedron Lett.*, 1969, **34**, 2885-2888.
10. B. Dietrich, J.-M. Lehn and J.-P. Sauvage, *Tetrahedron Lett.*, 1969, **34**, 2889-2892.
11. "The Nobel Prize in Chemistry 2016". Nobelprize.org. Nobel Media AB 2014. Web. 10 Mar 2018. <http://www.nobelprize.org/nobel_prizes/chemistry/laureates/2016/>.
12. J.-M. Lehn and J.-P. Sauvage, *J. Am. Chem. Soc.*, 1975, **97**, 6700-6707.
13. D. J. Cram, T. Kaneda, R. C. Helgeson and G. M. Lein, *J. Am. Chem. Soc.*, 1979, **101**, 6752-6754.
14. K. N. Trueblood, C. B. Knobler, E. Maverick, R. C. Helgeson, S. B. Brown and D. J. Cram, *J. Am. Chem. Soc.*, 1981, **103**, 5594-5596.
15. D. J. Cram, T. Kaneda, R. C. Helgeson, S. B. Brown, C. B. Knobler, E. Maverick and K. N. Trueblood, *J. Am. Chem. Soc.*, 1985, **107**, 3645-3657.
16. D. J. Cram, *Angew. Chem. Int. Ed. Engl.*, 1988, **27**, 1009-1020.
17. D. J. Cram and G. M. Lein, *J. Am. Chem. Soc.*, 1985, **107**, 3657-3668.
18. M. S. Lah and V. L. Pecoraro, *J. Am. Chem. Soc.*, 1989, **111**, 7258-7259.
19. R. M. Izatt, J. S. Bradshaw, S. A. Nielsen, J. D. Lamb and J. J. Christensen, *Chem. Rev.*, 1985, **85**, 271-339.
20. E. Mason and H. A. Eick, *Acta Cryst. B.*, 1982, **38**, 1821-1823.
21. M. S. Lah, M. L. Kirk, W. Hatfield and V. L. Pecoraro, *J. Chem. Soc. Chem. Commun.*, 1989, 1606.
22. V. L. Pecoraro, *Inorg. Chim. Acta*, 1989, **155**, 171.
23. G. Mezei, C. M. Zaleski and V. L. Pecoraro, *Chem. Rev.*, 2007, **107**, 4933-5003.
24. M. Ostrowska, I. O. Fritsky, E. Gumienna-Kontecka and A. V. Pavlishchuk, *Coord. Chem. Rev.*, 2016, 304-332.
25. D. Bacco, V. Bertolasi, F. Dallavalle, L. Galliera, N. Marchetti, L. Marchio, M. Remelli and M. Tegoni, *Dalton Trans.*, 2011, **40**, 2491-2501.

26. I. A. Golenya, E. Gumienna-Kontecka, A. N. Boyko, M. Haukka, I. O. Fritsky, *Inorg. Chem.*, 2012, **51** (11), 6221-6227.
27. J. Jankolovits, J. W. Kampf and V. L. Pecoraro, *Inorg. Chem.*, 2013, **52** (9), 5063-5076.
28. A. J. Stemmler, J. W. Kampf and V. L. Pecoraro, *Inorg. Chem.*, 1995, **34** (9), 2271-2272.
29. T. K. Si, S. Chakraborty, A. K. Mukherjee, M. G. B. Drew and R. Bhattacharyya, *Polyhedron*, 2008, **27**, 2233-2242.
30. A. Maspero, S. Brenna, S. Galli and A. Penoni, *J. Organomet. Chem.*, 2003, **672**, 123-129.
31. C.-S. Lim, J. Jankolovits, P. Zhao, J. W. Kampf and V. L. Pecoraro, *Inorg. Chem.*, 2011, **50** (11), 4832-4841.
32. J. T. Grant, J. Jankolovits and V. L. Pecoraro, *Inorg. Chem.*, 2012, **51** (15), 8034-8041.
33. J.J. Bodwin, A.D. Cutland, R.G. Malkani and V. L. Pecoraro, *Coord. Chem. Rev.*, 2001, **216**, 489.
34. P. Happ, C. Plenk and E. Rentschler, *Coord. Chem. Rev.*, 2015, **289**, 238-260.
35. C.M. Zaleski, S. Tricard, E.C. Depperman, W. Wernsdorfer, T. Mallah, M.L. Kirk and V. L. Pecoraro, *Inorg. Chem.*, 2011, **50**, 11348-11352.
36. M. Fang, H. Zhao, A.V. Prosvirin, D. Pinkowicz, B. Zhao, P. Cheng, W. Wernsdorfer, E. K. Brechin and K. R. Dunbar, *Dalton Trans.*, 2013, **42**, 14693-14701.
37. C.M. Zaleski, E.C. Depperman, J.W. Kampf, M.L. Kirk and V. L. Pecoraro, *Inorg. Chem.*, 2006, **45**, 10022-10024.
38. J.-M. Lehn, *Angew. Chem. Int. Ed.*, 1988, **27**, 89-112.
39. R. Chakrabarty, P. S. Mukherjee and P. J. Stang, *Chem. Rev.*, 2011, **111**, 6810-6918.
40. E. Wasserman, *J. Am. Chem. Soc.*, 1960, **82**, 4433-4434.
41. S. F. M. van Dongen, S. Cantekin, J. A. A. W. Elemans, A. E. Rowan and R. J. M. Nolte, *Chem. Soc. Rev.*, 2014, **43**, 99-122.
42. O. Safarowsky, B. Windisch, A. Mohry and F. Vögtle, *J. Prakt. Chem.*, 2000, **342**, 437-444.
43. G. Schill and A. Lüttringhaus, *Angew. Chem. Int. Ed.*, 1964, **3** (8), 546-547.
44. I.T. Harrison and S. Harrison, *J. Am. Chem. Soc.*, 1967, **89**, 5723-5724.
45. G. Agam, D. Graiver and A. Zilkha, *J. Am. Chem. Soc.*, 1976, **98**, 5206-5214.
46. C. O. Dietrich-Buchecker and J.-P. Sauvage, *J. Am. Chem. Soc.*, 1984, **106**, 3043-3045.
47. M. Cesario, C. O. Dietrich-Buchecker, J. Guilhem, C. Pascard and J.-P. Sauvage, *J. Chem. Soc. Chem. Commun.*, 1985, **5**, 244-247.
48. C. O. Dietrich-Buchecker, J.-P. Sauvage and J. P. Kintzinger, *Tetrahedron Lett.*, 1983, **24** (46), 5095-5098.
49. D. M. P. Mingos, J. Yau, S. Menzer and D. J. Williams, *Angew. Chem. Int. Ed. Engl.*, 1995, **34**, 1894-1895.
50. H. Schmidbaur, *Gold Bull.*, 1990, **32**, 11-21.

51. I. T. Harrison and S. Harrison, *J. Am. Chem. Soc.*, 1967, **89** (22), 5723-5724.
52. I. T. Harrison, *J. Chem. Soc. Chem. Commun.*, 1972, 231-232.
53. I. T. Harrison, *J. Chem. Soc. Perkin Trans.*, 1974, 301-304.
54. H. Ogina and K. Ohata, *Inorg. Chem.*, 1984, **23**, 3312-3316.
55. P. T. Glink, A. I. Oliva, J. F. Stoddart, A. J. P. White and D. J. Williams, *Angew. Chem. Int. Ed.*, 2001, **40**, 1870-1875.
56. M. Horn, J. Ihringer, P. T. Glink and J. F. Stoddart, *Chem. Eur. J.*, 2003, **9**, 4046-4054.
57. F. Aricó, T. Chang, S. J. Cantrill, S. I. Khan and J. F. Stoddart, *Chem. Eur. J.*, 2005, **11**, 4655-4666.
58. C. Dietrich-Buchecker, G. Rapenne and J.-P. Sauvage, *Coord. Chem. Rev.*, 1999, **185–186**, 167-176.
59. M. Gupta, S. Kang and M. F. Mayer, *Tetrahedron Lett.*, 2008, **49**, 2946-2950.
60. P. L. Anelli, N. Spencer and J. F. Stoddart, *J. Am. Chem. Soc.*, 1991, **113**, 5131-5133.
61. R. A. Bissell, E. Córdova, A. E. Kaifer and J. F. Stoddart, *Nature*, 1994, **369** (6476), 133-137.
62. J. P. Collin, P. Gavina and J.-P. Sauvage, *Chem. Commun.*, 1996, **17**, 2005-2006.
63. M. C. Jiménez, C. Dietrich-Buchecker and J.-P. Sauvage, *Angew. Chem. Int. Ed.*, 2000, **39** (18), 3284-3287.
64. Y. Liu, A. H. Flood, P. A. Bonvallet, S. A. Vignon, B. H. Northrop, H.-R. Tseng, J. O. Jeppesen, T. J. Huang, B. Brough, M. Baller, S. Magonov, S. D. Solares, W. A. Goddard, C.-M. Ho and J. F. Fraser, *J. Am. Chem. Soc.*, 2005, **127** (27), 9745-9759.
65. J. D. Badjić, V. Balzani, A. Credi, S. Silvi and J. F. Stoddart, *Science*, 2004, **303** (5665), 1845-1849.
66. T. J. Huang, B. Brough, C.-M. Hoa, Y. Liu, A. H. Flood, P. A. Bonvallet, H.-R. Tseng, J. F. Stoddart, M. Baller and S. Magonov, *Appl. Phys. Lett.*, 2004, **85**, 5391-5193.
67. V. Balzani, M. Clemente-Len, A. Credi, B. Ferrer, M. Venturi, A. H. Flood and J. F. Stoddart, *Proc. Natl. Acad. Sci. USA*, 2006, **103** (5), 1178-1183.
68. E. Kay, D. Leigh and F. Zerbetto, *Angew. Chem. Int. Ed.*, 2007, **46** (1-2), 72-191.
69. N. Koumura, R. W. J. Zijlstra, R. A. van Delden, N. Harada and B. L. Feringa, *Nature*, 1999, **401** (6749), 152-155.
70. J. Vachon, G. T. Carroll, M. M. Pollard, E. M. Mes, A. M. Brouwer and B. L. Feringa, *Photochem. Photobiol. Sci.*, 2014, **13**, 241-246.
71. R. A. van Delden, M. K. J. ter Wiel, M. M. Pollard, J. Vicario, N. Koumura and B. L. Feringa, *Nature*, 2005, **437** (7063), 1337-1340.
72. R. Eelkema, M. M. Pollard, J. Vicario, N. Katsonis, B. S. Ramon, C. W. M. Bastiaansen, D. J. Broer and B. L. Feringa, *Nature*, 2006, **440** (7081), 163-163.
73. S. P. Fletcher, F. Dumur, M. M. Pollard and B. L. Feringa, *Science*, 2005, **310** (5745), 80-82.

74. N. Ruangsupapichat, M. M. Pollard, S. R. Harutyunyan and B. L. Feringa, *Nat. Chem.*, 2011, **3**, 53-60.
75. M. Peplow, *Nature*, 2015, **525**, 18-21.
76. C. Cheng, P. R. McGonigal, S. T. Schneebeli, H. Li, N. A. Vermeulen, C. Ke and J. F. Stoddart, *Nat. Nanotech.*, 2015, **10**, 547-553.
77. Y. Shirai, A. J. Osgood, Y. M. Zhao, K. F. Kelly and J. M. Tour, *Nano Lett.*, 2005, **5** (11), 2330-2334.
78. J.-F. Morin, Y. Shirai and J. M. Tour, *Org. Lett.*, 2006, **8** (8), 1713-1716.
79. T. Kudernac, N. Ruangsupapichat and M. Parschau, *Maci. Nature*, 2011, **479** (7372), 208-211.
80. W. C. Zeise, *Annalen der Physik und Chemie*, 1834, **107** (27), 369-431.
81. T.L. Cottrell, *The Strengths of Chemical Bonds*, 2nd ed., Butterworths, London, 1958.
82. F. G. Bordwell, *Acc. Chem. Res.*, 1988, **21**, 456-463.
83. R. G. Pearson, *J. Am. Chem. Soc.*, 1963, **85** (22), 3533-3539.
84. K. S. Hagen and R. H. Holm, *J. Am. Chem. Soc.*, 1982, **104**, 5496-5497.
85. D. Swenson, N. C. Baenziger and D. Coucouvanis, *J. Am. Chem. Soc.*, 1978, **100** (6), 1932-1934.
86. S. A. Koch, L. E. Maelia and M. Millar, *J. Am. Chem. Soc.*, 1983, **105** (18), 5944-5945.
87. S. Han, R. S. Czernuszewicz and T. G. Spiro, *Inorg. Chem.*, 1986, **25** (13), 2276-2277.
88. K. S. Hagen, D. W. Stephan and R. H. Holm, *Inorg. Chem.*, 1982, **21** (11), 3928-3936.
89. J. A. Osborn, F. H. Jardine, J. F. Young and G. Wilkinson, *J. Chem. Soc. A*, 1966, 1711-1732.
90. Y. Yamashina, Y. Kataoka and Y. Ura, *Inorg. Chem.*, 2014, **53**, 3558-3567.
91. C. Tan, M. Jin, X. Ma, Q. Zhu, Y. Huang, Y. Wang, S. Hu, T. Sheng and X. Wu, *Dalton Trans.*, 2012, **41**, 8472-8476.
92. C. Tan, M. Jin, H. Zhang, S. Hu, T. Sheng and X. Wu, *CrystEngComm*, 2015, **17**, 5110-5115.
93. J. Wang, F. Jian, B. Huang and Z. Bai, *J. Solid State Chem.*, 2013, **204**, 272-277.
94. K. A. Jensen, *Z. anorg. Chem.*, 1944, **252**, 227.
95. P. Woodward, L. F. Dahl, E. W. Abel and B. C. Crosse, *J. Am. Chem. Soc.*, 1965, **87**, 5251-5253.
96. R. G. Hayter and F. S. Humiec, *J. Inorg. Nucl. Chem.*, 1964, **26**, 807.
97. N. R. Kunchur, *Acta Cryst. B.*, 1968, **24**, 1623-1633.
98. C.-F. Lee, D. A. Leigh, R. G. Pritchard, D. Schultz, S. J. Teat, G. A. Timco and R. E. P. Winpenny, *Nature*, 2009, **458**, 314-318.
99. H. Rath, G. A. Timco, V. Corradini, A. Ghirri, U. del Pennino, A. Fernandez, R. G. Pritchard, C. A. Muryn, M. Affronte and R. E. P. Winpenny, *Chem. Commun.*, 2013, **49**, 3404-3406.

Chapter 2

Synthesis and Formation of Tiara-like Complexes

2.1 Introduction

2.1.1 Tiara Nuclearity

The question of the nuclearity, or size, of tiara-like complexes has been of interest since 1984 following the synthesis of $[Ni(SC_5H_9N(CH_3)_2)_2]_4$, the first non-hexanuclear tiara-like complex.[1] The driving force behind the formation of a smaller tiara-like complex was attributed to the steric bulk of the piperidine ligands used in the tiara formation; it was surmised that impossibly short H···H contacts would result in any complex of a nuclearity greater than 4. Within a year the first octanuclear tiara[2] was published, $[Ni(SCH_2COOEt)_2]_8$, firmly establishing the capability of these toroidal complexes to attain a variety of sizes when they had been previously limited to hexanuclear. The rationale behind the observation of the larger tiara-like complex was justified by the occupation of the central void within the tiara ring by a re-entrant ligand. In addition, the authors were quick to examine and contrast the different structural features in $[Ni(SC_5H_9N(CH_3)_2)_2]_4$, $[Ni(SEt)_2]_6$[3] and $[Ni(SCH_2COOEt)_2]_8$. The structures of these complexes are compared in *Figure 2.1*.

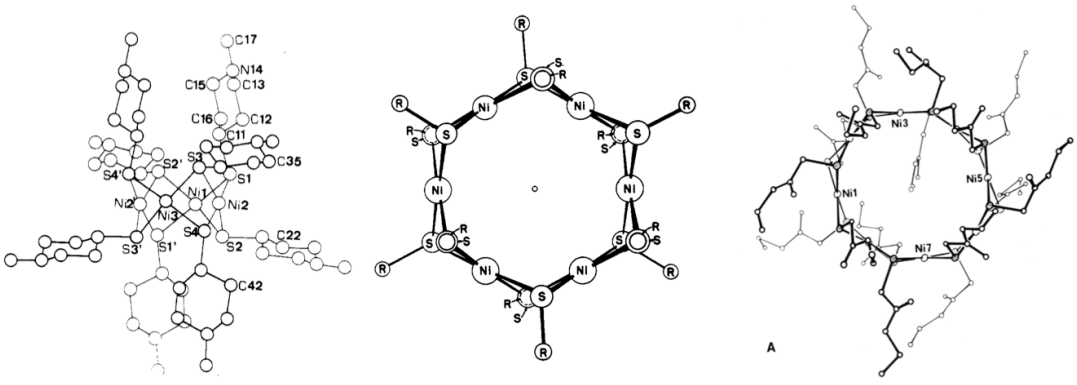


Figure 2.1: Structures of (from left to right): $[Ni(SC_5H_9N(CH_3)_2)_2]_4$,[1] $[Ni(SEt)_2]_6$,[3] and $[Ni(SCH_2COOEt)_2]_8$,[2] examples of a tetranuclear, hexanuclear and octanuclear tiara respectively.

With several exceptions, the vast majority of tiara-like complexes reported in the literature contain an even number of fused $[Pd(SR)_2]$ subunits. Tiara-like complexes that contain an

odd number of subunits are formed far less frequently and in generally lower yield relative to even numbered complexes.[4-9] The first pentanuclear complex was reported in 1987 as the complex $[Ni(SEt)_2]_5$, the structure of which is given in *Figure 2.2*.[4] Notably, this is the five-membered equivalent of $[Ni(SEt)_2]_6$, the first published tiara-like complex. Due to the incorporation of the same ligand, resulting in the identical composition of the two complexes, the two species differ only in the nuclearity.

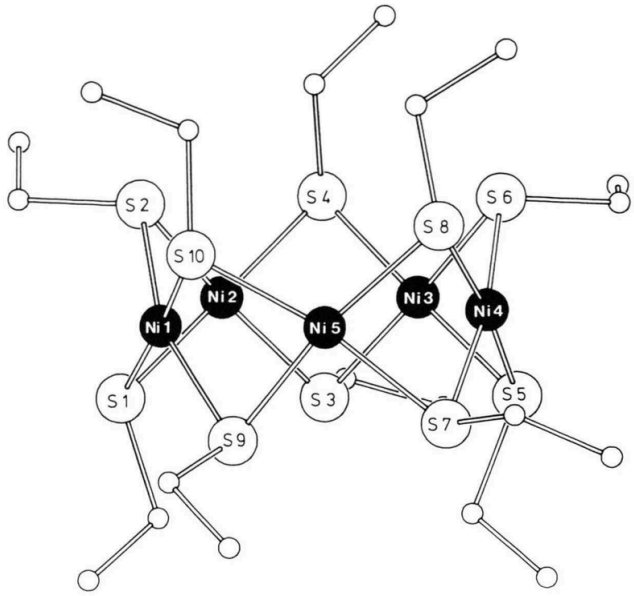


Figure 2.2: Structure of $[Ni(SEt)_2]_5$[4]

Examination of the synthetic methods used in the formation of the complexes offers no obvious explanations for the observations seen in these reactions. While $[Ni(SEt)_2]_5$ was formed by the reaction of ethanethiol with $NiCl_2$ in the presence of NaOMe, $[Ni(SEt)_2]_6$ was synthesised by the reaction of $NiCl_2$ and bis(ethylthio)dimethyltin. Interestingly, the former appears to follow the most conventional methodology for tiara formation but yields the more unusual product. The yields of the tiaras isolated were reported as 53% for $[Ni(SEt)_2]_6$ and 10% for $[Ni(SEt)_2]_5$, demonstrating the lower yield obtained for odd-numbered tiara-like complexes. There is an interesting structural feature in $Ni(SEt)_2]_5$ that arises from the odd number of $[Ni(SR)_2]$ units. For tiara-like complexes with an even number of subunits, the

thiolate ligands alternate between adopting an equatorial and an axial configuration around the ring, leading to the least amount of steric repulsion between the ligands. However, for this pentanuclear complex, the odd number of subunits leads to four of the adjacent thiolate ligands (S8/S10 axial/axial and S7/S9 equatorial/equatorial in *Figure 2.2*) adopting identical configurations. This forced configuration is sterically unfavourable, particularly for the axial/axial ligands; this can be evidenced by the > S10-Ni5-S8 bond angle, which adopts a value of 108.9(1)°, far removed from the ideal 90° angle in regular square planar geometry and much higher than the average value for comparable bond angles in the complex of 98.3°. The equatorial/equatorial geometry appears to be less strained as the > S9-Ni5-S7 angle is measured as 89.4(1)°, much lower than the average value and presumably made acute by the high strain axial/axial configuration on the same Ni unit.

This disruption of the ideal alternating equatorial/axial geometry around the ring may be one of the reasons for the lower yield of the odd nuclearity tiaras and their limited reporting when compared with even nuclearity complexes. Further justification may arise from the M - S π-bonding present in the structure. It has been suggested that the network of π-bonding orbitals contribute a significant effect in stabilising the structure of the complexes; in an even nuclearity tiara the orbitals zigzag around the complex and form a closed π-system whereas in a tiara with an odd number of $[Pd(SR)_2]$ units the orbitals are out of phase;[10-12] an example of Pd - S π-bonding is illustrated in *Figure 2.3*.

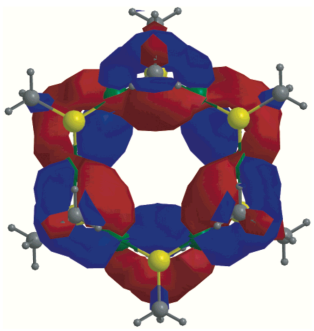


Figure 2.3: Example of Pd - S π-bonding in a hexanuclear Pd tiara[12].

Finally, the growth and termination phases of the tiara formation may favour even-nuclear tiaras. In the substitution - polycondensation - ring closure mechanism of tiara formation postulated by Chen *et al.*, rearrangement of the chains possessing an odd number of metal centres was required to avoid spatial hindrance on the head-to-tail ring closure to form the cyclic complex.[7] This theory was given in justification of the lower yields seen for odd nuclearity complexes; reaction of 2-phenylethanethiol with $Pd(NO_3)_2.2H_2O$ in the presence of triethylamine in acetonitrile resulted in the formation of $[Pd(SCH_2CH_2C_6H_5)_2]_n$ where $4 \leq n \leq 20$. Calculated structures for $4 \leq n \leq 10$ are shown in *Figure 2.4*. Separation of the complexes was achieved using preparative thin-layer chromatography (pTLC), however the origin of the multiple complexes observed was not fully explained.

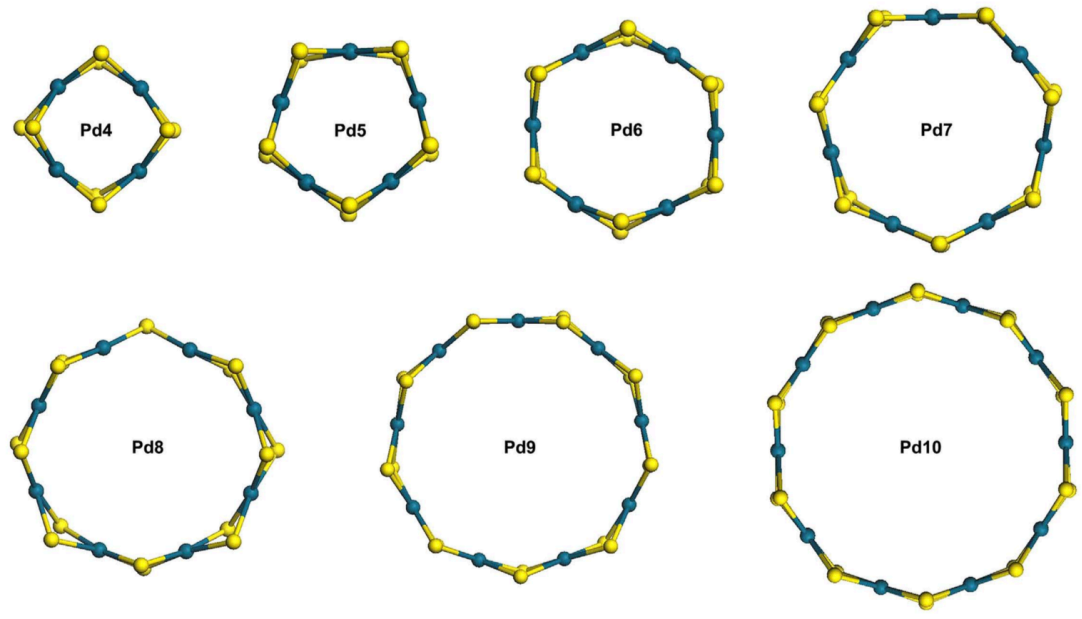


Figure 2.4: Calculated structures for tetranuclear to decanuclear $[Pd(SCH_2CH_2C_6H_5)_2]_n$ tiara-like complexes.[7] The structures were optimised for lowest energy state by density functional theory (DFT). The ethylphenyl ligand atoms were omitted for clarity.

Further complexes of unusual nuclearity have been documented. Nonanuclear and undecanuclear nickel tiara-like complexes $[Ni(SPh)_2]_9$ and $[Ni(SPh)_2]_{11}$ (see *Figure 2.5*) were reported in 2002 and were theorised to be stabilised by weakly attractive phenyl ··· phenyl

dispersion forces.[5] The larger complex was the first reported example of a tiara-like inclusion complex when it was shown that THF was encapsulated into the centre of the toroid on crystallisation, giving rise to the theory that the solvent acted as a template for the formation of a larger ring.

These complexes were synthesised using identical reagents and solvent; the change in product from nonanuclear to undecanuclear was effected by changing the experimental parameters; lowering of the reaction temperature from room temperature to 0°C and slowing of the thiol addition from instantaneous to dropwise over one hour. Both products were formed in their respective reactions in estimated yields of 20-30%, consistent with the lower yields expected for odd nuclearity tiaras.

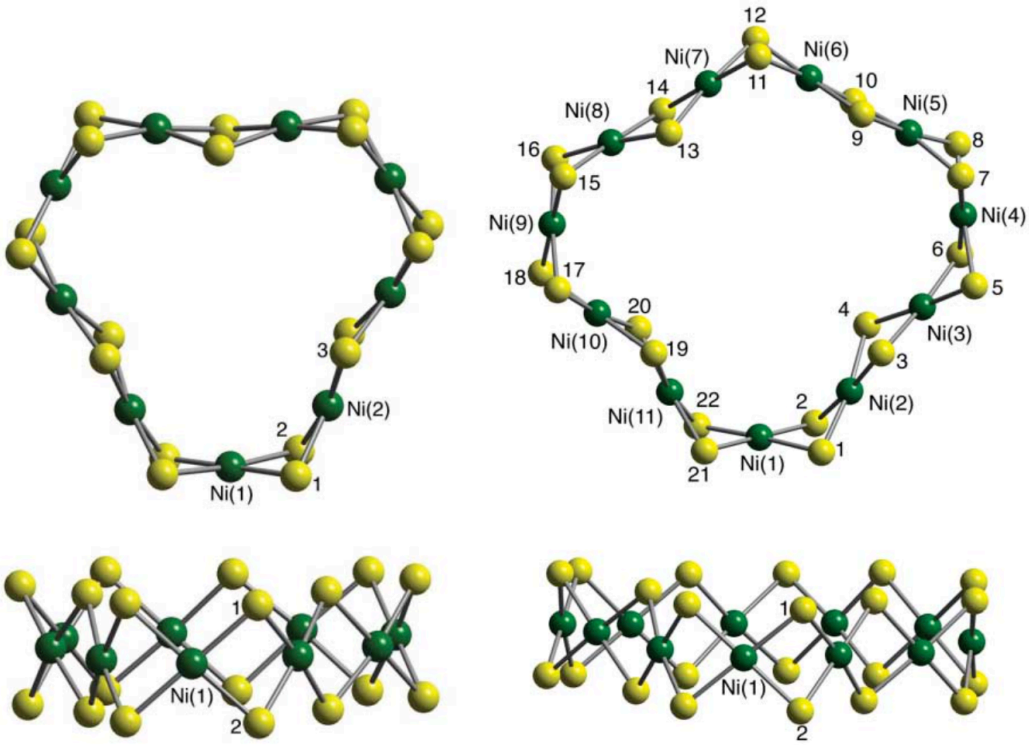


Figure 2.5: Crystal structures of $[Ni(SPh)_2]_9$ (left) and $[Ni(SPh)_2]_{11}$ (right). The phenyl ligand atoms were omitted for clarity.[5]

In 2006 the first decanuclear tiara was reported[13] and was achieved by adopting a 'mixed ligand' approach where two different thiolate ligands are included within the final complex. The complex, $[Ni(S\textit{t}Bu)(SCH_2CH_2SCH_3)]_{10}$, is theorised to be formed due to the large steric bulk of the tert-butyl thiolate ligands. It was shown to be able to encapsulate benzene as a guest within the core of the tiara crown. The structure of the inclusion complex is shown below in *Figure 2.6*.

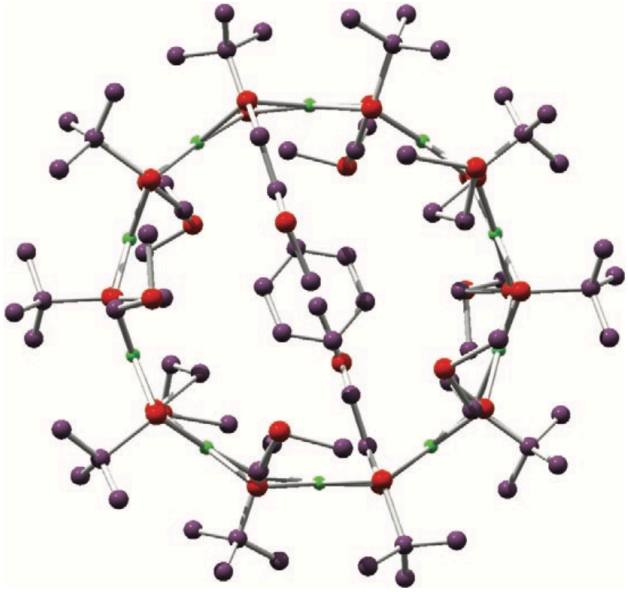


Figure 2.6: Crystal structure of the $([Ni(S\textit{t}Bu)(SCH_2CH_2SCH_3)]_{10} \subset C_6H_6)$ inclusion complex.[13]

A dodecanuclear variant of the above complex was published in 2010 by the same authors with the structure of $[Ni(S\textit{t}Bu)(SCH_2CH_2SCH_2CH_3)]_{12}$, i.e. extension of the ligand chain by a single methylene unit.[14] The enlargement of the central void allows the complex to encapsulate toluene rather than benzene.

At present therefore, there is a wide variety of sizes of tiara-like complexes, especially for nickel-based rings. It has been shown that while in general, the thiol used determines the size of the complex, in a few cases tiara-like complexes containing the same thiolate ligand can be

made to form rings of different sizes. These can be due to changes in the experimental parameters, for $[Ni(SPh)_2]_9$ / $[Ni(SPh)_2]_{11}$, or post-modification of the thiol following ring closure as for $[Pd(SCH_2COOMe)_2]_6$ / $[Pd(SCH_2COOMe)_2]_8$ or not yet fully understood reasons, such as for $[Pd(SCH_2CH_2C_6H_5)_2]_n$.

It should be apparent that the size of the tiara will have significant effects on the resultant properties of the complex, especially for supramolecular applications such as host-guest binding, or the construction of elaborate supramolecules such as catenanes or rotaxanes. Most examples of these tiaras that have unusual or multiple sizes were synthesised serendipitously and very little investigative research has been performed on understanding the origins of these effects.

2.1.2 Hydrogen Bonding

"The hydrogen bond is an attractive interaction between a hydrogen atom from a molecule or a molecular fragment X–H in which X is more electronegative than H, and an atom or a group of atoms in the same or a different molecule, in which there is evidence of bond formation."

The above description forms the current International Union of Pure and Applied Chemistry (IUPAC) definition of a hydrogen bond.[15] At its very simplest, it describes an attraction between an electronegative atom and a hydrogen bonded to another electronegative atom. This is often denoted as D-H···A wherein D represents the electronegative atom bonded to the hydrogen that forms the hydrogen bond donor and A represents an electronegative atom, often possessing at least one pair of electrons that are free to interact with the electropositive hydrogen atom that forms the hydrogen bond acceptor.[16] Such attractive forces can normally only tentatively denoted as 'bonds', with often quite low bond enthalpies and a long distance between the non-covalently-bonded electronegative atom and the the hydrogen atom.

However, depending on the electronegativities involved, hydrogen bonds can be strong interactions, particularly when multiple hydrogen bonds are involved. The strengths of individual hydrogen bonds may range anywhere from 4 kJmol^{-1} for weak hydrogen bonds, such as hydrogen atoms interacting with an electron-rich pi cloud[17] up to around 184 kJmol^{-1} for F-H···F interactions.[18-20]

When these interactions occur between hydrogen atoms and electron lone pairs on the acceptor atom, the angle of the bonding > D-H···A is typically between 130° to 180°. Because of this, hydrogen bonding can be considered to be strongly directional, and this allows for the formation of discrete, regular geometry- opening up a wide range of possibilities for supramolecular structures. Possibly the most widely recognised example of this phenomenon is found within the structure of deoxyribonucleic acid, DNA, constructed from the four nucleobases adenine, thymine, guanine and cytosine. The two strands are held together by a number of combined hydrogen bonds between the base pairs that also confer selectivity onto the assembly; adenine will form two hydrogen bonds with a complementary thymine on the secondary strand and vice versa, whereas cytosine will form three hydrogen bonds with guanine and again vice versa. This bonding is illustrated below in *Figure 2.7*.

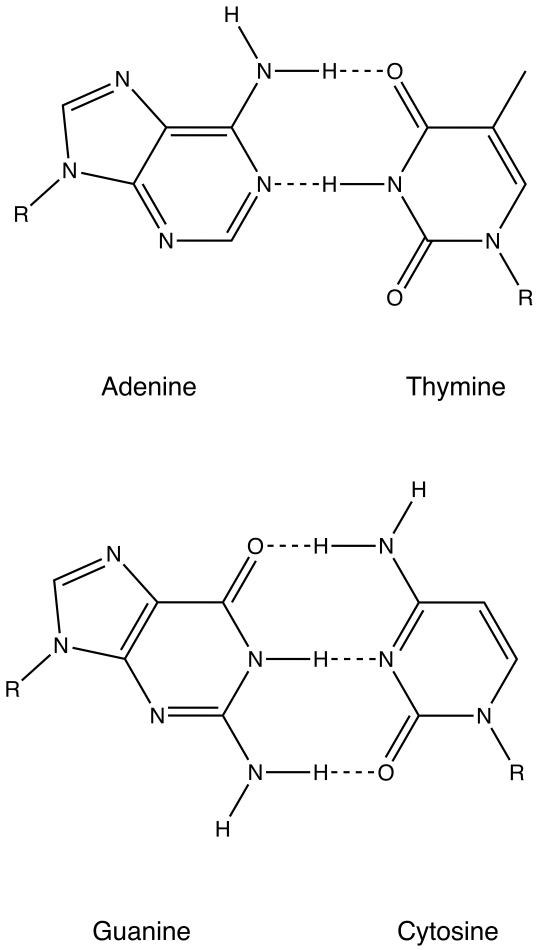


Figure 2.7: Structure of the four DNA nucleobases and their Watson-Crick hydrogen bonding pairing. The hydrogen bonding is strongly selective, as adenine and thymine will form two hydrogen bonds whereas guanine and cytosine form three. R groups represent the phosphate deoxyribose backbone of DNA.

The lengths of hydrogen bonds may be measured from the donor atom to the acceptor atom (D···A) or from the hydrogen atom to the acceptor atom (H···A). All hydrogen bonding distances in this work were calculated using crystallographic structures. Due to the small electron densities associated with hydrogen atoms coupled with the relatively low electronegativity of the element, they are usually exceedingly difficult to accurately locate by x-ray diffraction and were therefore placed at calculated positions. Hence, all hydrogen bonding interactions reported herein, unless otherwise specified, are reported corresponding to the donor-acceptor distance D···A for greater accuracy.

2.1.3 Purification of Tiara-like Complexes

Purification protocols for tiara-like complexes are generally limited, consisting ordinarily of precipitation or crystallisation of the product followed by washing and drying to remove excess thiol and solvent. This has often been sufficient to isolate analytically pure complex; however the efficacy of this procedure drops dramatically when applied to a reaction mixture of several tiara-like complexes. However, several groups have reported methods to separate tiara-like complexes containing either different ligands or the same ligand (identical composition but differing nuclearity).

In the original synthesis of $[Pt(SCH_2COOCH_3)_2]_8$, it was obtained along with the corresponding nona- and deca-nuclear toroids,[21] and the mixture was not successfully purified. True separation of a mixture of tiara-like complexes was not achieved until 2015 when Chen *et al.* successfully separated a mixture of $[Pd(SCH_2CH_2Ph)_2]_n$, where $4 \leq n \leq 20$ by using preparative thin-layer chromatography (pTLC), the result is given in *Figure 2.8*.[7]

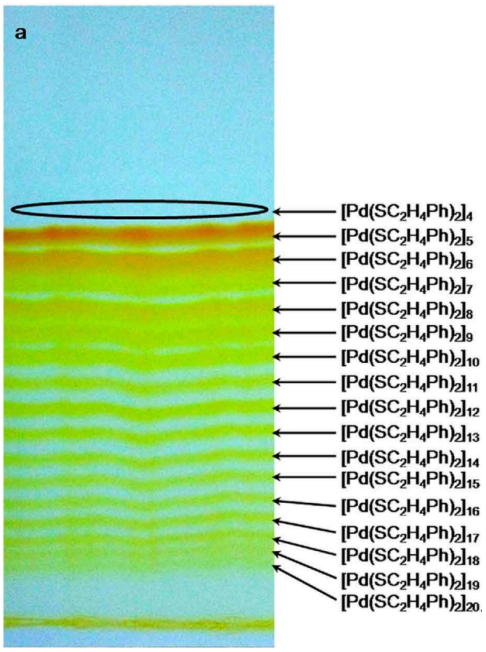
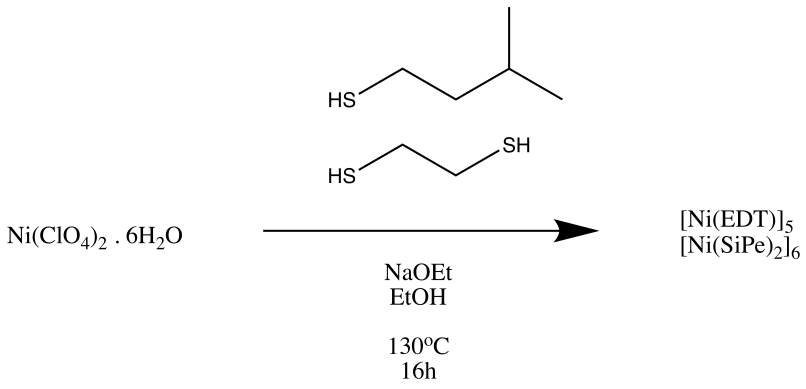


Figure 2.8: pTLC plate showing separation of a mixture of $[Pd(SCH_2CH_2Ph)_2]_n$ tiara-like complexes, where $4 \leq n \leq 20$ (eluted DCM: Petrol Ether, 1/3 v:v).[7]

The use of this technique in the separation of tiara-like complexes is wholly unique. The large

ligand present in the complex, consisting of -SCH_2CH_2Ph, is effective at solubilising the complex. The covering of the tiara core with phenyl substituents offers a large degree of π - C-H interactions that allow the complex to follow the mobile phase on silica. No other reports have noted successful chromatographical separation or purification of a tiara-like complex.

It has been shown that tiara-like complexes may also be separated by manual separation of crystals formed from the solvothermal synthesis of two different tiaras. In the reaction of nickel perchlorate hexahydrate with a mixture of isopentylthiol and 1,2-ethanedithiol, complexes were formed containing only a single thiol ligand rather than a mixture of ligands.[6] Following the conclusion of the solvothermal synthesis, the different complexes could be identified visually by differing crystal morphologies and manually separated.



Scheme 2.1: The solvothermal synthesis of $[Ni(EDT)]_5$ and $[Ni(SiPe)_2]_6$ within the same reaction vessel, a formation of two distinct and unmixed product complexes.[6]

In addition to the simultaneous crystallisation of tiara-like complexes of completely differing compositions, it is also possible to iteratively crystallise complexes containing the same ligand. The tiara-like complexes $[Ni(StBu)(SCH_2CH_2SCH_2CH_3)]_{10}$ and $[Ni(StBu)(SCH_2CH_2SCH_2CH_3)]_{12}$ were initially obtained as a mixture of products obtained via the same reaction.[14] The former product was initially purified by crystallisation from toluene/ HMDSO to separate the decanuclear tiara in 65% yield, leaving the dodecanuclear tiara in

the solution. This product was then crystallised following refrigeration of the solution at -29°C for several months to obtain a 5% yield of the larger dodecanuclear ring.

2.2 Results and Discussion

2.2.1 Formation of a New Series of Tiara-like Complexes

The first section of the bulk of this work will describe the synthesis and detail the properties of a series of tiara-like complexes. Each of the complexes that will be described in this chapter are related to the other by similarities in the structure of the ligand. Each ligand has at least one common structural feature with at least one other ligand, allowing for a logical comparison of the resulting complexes. The first three complexes are grouped together into a 'family' of tiara-like complexes due to high structural similarities and symmetrical features. The primary characterisation of these compounds was performed using mass spectrometry via Matrix-Assisted Laser Desorption Ionisation. Due to the size of the complexes, other methods of ionisation for mass spectrometry, such as Electrospray Ionisation (ESI) or Electron Impact (EI), were found to be ineffective and the complexes were not observed. The introduction of a 'soft' ionisation technique wherein a UV laser and a highly UV absorbent matrix are used to initiate ionisation increased the frequency of successful characterisations significantly. A summary of the ligands used in this work is given below in *Table 2.1*, including the full name of each along with the formulae and shorthand designations.

Ligand Name	Full Formula	Shortened Designation	Reference
N-acetylcysteamine	$HSCH_2CH_2NHCOCH_3$	NAC	*Chapter 2.2.2*
Ethyl thioglycolate	$HSCH_2COOCH_2CH_3$	ETG	*Chapter 2.2.3*
2-mercaptoethyl acetate	$HSCH_2CH_2OCOCH_3$	MEA	*Chapter 2.2.4*
Ethyl mercaptamide	$HSCH_2CONHCH_2CH_3$	EMA	*Chapter 2.2.6*
Methyl 3-mercaptopropionate	$HSCH_2CH_2COOCH_3$	MMP	*Chapter 2.2.7*

Table 2.1: The full names of the ligands used in this study, along with their chemical formulae. Due to the lengthy names of the ligands, each is abbreviated using a three-letter code which will be used continuously throughout this work.

2.2.2 Synthesis of Pd NAC

2.2.2.1 Formation of the Tiara-like Complex

N-acetylcysteamine (NAC) is an inexpensive, readily commercially available small organic molecule containing both a thiol and an amide functionality derived from cysteine by decarboxylation of the carboxylic acid and acetylation of the amine side chain; removal of the carboxylic acid causes loss of chirality in the ligand. It is relatively non-volatile, reducing the hazard from accidental inhalation and, unusually for a free thiol, also entirely non-odorous. It was therefore an attractive choice of ligand for tiara formation.

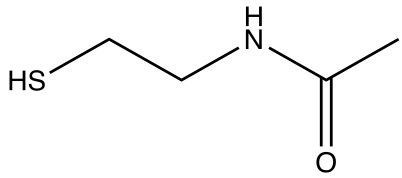
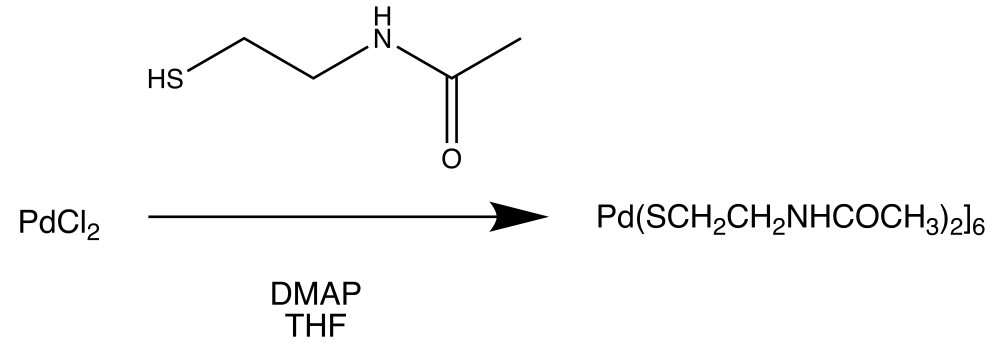


Figure 2.9: Chemical structure of *N*-acetylcysteamine.

The reaction was performed under similar conditions to existing procedures by combining 1 equivalent of palladium dichloride with 2 equivalents of *N*-acetylcysteamine and 2 equivalents of a base. Dimethylaminopyridine (DMAP) was selected as the base due in part to its ease of handling as solid crystals, and THF was selected as the solvent. The reaction was performed under an inert atmosphere by bubbling dinitrogen gas through the solvent for at least 5 minutes and a slow stream of nitrogen was continuously passed over the reaction mixture during the experiment. While not strictly necessary for the reaction, an inert atmosphere is often employed in the synthesis of tiara-like complexes to avoid any interference from oxygen and inhibit oxidation of the thiol reagent to the corresponding disulfide.



Scheme 2.2: Original synthesis of Pd NAC (**1**) by reaction of the ligand *N*-acetylcysteamine with palladium chloride in the presence of a base (DMAP) in THF.

Following the addition of all reactants to the flask, the reaction mixture was allowed to stir overnight. This was done as to allow maximum time for the formation of the product to run to completion, as tracking the progress of tiara-like complex forming reactions is difficult. Thin-layer chromatography (TLC), a technique commonly employed to monitor the progress of reactions, was unsuitable for these experiments due to two reasons; firstly the volatility of the thiol ligands renders them difficult to observe upon the silica plate, and secondly that the product tiara-like complexes themselves rarely travel on chromatagraphical media. Other methods of tracking reaction progress, such as via NMR or UV, were unusable owing to the need to remove malodourous thiols from containment.

Upon the completion of the reaction, the contents of the flask were transferred to a clean round bottomed flask and the remaining solvent and volatiles were removed under vacuum and a sample was taken for mass spectrometry analysis. The obtained spectrum is given below in *Figure 2.10*.

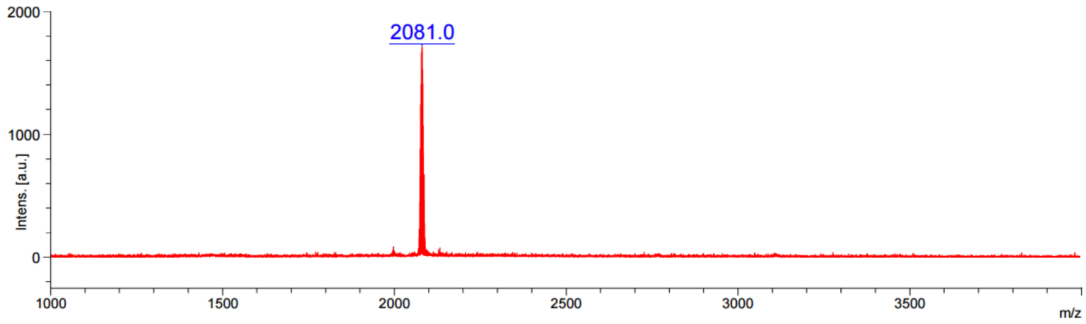


Figure 2.10: MALDI-ToF mass spectrum from 1000 m/z to 4000 m/z of **1** synthesised in THF, showing a single product complex obtained corresponding to the hexanuclear tiara $Pd_6(NAC)_{12}$ (2075.0 m/z, $[M+Na]^+$, calc. 2074.8). Matrix: DCTB, Mode: Positive.

The MALDI-ToF spectrum of the crude reaction mixture indicated a single tiara ring present. Due to the wide isotopic pattern of palladium, illustrated in *Table 2.2*, signals originating from tiara-like complexes in mass spectra have a distinctive broad series of peaks, making their identification in spectra straightforward.

Stable Isotope	Relative Abundance (%)
^{102}Pd	1.02
^{104}Pd	11.14
^{105}Pd	22.33
^{106}Pd	27.33
^{108}Pd	26.46
^{110}Pd	11.72

Table 2.2: Stable isotopes of palladium and their relative abundance.

Complex **1** is observed within the mass spectrum as a sodium adduct and shows the characteristic palladium isotopic pattern; analysis of the distribution (see *Figure 2.11*) provides further evidence of the acquisition of the hexanuclear ring only.

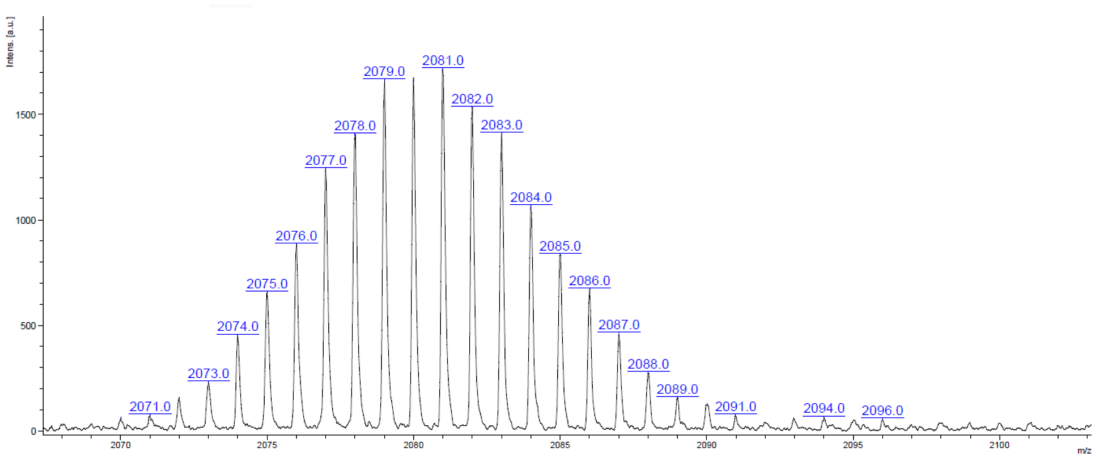


Figure 2.11: MALDI-ToF mass spectrum from 2067 m/z to 2103 m/z of **1** synthesised in THF with signals showing the characteristic Pd_6 isotopic pattern. Matrix: DCTB, Mode: Positive.

Purification of the product complex was achieved by complete dissolution of all reaction material in methanol and allowing the solution to slowly evaporate, wherein large red block crystals of $[Pd(NAC)_2]_6$ (**1**) grew readily. *Figure 2.12* shows the result of crystal growth from a slowly evaporating saturated solution of **1** in methanol; the large crystals shown were isolated and washed in THF.

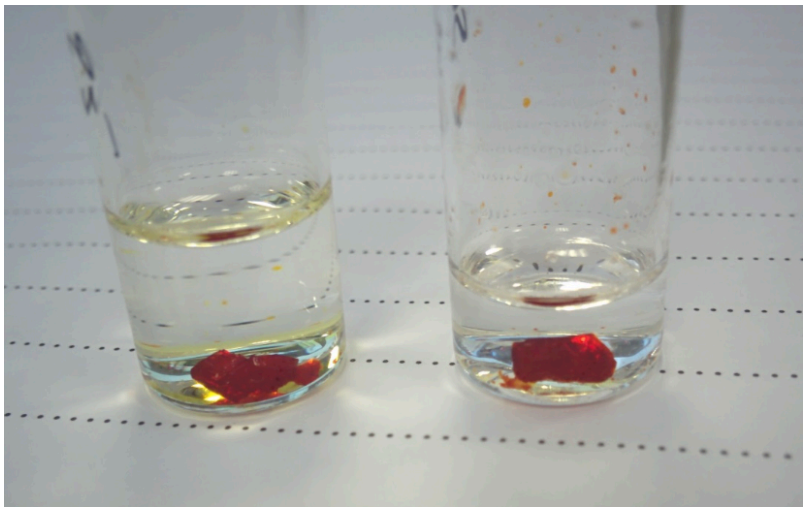


Figure 2.12: Crystals of **1** grown from methanol over several months. Crystals were washed and stored under THF.

The unanticipated degree of success in obtaining a large yield of pure material from crystallisation was paramount in further analysis of the complex. Due to preferential solubility

of **1** in water over organic solvents such as chloroform, waste products from the reaction such as [DMAP-H^+] [Cl^-] could not be removed by washing an organic solution of the crude reaction product with any aqueous mixtures. The purified crystals could then be characterised further by NMR and elemental analyses. The ^{1}H proton NMR spectrum of **1**, given in *Figure 2.13*, showed 6 distinct signals arising from the protons. This is not immediately justifiable from the simple chemical formula of $[Pd(NAC)_2]_6$ which should elicit only four distinct proton environments. However, performing the NMR experiments in methanol-d4 renders the NH signal unobservable due to rapid exchange of the proton with the hydroxy deuterium in huge excess. The signals in the spectrum arise from the configuration of the ligands around the complex; each ligand can adopt either an axial or equatorial geometry with relation to the ring. This separation renders the protons of the same chemical environment non-equivalent and gives rise to the two separate signals seen in the spectrum. This phenomenon has been documented previously for tiara-like complexes.

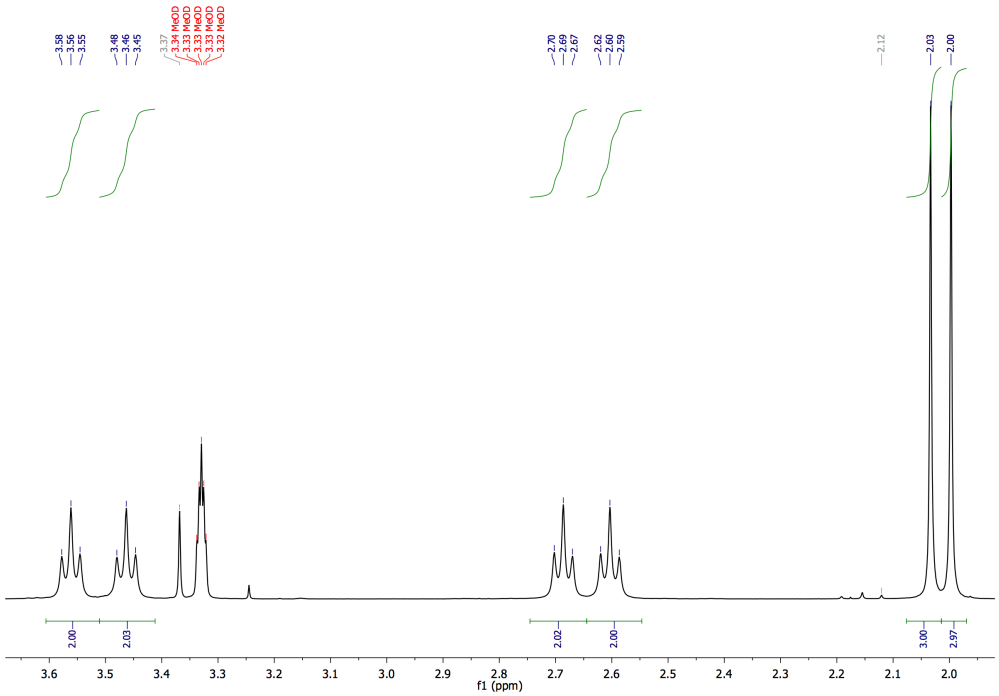


Figure 2.13: ^{1}H NMR spectrum from 1.9 ppm to 3.7 ppm of **1**. Solvent: methanol-d4, 16 scans.

Along with extended macrocrystalline structures, smaller single crystals could be isolated from the crystallisation vials and a suitable crystal was selected for single crystal X-ray Diffraction

(XRD) analysis. The complex crystallises in *P*-1 symmetry together with a single molecule of methanol and four molecules of water per unit cell to give a cell content of $C_{49}H_{105}N_{12}O_{17}Pd_6S_{12}$. It was found that the nature of the amide bond in the tiara gives rise to an extensive series of hydrogen bonds which have not previously been widely seen for these complexes. The hydrogen bond acceptor on the carbonyl C=O and the hydrogen bond donor of the amide N-H allows each ligand to participate in up to two hydrogen bonds, resulting in a maximum of 24 potential donors and acceptors per complex.

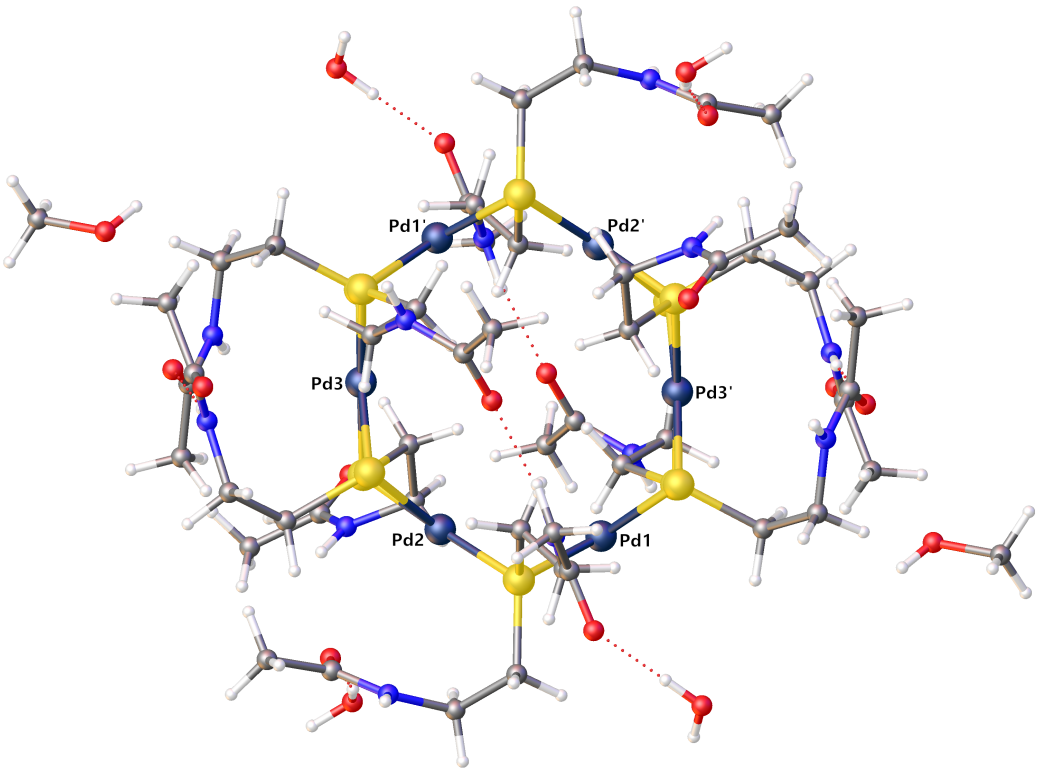


Figure 2.14: Crystal structure of **1** (top view). ' = 1-X, 1-Y, 1-Z. Atom colours: Pd-dark blue, S-yellow, C-grey, N-light blue, O-red, H-white. Hydrogen bonding interactions are illustrated by red dotted lines.

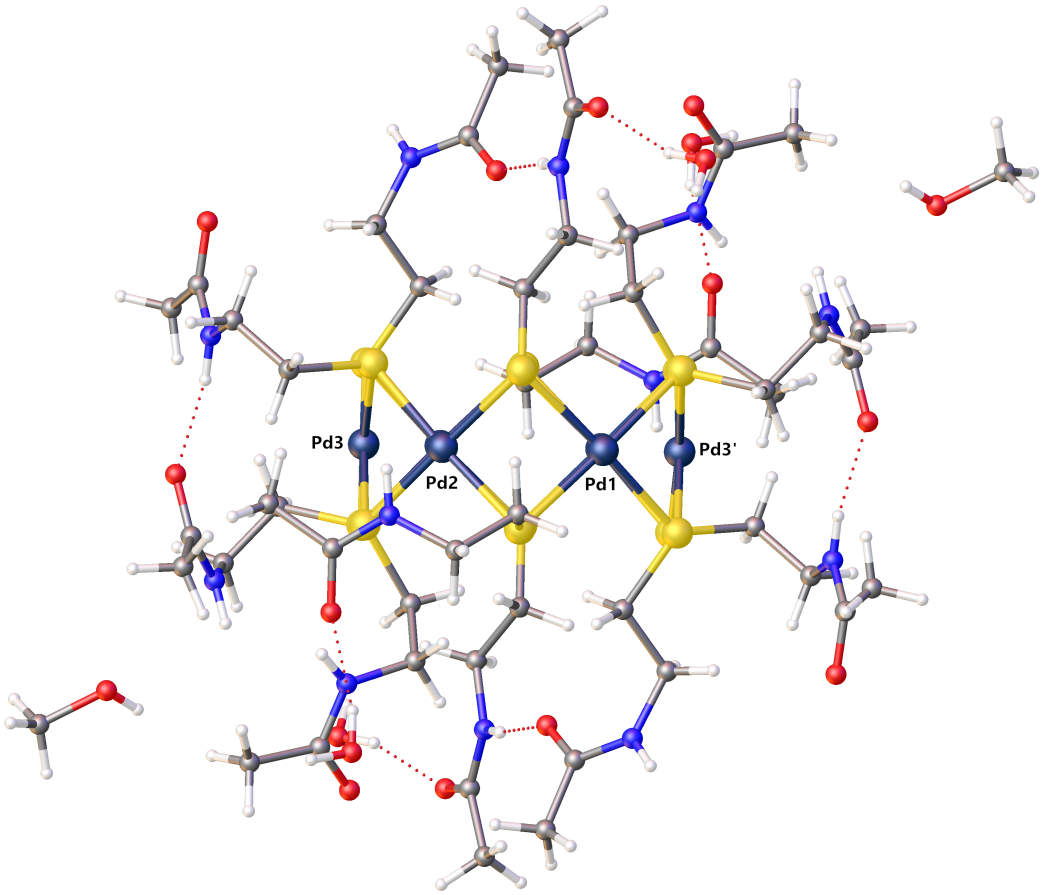


Figure 2.15: Crystal structure of **1** (side view). ' = 1-X, 1-Y, 1-Z. Atom colours: Pd-dark blue, S-yellow, C-grey, N-light blue, O-red, H-white. Hydrogen bonding interactions are illustrated by red dotted lines.

Due to this significant quantity of potential sites for inter- and intramolecular interactions, the degree of hydration within the crystal structure can be immediately justified. Each ligand arm is found to participate in at least one hydrogen bond to another ligand on the same complex. The hydrogen bond distances (N···O) are 2.836(3) Å (>N-H···O = 169°) for equatorial-equatorial bonds; 2.872(2) Å (>N-H···O = 168°) for equatorial-axial ligand bonds; 2.901(2) Å (>N-H···O = 135°) for axial-axial ligands. The ligand-water hydrogen bonds (N···O) range from 2.865(3) Å (>N-H…O = 164°) to 3.027(2) Å (>N-H···O = 175°). An extended network of hydrogen bonds illustrated below in *Figure 2.16* is formed by a cluster of water molecules in a cavity formed between adjacent tiara-like complexes.

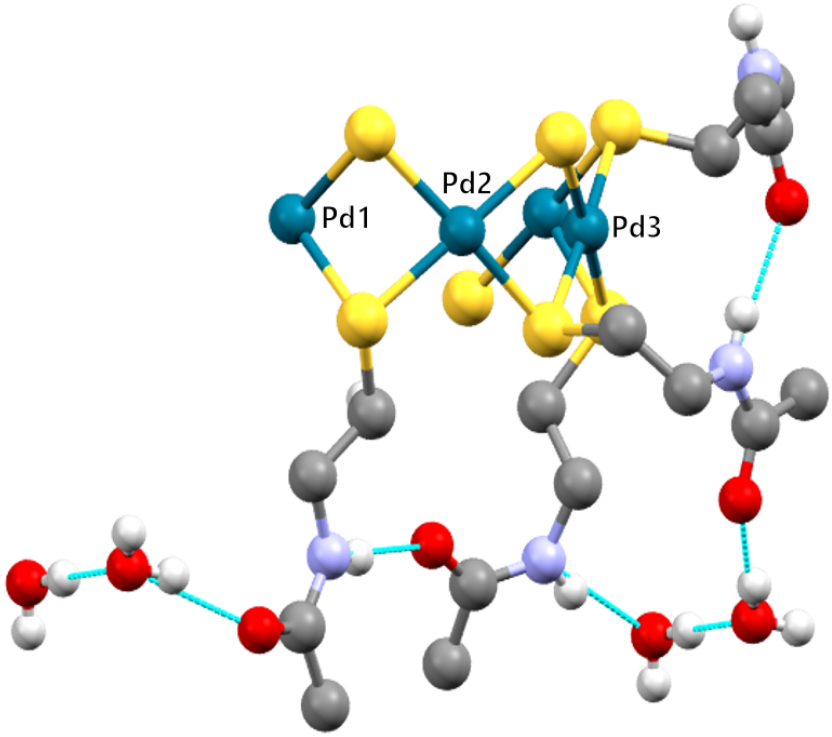


Figure 2.16: Extended hydrogen bonding network formed through the tiara amide groups and water solvent. Atom colours: Pd-teal, S-yellow, C-grey, N-light blue, O-red, H-white. CH_2 and CH_3 protons omitted for clarity. Hydrogen bonding interactions are illustrated by light blue dotted lines.

The degree of hydrogen bonding revealed by the single crystal structure gives reason for the insolubility of the complex in most organic solvents and the unusual solubility in H_2O. In some cases, particularly for large crystals, heating was required to ensure dissolution of the complex. The solubility of the complex is mainly limited to water, methanol, ethanol, propanol and DMF, making a determination of the strength of the self-association in solution difficult. During a dilution of a saturated solution of methanol-d4, the proton shifts were not found to change with decreasing concentration.

*2.2.2.2 Synthesis of **1** in Protic Solvents*

The limited solubility of **1** in THF prompted an investigation into whether the solvent used in the tiara formation would affect the synthesis of the complex. Previous experiments performed in the literature have not documented any effect of the solvent on the formation of any complexes yet reported. Nevertheless it was hypothesised that the protic nature of alcohol solvents would strengthen interactions between the growing tiara chain and the solvent, potentially hindering collapse of the tiara chain into the ring.

The original synthesis of **1** was repeated with the sole change of solvent; THF (5ml) was replaced with n-propanol (5ml), a previously used solvent for tiara formation. All other variables, including the quantity of reagents, choice of base and reaction time were kept identical. The resulting crude reaction mixture was worked up in an identical fashion consisting of removal of all volatiles and washing with diethyl ether. Analysis of the crude mixture by MALDI-ToF MS gave the spectrum seen in *Figure 2.17*.

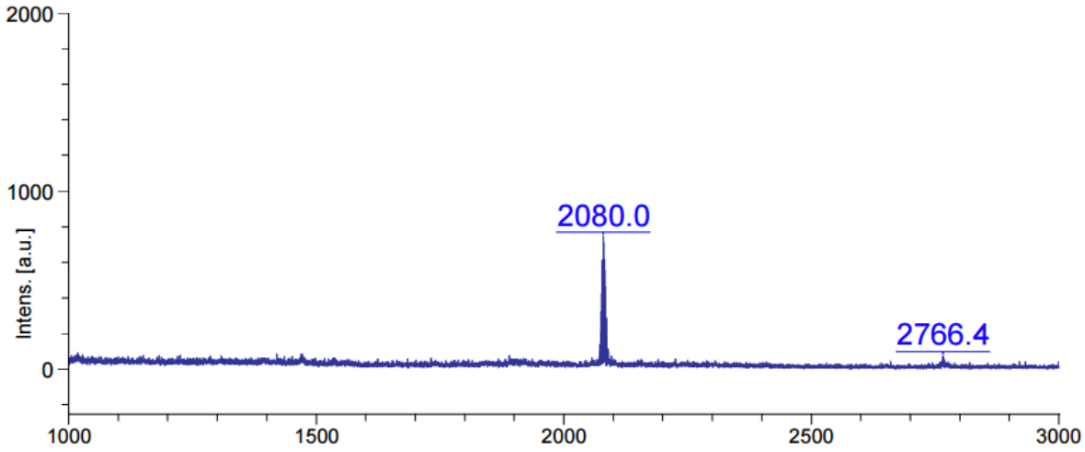


Figure 2.17: MALDI-ToF mass spectrum from 1000 m/z to 3000 m/z of the crude product of **1** synthesised from n-PrOH, showing acquisition of hexanuclear tiara (2080.0 m/z) and octanuclear tiara (2766.4 m/z). Matrix: DCTB, Mode: Positive.

While the obtained spectrum appears broadly similar to that already obtained for the original synthesis in THF, closer analysis of the spectrum reveals a small signal centred on 2766.4 m/

z. Calculation of the mass of the new signal suggested a chemical composition of $[Pd(NAC)_2]_8$, the larger octanuclear tiara-like complex. Due to the weak intensity of the signals obtained, analysis of the isotope distribution pattern could not be employed to support the assignation as the octanuclear tiara.

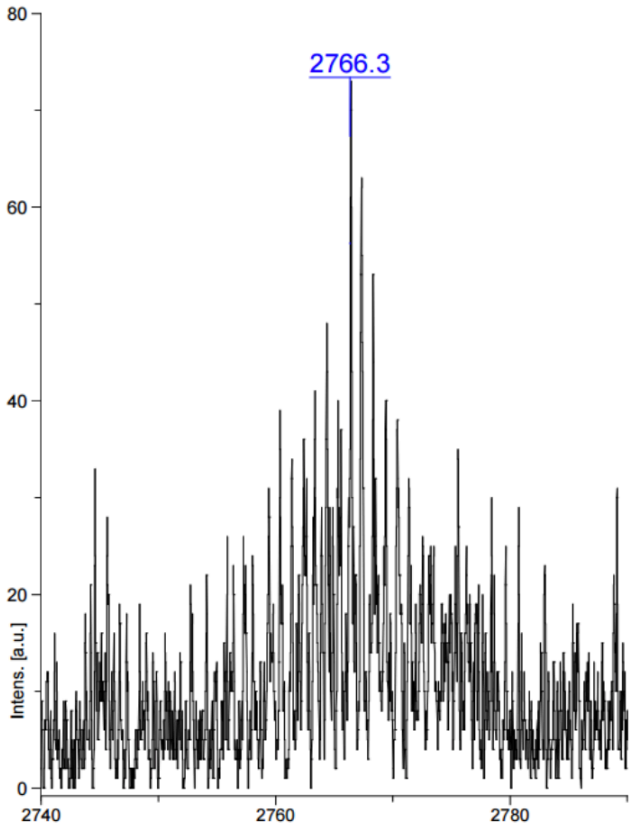


Figure 2.18: MALDI-ToF mass spectrum from 2740 m/z to 2790 m/z of **1** synthesised from n-PrOH showing weak intensity of new signal appearing in the spectrum. Matrix: DCTB, Mode: Positive.

To investigate this further, the solvent was substituted for methanol and the reaction was repeated, again consisting of otherwise identical conditions to the original THF synthesis. Characterisation gave the MALDI-ToF mass spectrum reported below in *Figure 2.19*.

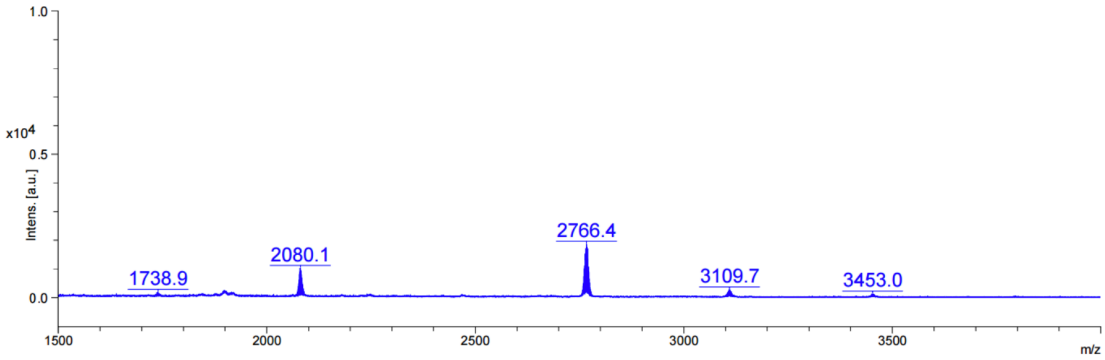


Figure 2.19: MALDI-ToF mass spectrum from 1500 m/z to 4000 m/z of **1** synthesised from MeOH showing $Pd_5(NAC)_{10}$ (1738.9 m/z), $Pd_6(NAC)_{12}$ (2080.1 m/z), $Pd_8(NAC)_{16}$ (2766.4 m/z), $Pd_9(NAC)_{18}$ (3109.7 m/z) and $Pd_{10}(NAC)_{20}$ (3453.0 m/z) tiara-like complexes. Matrix: DCTB, Mode: Positive.

It can be immediately seen that the resultant spectrum differs significantly from the reaction product obtained by reaction with either THF or n-PrOH. The signals tentatively assigned as the larger octanuclear tiara have increased greatly in intensity with respect to the hexanuclear tiara, enabling the analysis of the isotope pattern. Calculation of the expected pattern matches sufficiently with the experimental result to confirm the acquisition of the octanuclear tiara. Further, several new signals corresponding to tiara-like complexes of nuclearity 5, 9, 10 and 11 have been detected.

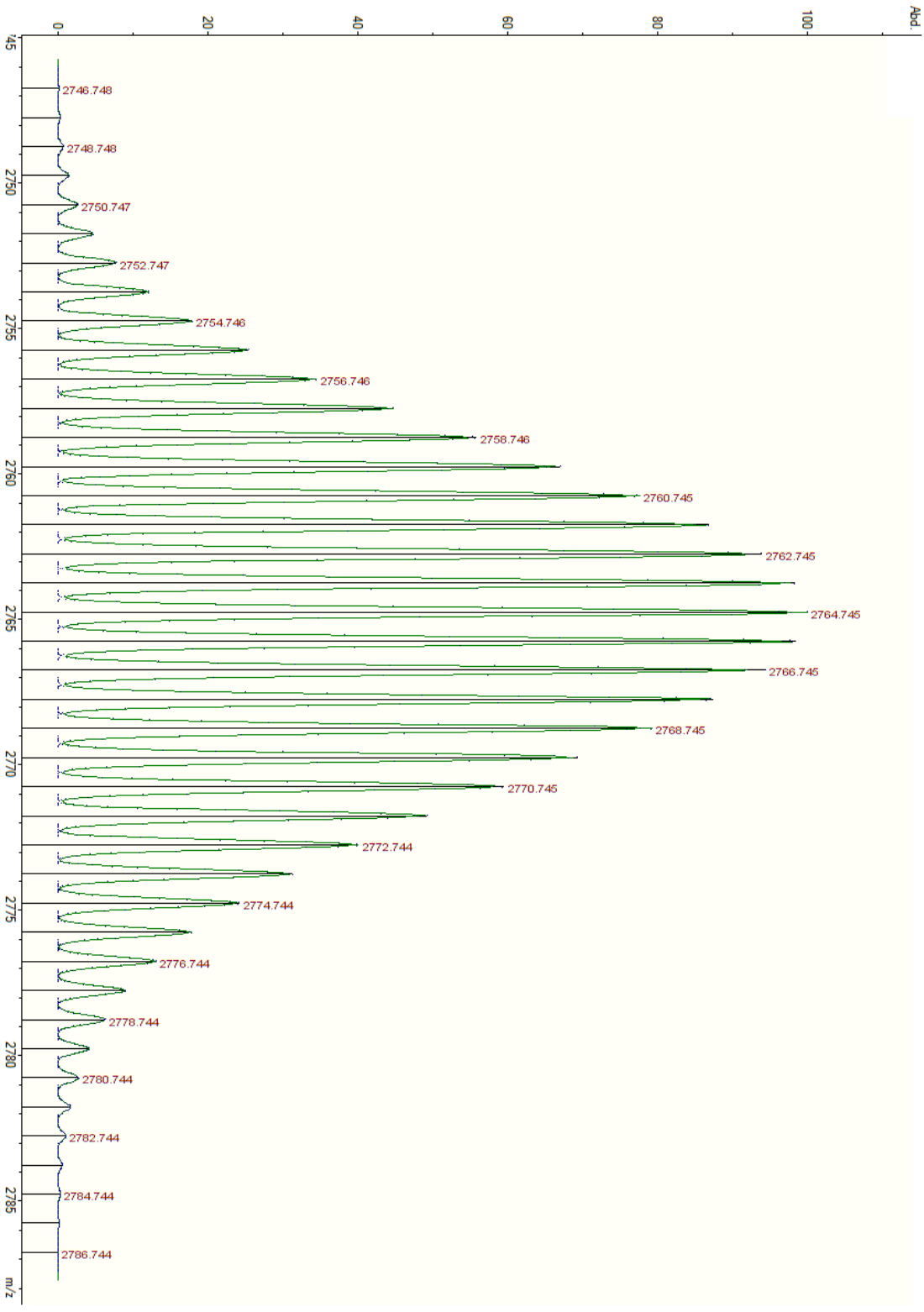


Figure 2.20: Calculated isotope pattern for $[Pd(NAC)_2]_8$.

To complete the analysis and ensure that the result matched the expected outcome, the reaction was repeated again with replacement of the solvent with ethanol (5ml). Owing to the structure and properties of ethanol being halfway between that of methanol and n-propanol, the expected spectrum would also lie somewhere between the two extremes. After following the same reaction and work-up procedures, the obtained mass spectrum, shown in *Figure 2.21*, was indeed confirmed to show an intensity of the octanuclear tiara greater than that of n-propanol but lower than that of methanol.

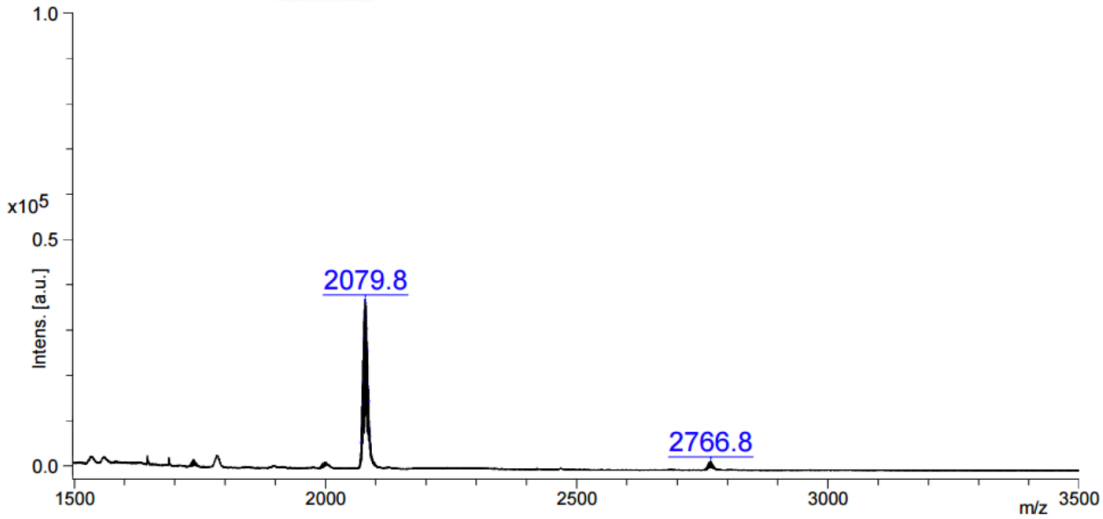


Figure 2.21: MALDI-ToF mass spectrum from 1500 m/z to 3500 m/z of **1** synthesised from EtOH showing $Pd_6(NAC)_{12}$ (2079.8 m/z) and $Pd_8(NAC)_{16}$ (2766.8 m/z) tiara-like complexes. Matrix: DCTB, Mode: Positive.

Crystals were grown from the reaction products obtained by the syntheses performed in ethanol and methanol. However, only one morphology of crystal could be identified and screening revealed the hexanuclear cell. It was concluded that the hexanuclear complex crystallises most favourably from the mixture of crude products. It can therefore be seen from these results that the choice of solvent has a significant effect on the outcome of the reaction; a result not previously reported for tiara-like complexes, therefore no precedent was available to explain these results. Consideration of the process of the formation of the tiara was necessary to justify these results.

2.2.2.3 Proposed Solvent Effects on Tiara Formation

By the current accepted mechanisms of tiara formation, the growing chain is considered to polymerise until reaching a termination point wherein the length is great enough for the ends to interact, displacing solvent and the original metal counterions to form the ring structure. For most tiara-like complexes, this length is six [PdS_2] units; sufficient length to ensure undistorted bond angles but minimising the size of the central void. For a small proportion of complexes, the termination point is greater; this is assumed to be when the central void is in some way stabilised. It is also necessary to consider entropic effects in the ring formation, as it would be expected that smaller tiaras would be favourable over larger tiaras due to the formation of additional rings; twenty four [PdS_2] subunits could react to form either four hexanuclear complexes or three octanuclear complexes.

For several tiara-like complexes of nuclearity above 6 published in the literature, the formation of larger rings can be attributed to solvent templating, wherein the solvent simply occupies the central void to support the extension of the polymer chain beyond 6. This theory was considered to support the experimental results obtained above, in particular the observed result that the intensity of the larger ring obtained increases on changing of the solvent from n-propanol > ethanol > methanol, the primary difference of which is the size/length of the solvent molecule. To examine whether the results obtained were due to simple occupation of the void by smaller solvents, the reaction was performed twice further using the small, non-protic solvents acetonitrile and dichloromethane, both of which should be of a size able to occupy the central void and stabilise a larger ring. In both cases, the MALDI-ToF mass spectra obtained showed only acquisition of the hexanuclear tiara with no rings of other sizes observed.

After exclusion of solvent templating as the sole origin of the larger rings seen by mass spectrometry, it was necessary to reconsider the hydrogen bonding hypothesis outlined above.

All solvents shown to form only hexanuclear tiaras, THF, dichloromethane and acetonitrile are aprotic in contrast to the alcohol series, which are able to both donate and accept hydrogen bonds on the hydroxyl OH group. Simiarly, the ligand *N*-acetylcysteamine is also able to both donate and accept hydrogen bonds due to the presence of an amide group. Therefore the interactions between the protic solvents and the growing tiara chain are theorised to be significantly stronger than for aprotic solvents. In aprotic solvents, the lack of available hydrogen bond donors and acceptors from the solvent causes the growing polymer chain to form interactions with itself; this self-association causes the growing chain to bend and wrap around. Once the chain has reached 6[PdS_2] units, these interactions are theorised to pull the chain into proximity for collapse of the chain into the ring structure, hindering any further elongation of the chain. This is illustrated further in *Figure 2.22*.

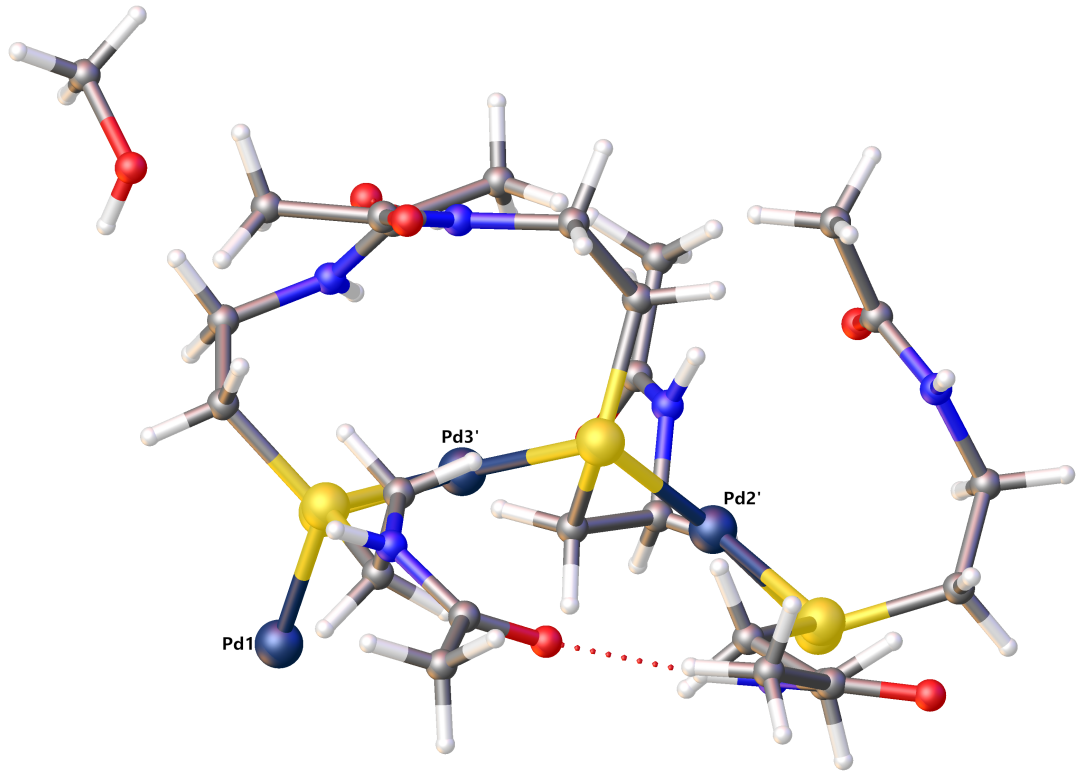


Figure 2.22: Interactions seen within the crystal structure of **1** caused by intramolecular hydrogen bonding. This is theorised to cause contraction of the growing chain during tiara formation. ' = 1-X, 1-Y, 1-Z. Atom colours: Pd-dark blue, S-yellow, C-grey, N-light blue, O-red, H-white. Hydrogen bonding interactions are illustrated by red dotted lines.

In contrast, protic solvents are able to compete for these hydrogen bonding sites on the growing polymer chain. Further, it may be assumed that the solvent molecules are in huge excess of the reagents and intermediate tiara oligomers. Due to this excess, the competition for hydrogen bonding sites on the ligands is sufficient to effectively 'shield' the ligands from self-association, hindering the chains from collapsing and subsequent termination of the polymer into the final complex. On changing the solvent from n-PrOH to EtOH to MeOH, the decreasing size of the solvent allows a greater number of molecules to cluster around the growing chain, increasing the effectiveness of the shielding. It is also theorised that the limited conformational freedom of MeOH over n-PrOH entropically favours the formation of hydrogen bonds to the tiara-chain.

2.2.3 Synthesis of Pd ETG

2.2.3.1 Ethyl thioglycolate

To examine the influence of the amide functional group on the tiara formation, a new ligand was selected to test the overall hypotheses. Ethyl thioglycolate (ETG), like *N*-acetylcysteamine, is readily commercially available, and the basic structural makeup is similar. Both ligands consist of five atoms within a chain and possess some form of carbonyl moiety. For ethyl thioglycolate however, the functional group is an ester. The other difference between the two is the placement of the carbonyl; in *N*-acetylcysteamine, the carbonyl is located on the fourth atom from the thiol group whereas for ethyl thioglycolate it is in closer proximity to the thiol, on the second atom. In both ligands the chain heteroatom is located at the 3-position.

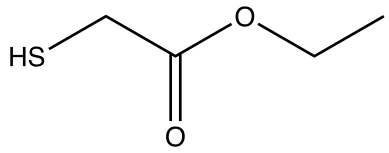
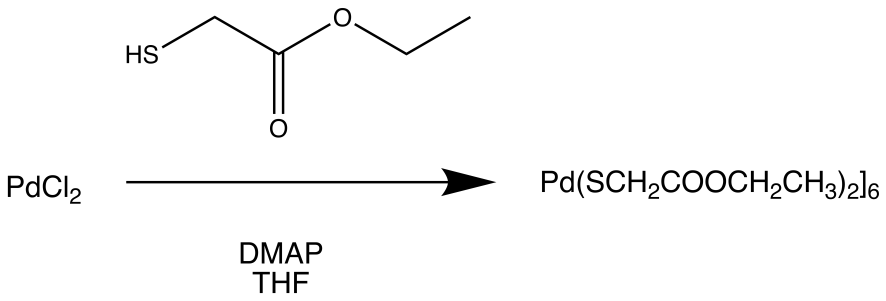


Figure 2.23: Chemical structure of ethyl thioglycolate.

Due to the difference in structure, mostly likely because of the change of functional group, ethyl thioglycolate readily volatilises to produce a noxious smelling vapour; the boiling point of the oily thiol liquid is 54°C. This necessitated a change of apparatus to contain the odorous chemical and prevent cross contamination of glassware and apparatus. A set of protocols to effectively contain the vapour and decontaminate any glassware, syringe or apparatus in contact with the stench liquid or vapour is given in *Appendix I*.

2.2.3.2 Synthesis of Pd ETG



Scheme 2.3: Synthesis of Pd ETG (**2**) by reaction of the ligand ethyl thioglycolate with palladium chloride in presence of a base (DMAP) in THF.

To maintain comparison between the results, identical conditions, as given by *Scheme 2.4*, were selected for the reaction. THF (5ml) was used as the solvent and DMAP (2 eq.) as the base. Due to the enhanced precipitation of the resulting product and existing precedent from the literature, the time for the reaction to go to completion was estimated at 6 hours. However, due to limiting circumstances involving the time windows in which stench chemistry could be performed, the reactions were often left to complete overnight, giving comparable reaction times for the synthesis of **1**. After removal of the volatile thiol and solvent, the crude compound could be washed with aqueous solutions in order to remove base salt by-products. At this point, the crude mixture was taken for analysis before full purification to ensure retention of all complexes for analysis.

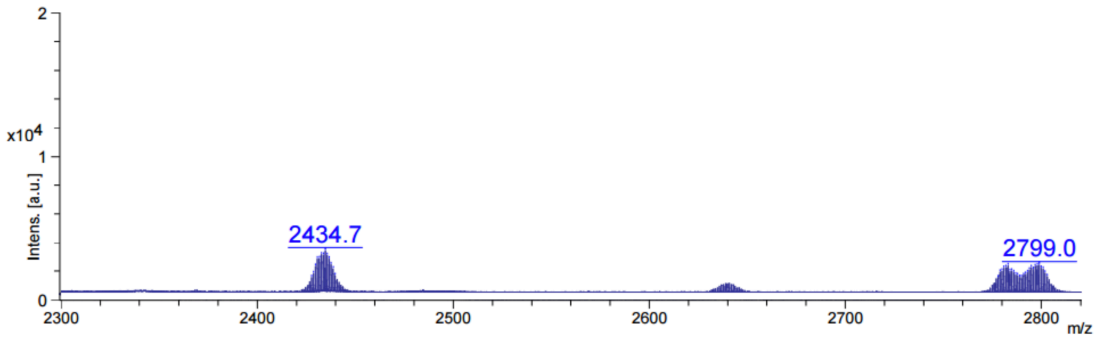


Figure 2.24: MALDI-ToF mass spectrum from 2300 m/z to 2820 m/z of **2** synthesised in THF, showing $Pd_7(ETG)_{14}$ (2430.7 m/z, $[M+Na]^+$, calc. 2430.5), $Pd_8(ETG)_{15}$ (2633.9, $[M+H]^+$, calc. 2633.5) and $Pd_8(ETG)_{16}$ (2744.0 m/z, $[M+Na]^+$, calc. 2744.5, 2790.0 m/z, $[M+K]^+$, calc. 2790.4). Matrix: DCTB, Mode: Positive.

The MALDI-ToF mass spectrum of the crude mixture, shown in *Figure 2.24*, indicates the detection of three distinct products, with isotopic masses corresponding to $[Pd_7(ETG)_{14}]$ (**A**), $[Pd_8(ETG)_{15}]$ (**B**) and $[Pd_8(ETG)_{16}]$ (**C**). However, it is likely that only the octanuclear tiara is formed as a result of the reaction and present in the crude mixture for several reasons. Firstly, **B** may be considered to be a fragment due to the mismatch of palladium to ligand. Signal **A**, corresponding to the hypothetical heptanuclear tiara, $[Pd_7(SCH_2COOCH_2CH_3)_{14}]$, is unlikely to exist due to the complete non-precedence of heptanuclear complexes previously reported.

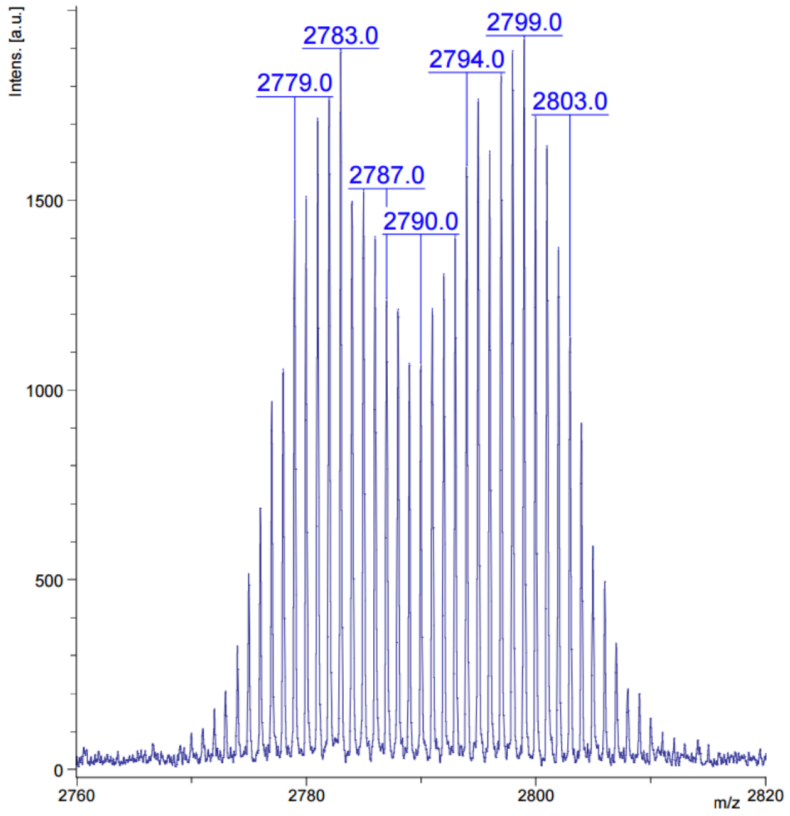


Figure 2.25: MALDI-ToF mass spectrum from 2760 m/z to 2820 m/z of **2** synthesised in THF showing signal from $Pd_8(ETG)_{16}$ with both Na^+ and K^+ adducts. Matrix: DCTB, Mode: Positive.

C is the only detected species likely to exist as a true product due to the detection of both sodium $[M+Na]^+$ and potassium $[M+K]^+$ adducts. For an octanuclear ring, it is feasible for K^+ to be included within the cavity of the ring on ionisation. However, it is likely that fragmentation of the octanuclear ring would result in the ring opening of the complex,

whereupon the included adduct is no longer bound and therefore not detected.

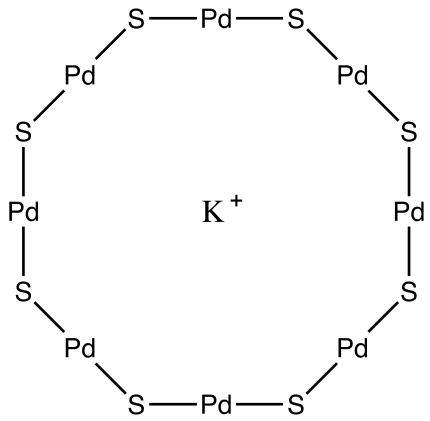


Figure 2.26: Hypothesised inclusion of K^+ within the cavity of the octanuclear toroid. Ligand arms not shown.

Following the analysis of the crude mixture, it was found that the impure tiara could be recrystallised from boiling n-propanol.

The ^1H NMR analysis of the purified compound revealed a broadly similar spectrum to that obtained for **1**; two sets of three signals. The splitting of the peaks into a quartet, triplet and singlet result from the altered placement of the carbonyl oxygen and is consistent with the expected coupling. Due to the movement of the carbonyl oxygen closer to the thiolate group compared to *N*-acetylcysteamine, the shift of the β-CH_2 group is shifted downfield and the terminal CH_3 group is shifted upfield; the changes in the multiplicity of the signals from the spectrum of **1** results from the new adjacency of the β-CH_2 group and the terminal CH_3 group, leaving the α-CH_2 to arise as a singlet within the spectrum.

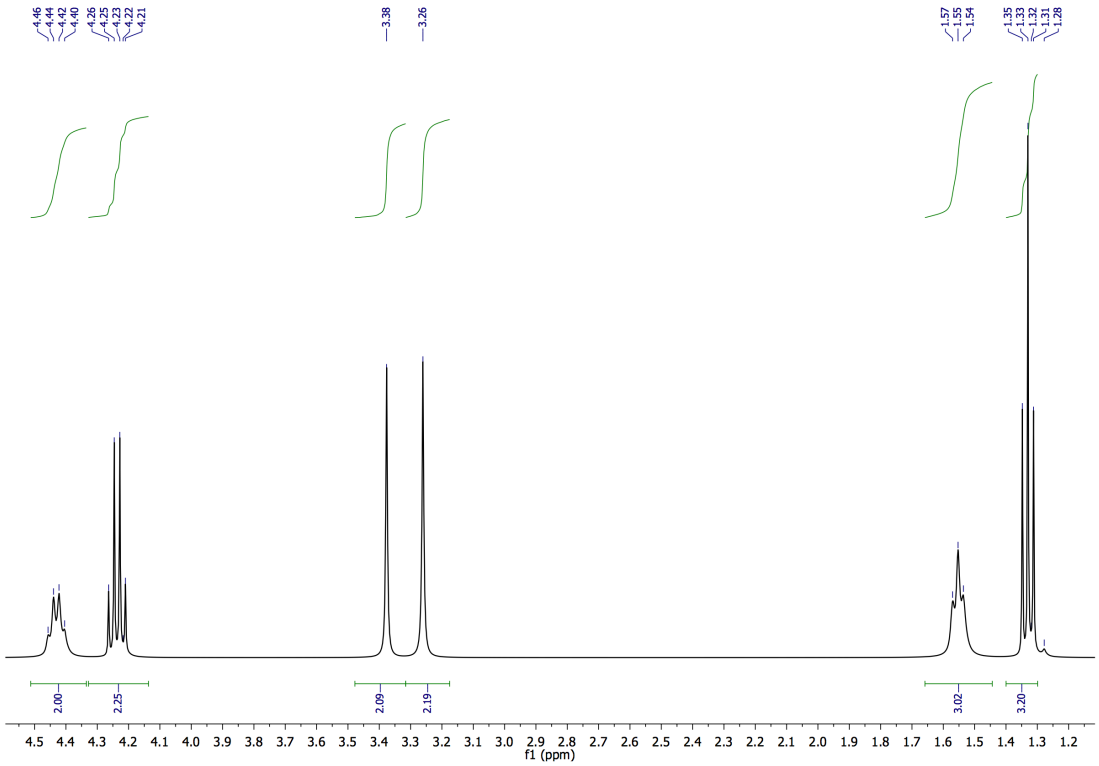


Figure 2.27: ^{1}H NMR spectrum from 1.1 ppm to 4.6 ppm of **2**. Solvent: chloroform-d, 16 scans.

2.2.3.3 Crystallography

Single crystals suitable for XRD analysis were grown by liquid layer diffusion, in which neat hexane was layered upon a saturated solution of the product in chloroform. On the lowering of the solubility of the complex, crystals began to grow slowly. After several days of growth, the crystals were isolated and one was mounted for diffraction. Previously studied octanuclear tiara-like complexes were solved in the space groups *P*-1 for $[Ni(SCH_2COOCH_2CH_3)_2]_8$ and *F*dd2 for $[Pd(SCH_2COOCH_3)_2]_8$; it was expected that **2** would adopt *P*-1 in the crystalline state, however screening of the crystal suggested a monoclinic crystal system.

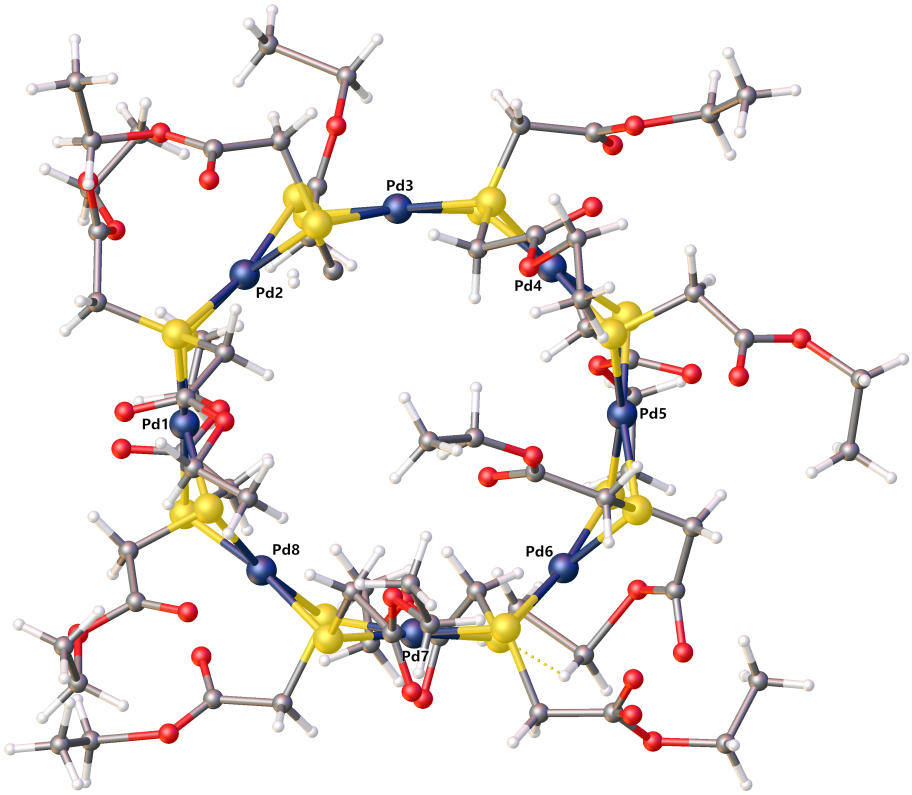


Figure 2.28: Crystal structure of **2** (top view). Atom colours: Pd-dark blue, S-yellow, C-grey, O-red, H-white.

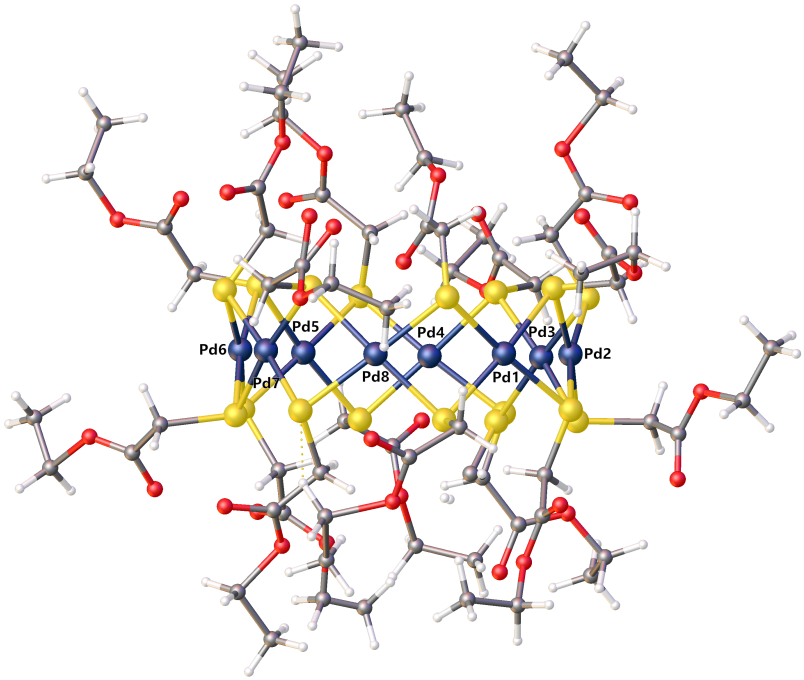


Figure 2.29: Crystal structure of **2** (side view). Atom colours: Pd-dark blue, S-yellow, C-grey, O-red, H-white.

After processing, the solution and refinement of the raw data confirmed the crystallisation of the octanuclear tiara $[Pd(ETG)_2]_8$; the final structures are shown in *Figure 2.28* and *Figure 2.29*. It was solved in the space group *C* 2/c and as expected adopts an octagonal geometry. Refinement of the structure was challenging due to the dynamic disorder of the ligand arms (see *Figure 2.30* and *Figure 2.31*) and significant restraints were employed to achieve convergence.

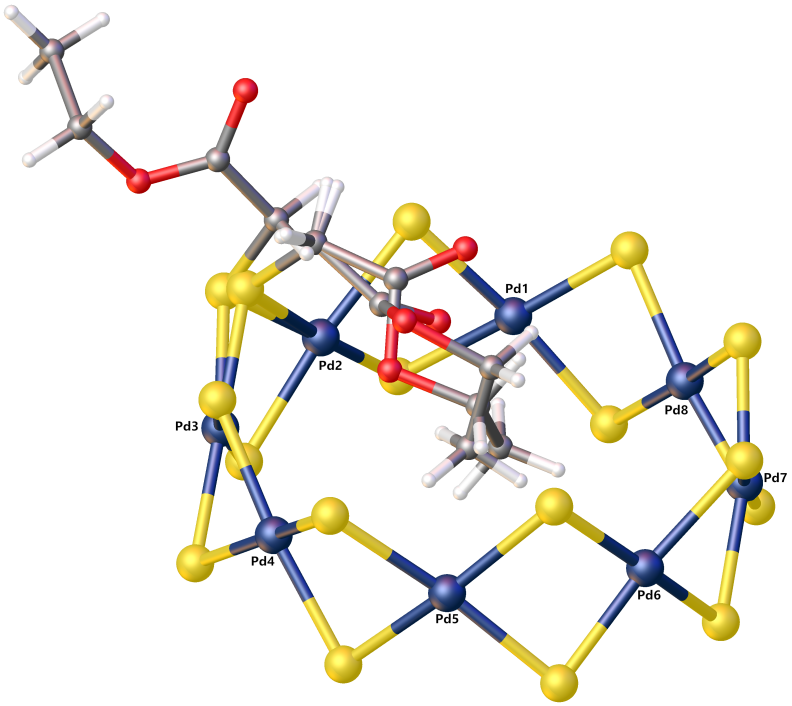


Figure 2.30: Observed disorder in the crystal structure of **2** caused by re-entrance of ligand arm into the central cavity (multiple ligands omitted for clarity). Atom colours: Pd-dark blue, S-yellow, C-grey, O-red.

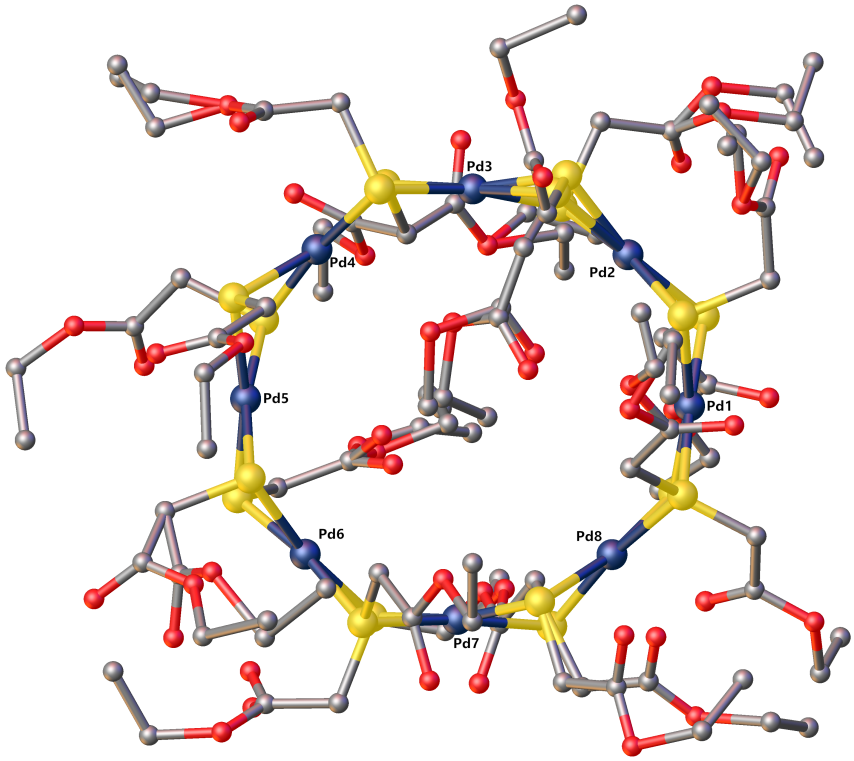


Figure 2.31: Crystal structure of **2** (top view) showing full disorder of all ligand arms (hydrogen atoms omitted for clarity). Atom colours: Pd-dark blue, S-yellow, C-grey, O-red.

As the palladium analog of the previously reported complex $[Ni(SCH_2COOCH_2CH_3)_2]_8$ by Dance *et al.*, the structure of **2** is very similar. While the former crystallises in the *P*-1 space group, the latter is C2/c symmetry, hence the unit cells differ significantly. A comparison of unit cells is given in *Table 2.3*.

	$[Ni(SCH_2COOCH_2CH_3)_2]_8$	**2**
Space Group	P-1	C2/c
a/Å	13.367(2)	24.3460(6)
b/Å	29.500(3)	26.3625(5)
c/Å	29.818(3)	31.9593(8)
α/°	61.64(1)	90.0
β/°	81.46(1)	113.960(3)
γ/°	81.35(1)	90.0
Volume/Å^3	10189(4)	20284.4(8)
Z	4	8

Table 2.3: Comparison of unit cell dimensions for the tiaras $[Ni(SCH_2COOCH_2CH_3)_2]_8$ (Ni ETG),[2] and $[Pd(SCH_2COOCH_2CH_3)_2]_8$ (Pd ETG, **2**).

The structures of the two complexes however are quite similar despite these differences in the solid state packing. Statistical values for the two complexes for comparison are: Ni-S = 2.191 Å, Pd-S = 2.318 Å, > S-Ni-S (internal) = 82.4°, > S-Pd-S (internal) = 82.56°, > S-Ni-S (external) = 98.3°, > S-Pd-S (external) = 97.65°, > Ni-S-Ni (ax) = 88.5°, > Pd-S-Pd (ax) = 88.8°, > Ni-S-Ni (eq) = 87.8°, > Pd-S-Pd (eq) = 88.0°. The average distance between adjacent metal atoms is Ni - Ni = 3.05 Å and Pd - Pd = 3.23 Å. A comparison of the packing of the complexes is shown below in *Figure 2.32* for Ni ETG and *Figure 2.33* for Pd ETG, **2**.

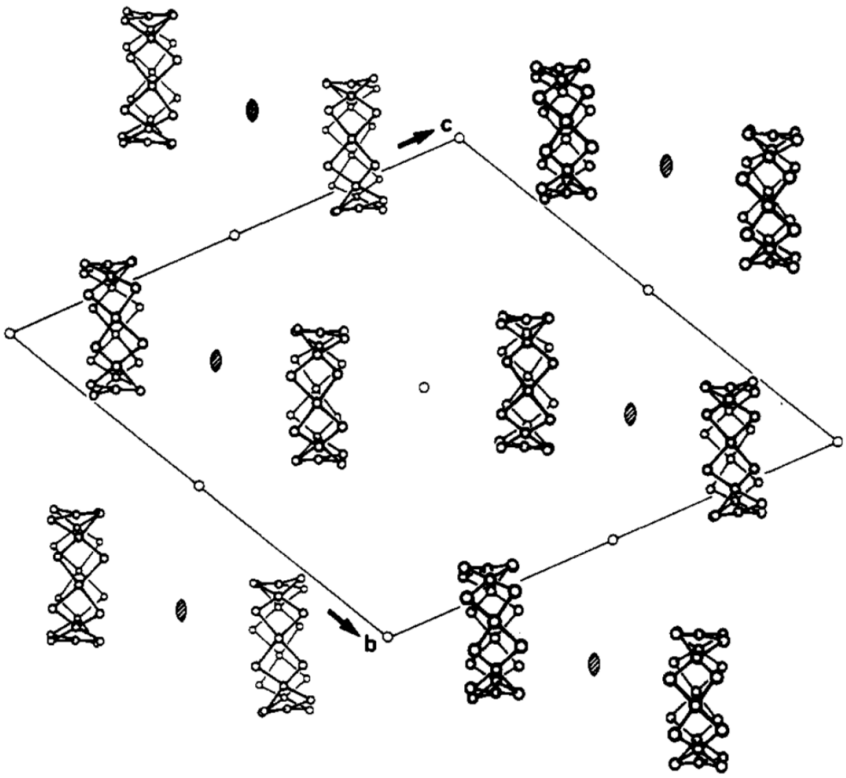


Figure 2.32: Extended packing of $[Ni(SCH_2COOCH_2CH_3)_2]_8$. The unit cell is indicated by solid black lines viewed along the *a* axis, Z = 4.[2]

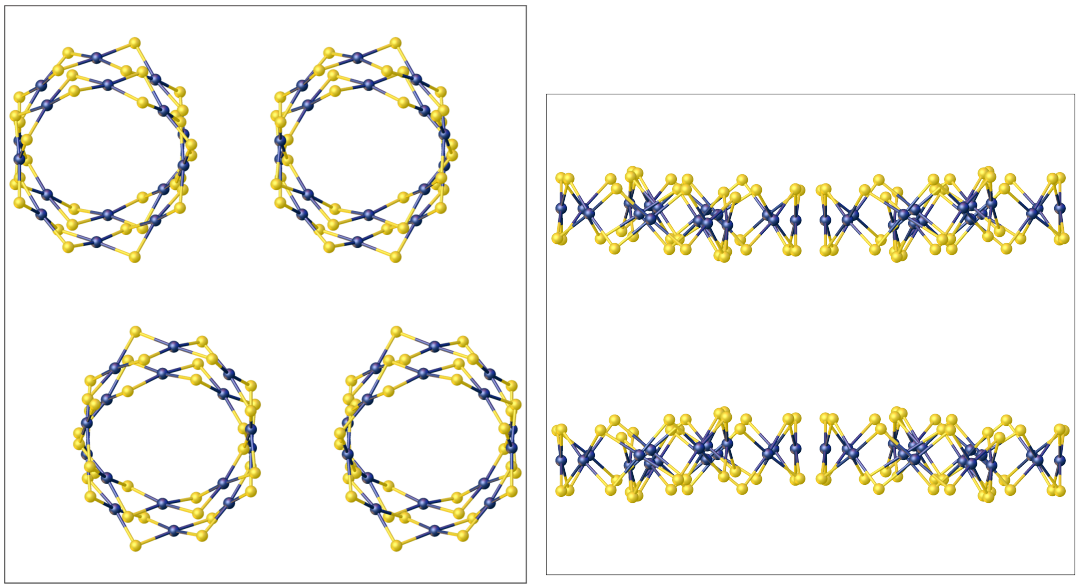


Figure 2.33: Extended packing of **2**. The unit cells are indicated by solid black lines, viewed along *a* axis (left) and *c* axis (right), Z = 8.

2.2.3.4 Influence of the Reaction Solvent on Tiara Nuclearity

The potential effects of the solvent on the formation of **2** were investigated as for **1** by replacement of THF (5ml) with n-PrOH (5ml). However, no peaks corresponding to any other tiara-like complexes were noted, and purification resulted in the isolation of pure **2**. Given the lack of hydrogen bond donors present on the ligand chains within **2**, it is likely that the dominant influence on the nuclearity of the complex is the placement of the carbonyl oxygen.

2.2.4 Synthesis of Pd MEA

2.2.4.1 2-mercaptoethyl acetate

After the collection of these results, it remained unclear why tiaras of differing nuclearities should be favoured by ethyl thioglycolate and *N*-acetylcysteamine. While there is evidence to suggest that the hydrogen bonding capability of the amide favours the formation of a smaller tiara-like complex, the placement of the carbonyl should not be overlooked as the primary reason behind the differing nuclearities. To examine which structural change was the origin of these results, a new ligand was selected and reacted with the same standard conditions.

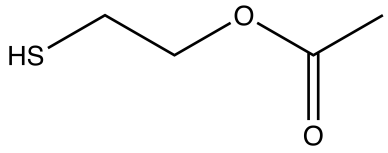


Figure 2.34: Chemical structure of 2-mercaptoethyl acetate.

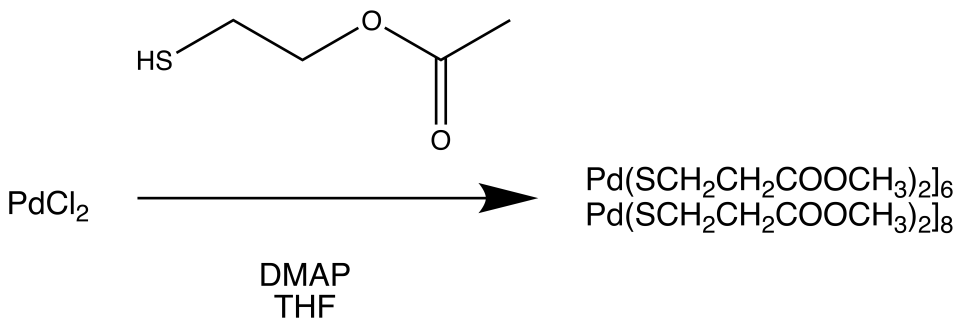
2-mercaptoethyl acetate (MEA), shown in *Figure 2.34*, possesses an ester functional group in its structure (as ethyl thioglycolate) however the placement of the carbonyl oxygen mimics that of *N*-acetylcysteamine; for these reasons it can be considered an intermediate between the two. As can be surmised from the name, it bears a similarity to the solvent ethyl acetate with the simple addition of a thiol moiety. It is commercially available but far less readily than either of the ligands used thus far, at a cost of £181.60/g.

The physical properties, while unknown, are suspected to be vastly similar to that of ethyl thioglycolate; they are structural isomers with a molecular mass of 120. Notably, the odour of the vapour is disagreeable but distinguishable from ethyl thioglycolate, indicating that the human olfactory receptors are potentially capable of recognising the structural difference.

Under the same conditions used previously (Base: DMAP, Solvent: THF), the nuclearity of

the resultant tiara Pd MEA would confirm the origin of the differing nuclearities evidenced by NAC and ETG. Formation of an octanuclear tiara would indicate that the placement of the carbonyl group was the determining factor in the size of the complex formed, whereas the synthesis of the smaller hexanuclear tiara would indicate that the nature of the functional group determined the most favourable size.

2.2.4.2 Synthesis of Pd MEA



Scheme 2.4: Synthesis of Pd MEA (**3**) by reaction of the ligand 2-mercaptoethyl acetate with palladium chloride in presence of a base (DMAP) in THF.

After reacting 2-mercaptoethyl acetate with these standard conditions illustrated in *Scheme 2.5*, the crude powder was worked up in the same manner as **2** by washing with aqueous solutions and drying. MALDI-ToF mass spectrometry gave the spectrum shown in *Figure 2.35*.

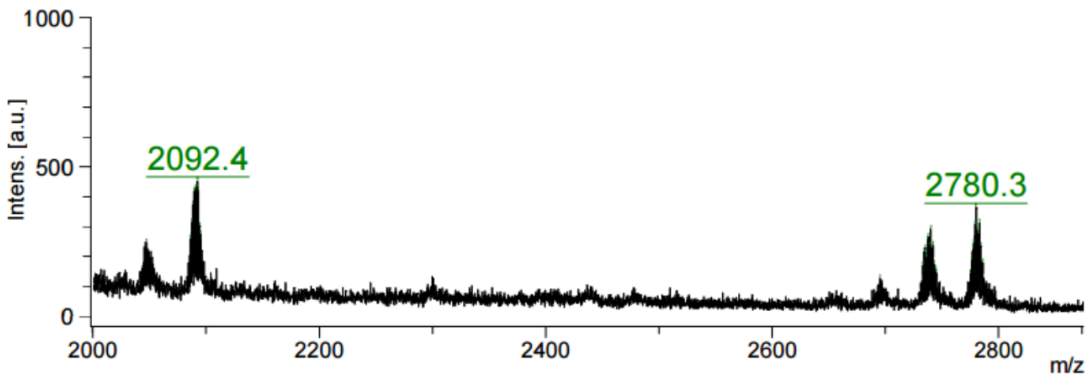


Figure 2.35: MALDI-ToF mass spectrum from 2000 m/z to 2900 m/z of Pd MEA (**3**) synthesised in THF showing $Pd_6(MEA)_{12}$ (2086.4 m/z, $[M+Na]^+$, calc. 2086.6) and $Pd_8(MEA)_{16}$ (2774.2 m/z, $[M+Na]^+$, calc. 2774.5). Matrix: DCTB, Mode: Positive.

The mass spectrum shows two distinct products in the crude mixture corresponding to the hexanuclear and octanuclear tiaras, leading to a reconsideration of the theories outlined above. The observed detection of both products indicated the influence of both the functional group and the placement of the carbonyl oxygen on determining the size of the complexes formed.

To rationalise the effect of the carbonyl location, it is necessary to reconsider the formation of **2**. As noted earlier, the stability of the larger complex results from the occupation of the larger (relative to hexanuclear) central cavity, either by solvent molecules or by a re-entrant ligand arm; for ethyl thioglycolate containing tiara-like complexes, one ligand arm occupies the core. When we consider 2-mercaptoethyl acetate, the altered position of the carbonyl group increases the steric bulk on the ligand distal to the ring. This may potentially hinder the movement of the ligand arm into the centre of the complex, decreasing the occupation of the void and rendering the larger octanuclear complex less favourable than the corresponding smaller hexanuclear complex.

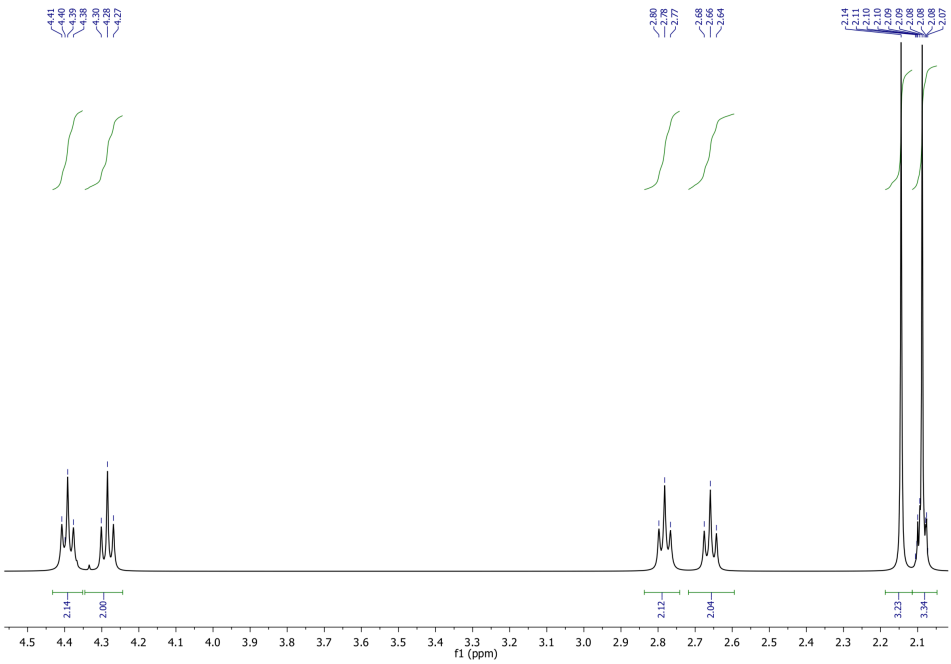


Figure 2.36: ^{1}H NMR spectrum from 2.0 ppm to 4.55 ppm of **3**. Solvent: chloroform-d, 16 scans.

The ^{1}H NMR spectrum of **3**, given in *Figure 2.36*, showed the same set of signals as for complex **1**, which was expected given the similarity of *N*-acetylcysteamine and 2-mercaptoethyl acetate. Small differences in the spectrum arose from the shift of the signals which was in line with the replacement of the amide functionality with an ester functionality. The increased electronegativity of the oxygen heteroatom over the nitrogen atom increases the chemical shift of each signal within the spectrum, an effect more pronounced for the CH_2 group closest to the carbonyl moiety. The effect is much smaller, almost negligible for the groups more distant from the carbonyl. These observations are summarised below in *Table 2.4*.

Proton Environment	Chemical Shift in **1** (ppm)	Chemical Shift in **3** (ppm)	Difference (ppm)
β-CH_2	3.57	4.39	+0.82
β-CH_2	3.44	4.29	+0.85
α-CH_2	2.67	2.78	+0.11
α-CH_2	2.58	2.66	+0.08
CH_3	2.02	2.14	+0.12
CH_3	1.98	2.09	+0.11

Table 2.4: Comparison of ^{1}H chemical shifts observed for each proton environment in complexes **1** and **3**.

2.2.4.3 Crystallography

Single crystals of the crude product were grown by slow evaporation of a concentrated chloroform solution. Screening of a suitable crystal indicated a triclinic cell of dimensions a = 11.6640(4) Å, b = 12.0973(4) Å, c = 13.5387(5) Å and a volume of 1836.53(11) Å^3. Due to the crystal system and small dimensions most similar to **1**, it was suspected to be the hexanuclear tiara, already thought to be the most favourable size of tiara-like complex to crystallise. The crystal structure of **3** is shown below in *Figure 2.37* and *Figure 2.38*.

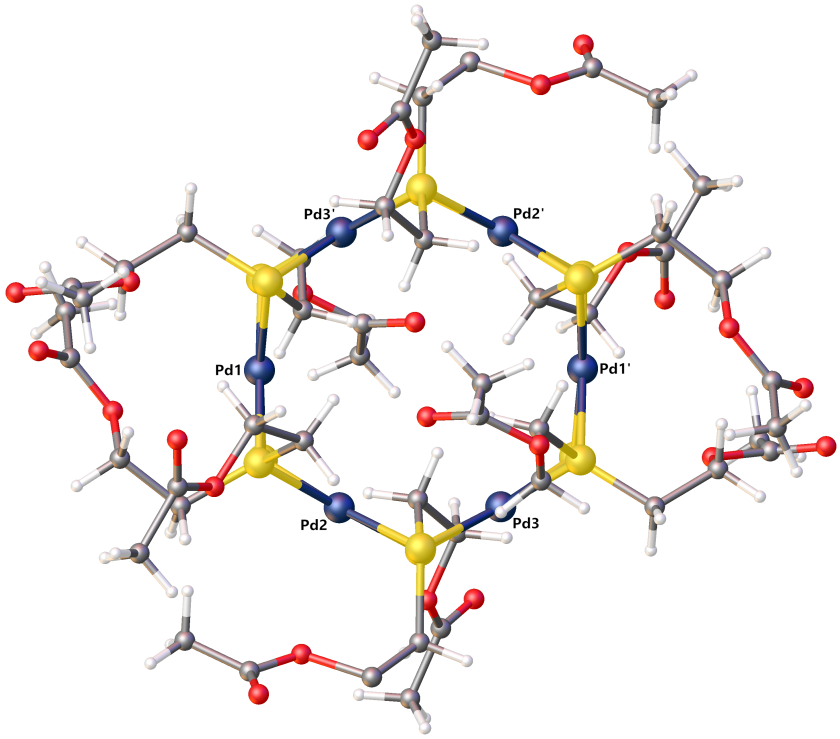


Figure 2.37: Crystal structure of ***3*** (top view). ' = 1-X, 1-Y, 1-Z. Atom colours: Pd-dark blue, S-yellow, C-grey, O-red, H-white.

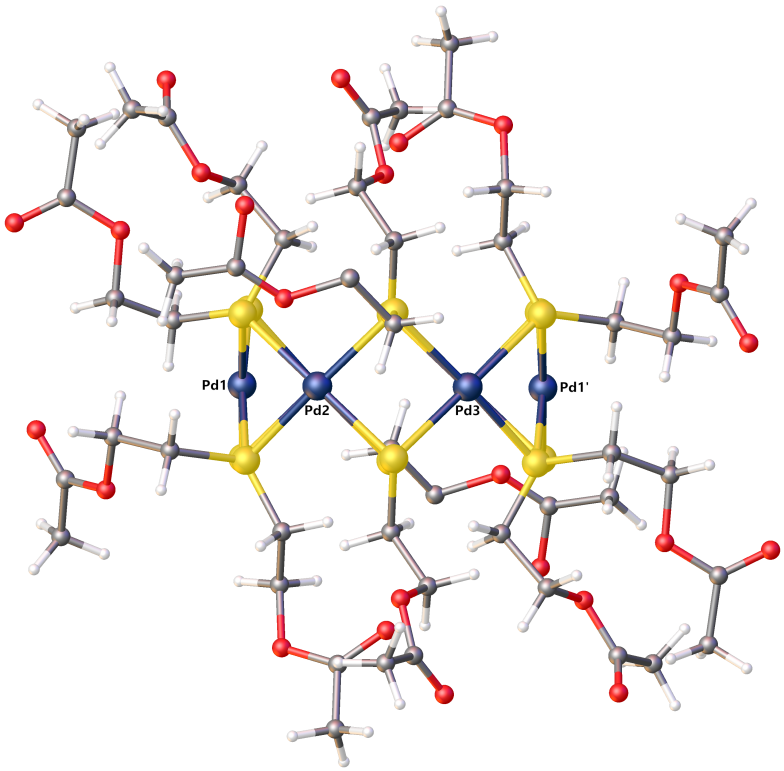


Figure 2.38: Crystal structure of ***3*** (side view). ' = 1-X, 1-Y, 1-Z. Atom colours: Pd-dark blue, S-yellow, C-grey, O-red, H-white.

Solution and refinement of the data confirmed the crystallisation of $[Pd(MEA)_2]_6$; the tiara adopts a solid state conformation equivalent to that of **1**. However, the lack of intramolecular hydrogen bonding allows a greater freedom of movement; given the absence of these interactions, the configuration adopted by this complex indicates the most favourable spatial positioning of the thiolate chains. Hydrogen bonding present in **1** is therefore sufficient to distort the conformation significantly. This is further shown by the internal angles of the hexagon; for **3** the > Pd-Pd-Pd angles are 119.3°, 119.7°, 121.0° whereas in **1**, this distortion leads to the adoption of 115.5°, 120.7° and 123.8° internal angles. A summary of S-Pd-S bond angles is given in *Table 2.5* and Pd-S-Pd angles in *Table 2.6*.

Vertices	Angle in **1**/°	Angle in **3**/ °
> S1-Pd1-S2	82.812(13)	83.10(3)
> S1-Pd1-S4	174.998(14)	174.71(4)
> S2-Pd1-S4	97.310(13)	96.98(4)
> S3-Pd1-S1	98.680(13)	98.19(4)
> S3-Pd1-S2	175.447(14)	178.47(4)
> S3-Pd1-S4	80.821(13)	81.66(4)
> S3-Pd2-S4	80.690(13)	81.60(4)
> S3-Pd2-S5	99.093(13)	98.73(4)
> S3-Pd2-S6	178.080(13)	178.86(4)
> S5-Pd2-S4	175.224(13)	175.68(4)
> S6-Pd2-S4	97.742(13)	98.06(4)
> S6-Pd2-S5	82.321(13)	81.53(3)
> $S2^1$-Pd3-$S1^1$	82.758(13)	82.73(4)
> S5-Pd3-$S1^1$	176.605(13)	175.03(3)
> S5-Pd3-$S2^1$	97.938(13)	98.26(4)
> S6-Pd3-$S1^1$	96.848(13)	96.99(3)
> S6-Pd3-$S2^1$	178.316(14)	178.55(3)
> S6-Pd3-S2	82.360(13)	81.89(4)

Table 2.5: > S-Pd-S bond angles for **1** and **3**.

Vertices	Angle in **1**/°	Angle in **3**/°
> Pd1-S1-Pd3[1]	83.294(12)	83.55(3)
> Pd1-S2-Pd3[1]	82.974(12)	83.40(3)
> Pd1-S3-Pd2	82.134(12)	82.92(3)
> Pd2-S4-Pd1	82.498(12)	82.32(3)
> Pd3-S5-Pd2	85.886(12)	83.97(3)
> Pd3-S6-Pd2	85.970(12)	84.52(3)

Table 2.6: > Pd-S-Pd bond angles for **1** and **3**.

2.2.5 Separation of Tiara-like Complexes

The separation of these tiara-like complexes described above poses unique challenges. As noted previously, the usual method of purification for tiara-like complexes is precipitation or crystallisation of the complex, but this method is unsuitable for reaction mixtures containing multiple tiara-like complexes.

Thin-layer chromatography on silica was employed in an attempt to separate the multiple tiara-like complexes obtained during the synthesis of **1** in MeOH and the synthesis of **3**. Various solvent systems were employed as the mobile phase however this method was unsuccessful in separating the different sized rings. Additionally, replacement of silica with alumina as the stationary phase had no effect on the movement of the adsorbed samples.

Size-exclusion Chromatography was trialled as a possible method to circumvent the ineffectiveness of chromatography as a means of separating tiara-like complexes. As noted previously, compounds soluble in organic solvents are normally run using gel polymers as the stationary phase (GPC) whereas aqueous solutions, including proteins and other polypeptides, utilise sugar and starch based stationary phases.

For the separation of **1**, it was necessary to select a dextran-based medium such as Sephadex, as short chain alcohols do not cause the gel media to swell. However, the solvent systems that can be used in these stationary phases are limited to a maximum of 25% methanol in water due to shrinkage of the polymers.

Under the conditions used, separation of the complexes could not be observed by analytical methods. While the difference in molecular weight is theoretically sufficient to be resolve $[Pd_x(SR)_{2x}]$ where $x < 11$ (minimum difference 10% of MW), separation occurs due to

differences in the molecular volume and is also influenced by other factors such as shape, charge and other differences between the species to be separated. The general shape of the complex is largely retained between tiaras of different sizes and the compositions are identical, leading to poor resolution of the series. Estimation of the difference in radii between tiaras Pd_x and Pd_{x+1} gives an approximate value of only ± 1.5 - 2 Å. Separation of the **3** isomers $[Pd(SR)_2]_6$ and $[Pd(SR)_2]_8$ was also attempted using GPC (Biobeads S-X, swelled in THF and run in $CHCl_3$) but without success.

While the attempted separations described here were unsuccessful, this technique could potentially be improved by the employment of a far longer column or extremely high resolution polymers for improved resolution and purification of the complexes.

2.2.6 Synthesis of Pd EMA

2.2.6.1 Ethyl mercaptamide

The results obtained by the reaction of 2-mercaptoethyl acetate with palladium chloride were not conclusive. The formation of both hexanuclear and octanuclear tiaras was anticipated but not regarded as a high probability outcome and left uncertainties about the key determining factors concerning the synthesis of these complexes; namely the position of the carbonyl and the nature of the functional group.

2-mercaptoethyl acetate can be considered to combine the ester functional group of ethyl thioglycolate with the position of the carbonyl from *N*-acetylcysteamine. It was recognised that a further member of this family of tiara-like complexes could be synthesised that combined the amide functional group of *N*-acetylcysteamine with the carbonyl placement of ethyl thioglycolate. The structure of the hypothesised ligand is given in *Figure 2.39*.

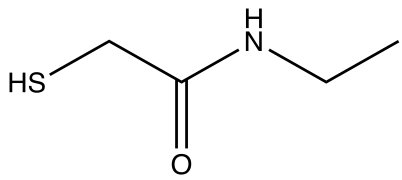


Figure 2.39: Chemical structure of ethyl mercaptamide (EMA), combining the carbonyl placement of ETG and the amide functionality of NAC.

The proposed ligand completes the four possible pairings of carbonyl placement and choice of functional group. This structure provides a direct comparison to ethyl thioglycolate with regards to the functional group, conserving the remainder of the structure between the two ligands. Similarly as for the synthesis of Pd MEA, formation of primarily octanuclear tiara would indicate that the position of the carbonyl (sterics) was the determining factor behind the complex nuclearity whereas the formation of primarily hexanuclear tiara would indicate that the hydrogen bonding capability of the amide was the driving force for a smaller ring.

However, formation of even a small amount of hexanuclear tiara, completely absent for Pd ETG, would indicate at least a small contribution from the amide in the formation of a smaller complex. The structures of the four possible combinations of functional group and carbonyl placements are given in *Figure 2.40*.

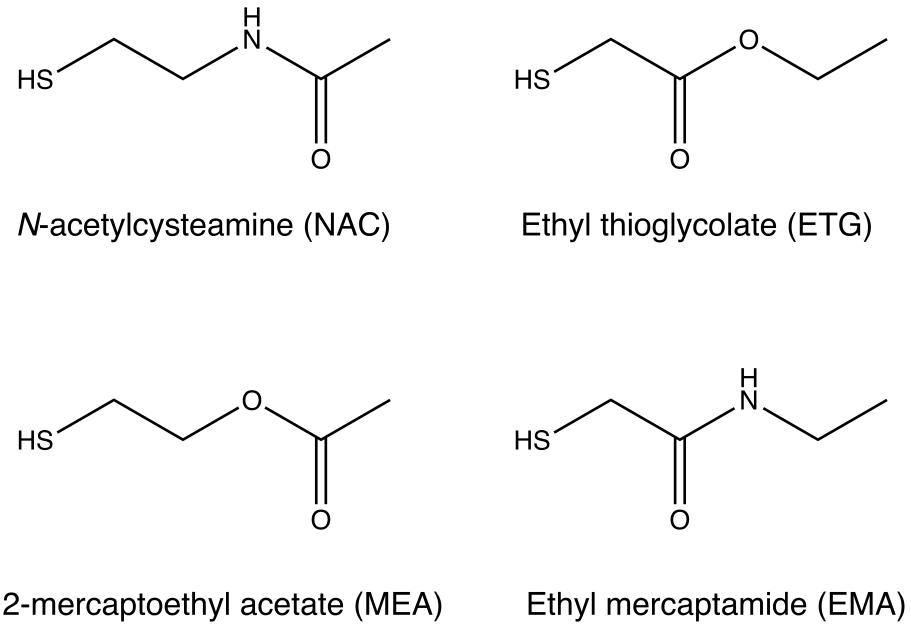


Figure 2.40: Structures of thiol ligands used in this study for comparison. Each has at least one feature in common with the others.

While only possessing a very slight difference in structure when compared to the other ligands used in this study, ethyl mercaptamide could not be obtained from commercial sources; therefore the ligand was required to be synthesised from precursor components.

2.2.6.2 Synthesis of ethyl mercaptamide

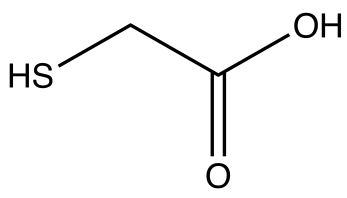
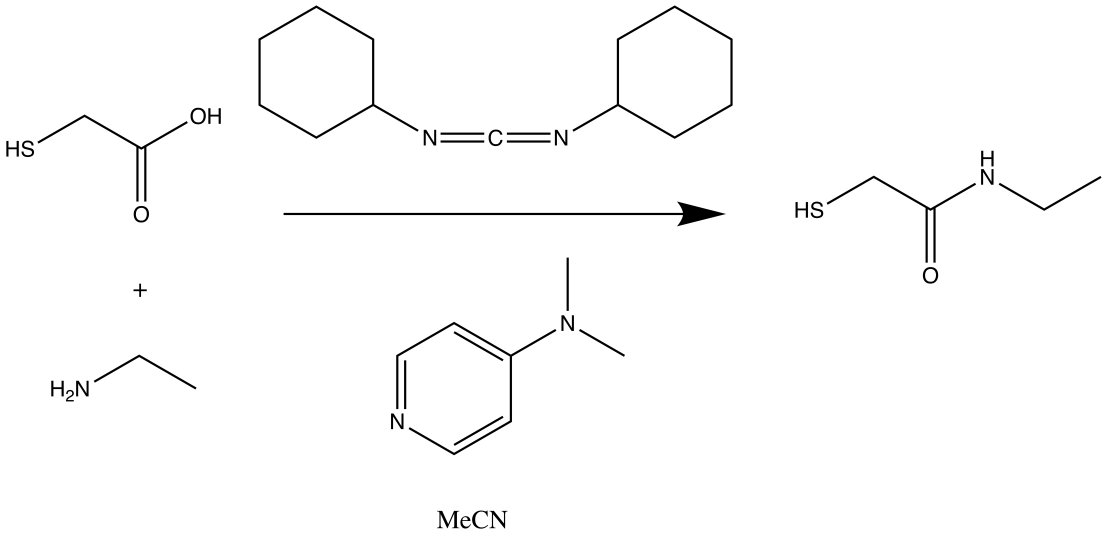


Figure 2.41: Chemical structure of thioglycolic acid.

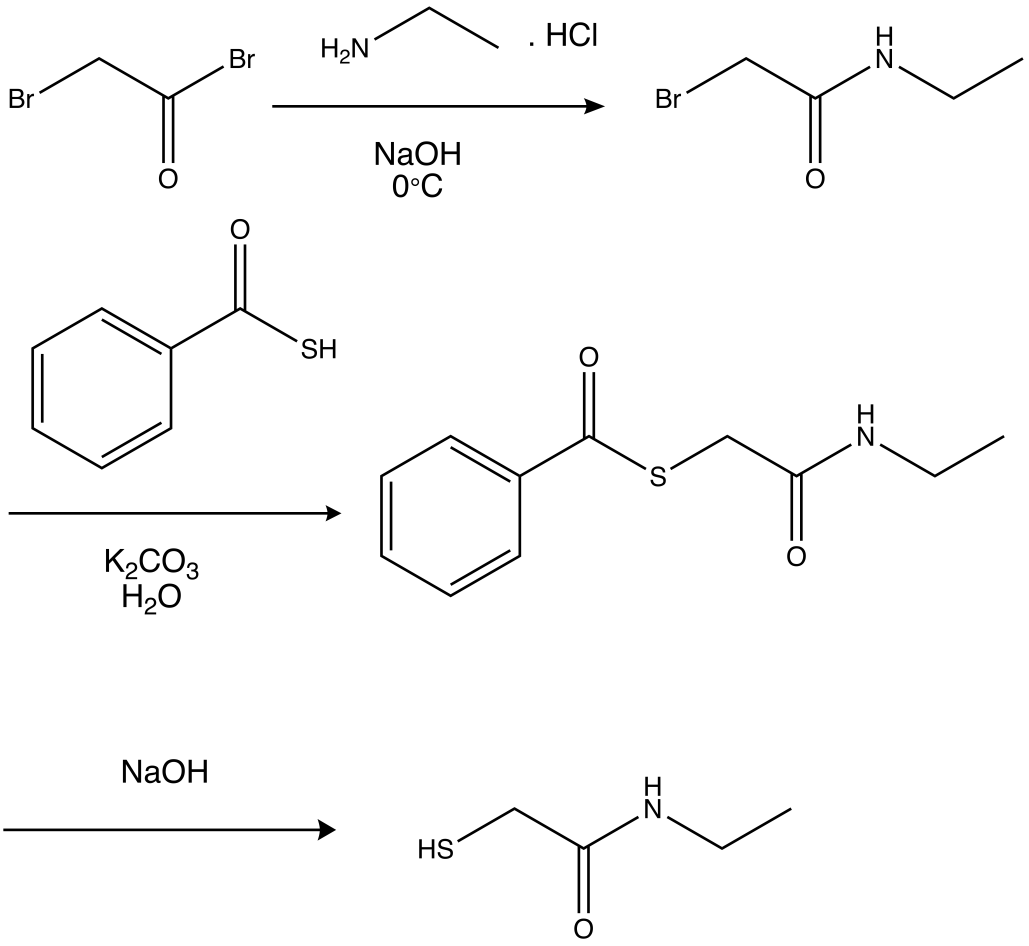
Thioglycolic acid (see *Figure 2.41*), is a simple, commercially available carboxylic acid containing a thiol group. It has been used previously to form hexanuclear tiara-like complexes; it is interesting to note that the carboxylic acid undergoes esterification with methanol during either complex formation or crystallisation, resulting in formation of $[Pd(SCH_2COOCH_3)]_6$, the hexanuclear analogue of $[Pd(SCH_2COOCH_3)]_8$ synthesised by Yamashina *et al.*, indicating that the thioglycolic acid chain is insufficient to form the larger octanuclear toroid.



Scheme 2.5: Original proposed synthesis of EMA, utilising a DCC coupling between thioglycolic acid and ethylamine catalysed by DMAP in acetonitrile.

The proposed synthetic route for the formation of ethyl mercaptamide outlined in *Scheme 2.6* features a coupling between thioglycolic acid and ethylamine facilitated by *N*, *N*-dicyclohexylcarbodiimide (DCC) as a dehydrating agent. The reaction was performed under typical conditions; to 1 eq. thioglycolic acid in 5ml anhydrous THF was added ethylamine (2M in THF, 4 eq.) and DMAP (8 eq.) and the mixture was cooled to 0°C. DCC (2 eq.) was added and the mixture was stirred for 2h at 0°C and 5h at room temperature. Upon cooling the reaction mixture to 0°C again, a crystalline solid precipitated which was filtered and the remaining reaction material analysed by both ESI-MS and MALDI-MS. A very small signal (14% rel. intensity) that could be attributed to ethyl mercaptamide (m/z 121.9, $M+H^+$) was

observed, however isolation of the product was challenging and analytically pure amide could not be obtained in any significant quantity or acceptable yield. A repeat of the reaction did not improve upon the yield or purity.



Scheme 2.6: Modified synthesis of EMA, consisting of an adapted literature one-pot procedure.

To resolve these issues, a new method, illustrated in *Scheme 2.7*, was chosen and trialled, adapted from a literature procedure. To facilitate attachment of the amine, the carboxylic acid was exchanged for an acyl bromide by replacement of thioglycolic acid as the starting component with bromoacetyl bromide. Ethylamine hydrochloride salt was used in replacement of ethylamine (2M in THF) and the reaction occurred in basic conditions at 0°C. Following this, in the same pot the thiol could be attached via a reaction of the crude amide with thiobenzoic acid, again under basic conditions. Cleavage of the thioester bond by

concentrated sodium hydroxide would then leave the desired compound.

Following work-up, the crude reaction mixture was subjected to silica chromatography ($CHCl_3$: MeOH : Acetic Acid, 100 : 2 : 0.1) to isolate a crystalline white solid which was indicated by ESI-MS to be the benzoate salt of the product; this tenative designation was later reinforced by NMR. This was serendipitously beneficial; as the acquisition of the salt improved handling and odour prevention considerably, however hydrolysis in air of the salt to the free thiol occurred over time, leading to the development of a yellow oil and disagreeable odour in the product flask.

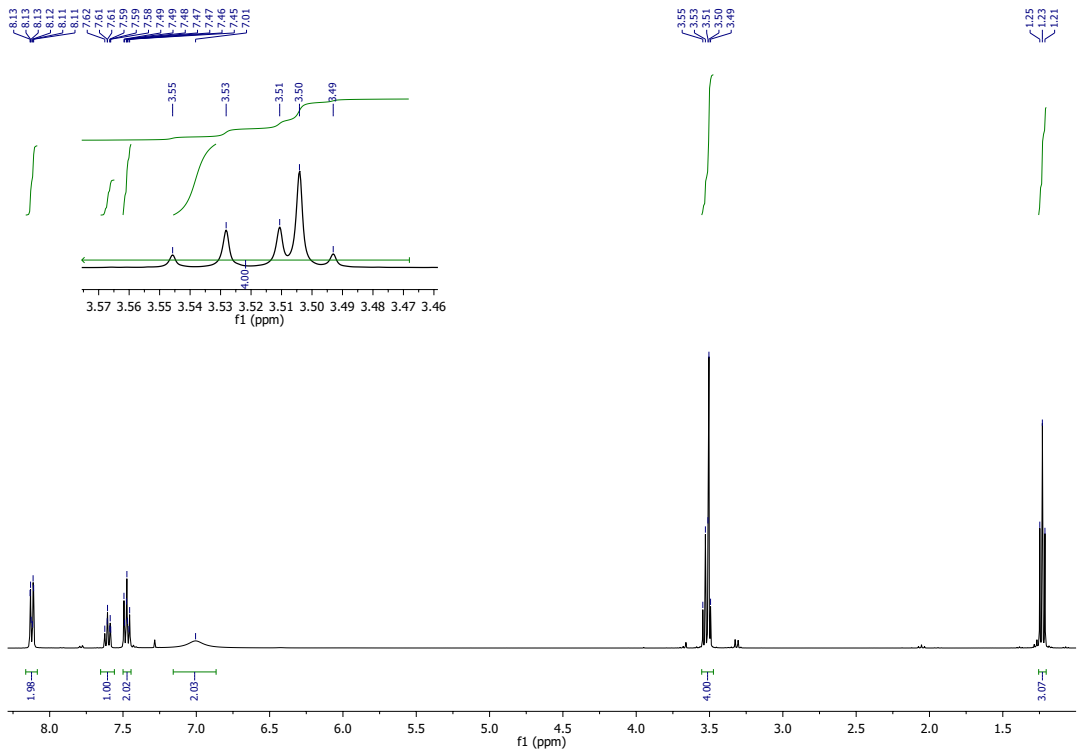


Figure 2.42: ^{1}H NMR spectrum from 1.0 ppm to 8.5 ppm of isolated reaction product (**4**). Solvent: chloroform-d (omitted for clarity), 16 scans.

The NMR assignations are given in *Figure 2.43*. The three multiplets in the aromatic region of the NMR spectrum were assigned to the benzoate protons; the broad signal at 7.01 ppm was attributed to the amide protons on the ethyl mercaptamide ligand, however the integration of

two protons could not be rationalised. No signal attributable to the thiol proton is located. Overlap of a quartet and singlet at approximately 3.52 ppm creates a multiplet; however integral analysis suggests 4 protons, consistent with 2 CH_2 environments. No MS signals corresponding to the unhydrolysed intermediate (m/z 223) were observed, discounting the possibility of isolating incompletely reacted thioester product.

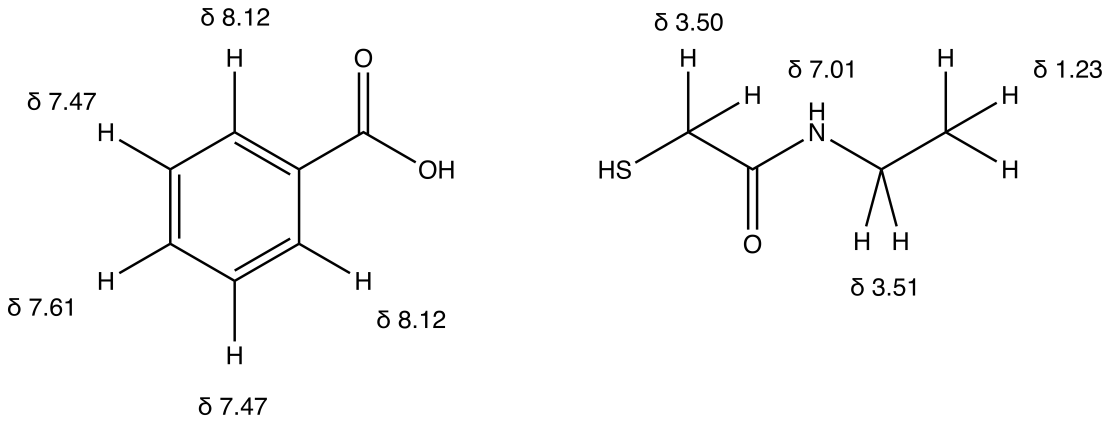
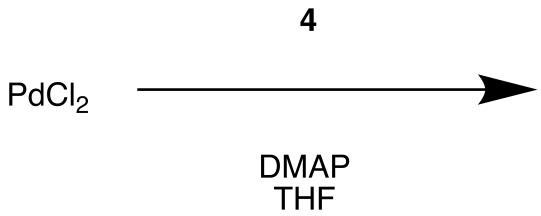


Figure 2.43: Proposed structure and NMR assignments of ^1H spectrum of **4**.

2.2.6.3 Synthesis of Pd EMA

Attempted synthesis of the tiara-like complex was carried out under the same conditions previously used, shown in *Scheme 2.8*, with the exception of the thiol being used in the form of a solid salt rather than the free thiol in oil form. Work up of the crude product was done by simple removal of the volatiles by evaporation under reduced pressure; washing with aqueous solutions was not performed under the suspicion that amide-containing tiara-like complexes formed may be preferentially soluble in water in a manner similar to **1**. This theory of similar solubilities was reinforced when addition of methanol was able to completely dissolve the crude mixture for mass spectrometry analysis.



Scheme 2.7: Attempted synthesis of an ethyl mercaptamide-containing tiara-like complex.

However, the MALDI mass spectrum of the crude mixture revealed no signals corresponding to tiara-like complexes in either positive or negative ionisation mode. In addition, attempts to crystallise the reaction mixture to identify the generated products via either slow evaporation of methanol solutions or slow vapour diffusion of diethyl ether into saturated methanol solutions were unsuccessful. Crystals were obtained only when methyl iodide was added to the crystallisation vials prior to attempted crystal growth; slow diffusion of diethyl ether into a saturated solution in 1:1 methanol : methyl iodide resulted in the growth of red plate crystals.

Screening of a suitable crystal immediately confirmed the absence of a tiara-like complex with unit cell dimensions a = 8.2556(6), b = 9.4564(8), c = 11.6746(7), V = 808.70(11), insufficient in size for even a hexanuclear tiara. Nevertheless, the data was collected to shed some light on the nature of the reaction products obtained. Solution and refinement of the data, as shown in *Figure 2.44*, initially suggested the crystallisation of $[Pd_2(SCH_2CONHCH_2CH_3)_2I_4]^{2-}$ $2[DMAPH]^+$.

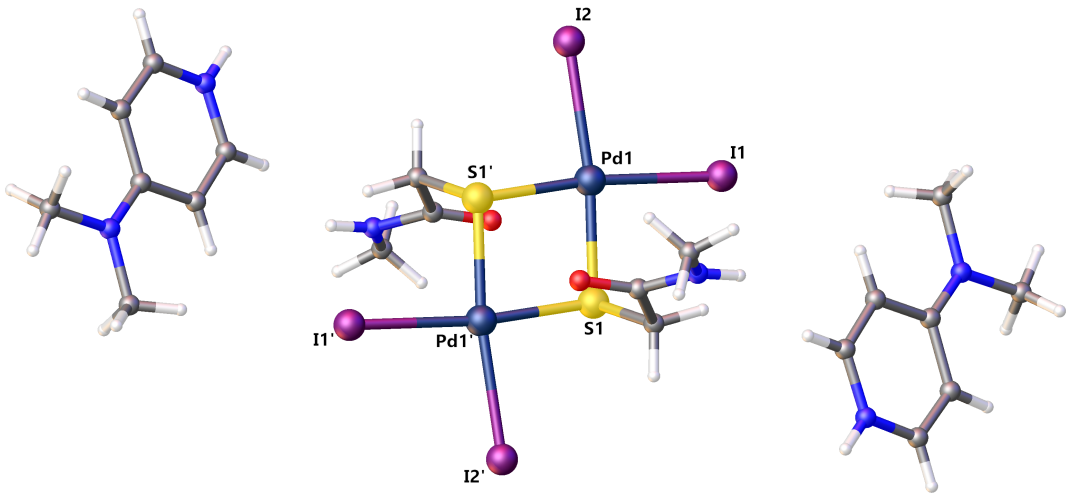


Figure 2.44: Initial solved crystal structure of the obtained single crystals. ' = 1-X, 2-Y, 1-Z. Atom colours: Pd-dark blue, S-yellow, I-purple, C-grey, N-light blue, O-red, H-white.

The terminal carbon atom on the thiolate chain could not be located, which was originally thought to be a result of insufficient data quality. However, persistent errors resulting from close contacts of the amide protons with other protons, along with a lack of electron density to suggest an N-H bond lead to the reassignment of the nitrogen atoms as oxygen atoms instead.

This small change had large implications for the reactions previously accomplished. While the amide may have been synthesised successfully, it had clearly been contaminated with the thioglycolic acid starting material, which had reacted during the attempted tiara formation with the palladium chloride. Crystallisation was then only accomplished via the addition of methyl iodide to the reaction mixture due to the esterification of the carboxylic acid by the reactive alkyl halide.

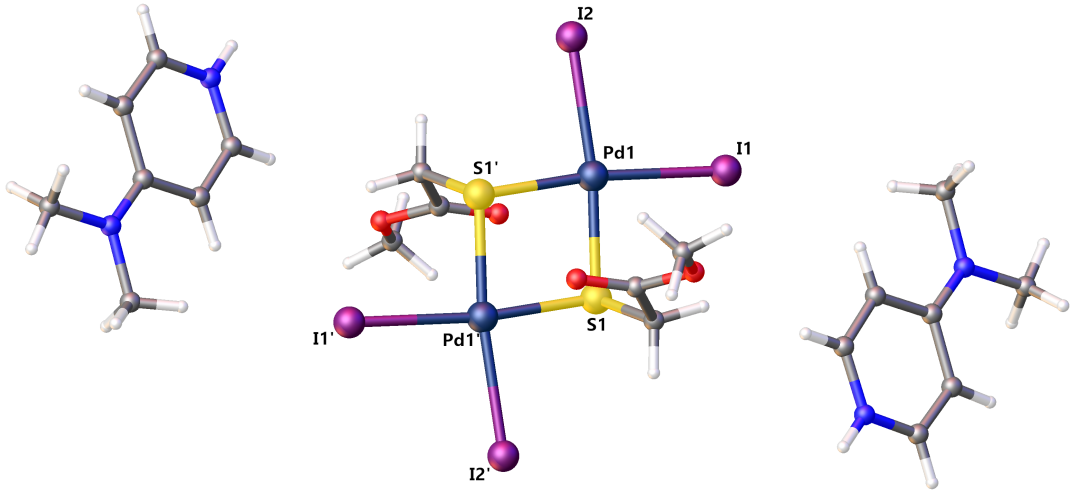


Figure 2.45: Final solved crystal structure of $[Pd_2(SCH_2COOCH_3)_2I_4]$**.**$2[HNC_5H_4N(CH_3)_2]$ (**5**). ' = 1-X, 2-Y, 1-Z. Atom colours: Pd-dark blue, S-yellow, I-purple, C-grey, N-light blue, O-red, H-white.

The obtained structure, shown in *Figure 2.45*, can be thought of as the tiara monomer; the palladium chloride is thought to react with one equivalent of thiol and presumably then dimerises to fill the unoccupied coordination site of the two palladium centres. Notably, the iodides that occupy the terminal coordination sites must originate from the reactive methyl iodide used in the crystallisation, indicating that a tiara complex is not formed during the initial reaction. Later studies have confirmed the stability of tiara-like complexes to methyl iodide (see *Chapter 3.2.4*).

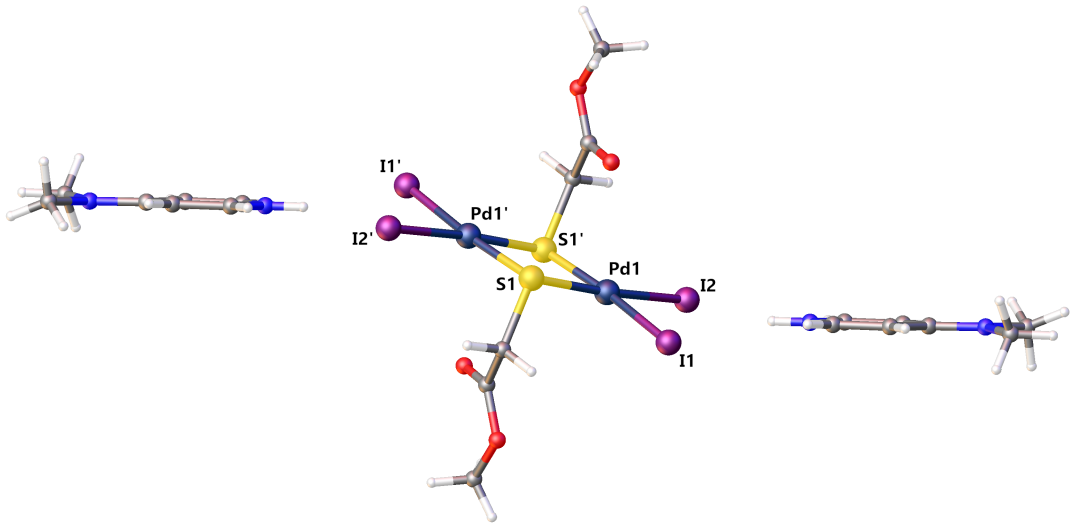


Figure 2.46: Packing of complex and protonated DMAP in the crystal structure of **5**. ' = 1-X, 2-Y, 1-Z. Atom colours: Pd-dark blue, S-yellow, I-purple, C-grey, N-light blue, O-red, H-white.

Initially it was suspected that the dimethylaminopyridine residues located in the crystal structure may have been methylated on the nucleophilic pyridyl nitrogen from a reaction between methyl iodide and DMAP; charged quaternary nitrogen formed from a reaction with methyl iodide would provide a large stable counterion to support packing of the complex in an extended crystalline structure. The introduction of a large positive counterion could then allow crystal growth to occur.

No significant electron density that could be attributed to a methyl group was detected; and closer inspection of the packing of the crystal structure, as given in *Figure 2.46* and *Figure 2.47*, places the pyridyl nitrogens in close proximity to the complex, indicating instead simple protonation rather than methylation of the basic nitrogen. The protonated DMAP molecules are likely to have been formed previously in the reaction as a result of deprotonating the thiol, hence the role of the methyl iodide in initiating the crystal growth is likely to be the esterification of the ligand.

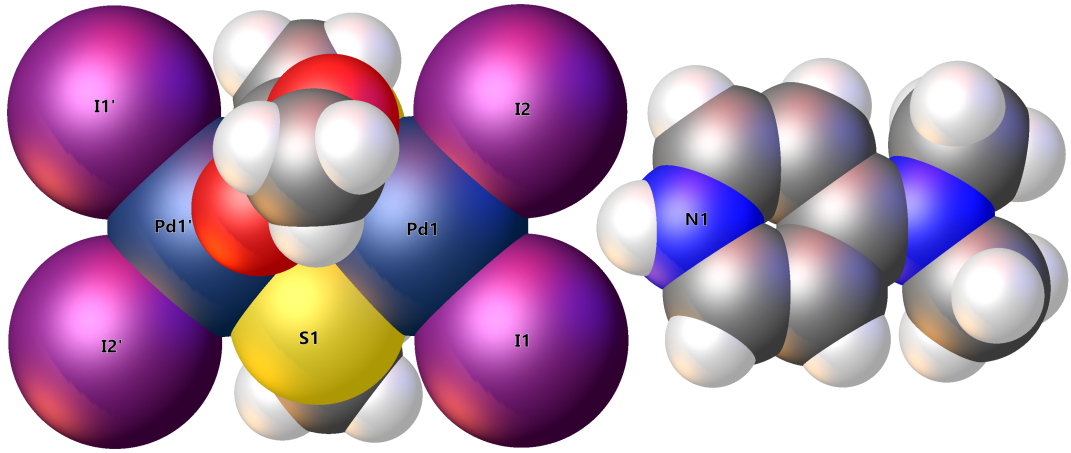


Figure 2.47: Close range interaction between protonated DMAP and iodide substituents in **5**. ' = 1-X, 2-Y, 1-Z. Atom colours: Pd-dark blue, S-yellow, C-grey, N-light blue, O-red, H-white.

The $DMAPH^+$ molecules within the crystal structure appear to stack to create pi-pi assemblies (see *Figure 2.48*). Two DMAP rings are found in an antiparallel conformation at a

vertical distance of 3.887 Å and a shift of 1.621 Å. The antiparallel stacking of the two molecules may not only serve to stabilise the partial positive and negative electrostatic regions of the pyridyl ring but also orientating the positively charged pyridyl nitrogen towards the electronegative amino nitrogen, further stabilising the crystal structure.

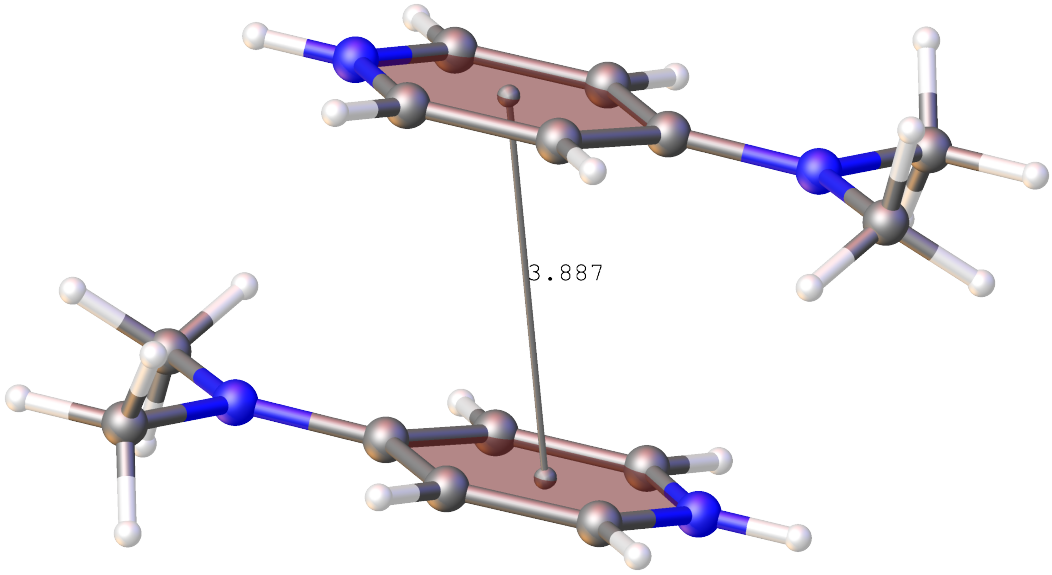


Figure 2.48: π-π stacking of two protonated DMAP molecules in the crystal structure of **5**. Atom colours: C-grey, N-light blue, H-white. The distance between the centre of the phenyl rings is shown by a solid grey line.

As it is extremely challenging to locate or even prove the existence of hydrogen atoms in x-ray diffraction due to their very limited scattering power, it may be debated whether or not the nature of the interaction between the iodides and the pyridyl ring represents hydrogen bonding (which would be the case for protonated DMAP) or halogen bonding (which would be the case for unprotonated DMAP). Several factors suggest that the former is more likely than the latter. Firstly, unprotonated DMAP required for halogen bonding would result in the negative charge of the palladium complex being unbalanced. Secondly, the nature of the > Pd-I···N bond angle is 96.6°, far removed from the ideal 180° angle where the anisotropy of the electron density around the iodide results in a δ+ region suited to interact with the δ- lone pair of the nitrogen atom.[22]

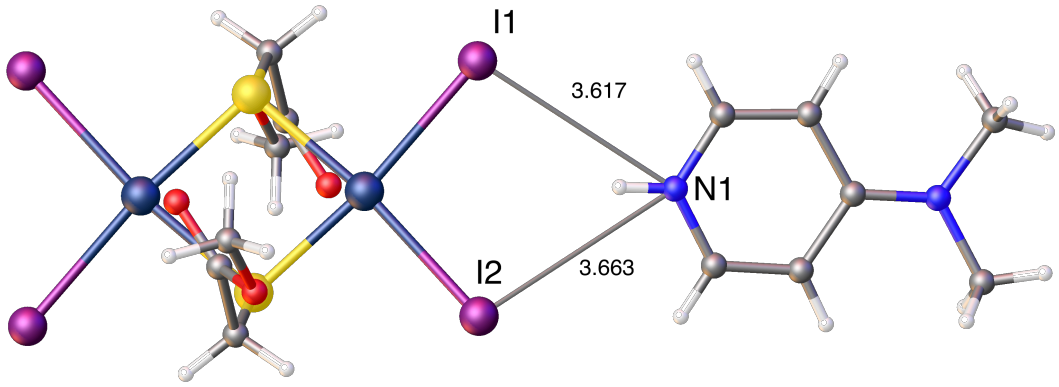


Figure 2.49: Possible hydrogen bonding interactions between I1···N1 and I2···N1 in the crystal structure of **5**. Atom colours: Pd-dark blue, S-yellow, I-purple, C-grey, N-light blue, O-red, H-white.

The I1···N2 hydrogen bond is at a distance of 3.617 Å (> Pd-I···N 97.60°, > I···H-N 140.0°) and the I2···N2 hydrogen bond is at a distance of 3.663 Å (> Pd-I···N 96.59°, > I···H-N 136.9°). These distances therefore suggest quite weak hydrogen bonds, which is not unexpected for a nitrogen donor and an iodide acceptor.[23] Nevertheless when combined with the π-stacking interactions of the protonated DMAP molecules, the intramolecular interactions of the crystal structure may sum to be significant effects in the stabilisation of the packing.

The reason for the formation of this unusual complex over a tiara-like complex is unclear. The 1 : 1 content of thiolate to palladium would suggest that the stoichiometry of the reactants in the synthesis was erroneous. The reaction was repeated using a large excess of thiol and base over the palladium chloride, however absence of signals corresponding to tiara-like complexes persisted in the mass spectrometry analysis. Esterification of the thioglycolic acid chains may be a requirement for the formation of the complex.

2.2.7 Synthesis of Pd MMP

2.2.7.1 Methyl 3-mercaptopropionate

The final tiara-like complex described here is a further isomer from the earlier family detailed above. It was synthesised from methyl 3-mercaptopropionate, a structural isomer of 2-mercaptoethyl acetate by differing orientation of the ester group. The structure of this thiol is given in *Figure 2.50*.

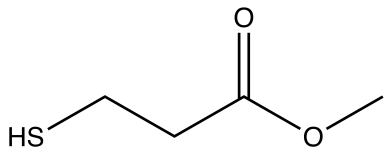


Figure 2.50: Chemical structure of methyl 3-mercaptopropionate (MMP).

It is also a structural isomer of ethyl thioglycolate, retaining the orientation of the ester group but translation of the group down the backbone by one unit; in effect the methylene -CH_2- from the far end of the chain in ethyl thioglycolate is moved proximal to the thiol group.

As an isomer of ethyl thioglycolate, the two share very similar physical properties. The boiling point of methyl 3-mercaptopropionate (MMP) is 54-55°C, compared to 54°C for ethyl thioglycolate and the density is 1.085 g/ml compared to 1.096 g/ml for ethyl thioglycolate. Notably again, as observed for 2-mercaptoethyl acetate, the odour of methyl 3-mercaptopropionate remains disagreeable but distinguishable from either of the two isomers.

2.2.7.2 Synthesis of Pd MMP

Attempted synthesis of the tiara-like complex containing MMP was undertaken under the same conditions as previously described, using THF as the solvent and DMAP as the base. MALDI-MS analysis (see *Figure 2.51*) of the resulting orange powder after workup indicated the major product of the reaction as being the hexanuclear tiara, $[Pd(MMP)_2]_6$ (**6**). However,

minor products obtained from the reaction included the octanuclear, nonanuclear and decanuclear tiaras.

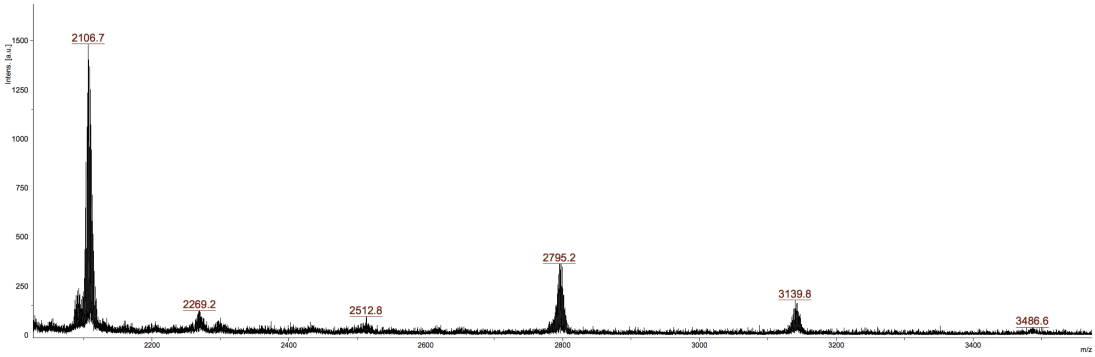


Figure 2.51: MALDI-ToF mass spectrum from 2000 m/z to 3600 m/z of **6** synthesised in THF showing $Pd_6(MMP)_{12}$ (2102.3 m/z, $[M+K]^+$, calc. 2102.6), $Pd_8(MMP)_{16}$ (2790.4 m/z, $[M+K]^+$, calc. 2790.5), $Pd_9(MMP)_{18}$ (3134.6 m/z, $[M+K]^+$, calc. 3134.4) and $Pd_{10}(MMP)_{20}$ (3478.3 m/z, $[M+K]^+$, calc. 3478.3). Matrix: DCTB, Mode: Positive.

Similarly for the other tiara-like complexes described previously and analysed by MALDI-MS, no peak for the heptanuclear tiara-like complex was observed even under higher laser powers, supporting the acquisition of true tiara-like complexes over non-cyclic linear $[Pd(SR)_2]_n$ polymer chains.

The ^1H NMR spectrum of **6**, given in *Figure 2.52*, showed several differences over the spectra obtained for **2** and **3** due to the structural rearrangement of the ligand. The ligand present in **6**, methyl 3-mercaptopropionate is broadly structurally similar to the ligand in **3**, 2-mercaptoethyl acetate, and the spectrum was expected to consist again of four triplets and two singlets. The inversion of the carbonyl moiety such that the oxygen heteroatom within the chain is adjacent to the CH_3 group rather than the β-CH_2 group shifts the signal for the CH_3 group downfield and the α-CH_2 and β-CH_2 upfield.

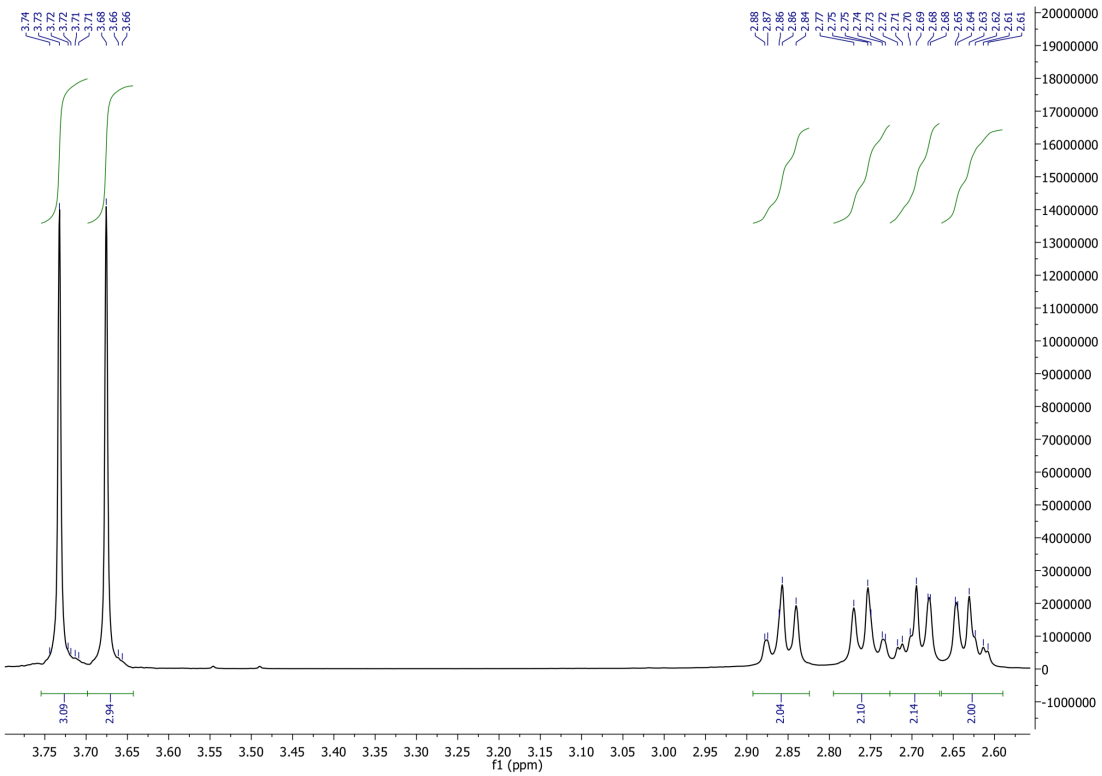


Figure 2.52: [1]H NMR spectrum from 2.55 ppm to 3.80 ppm of **6**. Solvent: chloroform-d, 16 scans.

The triplets in the spectrum show a strong coupling to each other such that the signals appeared to "roof" within the spectrum, making analysis of the spectrum more challenging. However, the integration measurements conform to approximately 2 protons per signal, supporting the assignments as the α-CH2 and β-CH2 environments.

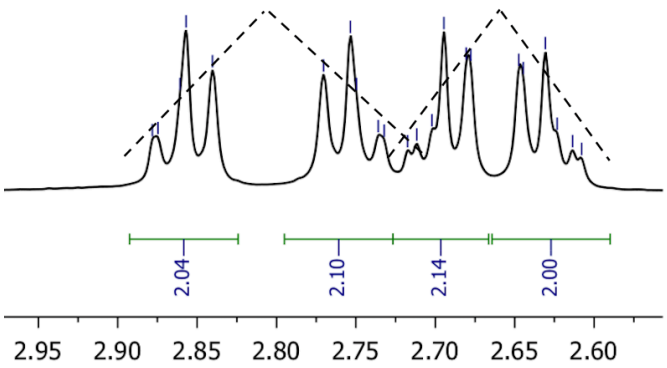


Figure 2.53: [1]H NMR spectrum from 2.55 ppm to 3.00 ppm of **6**, showing the "roofing" effect seen in the CH_2 triplets.

2.2.7.3 Crystallography

Single crystals of **6** were grown by slow vapour diffusion of pentane into a saturated chloroform solution of the complex. Initial screening of a suitable crystal suggested a *P*-1 space group; this was expected given the similarity between the previous hexanuclear tiaras **1** and **3**. However, on solution, persistent non-positive definite atoms rendered refinement to convergence impossible. The data was recollected and resulted in the same errors, however screening of a third crystal resulted in the suggestion of the higher symmetry *R*-3 space group. Solution of the data allowed for complete refinement of the complex, as shown by *Figure 2.54* and *Figure 2.55*.

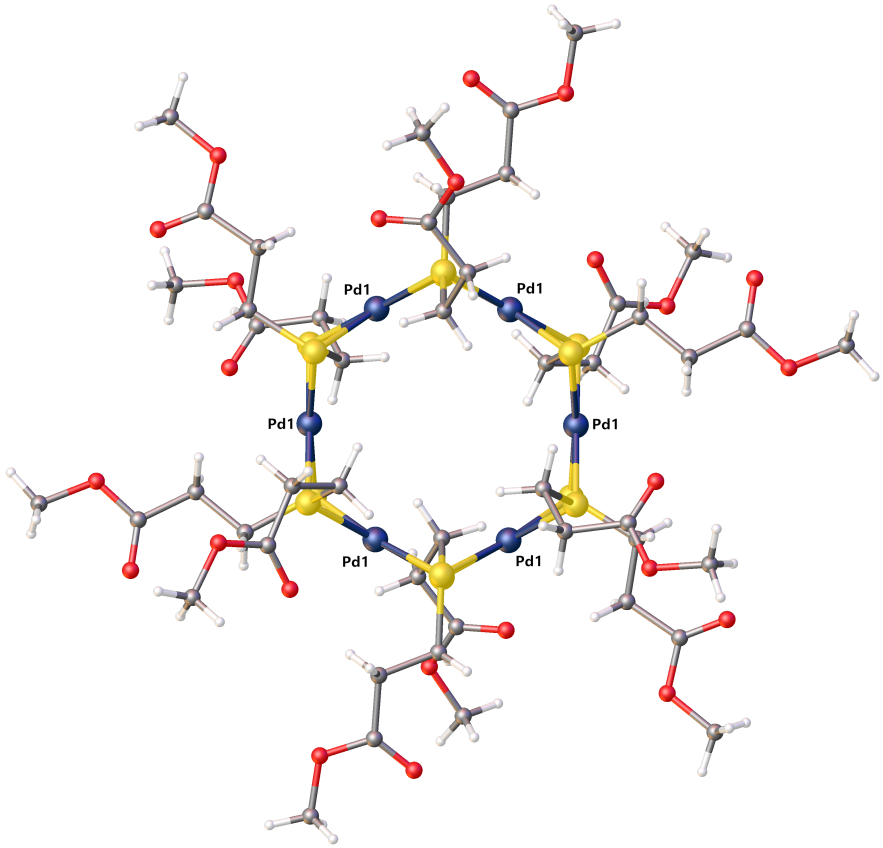


Figure 2.54: Crystal structure of **6** (top view). Atom colours: Pd-dark blue, S-yellow, C-grey, O-red, H-white.

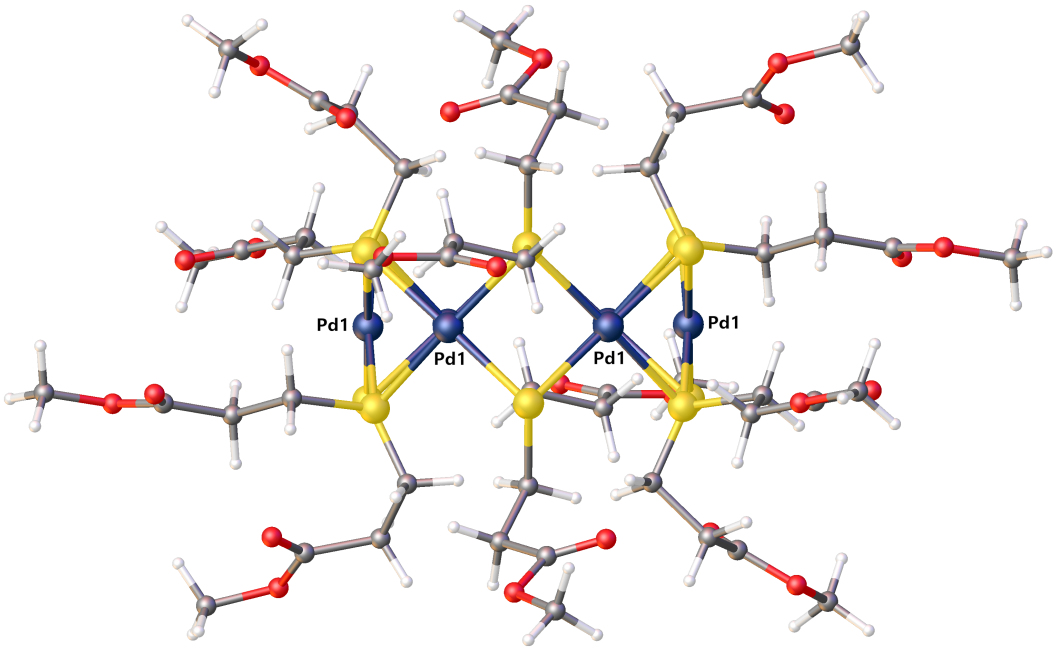


Figure 2.55: Crystal structure of **6** (side view). Atom colours: Pd-dark blue, S-yellow, C-grey, O-red, H-white.

	3	**6**
Empirical Formula	$C_{48}H_{84}O_{24}Pd_6S_{12}$	$C_{48}H_{84}O_{24}Pd_6S_{12}$
Formula Weight	2068.27	2068.27
Temperature / K	120(2)	120(2)
Crystal System	triclinic	trigonal
Space Group	P-1	R-3
a/Å	11.6604(4)	25.0075(4)
b/Å	12.0973(4)	25.0075(4)
c/Å	13.5387(5)	10.0682(2)
α/°	74.597(3)	90.0
β/°	87.925(3)	90.0
γ/°	85.810(3)	120.0
Volume/Å^3	1836.53(11)	5452.8(2)
Z	1	3
D_{calc}/cm^3	1.870	1.890
μ/mm^{-1}	15.383	15.543
F(000)	1032.0	3096.0
Crystal size/mm^3	0.154 x 0.077 x 0.03	0.071 x 0.057 x 0.014
Radiation	CuKα (λ = 1.54184)	CuKα (λ = 1.54184)
2Θ range for data collection/°	6.774 ≤ 2Θ ≤ 147.362	7.07 ≤ 2Θ ≤ 154.82

Index Ranges	-14 ≤ h ≤ 13, -10 ≤ k ≤ 14, -16 ≤ l ≤ 16	-29 ≤ h ≤ 30, -24 ≤ k ≤ 31, -12 ≤ l ≤ 12
Reflections Collected	13441	11542
Independent Reflections	7197 [R_{int} = 0.0234, R_{sigma} = 0.0300]	2531 [R_{int} = 0.0481, R_{sigma} = 0.0269]
Data/restraints/parameters	7197 / 0 / 412	2531 / 0 / 138
Goodness-of-fit on F2	1.047	1.204
Final R indexes [I > 2σ(I)]	R_1 = 0.0344, wR_2 = 0.0938	R_1 = 0.0337, wR_2 = 0.1033
Final R indexes [all data]	R_1 = 0.0358, wR_2 = 0.0951	R_1 = 0.0352, wR_2 = 0.1062
Largest diff. peak/hole / e Å^{-3}	1.82 / -1.27	0.70 / -1.39

Table 2.7: Crystallography tables for Pd MEA (**3**) and Pd MMP (**6**)

The structure of **6** is most similar to that of **3**; the crystallographic details are compared in *Table 2.7*. As previously mentioned, the two differ only by the arrangement of the ester group, with the carbonyl oxygen closer to the sulfur thiolate in **6**. This change, potentially providing more efficient packing within the solid state, causes small shifts in the geometry of the tiara ring. As noted in *Chapter 2.2.4.3*, for **3** the > Pd-Pd-Pd angles are 119.3°, 119.7° and 121.0° which prevent perfect hexagonal symmetry. For **6** however, each of the > Pd-Pd-Pd internal angles is exactly 120° which allow for the adoption of a trigonal crystal system. The packing of the tiara is shown below in *Figure 2.56* and *Figure 2.57*.

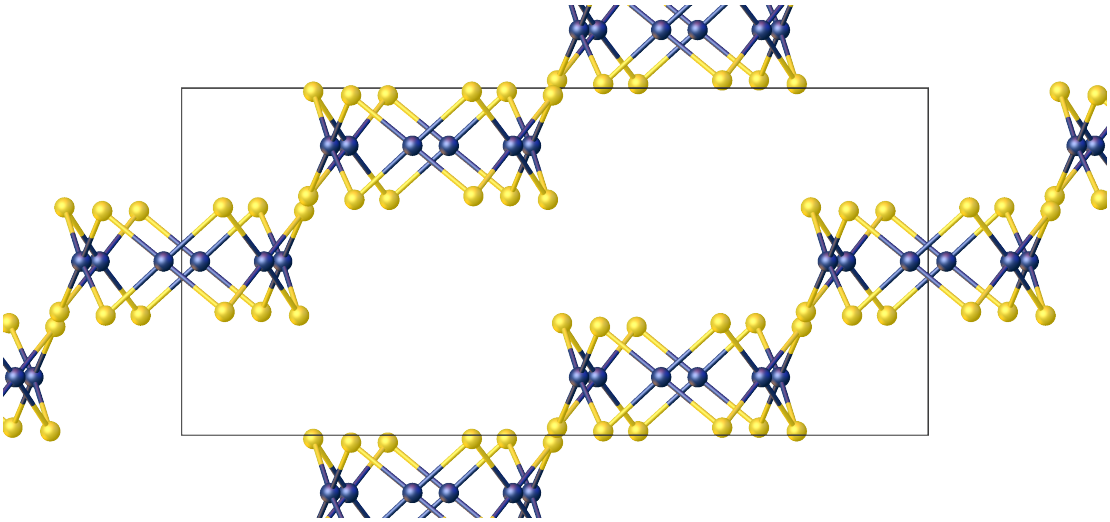


Figure 2.56: Extended packing of **6** in the crystal structure. The unit cell is indicated by solid black lines, viewed along the *a* axis.

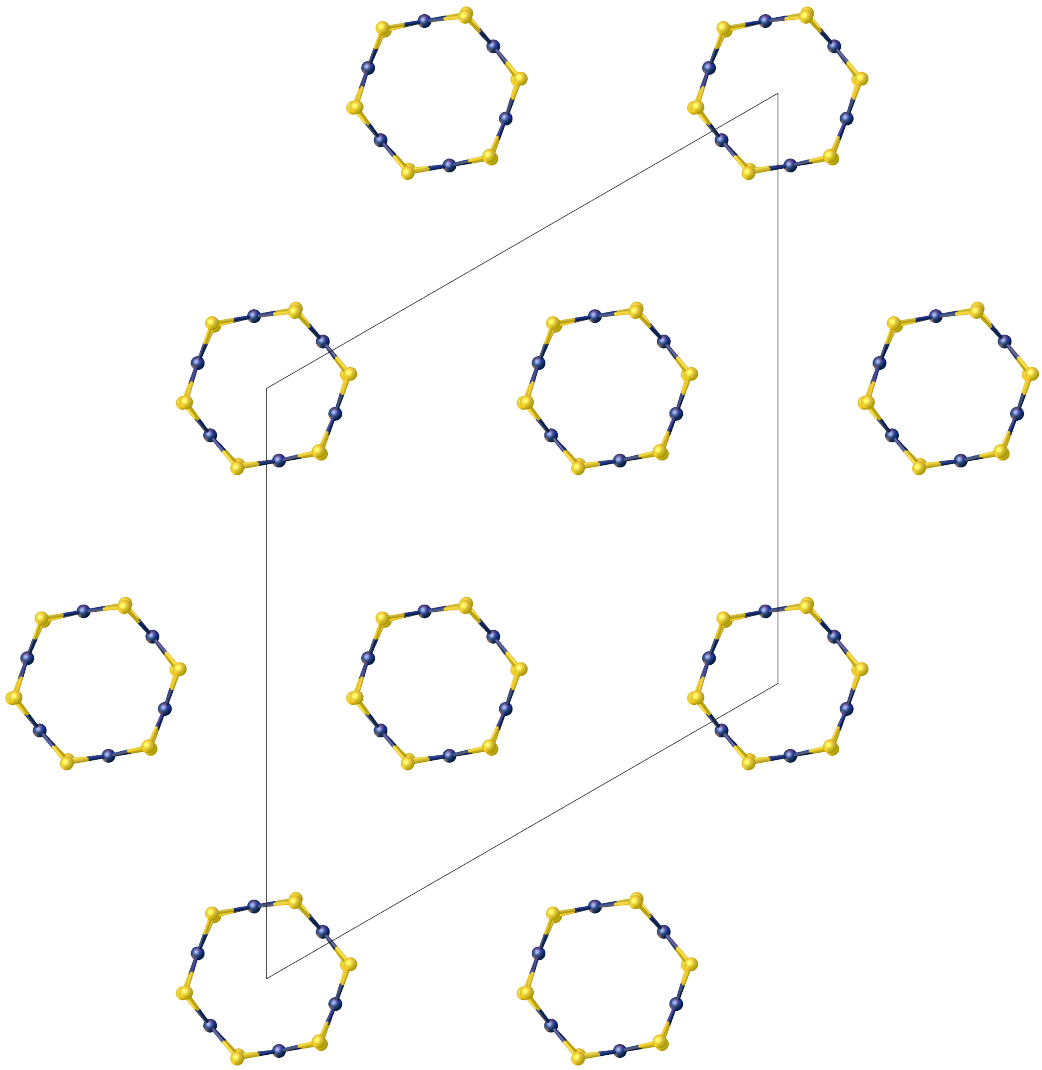


Figure 2.57: Extended packing of **6** in the crystal structure. The unit cell is indicated by solid black lines, viewed along the *c* axis.

This tiara-like complex is most comparable with the isomeric Pd ETG (**2**) and Pd MEA (**3**). The structural change from ethyl thioglycolate to methyl 3-mercaptopropionate is smaller than the modification from ethyl thioglycolate to 2-mercaptoethyl acetate, as the ester group retains the original orientation and the branched oxygen is closer to the sulfur atom. On this basis it would be expected for the distribution of products (and the resultant mass spectrum) of the reactions of ethyl thioglycolate to more closely resemble that of methyl 3-mercaptopropionate, rather than 2-mercaptoethyl acetate (see *Figure 2.58*).

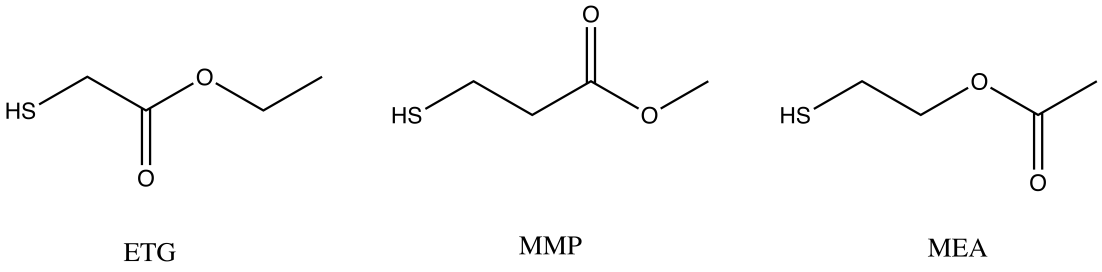


Figure 2.58: The chemical structures of (left to right): ethyl thioglycolate (ETG), methyl 3-mercaptopropionate (MMP) and 2-mercaptoethyl acetate (MEA).

Interestingly however, this does not appear to be the case. The intensity of the octanuclear tiara-like complex signal in the reaction products resulting from the reaction of methyl 3-mercaptopropionate is much lower in intensity relative to the hexanuclear signal than can be observed for the mass spectrum of the reaction products obtained from the mixing 2-mercaptoethyl acetate with palladium chloride, where the relative intensities of the hexanuclear and octanuclear tiaras are approximately equal.

However, the mass spectrum for methyl 3-mercaptopropionate shows acquisition of nona- and deca-nuclear tiaras in addition to the octanuclear, something not observed for either ethyl thioglycolate or 2-mercaptoethyl acetate and more closely resembles the spectra obtained for **1** using either ethanol or methanol as the reaction solvent. If it is assumed that the methyl 3-mercaptopropionate ligands are not strongly associating during the tiara formation, then this observation supports the theory that the presence of higher nuclearity complexes during the formation of *N*-acetylcysteamine tiaras may be attributable to the solvent disrupting the intra-molecular hydrogen bonds.

Methyl 3-mercaptopropionate possesses less steric bulk on the terminus of the ligand chain when compared with 2-mercaptoethyl acetate yet hexanuclear tiaras are still vastly more favourable over complexes of greater nuclearity. It is notable that both ligands will produce a

range of sizes of tiara-like complexes whereas ethyl thioglycolate selectively forms octanuclear complexes. This suggests that the carbonyl oxygen may be located on a particular position especially conducive towards the formation of octanuclear complexes. However, the position of the carbonyl is not the sole deciding factor, as the previously mentioned thioglycolic acid (see *Figure 2.59*) reacts with palladium chloride to form hexanuclear tiaras.

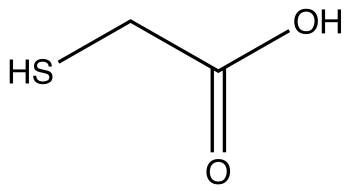


Figure 2.59: Chemical structure of thioglycolic acid. The ligand differs from ethyl thioglycolate by de-esterification of the $-CH_2CH_3$ ligand "tail".

In this case, it is likely that the absence of a 'tail' after the carbonyl group renders the ligand unable to occupy the central void effectively, destabilising the octanuclear tiara and causing the hexanuclear tiara to be formed preferentially. However, it is also possible that the presence of the carboxylic acid functional group allows for intramolecular hydrogen bonding interactions, similar to those that are suspected to exist for complex **1**. These would hypothetically act in a similar manner to cause early termination of the growing tiara polymer and favour a hexanuclear tiara over those of larger nuclearities.

2.3 Conclusions

A number of new tiara-like complexes have been synthesised and characterised. **1**, **2**, **3** and **6** have not previously been reported despite the clear potential of synthesising structurally similar tiara-like complexes. Each of the complexes has been purified and the structures and solid state packing have been investigated by single crystal x-ray crystallography.

The introduction of small changes to the structure of the thiol ligand used in the tiara formation has a significant effect on the final structure of the tiara-like complex formed. For ethyl thioglycolate, 2-mercaptoethyl acetate and methyl 3-mercaptopropionate, very small rearrangements of the structure of the ligands results in a marked difference in the tiara-like complexes formed. When the carbonyl oxygen is located on the second carbon atom from the thiol group, octanuclear tiaras are selectively synthesised but any other placement of the carbonyl oxygen results in the formation of primarily hexanuclear complexes.

For MEA (**3**) and MMP (**6**), while hexanuclear tiaras are the primary products formed, the reactions are not selective and side products including octanuclear, nonanuclear and decanuclear complexes are also observed in the mass spectra. Isolation of these side products was not possible due to the similar radii of the complexes, requiring much higher resolution size exclusion chromatography. Alternatively, performing the synthesis on a larger scale to increase the amount of side products obtained could allow for concurrent crystallisation of one or more side products along with the crystallisation of the hexanuclear tiara.

For **1**, the presence of an amide functional group rather than an ester causes different products to be formed in the reaction by changing the solvent. When the synthesis is performed in an aprotic solvent such as THF, only hexanuclear tiaras are observed in the mass

spectra. Intramolecular interactions, formed via the hydrogen bonding self-association of the ligands in the growing tiara chain, are theorised to cause early collapse of the linear chain, resulting in the selective formation of the hexanuclear product. Disruption of these hydrogen bonds by a protic solvent able to participate in hydrogen bonding prevents this effect; this causes larger nuclearity tiaras to be formed as side products in a similar manner as the synthesis of ***3*** or **6** in THF.

2.4 Experimental

2.4.1 Materials

All reagents were purchased from commercial suppliers (Sigma-Aldrich or VWR international) and used without further purification. All solvents were degassed by bubbling through N_2 for at least 10 minutes prior to use.

2.4.2 Spectroscopic Methods

2.4.2.1 NMR Spectroscopy

^{1}H NMR experiments were recorded using either a Bruker AV(III)400 or a Bruker AV(III)400HD. Chemical shifts are reported relative to the MeOD residual peak at 3.31ppm or the $CDCl_3$ residual peak at 7.26 ppm. For ^{1}H spectroscopy, splitting patterns are described in brackets after the chemical shift (s=singlet, t=triplet, q=quartet, bs=broad singlet, m=multiplet), followed by the number of protons and the proton assignation.

2.4.2.2 Single Crystal X-ray Diffraction

Single crystal X-ray diffraction experiments were performed on an Oxford Diffraction SuperNova Duo Atlas diffractometer or on an Agilent GV1000 AtlasS2 diffractometer. In all cases data was collected at 120K using monochromated Cu Kα radiation (λ = 1.54184 Å) and processed using CrysAlisPro.[24] Structures were solved either using ShelXS via Direct Methods or by ShelXT via Intrinsic Phasing and in all cases refined by ShelXL[25] via a Least Squares method within Olex2.[26] Non-hydrogen atoms were refined anisotropically and hydrogen atoms placed at calculated positions.

2.4.2.3 Mass Spectrometry

MALDI-ToF mass spectra were recorded with a Bruker Ultraflex III mass spectrometer.

Trans-2-[3-(4-tert-butylphenyl)-2-methyl-2-propenylidene]-malononitrile (DCTB) was used as the matrix and sodium trifluoroacetate was used as a cationising agent where necessary. ESI mass spectra were recorded using a Bruker MicroTOF using methanol as solvent.

2.4.3 Synthesis of Tiara-like Complexes

*2.4.3.1 Synthesis of Pd NAC (**1**)*

To a solution of *N*-acetylcysteamine (60 µl, 0.56 mmol) and DMAP (68 mg, 0.56 mmol) in THF (5 ml) was added $PdCl_2$ (50 mg, 0.28 mmol) and the mixture was stirred for 18 hours. The solvent was removed and the solid product washed with diethyl ether. Orange block crystals of **1** were grown by slow evaporation of a saturated methanol solution (58 mg, 61%). ^{1}H NMR (400MHz, MeOD) δ 3.57 (t, 12H, β-CH_2), 3.44 (t, 12H, β-CH_2), 2.67 (t, 12H, α-CH_2), 2.58 (t, 12H, α-CH_2), 2.02 (s, 18H, CH_3), 1.98 (s, 18H, CH_3). MS MALDI (+) (MeOH, DCTB/MeCN) m/z 2077.9 $[M+Na]^+$. Analytically pure samples were recrystallised from MeCN. Anal. Calcd for $Pd_6S_{12}N_{12}O_{12}C_{48}H_{96}.CH_3CN$: C, 28.62; H, 4.58; N, 8.68. Found: C, 29.18; H, 4.79; N, 8.46.

*2.4.3.3 Synthesis of Pd ETG (**2**)*

To a solution of ethyl thioglycolate (61 µl, 0.56 mmol) and DMAP (68 mg, 0.56 mmol) in THF (5 ml) was added $PdCl_2$ (50 mg, 0.28 mmol) and the mixture stirred for 6 hours. The solvent was removed and the solid dissolved in CH_2Cl_2, washed with NaOH (0.1M) and brine and dried over magnesium sulfate. Following evaporation of the solvent, the orange solid was recrystallised from isopropanol (56 mg, 58%). ^{1}H NMR (400MHz, $CDCl_3$) δ 4.44 (q, 12H, β-CH_2), 4.24 (q, 12H, β-CH_2), 3.39 (s, 12H, α-CH_2), 3.27 (s, 12H, α-CH_2), 1.56 (t, 18H, CH_3), 1.34 (t, 18H, CH_3). MS MALDI (+) ($CHCl_3$, DCTB/MeCN) m/z 2783.0 $[M+Na]^+$, 2799.0 $[M+K]^+$. Anal. Calcd for $Pd_8S_{16}O_{32}C_{64}H_{112}$: C, 27.87; H, 4.09; N, 0. Found: C, 27.68; H, 3.91; N, 0.

*2.4.3.2 Synthesis of Pd MEA (**3**)*

To a solution of 2-mercaptoethyl acetate (61 µl, 0.56 mmol) and DMAP (68 mg, 0.56 mmol) in THF (5 ml) was added $PdCl_2$ (50 mg, 0.28 mmol) and the resulting orange suspension was stirred for 18 hours. The solvent was removed and the solid dissolved in CH_2Cl_2, washed with NaOH (0.1M) and brine and dried over magnesium sulfate. Single crystals were obtained following slow evaporation of a saturated $CHCl_3$ solution (63 mg, 65%). ^1H NMR (400MHz, $CDCl_3$) δ 4.39 (t, 12H, β-CH_2), 4.29 (t, 12H, β-CH_2), 2.78 (t, 12H, α-CH_2), 2.66 (t, 12H, α-CH_2), 2.14 (s, 18H, CH_3), 2.09 (s, 18H, CH_3). MS MALDI (+) ($CHCl_3$, DCTB/MeCN) m/z 2091.9 $[M+Na]^+$. Anal. Calcd for $Pd_8S_{16}O_{32}C_{64}H_{112}$: C, 27.87; H, 4.09; N, 0. Found: C, 27.72; H, 4.06; N, 0.

*2.4.3.4 Other Syntheses of Pd NAC (**1**)*

Pd NAC (**1**) was successfully synthesised in solvents other than tetrahydrofuran, resulting in the formation of small amounts of $Pd_x(SCH_2CH_3CONHCH_3)_{2x}$ where x = 5, 8, 9, 10, 11. The general synthetic method is identical to that described above, except with the replacement of THF (5ml) with either methanol (5 ml), ethanol (5ml) or n-propanol (5ml). Separation of the isomers was unsuccessful.

*2.4.3.5 Synthesis of ethyl mercaptamide (**4**)*

To a solution of NaOH (20ml, 2M) at 0°C was added ethylamine.HCl (1 g, 12.5 mmol) and the mixture stirred until dissolution. Bromoacetyl bromide (1.1 ml, 12.5 mmol) was added dropwise and the mixture was allowed to rise to room temperature. After stirring for 3.5 hours, a suspension of thiobenzoic acid (1.5 ml, 12.5 mmol) and potassium carbonate (1.2 g, 8.75 mmol) in water (15 ml) was added to the flask and the mixture was stirred overnight. The reaction mixture was filtered, acidified and extracted into ethyl acetate. The organic phase was washed with brine and dried over magnesium sulfate. Evaporation of the solvent yielded

an orange oil (benzoyl-thio intermediate, m/z 246). To a suspension of the oil in water was added concentrated NaOH and the mixture was stirred for 2 hours whereupon the mixture was acidified and extracted into ethyl acetate, washed with brine and dried over magnesium sulfate. Silica gel chromatography of the yellow-orange oil ($CHCl_3$: Methanol : Acetic Acid, 100 : 2 : 0.1) yielded an off-white solid which rapidly hydrolysed. ^{1}H NMR (400MHz, $CDCl_3$) δ 8.12 (d, 2H, ortho-CH), 7.61 (t, 1H, para-CH), 7.47 (t, 2H, meta-CH), 3.52 (m, 4H, α-CH_2 / β-CH_2), 1.23 (t, 3H, CH_3). MS ESI (+) 121.03 $(M+H)^+$.

*2.4.3.6 Synthesis of Pd EMA (**5**)*

To a solution of **4** (153 mg, 0.56 mmol) and DMAP (68 mg, 0.56 mmol) in THF (5 ml) was added $PdCl_2$ (50 mg, 0.26 mmol) and the mixture was stirred for 16 hours. The solvent was removed and the orange-red solid dissolved in the minimum volume of methanol : methyl iodide (1:1). Single crystals suitable for XRD analysis were grown by slow diffusion of diethyl ether into the saturated solution.

*2.4.3.7 Synthesis of Pd MMP (**6**)*

To a solution of methyl 3-mercaptopropionate (61 μl, 0.56 mmol) and DMAP (68 mg, 0.56 mmol) in THF (5 ml) was added $PdCl_2$ and the mixture was stirred for 18 hours. The solvent was removed and the solid dissolved in CH_2Cl_2, washed with NaOH (0.1 M) and brine and dried over magnesium sulfate. Single crystals suitable for XRD analysis were obtained by vapour diffusion of pentane into a saturated solution in chloroform (67 mg, 69%). ^{1}H NMR (400MHz, $CDCl_3$) δ 3.73 (s, 3H, CH_3), 3.68 (s, 3H, CH_3), 2.86 (t, 2H, α-CH_2), 2.75 (t, 2H, α-CH_2), 2.69 (t, 2H, β-CH_2), 2.63 (t, 2H, β-CH_2). MS MALDI (+) ($CHCl_3$, DCTB/MeCN) m/z 2091.9 $[M+Na]^+$.

2.4.4 Crystallographic data

*2.4.4.1 Crystal data for **1***

Single crystals suitable for XRD analysis were grown by slow evaporation of a saturated methanol solution. The data was collected on a GV1000 Atlas S2 diffractometer, processed using CrysAlis Pro and solved by ShelXT using Intrinsic Phasing.

Crystal Data for $C_{49}H_{105}N_{12}O_{17}Pd_6S_{12}$ (M = 2157.56 g/mol): triclinic, space group *P*-1 (no. 2), a = 12.20826(12) Å, b = 12.65614(11) Å, c = 14.81683(10) Å, α = 93.1977(6)°, β = 110.0979(8)°, γ = 108.7469(8)°, V = 2000.00(3) Å^3, Z = 1, T = 120(2) K, μ(CuKα) = 14.128 mm^{-1}, D_{calc} = 1.791 g/cm^3, 124159 reflections measured (6.466° ≤ 2Θ ≤ 147.374°), 8023 unique (R_{int} = 0.0404, R_{sigma} = 0.0134) which were used in all calculations. The final R_1 was 0.0169 (I > 2σ(I)) and wR_2 was 0.0431 (all data).

*2.4.4.2 Crystal data for **2***

Single crystals suitable for XRD analysis were grown by slow diffusion of hexane into a saturated chloroform solution. The data was collected on a SuperNova Duo Atlas diffractometer, processed using CrysAlis Pro and solved by ShelXS using Direct Methods.

Crystal Data for $C_{64}H_{120}O_{32.5}Pd_8S_{16}$ (M = 2773.75 g/mol): monoclinic, space group *C* 2/c (no. 15), a = 26.3460(6) Å, b = 26.3625(5) Å, c = 31.9593(8) Å, β = 113.960(3)°, V = 20284.4(8) Å^3, Z = 8, T = 120(2) K, μ(CuKα) = 14.862 mm^{-1}, D_{calc} = 1.817 g/cm^3, 78154 reflections measured (6.052° ≤ 2Θ ≤ 149.6°), 20407 unique (R_{int} = 0.0491, R_{sigma} = 0.0289) which were used in all calculations. The final R_1 was 0.0669 (I > 2σ(I)) and wR_2 was 0.1971 (all data).

*2.4.4.3 Crystal data for **3***

Single crystals suitable for XRD analysis were grown by slow evaporation of a saturated chloroform solution. The data was collected on a GV1000 Atlas S2 diffractometer, processed

using CrysAlis Pro and solved by ShelXT using Intrinsic Phasing.

Crystal Data for $C_{48}H_{84}O_{24}Pd_6S_{12}$ (M = 2068.27 g/mol): triclinic, space group *P*-1 (no. 2), a = 11.6640(4) Å, b = 12.0973(4) Å, c = 13.5387(5) Å, α = 74.597(3)°, β = 87.925(3)°, γ = 85.810(3)°, V = 1836.53(11) Å^3, Z = 1, T = 120(2) K, μ(CuKα) = 15.383 mm^{-1}, D_{calc} = 1.870 g/cm^3, 13441 reflections measured (6.774° ≤ 2Θ ≤ 147.362°), 7197 unique (R_{int} = 0.0234, R_{sigma} = 0.0300) which were used in all calculations. The final R_1 was 0.0344 (I > 2σ(I)) and *w*R_2 was 0.0951 (all data).

	1	**3**	**2**
Empirical Formula	$C_{49}H_{105}N_{12}O_{17}Pd_6S_{12}$	$C_{48}H_{84}O_{24}Pd_6S_{12}$	$C_{64}H_{120}O_{32.5}Pd_8S_{16}$
Formula Weight	2157.56	2068.27	2773.75
Temperature / K	120(2)	120(2)	120(2)
Crystal System	triclinic	triclinic	monoclinic
Space Group	*P*-1	*P*-1	*C* 2/c
a/Å	12.20826(12)	11.6604(4)	26.3460(6)
b/Å	12.65614(11)	12.0973(4)	26.3625(5)
c/Å	14.81683(10)	13.5387(5)	31.9593(8)
α/°	93.1977(6)	74.597(3)	90.0
β/°	110.0979(8)	87.925(3)	113.960(3)
γ/°	108.7469(8)	85.810(3)	90.0
Volume/Å^3	2000.00(3)	1836.53(11)	20284.4(8)
Z	1	1	8
D_{calc}/cm^3	1.791	1.870	1.817
μ/mm^{-1}	14.128	15.383	14.862
F(000)	1087.0	1032.0	11104.0
Crystal size/mm^3	0.152 x 0.091 x 0.035	0.154 x 0.077 x 0.03	0.293 x 0.235 x 0.108
Radiation	CuKα (λ = 1.54184)	CuKα (λ = 1.54184)	CuKα (λ = 1.54184)
2Θ range for data collection/°	6.466 ≤ 2Θ ≤ 147.374	6.774 ≤ 2Θ ≤ 147.362	6.052 ≤ 2Θ ≤ 149.6
Index Ranges	-14 ≤ h ≤ 15, -15 ≤ k ≤ 15, -18 ≤ l ≤ 18	-14 ≤ h ≤ 13, -10 ≤ k ≤ 14, -16 ≤ l ≤ 16	-32 ≤ h ≤ 27, -32 ≤ k ≤ 32, -38 ≤ l ≤ 39
Reflections Collected	124159	13441	78154

Independent Reflections	8023 [R_{int} = 0.0404, R_{sigma} = 0.0134]	7197 [R_{int} = 0.0234, R_{sigma} = 0.0300]	20407 [R_{int} = 0.0491, R_{sigma} = 0.0289]
Data/restraints/ parameters	8023 / 9 / 456	7197 / 0 / 412	20407 / 3741 / 1542
Goodness-of-fit on F2	1.064	1.047	1.028
Final R indexes [I > 2σ(I)]	R_1 = 0.0169, wR_2 = 0.0429	R_1 = 0.0344, wR_2 = 0.0938	R_1 = 0.0669, wR_2 = 0.1926
Final R indexes [all data]	R_1 = 0.0172, wR_2 = 0.0431	R_1 = 0.0358, wR_2 = 0.0951	R_1 = 0.0709, wR_2 = 0.1971
Largest diff. peak/ hole / e Å^{-3}	0.70 / -0.49	1.82 / -1.27	2.71 / -1.58

Table 2.8: Crystallography tables for **1**, **3** and **2**.

2.4.4.4 Crystal data for ***5***

Single crystals suitable for XRD analysis were grown by vapour diffusion of diethyl ether into a saturated solution of methanol : methyl iodide (1:1). The data was collected on a SuperNova Duo Atlas diffractometer, processed using CrysAlis Pro and solved by ShelXT using Intrinsic Phasing.

Crystal Data for $C_{20}H_{32}I_4N_4O_4Pd_2S_2$ (M =1177.01 g/mol): triclinic, space group *P*-1 (no. 2), a = 8.2556(6) Å, b = 9.4564(8) Å, c = 11.6746(7) Å, α = 80.324(6)°, β = 69.511(6)°, γ = 71.666(7)°, V = 808.70(11) Å^3, Z = 1, T = 120(2) K, μ(CuKα) = 40.419 mm^{-1}, D_{calc} = 2.417 g/cm^3, 5545 reflections measured (8.102° ≤ 2Θ ≤ 149.014°), 3187 unique (R_{int} = 0.0429, R_{sigma} = 0.0506) which were used in all calculations. The final R_1 was 0.0518 (I > 2σ(I)) and wR_2 was 0.1433 (all data).

2.4.4.5 Crystal data for ***6***

Single crystals suitable for XRD analysis were grown by slow diffusion of pentane into a saturated chloroform solution. The data was collected on a XtaLAB Pro: Kappa single diffractometer, processed using CrysAlis Pro and solved by ShelXT using Intrinsic Phasing.

Crystal Data for $C_{48}H_{84}O_{24}Pd_6S_{12}$ (M =2068.27 g/mol): trigonal, space group *R*-3 (no. 148), a = 25.0075(4) Å, c = 10.0682(2) Å, V = 5452.8(2) $Å^3$, Z = 3, T = 120(2) K, μ(CuKα) = 15.543 mm^{-1}, D_{calc} = 1.890 g/cm^3, 11542 reflections measured (7.07° ≤ 2Θ ≤ 154.82°), 2531 unique (R_{int} = 0.0481, R_{sigma} = 0.0269) which were used in all calculations. The final R_1 was 0.0337 (I > 2σ(I)) and *w*R_2 was 0.1062 (all data).

2.5 References

1. W. Gaete, J. Ros, X. Solans, M. Font-Altaba and J. L. Brianso, *Inorg. Chem.*, 1984, **23**, 39-43.
2. I. G. Dance, M. L. Scudder and R. Secomb, *Inorg. Chem.*, 1985, **24**, 1201.
3. P. Woodward, L. F. Dahl, E. W. Abel and B. C. Crosse, *J. Am. Chem. Soc.*, 1965, **87**, 5251-5253.
4. M. Kriege and G. Henkel, *Z. Naturforsch. B*, 1987, **42**, 1121-1128.
5. S. A. Ivanov, M. A. Kozee, W. A. Merrill, S. Agarwal and L. F. Dahl, *Dalton Trans.*, 2002, 4105-4115.
6. C. Tan, M. Jin, H. Zhang, S. Hu, T. Sheng and X. Wu, *CrystEngComm*, 2015, **17**, 5110-5115.
7. J. Chen, L. Liu, L. Weng, Y. Lin, L. Liao, C. Wang, J. Yang and Z. Wu, *Sci. Rep.*, 2015, **5**, 16628-16635.
8. A. H. Mahmoudkhani and V. Langer, *Inorg. Chim. Acta*, 1999, **294**, 83-86.
9. B. K. Koo, E. Block, H. Kang, S. Liu and J. Zubieta, *Polyhedron*, 1988, **7**, 1397-1399.
10. A. Datta, N. S. John, G. U. Kulkarni and S. K. Pati, *J. Phys. Chem. A*, 2005, **109** (51), 11647-11649.
11. P. Alemany and R. Hoffmann, *J. Am. Chem. Soc.*, 1993, **115**, 8290-8297.
12. K. Nobusada and T. Yamaki, *J. Phys. Chem. A*, 2004, **108** (10), 1813-1817.
13. C. Zhang, S. Takada, M. Kölzer, T. Matsumoto and K. Tatsumi, *Angew. Chem. Int. Ed.*, 2006, **45**, 3768-3772.
14. C. Zhang, T. Matsumoto, M. Samoc, S. Petrie, S. Meng, T. C. Corkery, R. Stranger, J. Zhang, M. G. Humphrey and K. Tatsumi, *Angew. Chem. Int. Ed.*, 2010, **49**, 4209-4212.
15. E. Arunan, G. R. Desiraju, R. A. Klein, J. Sadlej, S. Scheiner, I. Alkorta, D. C. Clary, R. H. Crabtree, J. J. Dannenberg, P. Hobza, H. G. Kjaergaard, A. C. Legon, B. Mennucci and D. J. Nesbitt, *Pure Appl. Chem.*, 2011, **83**, 1637-1641.
16. L. Pauling, *The Nature of the Chemical Bond*, Cornell University Press, Ithaca, NY, 1960.
17. G. R. Desiraju, *Acc. Chem. Res.*, 2002, **35**, 565-573.
18. S. Humbel, *J. Phys. Chem. A*, 2002, **106**, 5517-5520.
19. P. G. Wenthold, R. R. Squires, *J. Phys. Chem.*, 1995, **99**, 2002-2005.
20. S. Gronert, *J. Am. Chem. Soc.*, 1993, **115**, 10258-10266.
21. Y. Yamashina, Y. Kataoka and Y. Ura, *Inorg. Chem.*, 2014, **53**, 3558-3567.
22. G. Cavallo, P. Metrangolo, R. Milani, T. Pilati, A. Priimagi, G. Resnati and G. Terraneo, *Chem. Rev.*, 2016, **116**, 2478-2601.
23. T. M. Gesing, E. Lork, H. Terao and H. Ishihara, *Z. Naturforsch. B*, 2016, **71** (3), 241-248.

24. CrysAlisPro, 2013, Agilent Technologies UK Ltd. Oxford, UK.
25. G. Sheldrick, *Acta Crystallogr. A*, 2008, **64**, 112-122.
26. O. V. Dolomanov, L. J. Bourhis, R. J. Gildea, J. A. K. Howard and H. Puschmann, *J. Appl. Cryst.*, 2009, **42**, 339-341.

Chapter 3

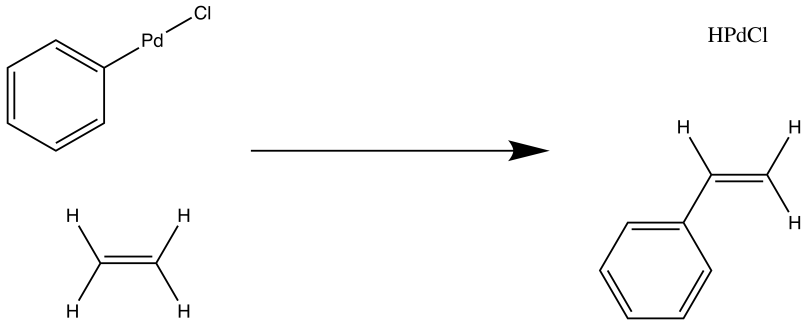
Properties and Applications of Tiara-like Complexes

3.1 Introduction

3.1.1 Catalytic Properties of Palladium

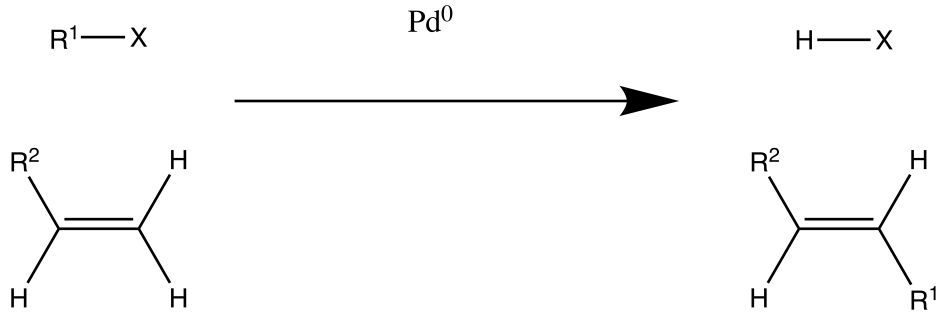
Like most platinum group metals, palladium possesses extensive noted catalytic properties and is possibly best known to the world as a major component of catalytic convertors present in car exhaust pipes that break down the most harmful air pollutants expelled from the internal combustion engine. This idea was first proposed by the French chemist Michel Frenkel in 1909, suggesting "supplementary combustions in the exhaust box, with the aid of a catalytic agent",[1] though palladium was not originally envisioned. However, despite this early perception of their need, modern catalytic converters have only come into existence within the last fifty years, in particular with the invention of the three-way catalytic converter which combines a rhodium agent to facilitate reduction of NO_x to N_2 along with the palladium/ platinum catalyst to provide oxidation of CO to CO_2.

Concurrently with these advances in exhaust pollutant dispersal, palladium has also developed catalytic properties of greater application to the organic chemist. Beginning with the recognition that palladium could catalyse the transformation of ethylene to acetaldehyde, this discovery would then be refined into the Wacker process that allowed for the industrial oxidation of olefins to carbonyls.[2,3] Olefins would continue to be of experimental interest with the publication in 1968 of a series of papers describing carbon-carbon bond formation by organopalladium reagents.[4-10]



Scheme 3.1: Addition of phenylpalladiumchloride to ethene to give a cross-coupled product.

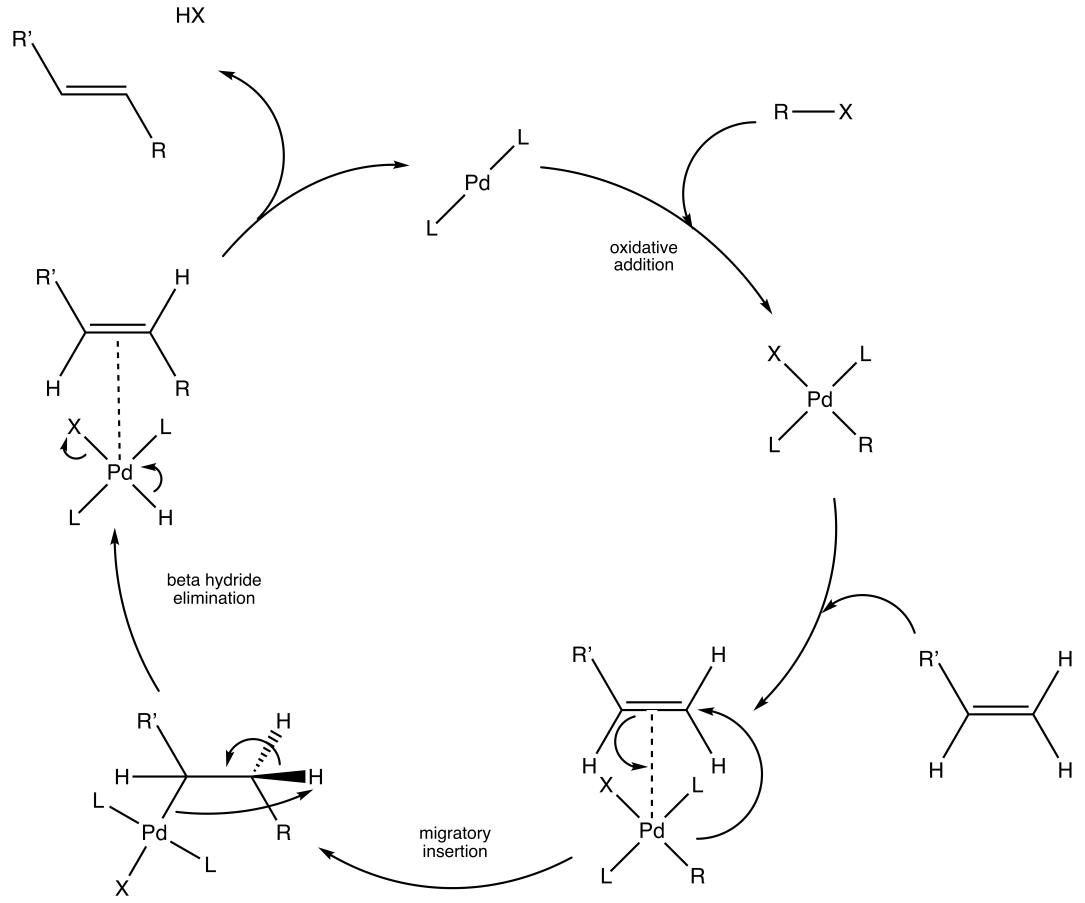
This reaction, described by Richard F. Heck and illustrated above in *Scheme 3.1*, was not originally catalytic with respect to the palladium used in the reaction, however in a following paper published in the same issue a solution was outlined that utilised $CuCl_2$ to regenerate the Pd^0 active catalyst (see *Scheme 3.2*).[8] A mechanism for the coupling was published a year later following extensive studies.[11] This discovery would later be refined by Heck to eliminate the need for the reoxidant cupric salts by generation of the palladium catalyst in situ via an oxidative addition of the starting material, R-X.[12] This improved reaction was also reported independently by Mizoroki in 1971.[13]



Scheme 3.2: Basic palladium catalysed carbon-carbon bond formation (Heck reaction).

This derivation would become the modern Heck reaction (also known as the Mizoroki-Heck reaction) that continues to be utilised in both a laboratory and industrial setting. The mechanism of the catalytic cycle is given below in *Scheme 3.3*. However, it suffers from some limitations, including the incompatibility with base-sensitive compounds and the requirement

of using aryl, benzyl or vinyl organic halide derivatives.[13] The reaction has continued to be developed in recent times, with several marked improvements on the original, including the ability to perform the reaction under microwave heating,[14] in ionic liquids,[15,16] the replacement of the phosphine ligands with *N*-heterocyclic carbenes (NHCs),[17] asymmetric synthesis[18] and recoverable catalysts.[19]

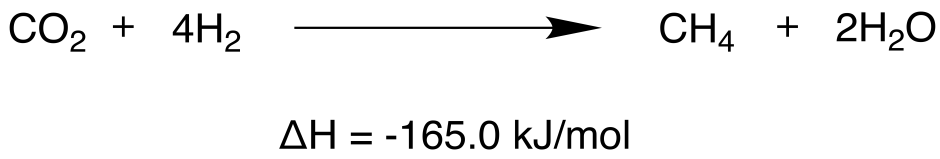


Scheme 3.3: Mechanism of catalysis of the modern Mizoroki-Heck reaction

The field of palladium-catalysed cross couplings has continued to expand with a number of related reactions, including the Negishi and Suzuki reactions, discovered by Ei-ichi Negishi in 1977[20-23] and Akira Suzuki in 1979.[24,25] The Negishi and Suzuki reactions differ from the earlier Heck reaction by replacement of the organic halide with an organozinc and organoboron compound respectively, increasing the number of substrates that could be

coupled. The versatility and power of these three cross-coupling reactions won their discoverers a shared Nobel prize in Chemistry in the year 2010 for "*Palladium-catalysed Cross Couplings in Organic Synthesis*".

A catalytic feature of palladium of use both within the chemical industry and to the practicing chemist is that of hydrogenation of unsaturated compounds; i.e. the transformation of C=C bonds to HC-CH saturation. This property extends to the other members of Group 10 of the periodic table, as platinum and nickel are also capable of effecting such reductions; the latter in particular being reported in the late 19th century / early 20th century as a finely powdered catalyst for the reduction of carbon dioxide to methane; this was discovered by Paul Sabatier (see *Scheme 3.4*). For his work on hydrogenation, Sabatier shared the 1911 Nobel Prize in Chemistry with Victor Grignard. A similar discovery was made by Wilhelm Normann, who would be awarded patents in Germany and England in 1902 and 1903 respectively for the hydrogenation of liquid oils.

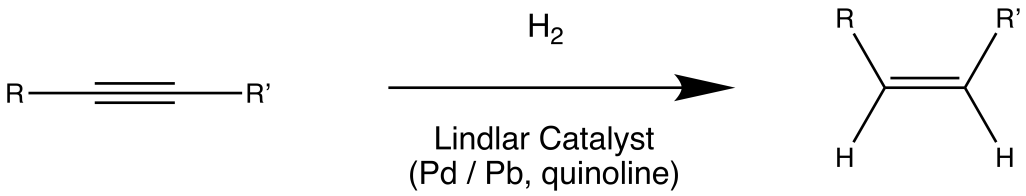


Scheme 3.4: The Sabatier Process (aided by a nickel catalyst). Carbon dioxide and hydrogen are combined at a high temperature to yield methane and water.

Nickel was the favoured catalyst for these processes during the early days of hydrogenation, particularly with the introduction of Raney nickel, an alloy of nickel and aluminium, to the world. However, palladium has grown in popularity despite its higher cost when compared to nickel. Typical compositions of the catalysts consist of the metal, finely powdered, mixed with a support medium such as carbon (Pd/C) which serves as a common catalyst today. The introduction of the support medium serves to increase the surface area of the metal, thereby

increasing its activity. Other support media include aluminium oxide (alumina), calcium carbonate and barium sulfate.

Several advances in this technology have been possible over the years since its inception. The reporting in 1952 by Herbert Lindlar of a palladium catalyst that would selectively reduce triple bonds to double bonds was another technique of use to organic chemists. This is achieved by pre-poisoning the metal catalyst with an inhibitor such as lead and/or quinoline; these are thought to serve by reducing the amount of H_2 adsorbed while simultaneously lowering the activity of the catalyst. This allows for a selective reduction of the triple bond to a double bond by addition of 1 molar equivalent of dihydrogen, whereas for unpoisoned catalysts the products obtained usually result in a mixture of unreacted alkyne, desired alkene and unwanted alkane.



Scheme 3.5: Hydrogenation of an alkyne to an alkene by Lindlar's Catalyst

Note that the hydrogen adds syn across the triple bond due to the adsorption of the substrate onto the catalyst surface, resulting in the formation of the cis-alkene (see *Scheme 3.5*).[26]

3.1.2 Metal Nanoparticles

The catalytic property of palladium to reduce unsaturated π systems is dependent on finely powdering the metal or by suspending the metal on a support medium such as carbon. In both cases the reactivity of the catalyst is driven by the increased surface area obtained by grinding or suspending the metal particles. However, there is a limit on the size of the

particles that can be generated in this 'top-down' manner, and so recent developments have more often been focussing on a 'bottom-up' approach to particle manufacturing.[27]

Metal nanoparticles are a class of inorganic nanoparticles that as their name suggests, consist of metal atoms bound within a particle of sizes of between 1 and 100nm.[28,29] Despite their recent surge in interest,[30] nanoparticles have been known to humanity since ancient times in the form of colloidal gold[31,32] which often takes on colourful hues- the visible absorbance, and therefore colour of which are size-dependent with respect to the radius of the particles.[33] This optical effect, not observed for the bulk material, is generally attributed to the surface plasmon resonance effect,[34] the localised resonance oscillations of free conduction electrons. The mechanism of the formation of colloidal solutions was later worked on and reported by Michael Faraday in 1857.[35]

Since their use in artwork and pottery in ancient times, nanoparticles are now developing further uses in both the areas of science and health. Gold, normally an unreactive and noble metal, can serve as an efficient catalyst when dispersed into a colloidal solution.[36-38] Nanoparticles can be utilised for biomedical imaging as contrast and may serve a dual purpose as therapeutic agents.[31] Gold and palladium nanoparticles have recently been studied as catalysts assisting the generation of dihyrogen from the decomposition of formic acid.[39] This latter property of palladium represents an inversion of its earlier-known catalytic abilities, with hydrogenation of organic compounds, i.e. the addition of dihydrogen to unsaturated systems, replaced by dehydrogenation, i.e. the generation of dihydrogen by oxidising organic carboxylic acids.

Formation of colloidal solutions can be achieved by many methods, but a common route to their synthesis is via the reduction of metal salts dissolved in solution, often chemically by

reagents such as sodium borohydride[40] and hydrazine.[41] However, reduced metal species tend to aggregate and form larger associations in the solution of a microparticlar or greater size, thereby necessitating a surfacting agent to stabilise the nanoparticles and prevent accumulation; a popular class of these agents are thiol ligands.[42,43]

As metal-thiolate complexes, tiaras are therefore attractive precursors for nanoparticle formation, and evidence for this was reported in 2007 when highly monodisperse nanoparticles were generated by the thermolysis of $[Pd(S(CH_2)_{11}CH_3)_2]_6$.[44,45] With a diameter of 2.87 ± 0.51 nm the synthesised particles were observed to be well stabilised by the lengthy dodecanethiolate species on the surface of the particles preventing aggregation to microparticles. A TEM image of the nanoparticles is given in *Figure 3.1*.

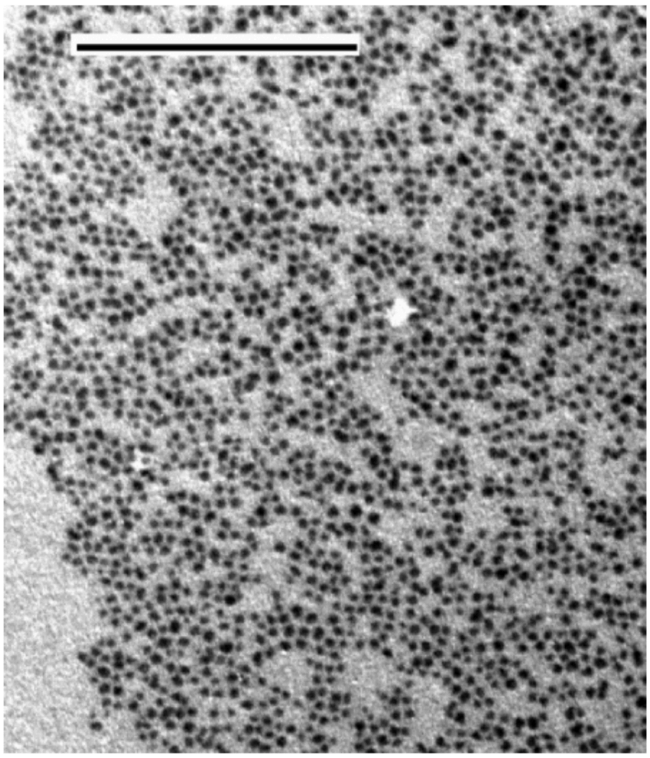
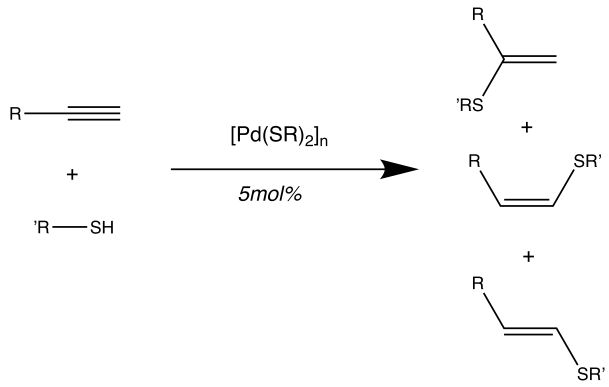


Figure 3.1: TEM image of nanoparticles generated by the solution-phase thermolysis of $[Pd(S(CH_2)_{11}CH_3)_2]_6$ (scale bar = 100 nm).[44]

The synthesised nanoparticles were found to be stable for months without any appreciable

change in the solution appearance, which suggested that the formation of nanoparticles from tiara-like complexes may be a robust method to the creation of high quality nanoscale palladium assemblies for use in catalysis or other processes.

Evidence to support this hypothesis was given by the reporting of the addition of alkylthiols to alkynes catalysed by palladium-thiolate nanoparticles (see *Scheme 3.6*).[46] In an experiment examining a variety of alkyne and thiol species, assisted by microwave heating, conversion yields of up to 99% and > 99 : 1 selectivity for the Markovnikov product were reported. It was shown that the structure of the palladium catalyst nanoassembly was vital to the catalytic properties, as lower conversion yields were obtained when the structure was modified.



Scheme 3.6: Catalysed thiol addition to alkynes by Pd-thiolate nanospecies to give selectivity to the Markovnikov product.

Importantly, the catalyst was found to be unchanged on completion of the reaction. The size and shape of the particles did not observably differ by SEM, rendering the catalyst re-usable and demonstrating the effective catalytic potential of Pd-thiolates.

3.1.3 Tiaras as Molecular Hosts for Small Guest Molecules

The observation that tiara-like complexes possessed the potential to act as molecular hosts to entrap small guest molecules was first noted in the original report of the first tiara-like

complex, $[Ni(SEt)_2]_6$, wherein the authors postulated that "the tiara or girdle of nickel-sulfur atoms may be regarded as acylindrical 'mousetrap' waiting to devour any suitably electron-rich or clathrate-prone 'mouse'".[47] Despite this description, no evidence of any guest inclusion was detected and even the synthesis in 1985 of the first octanuclear tiara, $[Ni(SCH_2COOCH_2CH_3)_2]_8$, yielded no evidence of guests entrapped within the central void.[48]

The first report of tiara-like complexes engaging in host-guest chemistry was not until 2002 wherein the undecanuclear tiara $[Ni(SPh)_2]_{11}$ was observed to encapsulate a molecule of THF within the large void (see *Figure 3.2*); this was theorised to act as a template for the formation of the larger complex.[49] This was demonstrated by the single crystal x-ray analysis and supported by electron density difference maps, the same analysis definitively discounted the possibility of THF inclusion within the smaller nonanuclear $[Ni(SPh)_2]_9$. Analysis of the molecular parameters suggested no specific interactions between the host and the guest, instead necessitating the involvement of weak dispersive forces to stabilise the host-guest complex.

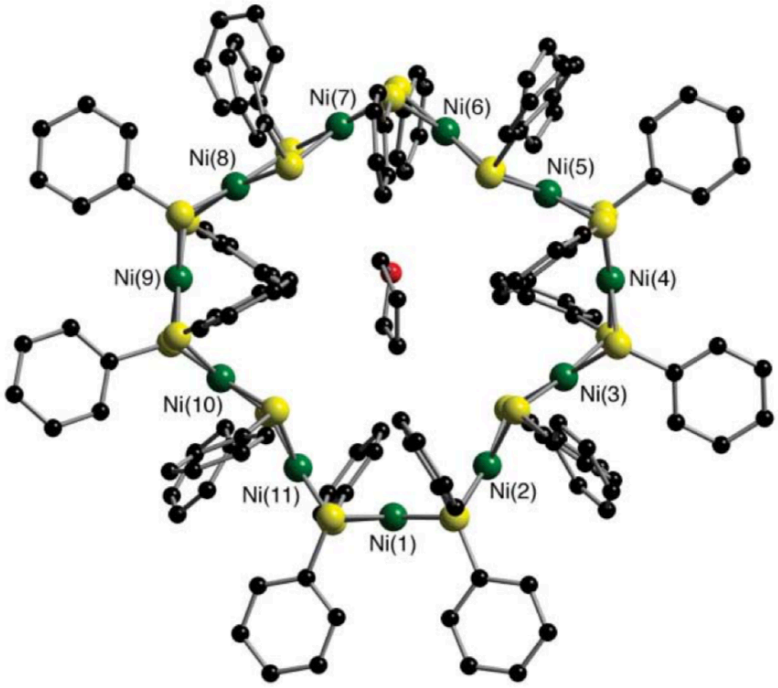


Figure 3.2: Inclusion of THF within $[Ni(SPh)_2]_{11}$ resulting in the first reporting of a tiara-like inclusion complex.[49]

Since 2002, the number of tiara-like inclusion complexes has rapidly increased. The complex $[Ni(S\textit{t}Bu)(SCH_2CH_2SCH_3)]_{10}$, reported in 2006, encapsulated a molecule of benzene within the crystal structure[50] and its dodecanuclear analog $[Ni(S\textit{t}Bu)(SCH_2CH_2SCH_2CH_3)]_{12}$ published in 2010 was shown to form an inclusion complex with toluene.[51] The palladium and platinum complexes recently reported in 2014 extensively examined solvent inclusion within the rings, with the inclusion of dichloromethane, 1,2-dichloroethane, dibromomethane and methyl iodide.[52] The authors examined and compared in detail the single crystal structural parameters of the complexes both with and without inclusion of solvent molecules and were able to detect halogen to ligand (CH···X, X = Cl or Br) hydrogen bonding. This represents the first stabilisation of a tiara-like inclusion complex beyond weak dispersive interactions. The strongest hydrogen bonds in the reported complexes are in the range of 2.50 Å to 2.99 Å (average 2.79(22) Å) for $[CH_2Cl_2{\subset}Pd(SCH_2COOCH_3)_2]_8$, and so the hydrogen bonds are reasonably weak interactions. As expected, the weakest hydrogen bonds reported are for the platinum complex $[CH_2Br_2{\subset}Pt(SCH_2COOCH_3)_2]_8$, which are stated in the range

of 2.86 Å to 3.18 Å (average 2.98(11) Å). Also noted for the palladium tiara were interactions between the halogen atoms of the guests and the metal atoms of the ring; the halogens were located at distances slightly shorter than the sum of the van der Waals spheres indicating weak coordination to the palladium. These interactions are all shown below in *Figure 3.3*.

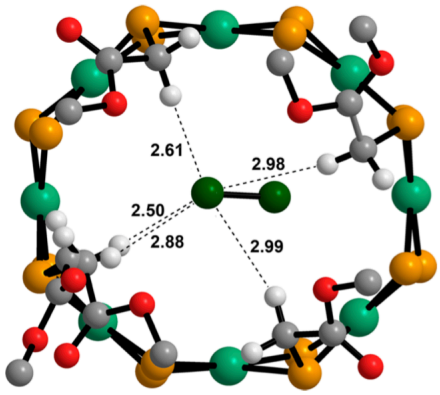


Figure 3.3: Inclusion complex of the guest molecule dichloromethane inside $[Pd(SCH_2COOCH_3)_2]_8$, showing interactions between the guest and the thiolate ligand arms (some atoms were omitted for clarity). Atom colours: Pd-light green, S-orange, C-grey, O-red, H-white, Cl-dark green. Hydrogen bonds are shown by dotted lines. Bond distances are printed adjacent; distances are given in angstroms.[52]

Some theoretical calculations for tiara - guest interactions have also been published.[53] From an early point the potential for small molecules to coordinate to the metal atoms of the tiara was noted, as in an M^{2+} complex (where M = Ni, Pd, Pt) the d_{z^2} and p_z orbitals are orientated perpendicular to the Ni-S plane, pointing into the centre of the toroid. In principle these orbitals are available for bonding interactions with a guest molecule, however calculations for possible inclusion complexes with small molecules such as I_2, CO_2 and acetylene rendered overall unfavourable binding energies due to electron repulsion. For CO, a slightly favourable binding energy was calculated due to the mixing of empty tiara orbitals with CO-thiolate bonding combinations; slightly destabilising the tiara complex.

However, the overall conclusion of the work was that strong tiara-guest complexes should not be expected. Two solutions were offered to strengthen interactions between the hosts and

small guest molecules; the first being the replacement of the thiolate sulfurs with oxygens. The increased electronegativity of the oxygen atoms would bring the resultant tiara bonding orbitals into a closer overlap with a central guest, pushing the host-guest anti-bonding orbitals over the tiara anti-bonding orbitals, transferring two electrons to a lower lying orbital. The second solution was to coordinate further ligands on the outer surface of the torus to create square pyramidal geometry metal centres rather than square planar. This would 'focus' the d_{z^2} and p_z orbitals to the centre of the complex, this was partially achieved experimentally with the synthesis (see *Figure 3.4*) of a hexanuclear nickel tiara-like complex, $[Ni(SCH_2CH_2SC_6H_4Cl)_2]_6$, containing both NiS_4 square planar subunits and NiS_5 square pyramidal subunits.[54]

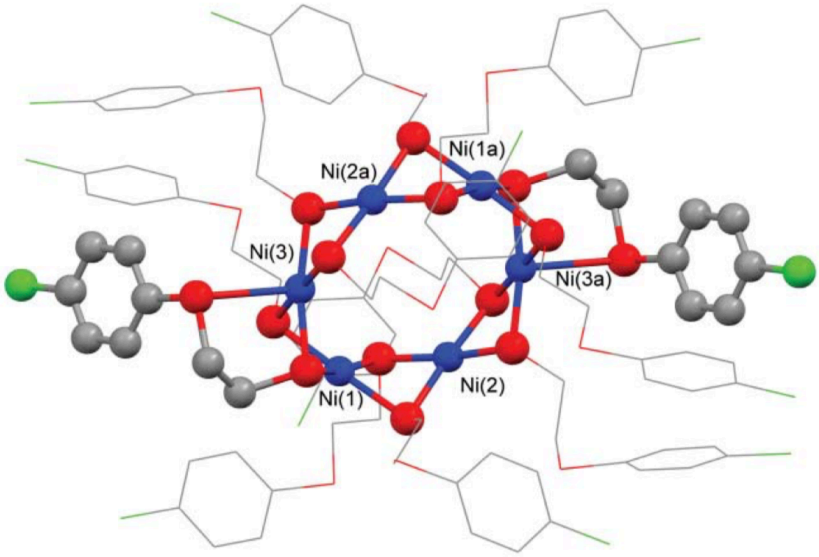


Figure 3.4: Crystal structure of $[Ni(SCH_2CH_2SC_6H_4Cl)_2]_6$. Atom colours: Ni-blue, S-red, C-grey, Cl-green. Hydrogen atoms omitted for clarity.[54]

No guest molecules were detected analytically within the centre of the hexanuclear complex however, most likely due to the small size of the toroid and the bulky ligands preventing access to the centre.

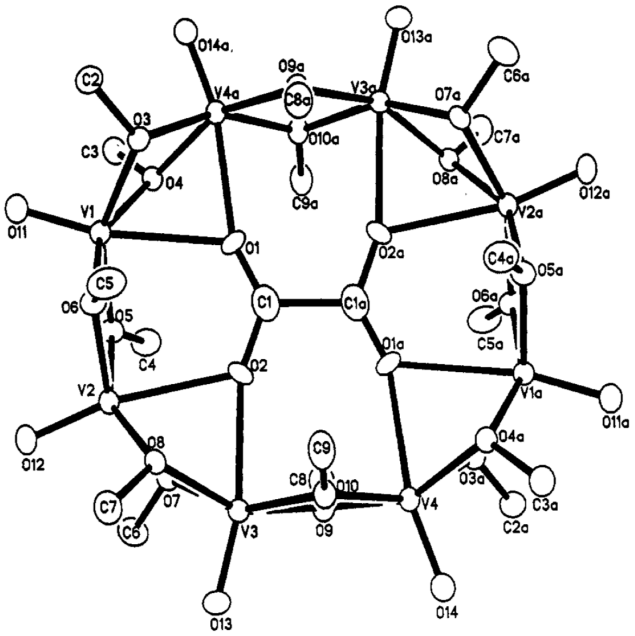


Figure 3.5: Structure of $[V_8O_8(OCH_3)_{16}(C_2O_4)]^{2-}$. Hydrogen atoms omitted for clarity.[55]

It is worth noting that chemically complex inclusion compounds were synthesised that satisfied both of the criteria discussed above. The complexes $[(n\text{-}C_4H_9)_4N]_2[Mo_8O_{16}(OCH_3)_8(C_2O_4)]$[56] and a vanadium analog $[(n\text{-}C_4H_9)_4N]_2[V_8O_8(OCH_3)_{16}(C_2O_4)]$,[55] despite not being Group 10 metal compounds, can be considered to be tiara-like complexes due to the high levels of structural similarity. Both were synthesised containing a molecule of oxalate within the central cavity but the reversibility of the binding of the oxalate guest to the tiara framework was doubtful, leaving some uncertainty as to whether or not this binding can be treated as supramolecular host-guest chemistry or coordination of another ligand to the complex.

3.2 Results and Discussion

3.2.1 NMR Spectroscopy

3.2.1.1 Correlation Spectroscopy (COSY) NMR

The ^{1}H NMR spectra of the tiara-like complexes synthesised in *Chapter 2* has already been discussed, and generally these experiments are often considered sufficient to explore the magnetic resonance properties of these complexes. There is a conspicuous shortage of two-dimensional NMR data present in the established literature, therefore complexes **1**, **2**, **3**, and **6** were subjected to a variety of 2D techniques to elucidate further information about their properties.

Firstly, a simple proton-proton correlation experiment (COSY) was performed on complex **1** to examine the through-bond couplings between the protons of the complex, the results of which are given in *Figure 3.6*.

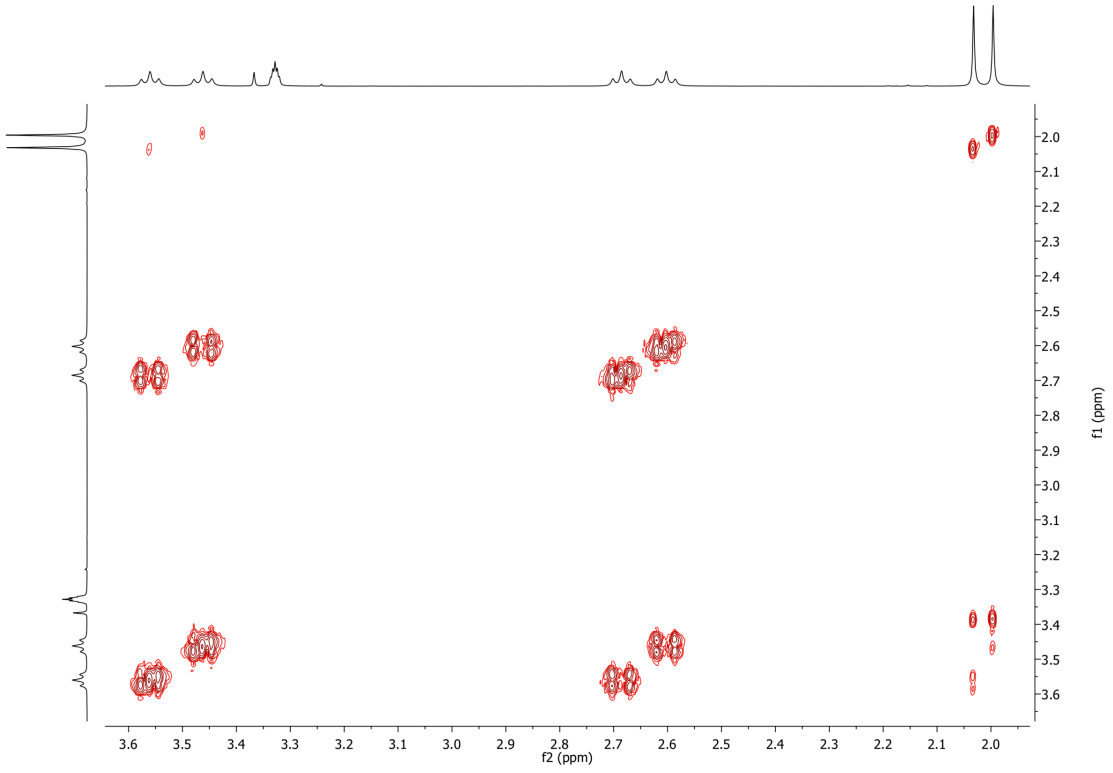


Figure 3.6: ^{1}H-^{1}H COSY NMR spectrum from 1.9 ppm to 3.6 ppm of **1**, showing strong correlations between the CH_2 groups. Solvent: methanol-d4.

As can be seen in the 2D spectrum, there is a correlation between the triplet at 3.57 ppm and the triplet at 2.67 ppm. Similarly, there is a correlation between the triplet at 3.44 ppm and 2.58 ppm. As the triplets at 3.57 ppm and 3.44 ppm arise from the non-equivalent axial and equatorial β-CH_2 groups and the triplets at 2.67 ppm and 2.58 ppm arise from the α-CH_2 groups, it can be surmised that the axial β-CH_2 and α-CH_2 protons are able to couple through bonds, which is to be expected from the structure of the complex. The same is true of the equatorial protons but no coupling is seen between axial and equatorial protons; again this follows the expected observation as the two groups are separated by a large number of bonds.

Additionally, there is a weak coupling between the triplet at 3.57 ppm and the singlet at 2.02 ppm and a weak coupling between the triplet at 3.44 ppm and the singlet at 1.98 ppm. The singlets arise from the coupling of the (both axial and equatorial) protons in the β-CH_2 and terminal CH_3 groups on the ligand arms, therefore the coupling observed in the spectrum in this instance must occur over five bonds, making it relatively long-ranged scalar coupling. The scalar coupling may be enhanced by the partial double bond nature of the amide N-C <-> N=C bond, allowing it to be resolved over a greater distance. Alternatively, longer ranged scalar coupling such as this may be seen due to the ligand arms being constrained within a particular position; such a conformation could arise due to hydrogen-bonding originating from the ligand arms. This coupling is illustrated in *Figure 3.7*.

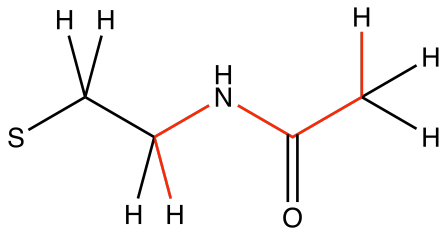


Figure 3.7: Long ranged scalar coupling in **1** indicated by red bonds

A total correlation spectroscopy experiment (TOCSY) of complex **1** did not show significant

additional correlation.

There is a very similar observation seen when COSY NMR is performed on a solution of complex **2**. The resulting spectrum is shown in *Figure 3.8*.

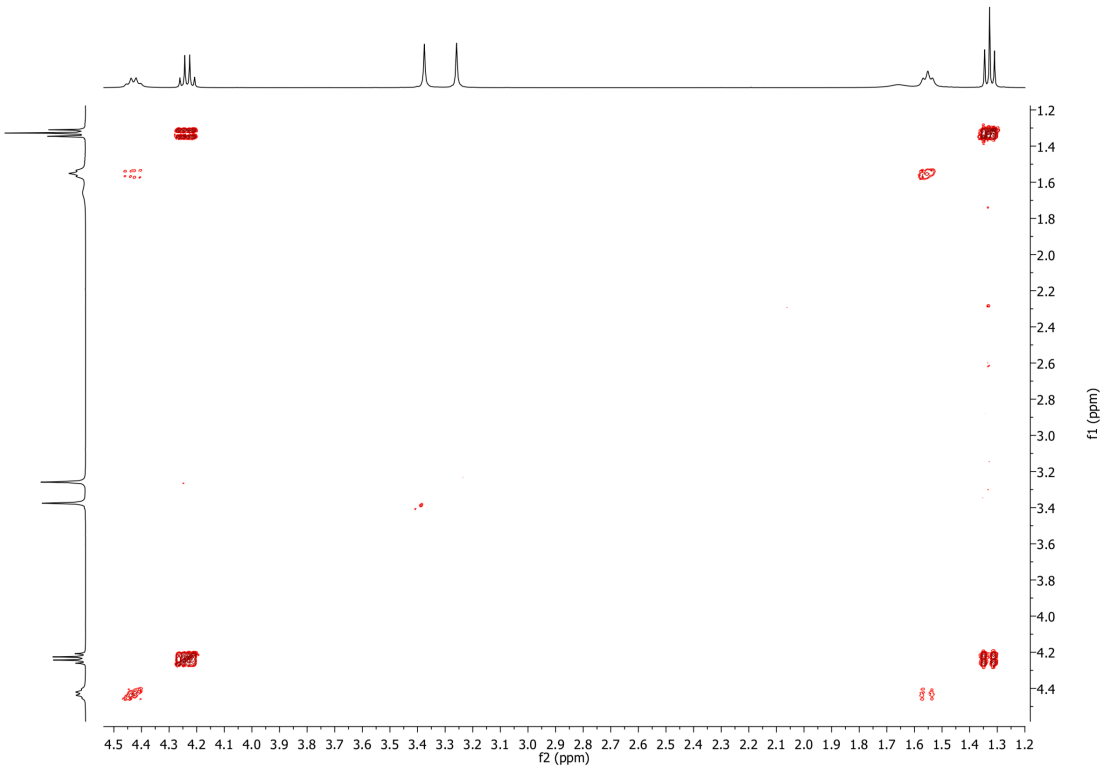


Figure 3.8: ^{1}H-^{1}H COSY NMR spectrum from 1.2 ppm to 4.5 ppm of **2**, showing correlations between the β-CH_2 and CH_3 groups. Solvent: chloroform-d.

Cross peaks can be observed between the quartet at 4.44 ppm and the triplet at 1.56 ppm, along with coupling between the quartet at 4.24 ppm and the triplet at 1.34 ppm. The quartets correspond to the β-CH_2 protons and the triplets arise from the terminal CH_3 protons; no longer range coupling is observed in this case, even between the α-CH_2 and the β-CH_2 protons, possibly due to the replacement of the amide functionality thereby removing the partial double bond character from the ligand chain. The CH_2 to CH_3 scalar coupling is illustrated in *Figure 3.9*.

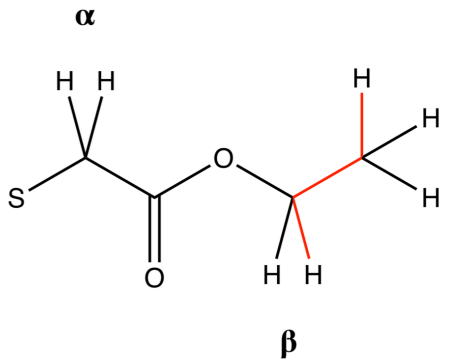


Figure 3.9: Scalar coupling seen in **2** indicated by red bonds

3.2.1.2 Nuclear Overhauser Effect Spectroscopy (NOESY) and Rotating Frame Overhauser Effect Spectroscopy (ROESY) NMR

Through-space interactions also show interesting results for these complexes. The NOESY spectrum of **2** (see *Figure 3.10*) shows cross peaks of the same sign as the diagonal arising between the axial and equatorial signals, which was originally characterised as a true through-space interaction. However, it was also possible that the observed correlation in the spectrum could arise from chemical exchange; in this case arising from the inversion of the sulfur to alter the orientation of the ligand from the axial configuration to equatorial, and vice versa.

There is also a weak signal arising between the quartets and the triplets in the spectrum. This signal is of the opposite sign to the diagonal, implying a difference in the nature of the interaction and giving further weight to the theory that chemical exchange could be the origin behind the cross peaks seen between the axial and equatorial signals.

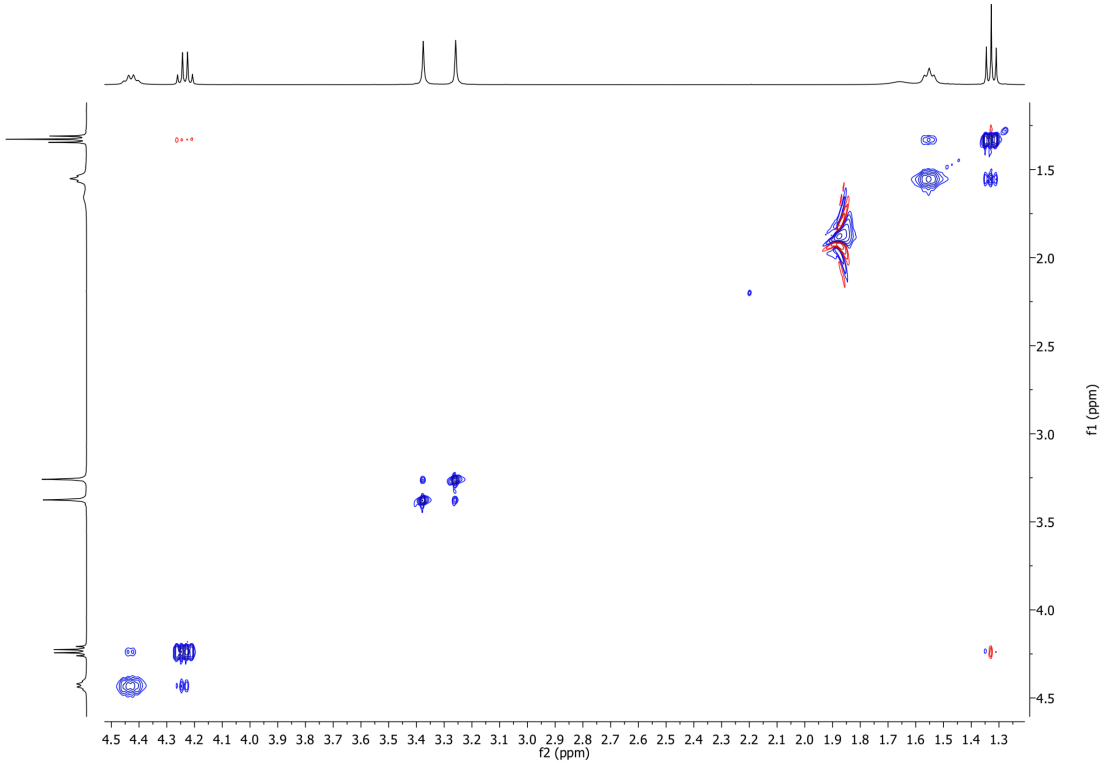


Figure 3.10: NOESY NMR spectrum from 1.2 ppm to 4.5 ppm of **2**, showing correlations between axial and equatorial protons. Solvent: chloroform-d.

As the nature of the origin of cross peaks seen between the axial/equatorial signals could not be determined by the NOESY experiment, the same sample was rerun as a ROESY instead, as cross peaks resulting from through-space interactions in a ROESY spectrum will always appear as the opposite sign to the diagonal.

This was confirmed in the ROESY spectrum (see *Figure 3.11*) from the observation of same-sign axial/equatorial cross peaks. Opposite-sign cross peaks arose between the quartet at 4.24 ppm and the triplet at 1.34 ppm, along with a correlation between the quartet at 4.44 ppm and the singlet at 3.39 ppm. These are likely to result from through-space interactions between the β-CH_2 and terminal CH_3 protons via the Nuclear Overhauser Effect (NOE) rather than chemical exchange.

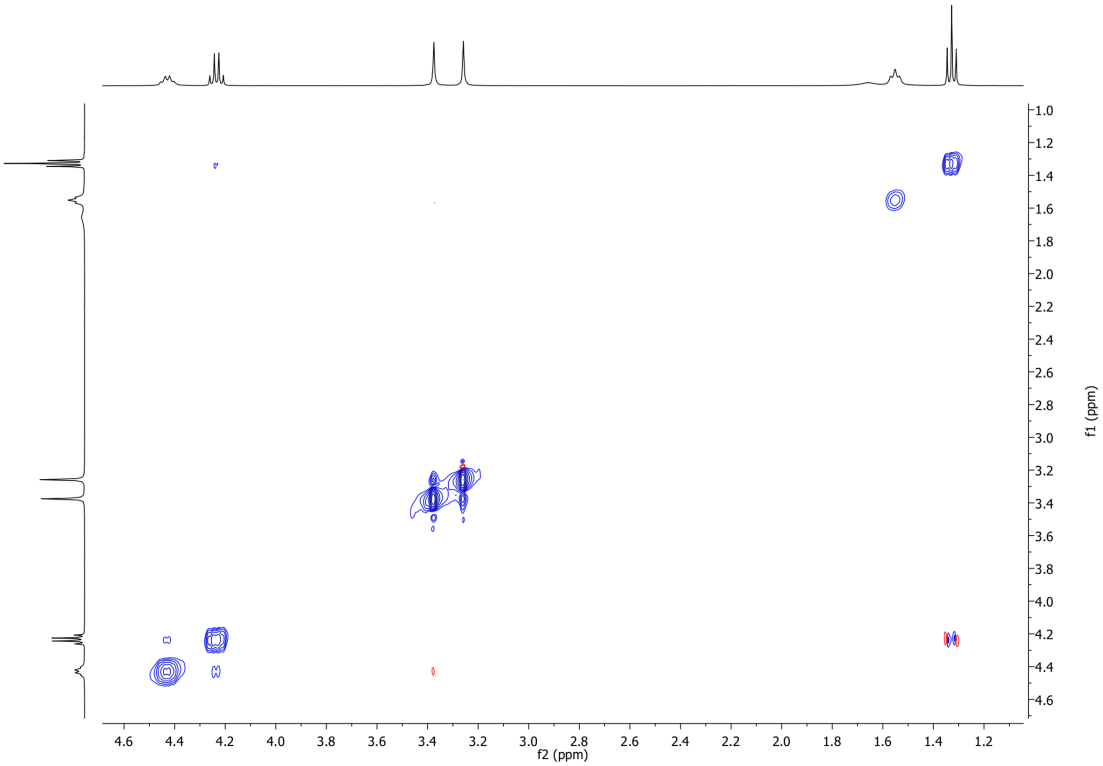


Figure 3.11: ROESY NMR spectrum from 1.2 ppm to 4.6 ppm of **2** showing same-sign cross-peaks between the axial and equatorial protons, indicating chemical exchange rather than through-space interactions. Solvent: chloroform-d.

Interestingly the NOESY spectrum of **1**, given in *Figure 3.12*, does not show chemical exchange arising between the axial/equatorial pairs of signals. As the two ligands are broadly similar, it is not immediately clear why the two complexes should give such different results. While **2** possesses an ester functional group and no strong intramolecular interactions, the functional group in complex **1** is an amide, possessing strong intramolecular hydrogen bonding interactions. Further to this, the NMR solvent for **2** was chloroform-d, preventing strong solvent-complex interactions, whereas for **1** the complex was dissolved in methanol-d4 for the experiment; as methanol is also capable of participating in hydrogen bonding, it is possible that intramolecular hydrogen bonding or intermolecular hydrogen bonding to methanol may prevent inversion of the ligands, thereby showing no cross peaks in the NOESY spectrum.

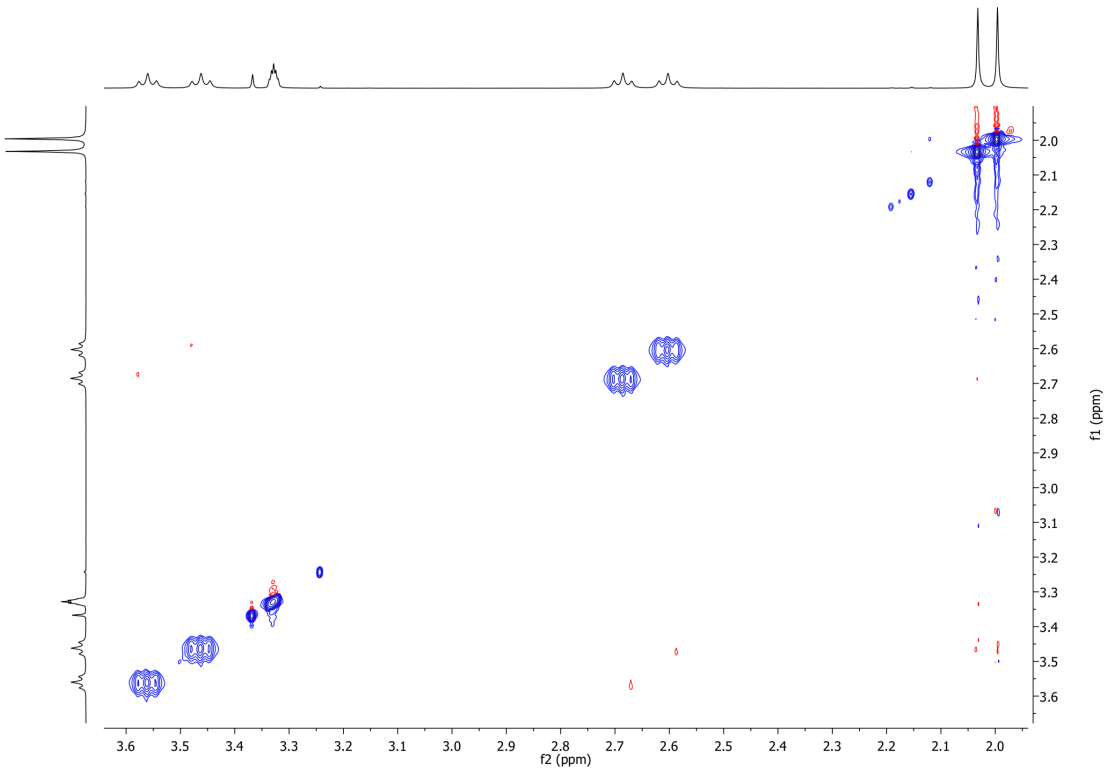


Figure 3.12: NOESY NMR spectrum from 2.0 ppm to 3.6 ppm of **1**, showing no chemical exchange but correlations between the α-CH_2 and β-CH_2 groups. Solvent: chloroform-d.

The spectrum does, however, continue to show a weak correlation between the triplets at 2.6 - 2.7 ppm and the triplets at 3.45 - 3.55 ppm, constituting the α-CH_2 and the β-CH_2 protons, implying that a through-space interaction continues to be observed. It should be noted that the interaction may arise from a close spatial configuration between protons located on different ligands on the same molecule. The results of the NOESY experiments are summarised in *Figure 3.13* below.

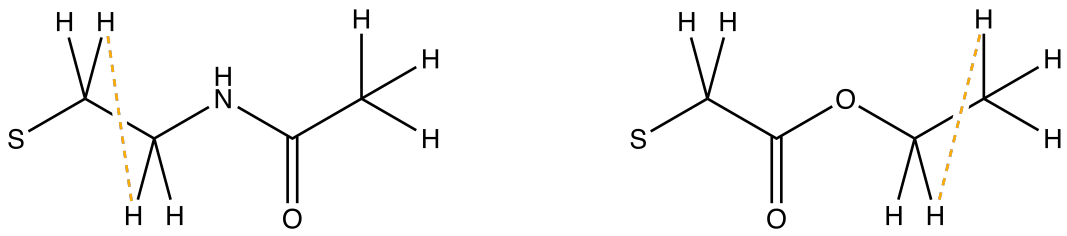


Figure 3.13: Summary of through-space interactions for complexes **1** (left) and **2** (right), indicated by orange dashed bonds. Note that the interaction may not necessarily occur between the protons on the same ligand (vide ante).

3.2.1.3 Variable Temperature (VT) NMR

In order to examine the behaviour of the complexes at higher and lower temperatures, variable temperature (VT) experiments were performed on both complexes. This was expected to alter the configuration/ movement of the ligand arms around the central ring, and the resultant change detected by ^{1}H NMR spectroscopy.

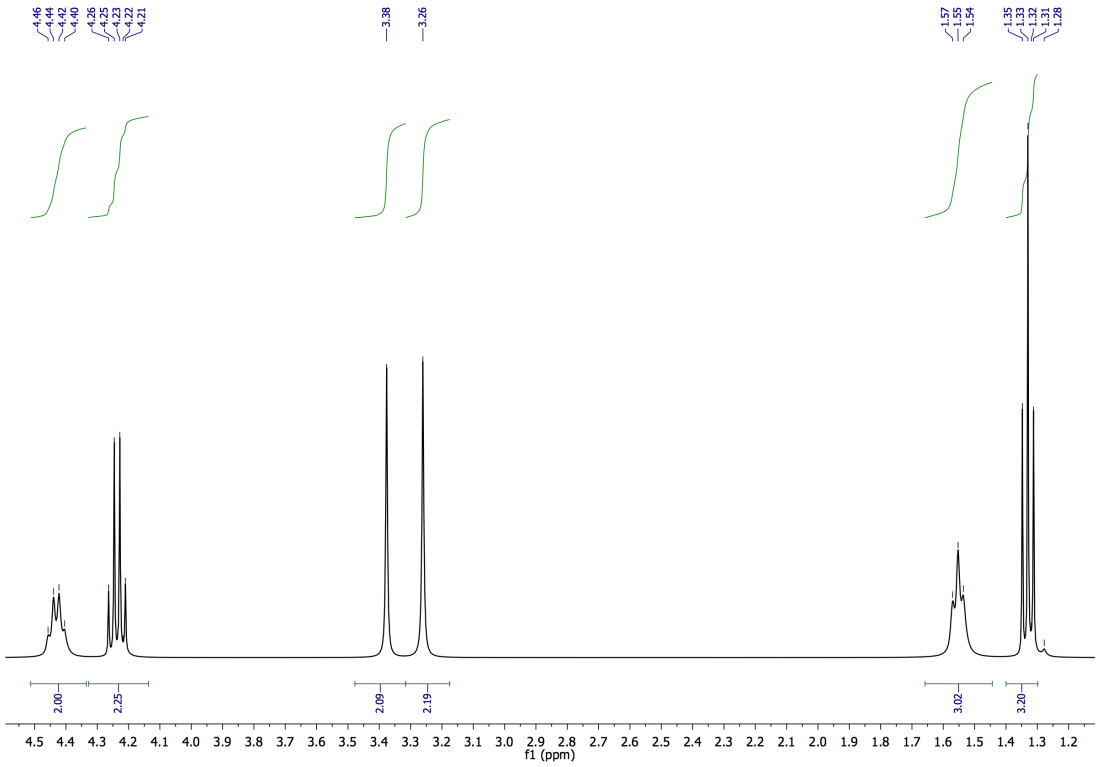


Figure 3.14: ^{1}H NMR spectrum from 1.1 ppm to 4.5 ppm of **2** at room temperature. Solvent: chloroform-d, 16 scans.

In the room temperature ^{1}H NMR spectrum of complex **2** (see *Figure 3.14*), the quartet at 4.44 ppm and the triplet at 1.56 ppm show a broader signal when compared with the quartet at 4.24 ppm and the triplet at 1.34 ppm. Previous studies have attributed selective line broadening to the movement of the axial ligand arm into the centre of the toroid, a property observed in octanuclear complexes but not in hexanuclear due to the reduced size of the complexes.

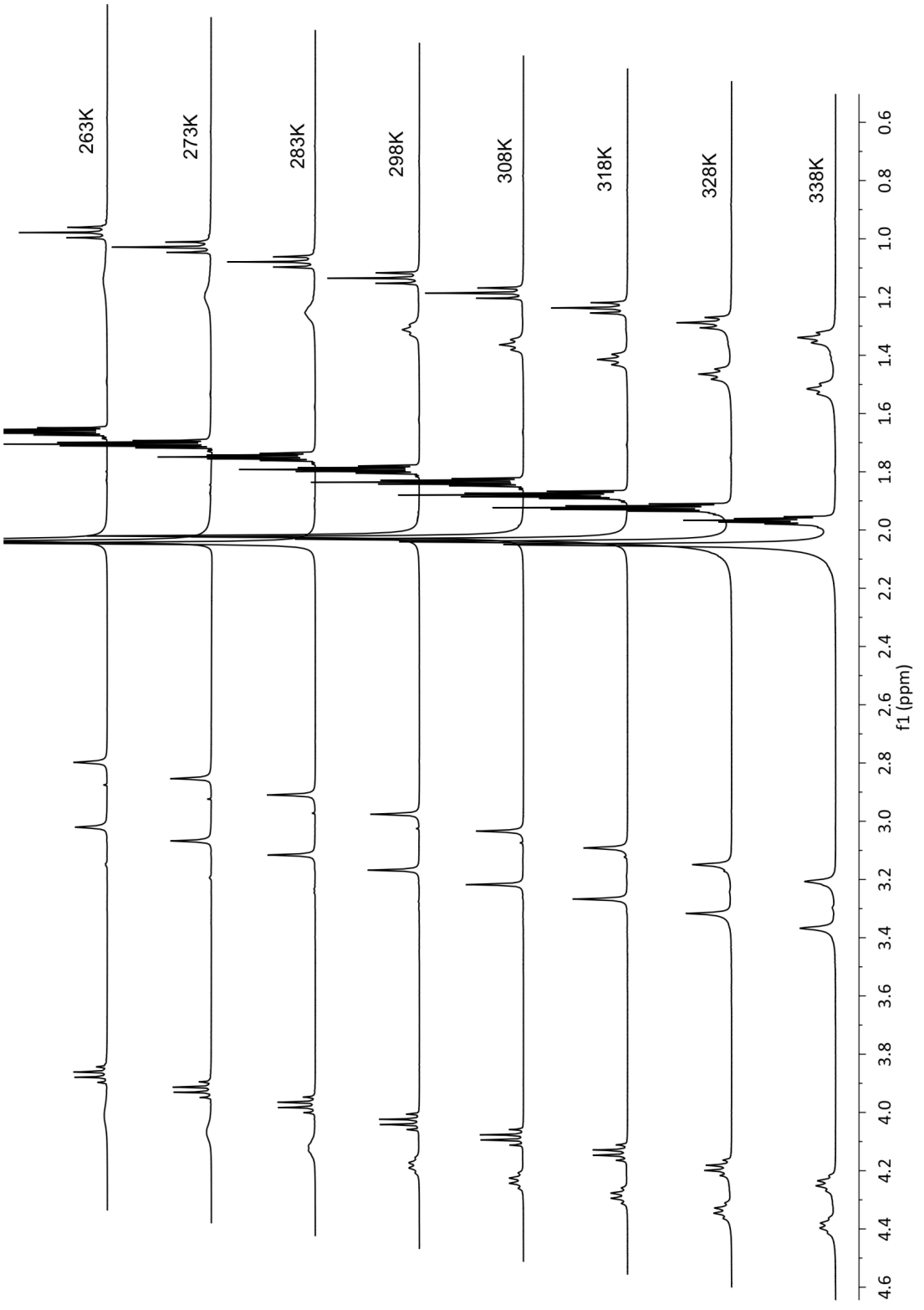


Figure 3.15: VT ^{1}H NMR spectrum from 0.6 ppm to 4.6 ppm of **2** in MeCN-d3 from 263K to 338K, showing asymmetric broadening of the axial and equatorial proton environments.

As can be seen in *Figure 3.15*, on reduction of the experiment temperature from 298K to 263K, the broad quartet at 4.44 ppm and the broad triplet at 1.56 ppm broaden further, almost becoming invisible within the spectrum, however the sharp quartet at 4.24 ppm and the sharp triplet at 1.34 ppm show no line broadening at all. This is likely indicative of the configuration differences between the axial and equatorial conformations of the ligands and may represent the movement of the axial ligand arm into the centre of the toroid.

On increasing the temperature from 298K to 318K, the previously sharper quartet at 4.24 ppm and the sharp triplet at 1.34 ppm begin to broaden independently. The quartet at 4.44 ppm and the triplet at 1.56 ppm appear to continue sharpening, following the trend on increasing the temperature from 263K. The trend appears to reverse, however, on increasing the temperature further from 318K to 338K, where both signals appear to broaden simultaneously. This results in a ^{1}H NMR spectrum where both axial and equatorial signals appear to be nearly identical in appearance, and may represent that the two different conformations of the ligand arms behave more similarly to each other under the rapid movement at high (65°C) temperature.

It is worth noting that the singlets corresponding to the α-CH_2 protons appear to show a slight degree of sharpening and broadening within the spectrum that seem to follow the same pattern as the other signals. This can be judged by the relative height of the peaks when compared with each other and may be justified by the lower degree of freedom for protons located closer to the ring. One observation that appears to be unique to the singlets is a small change in the chemical shift of the signals, moving closer to each other at high temperature and farther apart at lower temperatures. It may be that this, along with the identical broadening at high temperatures, represents a move towards eventual coalescence where the axial-equatorial exchange becomes too rapid to observe on the NMR timescale.

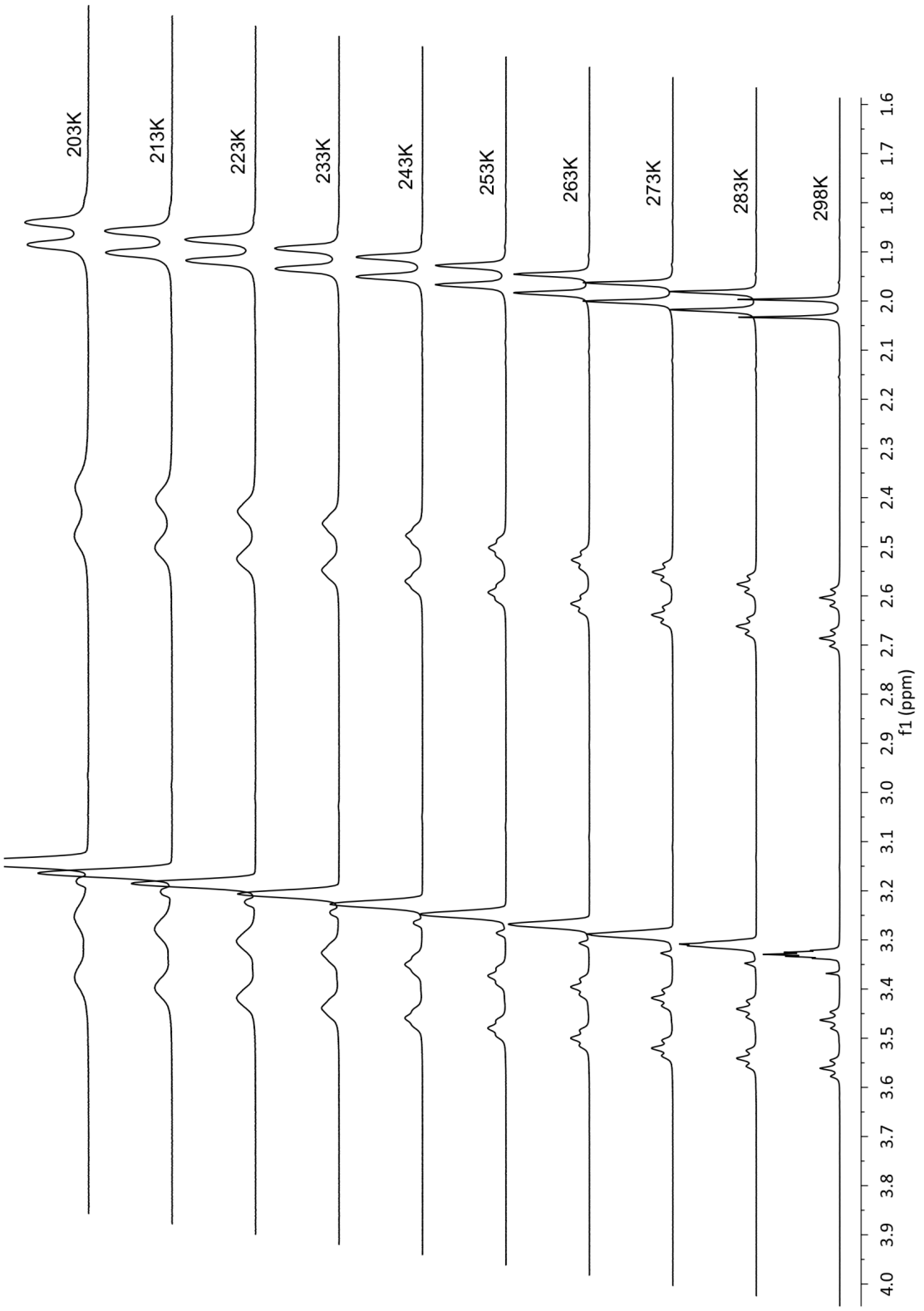


Figure 3.16: VT ^{1}H NMR spectrum from 1.6 ppm to 4.0 ppm of **1** in MeOH-d4 from 203K to 298K, showing symmetrical broadening of the axial and equatorial proton environments.

In contrast to the VT spectrum of **2**, for a sample of **1** dissolved in methanol-d4, each signal from the complex protons undergoes broadening simultaneously on reduction of the temperature from 298K to 203K (spectrum given in *Figure 3.16*). This is due to the fact that complex **1** is a hexanuclear tiara and the central void is of insufficient size to accommodate re-entry of the axial ligand arms; therefore both axial and equatorial ligands behave alike in the solution phase. The lack of any independent broadening suggests that a single size of tiara is present, as larger ring species would be expected to undergo selective line broadening. Any interconversion between different sizes of tiara-like complexes is therefore either not present or occurring faster than can be observed by NMR spectroscopy.

3.2.1.4 Diffusion Ordered Spectroscopy (DOSY) NMR

The variable temperature NMR experiments indicated that only a single species of tiara was present in the sample of **1** subjected to the spectroscopy, which was expected due to its purification via crystallisation. However, the technique could not definitively conclude whether or not this was correct. To examine the possibility that there could be multiply sized rings in solution, or that the rings could be interconverting between sizes on a rapid timescale, Diffusion Ordered Spectroscopy (DOSY) NMR was employed to examine this further.

Measurements were recorded in methanol-d4 and water-d2 for complex **1** and chloroform-d for complex **2** and complex **6** using initially a double stimulated echo pulse program (dstebpgp3s sequence) to compensate for convection, later experiments used the ledbpg2s sequence without convection compensation; 32 datapoints were collected in all cases.

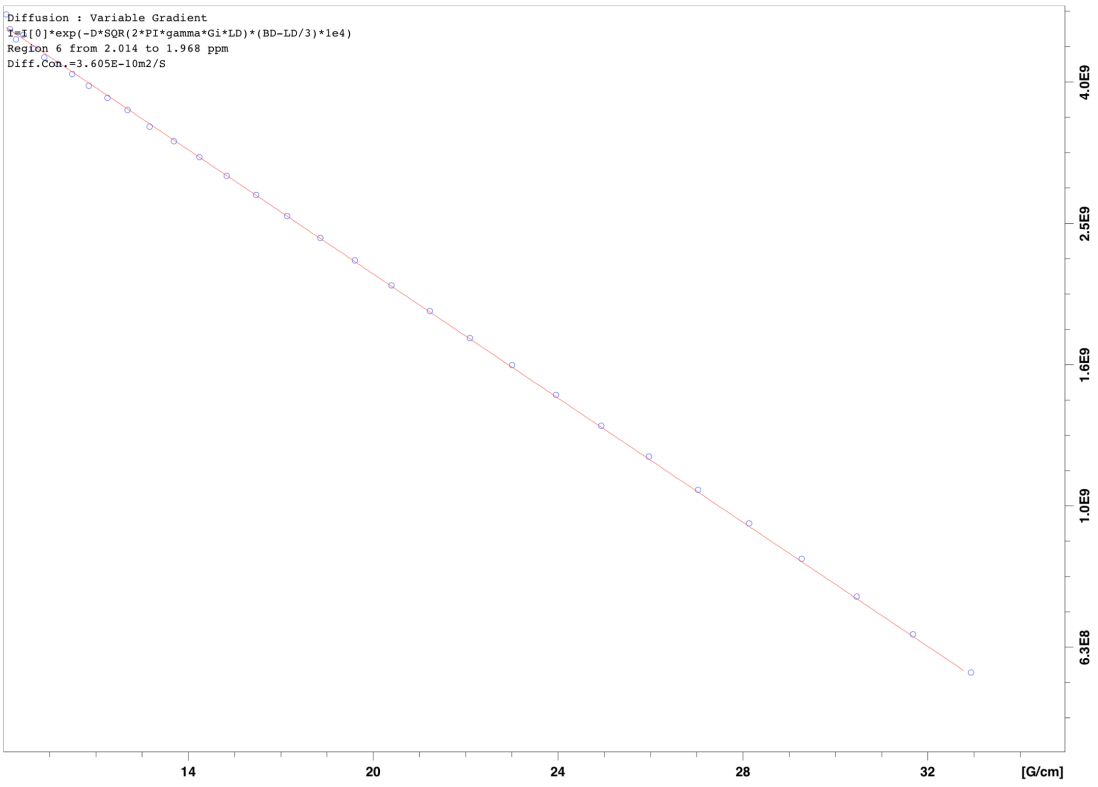


Figure 3.17: DOSY plot of **1** in methanol-d4, providing a nominal diffusion coefficient of 3.605×10^{-10} m^2/s.

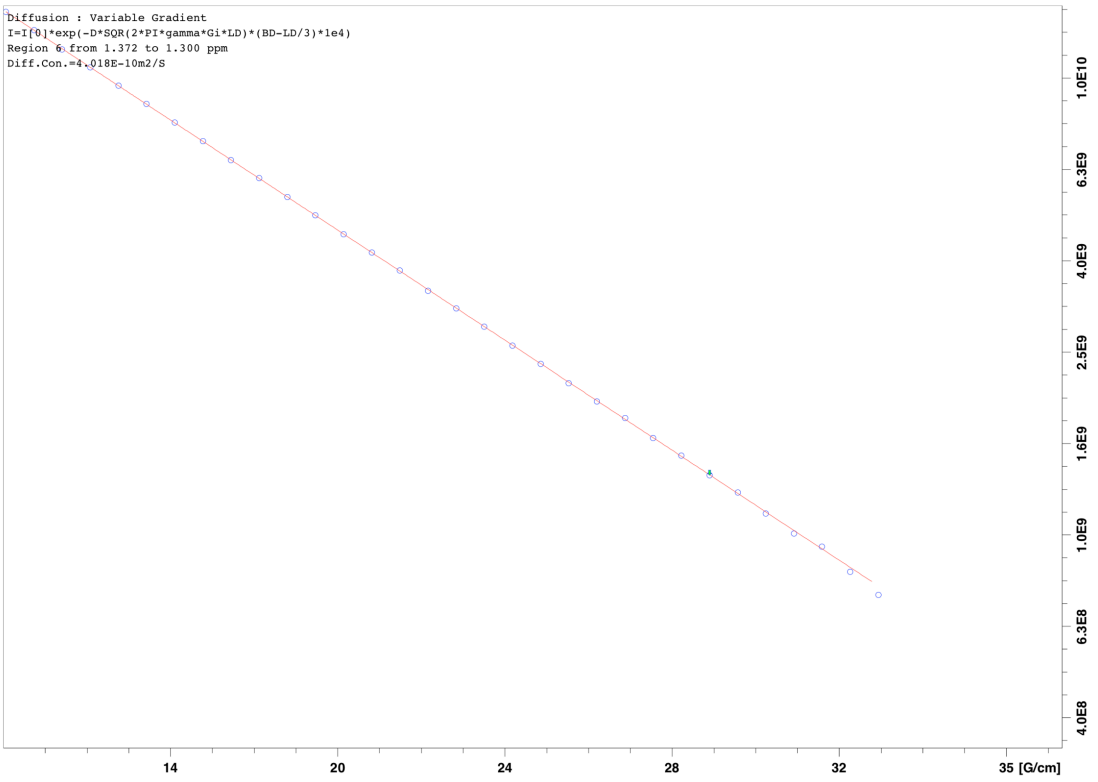


Figure 3.18: DOSY plot of **2** in chloroform-d, providing a nominal diffusion coefficient of 4.108×10^{-10} m^2/s.

The data obtained provided a nominal diffusion coefficient of $3.605E^{-10}$ m^2/s for complex **1** in methanol-d4 (plot given in *Figure 3.17*) and a coefficient of $4.018E^{-10}$ m^2/s for complex **2** in chloroform-d (plot given in *Figure 3.18*). The recording of a higher diffusion coefficient for complex **2** indicates faster diffusion through the solvent, however this was unexpected given the larger size and higher molecular weight of the octanuclear complex.

To explain this result it is necessary to consider the effect of the solvent viscosity on the diffusion of the molecules. Solvent viscosity data used here was taken from the data provided by Morris *et al.* and obtained from www.reaxys.com and Landolt-Börnstein online databases. Due to the large isotopic effect for water-d2, viscosity data for this solvent was used as is, whereas solvent data for methanol-d4 and chloroform-d was estimated by multiplying the source values for the protio solvent by the ratio of the deuterio- and protio- molecular weights. This was found to cause a negligible change in the experimentally-determined results from the predicted values; resulting in a percentage deviation of 0.03%.

Utilising this data, methanol-d4 possesses a viscosity of $6.02E^{-4}$ kg m^{-1} s^{-1}, which is significantly higher than that of chloroform-d at $5.28E^{-4}$ kg m^{-1} s^{-1}, resulting in a slower rate of diffusion. To examine the degree to which the viscosity affects the diffusion rate, the DOSY experiment for complex **1** was repeated in water-d2, which has a higher viscosity of $1.10E^{-3}$ kg m^{-1} s^{-1}. The determined diffusion coefficient for the complex was $2.428E^{-10}$ m^2/s, significantly lower than the diffusion rate for the same sample in methanol-d4. This is illustrated in the plot given by *Figure 3.19*.

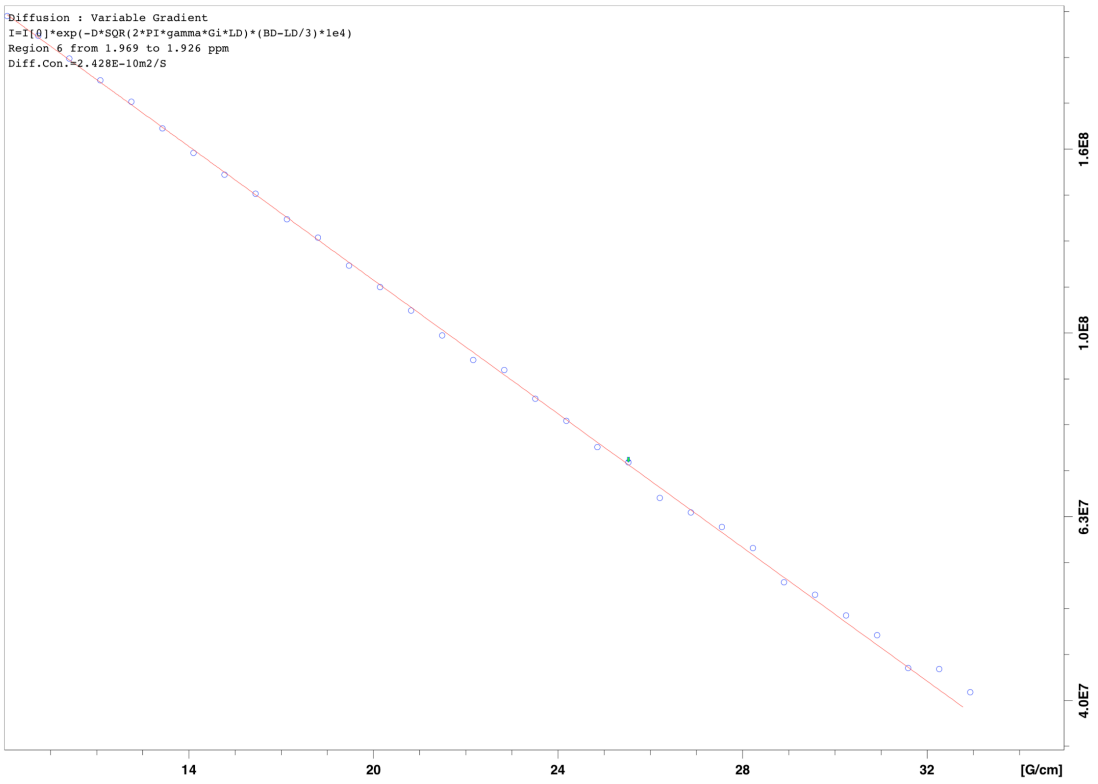


Figure 3.19: DOSY plot of **1** in water-d2, providing a nominal diffusion coefficient of 2.428×10^{-10} m^2/s.

Therefore very few conclusions can be drawn from the absolute values recorded here as nominal diffusion coefficients, and even comparing the relative coefficients may be misleading due to the significant effect that the change of solvent has on the diffusion rate of the molecules. However, a meaningful inference may be drawn from the plots of the data, as both sets of data provide straight line fits when plotted to a graph, indicating that the diffusion correlates to a one-component system, suggesting that only a single size of tiara is present, unless interconversion between different nuclearities of tiara-like complex is occurring. Due to the slow rate of diffusion when compared to chemical reactions, and the lengthy nature of the DOSY experiment, such activity is unlikely to be picked up here.

To obtain a set of data to allow for a more accurate comparison of diffusion coefficients as a function of the tiara nuclearity, a DOSY experiment was performed on a solution of complex **6** in chloroform-d. This could then be compared to the results obtained for complex **2**. Due to

the conservation of the solvent and the similarity of the ligands, any difference in the diffusion coefficient could potentially be attributable to the different sizes of the complexes- hexanuclear for **6** and octanuclear for **2**. This plot is given in *Figure 3.20*.

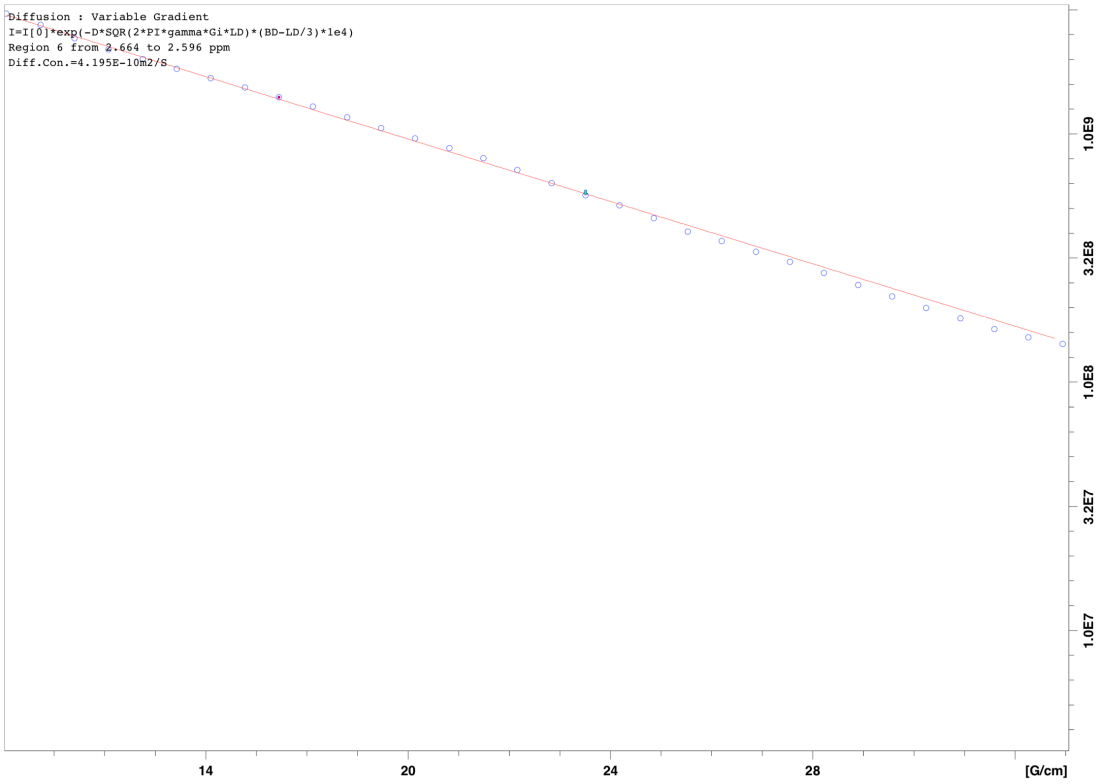


Figure 3.20: DOSY plot of **6** in chloroform-d, providing a nominal diffusion coefficient of 4.195×10^{-10} m^2/s.

The measured diffusion coefficient for complex **6** in chloroform-d was $4.195E^{-10}$ m^2/s. When this value is contrasted with the obtained result for complex **2** in chloroform-d of $4.018E^{-10}$ m^2/s, it can be seen that there is only a modest increase in the diffusion coefficient on proceeding from an octanuclear to a hexanuclear tiara-like complex ($\sim 0.177E^{-10}$ m^2/s; approximately a 4.2% increase). The small magnitude of this change is surprising for a significant change in molecular weight (from 2758 Da for **2** to 2068 Da for **6**; a 25% decrease), but this is rationalised by considering that the decrease in the size of the molecule does not scale to the decrease in molecular weight as organic molecules tend to. However, it can be seen now that the larger octanuclear ring does diffuse more slowly than the smaller

hexanuclear ring when the two complexes are examined in the same solvent. Further to this, the graph of the data again forms a linear line when plotted, indicating a single component.

The summarised DOSY data, including solvent viscosities and diffusion coefficients of **1**, **2** and **6** is given in *Table 3.1*.

Complex	Solvent	Viscosity (kg m^{-1} s^{-1})	Diffusion Coefficient (E^{-10} m^2/s)
1	Methanol-d4	$6.12E^{-4}$	3.605
1	Water-d2	$1.10E^{-3}$	2.428
2	Chloroform-d	$5.44E^{-4}$	4.018
6	Chloroform-d	$5.44E^{-4}$	4.195

Table 3.1: Table of solvent viscosities for methanol-d4, water-d2 and chloroform-d and diffusion coefficients for complexes **1**, **2** and **6**.

3.2.2 IR and UV/vis Spectroscopy

3.2.2.1 Infra-red Spectroscopy

Much like the 2D NMR spectroscopy, there have been few detailed IR experiments of tiara-like complexes, which makes it compelling to obtain spectra for each complex synthesised in *Chapter 2* and compare the results to examine the effects of nuclearity, functional group and isomerisation on the resultant spectra.

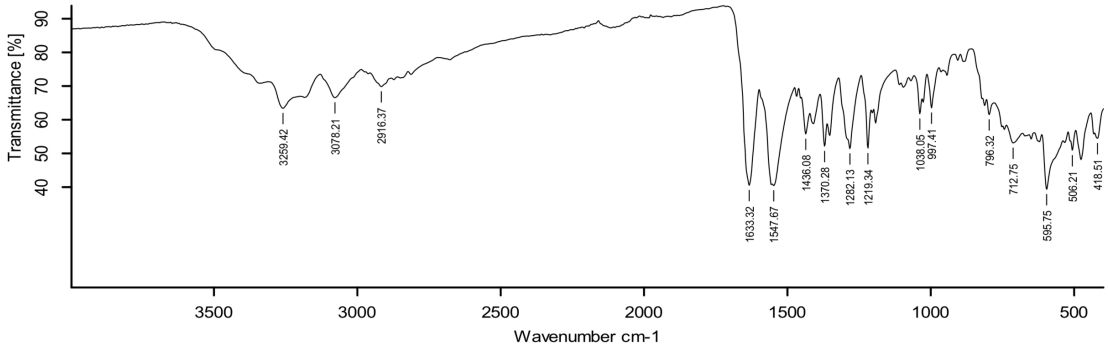


Figure 3.21: ATR-IR spectrum from 4000 cm^{-1} to 400 cm^{-1} of **1**.

The IR spectrum recorded for **1**, shown in *Figure 3.21*, is in good agreement with the expected amide composition of the tiara-like complex $[Pd_6(SCH_2CH_2NHCOCH_3)_2]_6$. The amide N-H band is located at 3259 cm^{-1} with C-H stretching bands at 3078 cm^{-1} and 2916 cm^{-1}. The broad absorptions here may result from residual H_2O co-crystallised with the sample. The strong carbonyl absorption occurs at 1633 cm^{-1}, characteristically low for an amide functionality. The absorption at 1548 cm^{-1} may represent the N-H bend.

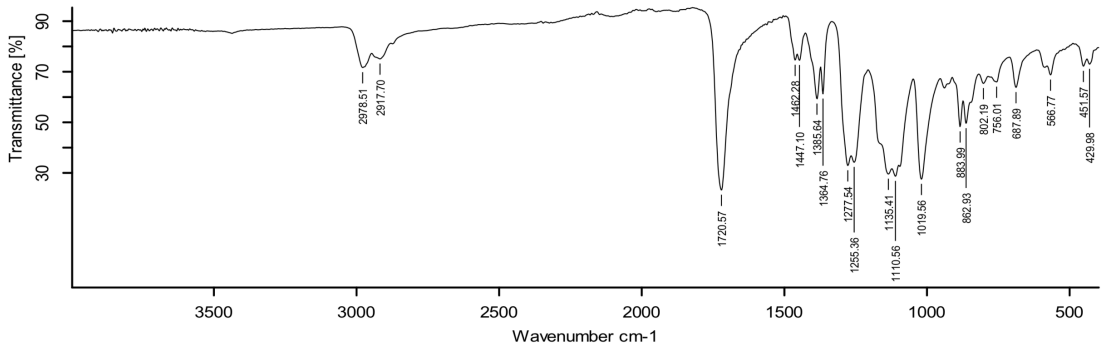


Figure 3.22: ATR-IR spectrum from 4000 cm^{-1} to 400cm^{-1} of **2**.

In contrast to the spectrum of **1**, the ATR-IR spectrum of **2**, given in *Figure 3.22*, does not show absorptions corresponding to the amide N-H. However, it retains the C-H stretches, at 2979 cm^{-1} and 2918 cm^{-1}. The carbonyl peak is observed at 1721 cm^{-1}, which is expected for an ester. There are no absorptions noted between 2600 cm^{-1} and 2500 cm^{-1}, indicating the absence of the thiol starting reagent.

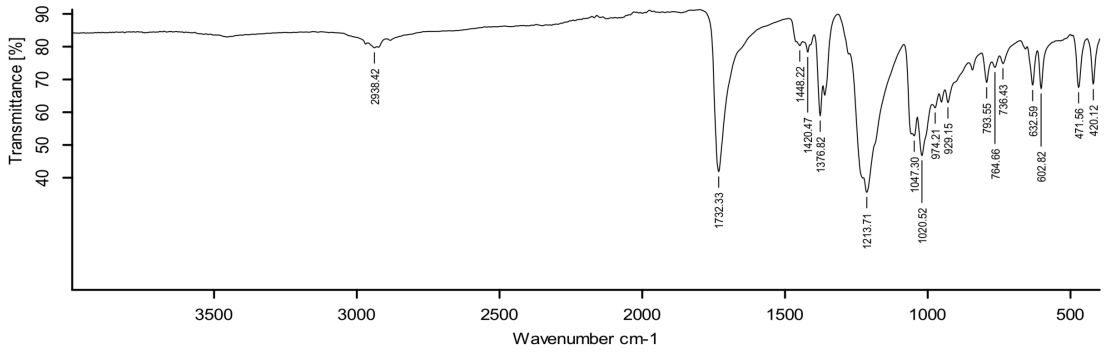


Figure 3.23: ATR-IR spectrum from 4000 cm^{-1} to 400cm^{-1} of **3**.

The ATR-IR spectrum of **3**, given in *Figure 3.23*, bears a strong similiarity to that of **2**, which is to be expected given the similiarity of the ligands. The C-H stretch is noted at 2938 cm^{-1} and the ester carbonyl absorption occurs at 1732 cm^{-1}. This is shifted to a slightly higher wavenumber than that of **2**, which may result from the repositioning of the carbonyl group. Similarly, no thiol S-H absorbances are observed in the spectrum. As expected, there do not appear to be any strong effects from the tiara nuclearity on the IR spectrum, and the most significant changes appear to result from the change of the functional group from an amide to an ester.

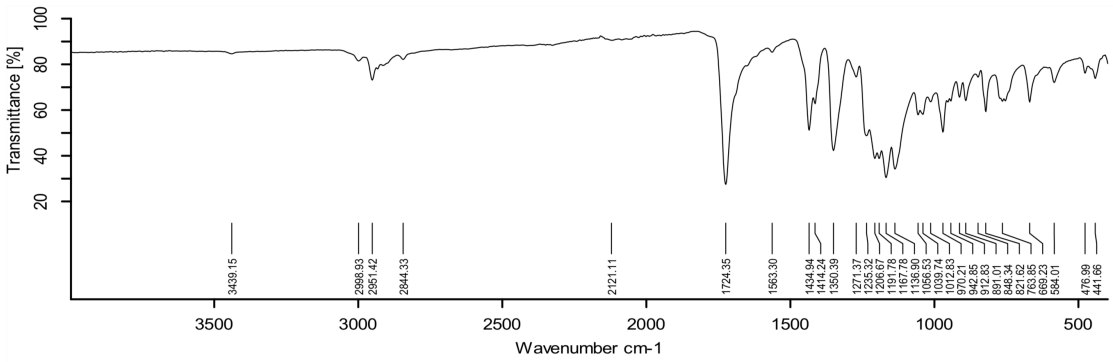


Figure 3.24: ATR-IR spectrum from 4000 cm^{-1} to 400cm^{-1} of **6**.

The ATR-IR spectrum of **6**, given in *Figure 3.24*, shows good consistency with the spectra of **2** and **3**. Aside from small adjustments to the wavenumbers of the absorptions resulting from the relocation of the carbonyl group, the features are conserved almost exactly between the isomers.

3.2.2.2 UV/vis Spectroscopy

The UV/vis spectra for complexes **1**, **2**, **3** and **6** are all consistent with each other, though little data has been published previously concerning UV/vis absorbances making comparisons with existing complexes difficult. In one study, the UV/vis spectrum of $[Pd(SCH_2CH_2Ph)_2]_6$ was published reporting absorbances at approximately 280, 325 and 415 nm. This data lines up well with the UV/vis spectra obtained for complex **1** and **3**. For complex **2**, the absorbance at > 400 nm shifts to a lower wavelength to 392 nm. This is consistent with the published spectrum of $[Pd(SCH_2CH_2Ph)_2]_8$ where the absorbance shifts from 415 nm (for the hexanuclear complex) to approximately 400 nm, suggesting that octahedral complexes absorb at a lower wavelength than hexanuclear complexes. This may be of use when attempting to identify the nuclearity of tiara-like complexes synthesised in the future.

The UV/vis spectra for **1**, **2**, **3** and **6** are given in *Figure 3.25*, *Figure 3.26*, *Figure 3.27* and *Figure 3.28* respectively.

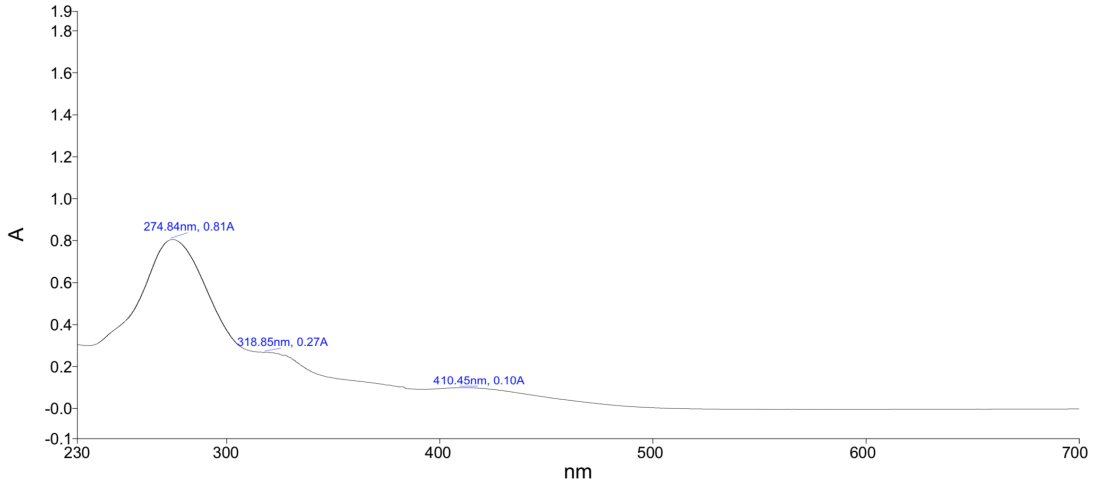


Figure 3.25: UV/vis spectrum from 230 - 700 nm of **1** showing strong absorbances in the short wavelength, high energy violet region, resulting in intensely yellow-coloured solutions.

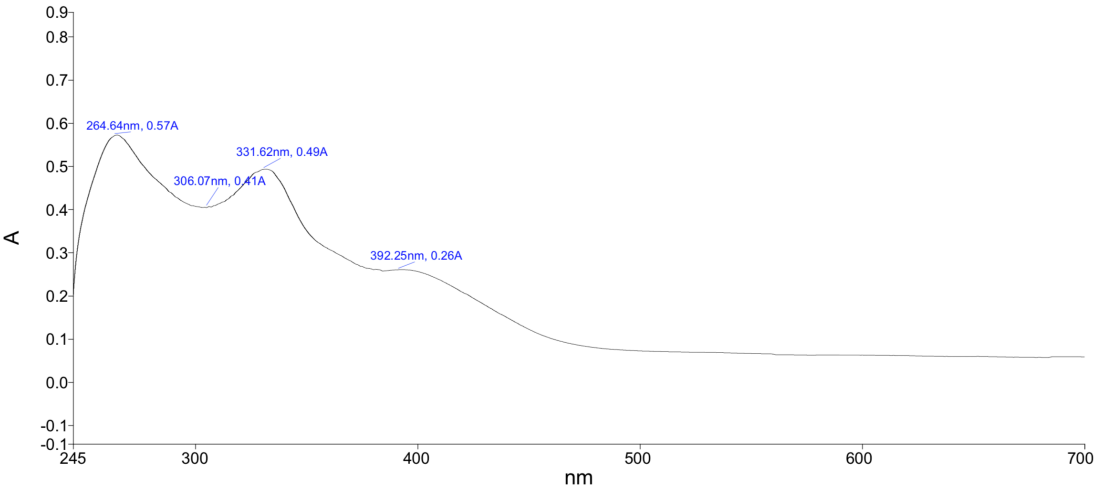


Figure 3.26: UV/vis spectrum from 245 - 700 nm of **2** showing strong absorbances in the short wavelength, high energy violet region, resulting in intensely yellow-coloured solutions. There are no absorbances above 400nm, in contrast to the hexanuclear tiaras **1**, **3** and **6**.

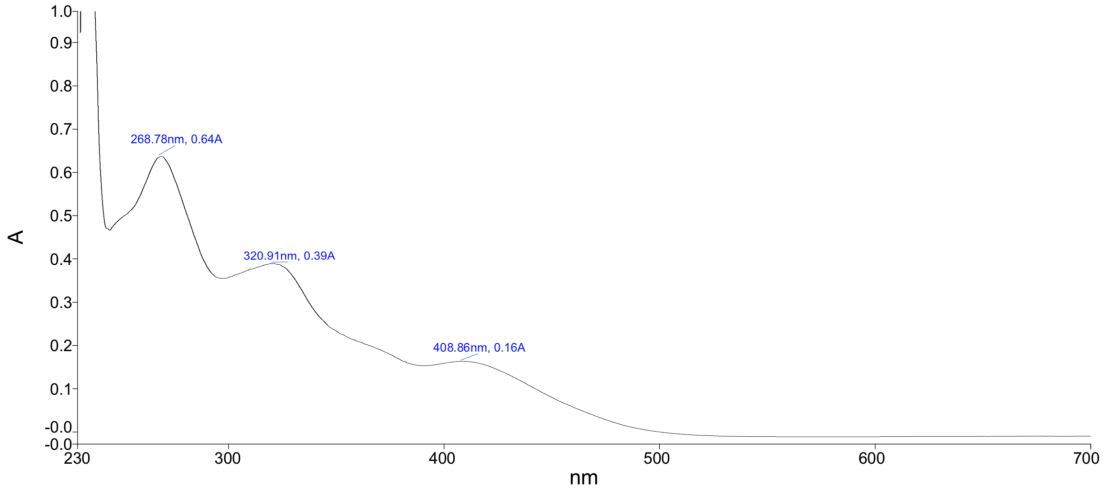


Figure 3.27: UV/vis spectrum from 230 - 700 nm of **3** showing strong absorbances in the short wavelength, high energy violet region, resulting in intensely yellow-coloured solutions.

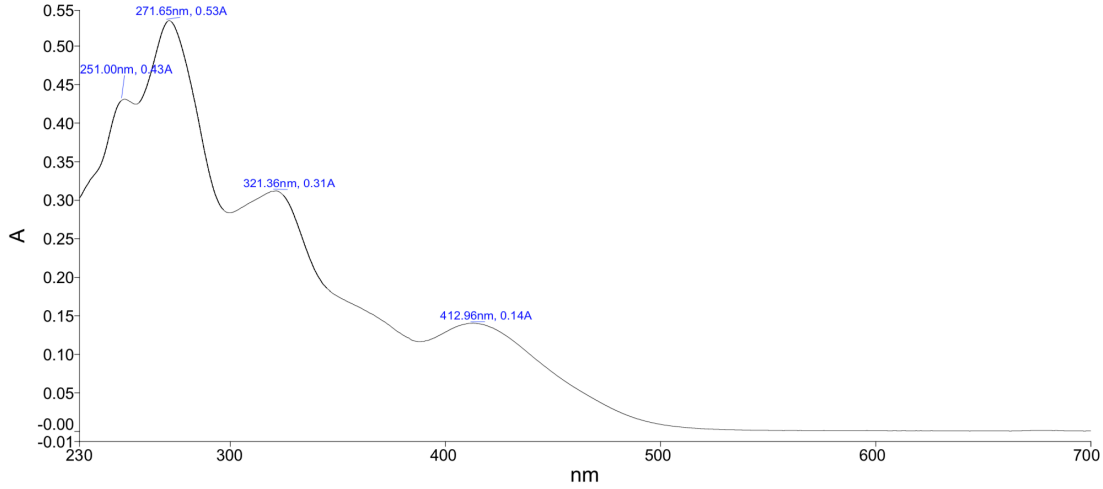


Figure 3.28: UV/vis spectrum from 230 - 700 nm of **6** showing strong absorbances in the short wavelength, high energy violet region, resulting in intensely yellow-coloured solutions.

The molar extinction coefficients for complexes **1**, **2**, **3** and **6** are presented in *Table 3.2* - *Table 3.5*, along with the coefficient divided by the number of PdS_2 subunits present in the complex (i.e. 6 for complexes **1**, **3** and **6**, and 8 for complex **2**).

λ (nm)	ε	ε / PdS_2
410.45	13,330	2,220
318.85	36,000	6,000
274.84	108,000	18,000

Table 3.2: UV/vis maxima, extinction coefficients and extinction coefficients per PdS_2 for **1**.

λ (nm)	ε	ε / PdS_2
392.25	34,670	4,330
331.62	65,330	8,170
264.64	76,000	12,670

Table 3.3: UV/vis maxima, extinction coefficients and extinction coefficients per PdS_2 for **2**.

λ (nm)	ε	ε / PdS_2
408.86	21,330	3,560
320.91	52,000	8,670
268.78	85,330	14,220

Table 3.4: UV/vis maxima, extinction coefficients and extinction coefficients per PdS_2 for **3**.

λ (nm)	ε	ε / PdS_2
412.96	22,060	3,680
321.36	47,490	7,920
271.65	81,190	13,530
251.00	65,870	10,980

Table 3.5: UV/vis maxima, extinction coefficients and extinction coefficients per PdS_2 for **6**.

These complexes all possess very strong absorbances in the visible light spectrum corresponding to the high energy green to violet wavelengths. This results in very intensely coloured yellow-orange solutions at low complex concentrations. In general the features are well retained between the complexes, especially for complexes **3** and **6**.

The high extinction coefficients recorded for these complexes, leading to the strong absorbances observed in the solution phase suggest that the transitions may be ligand-to-metal charge transfer (LMCT) transitions.

3.2.3 Electrochemistry, DLS and TEM

3.2.3.1 Cyclic Voltammetry

As previously discussed in *Chapter 3.1*, previous groups have reported interesting electrochemical experiments on tiara-like complexes to examine the effect of nuclearity and to explore the potential of nickel-thiolate complexes as hydrogen reducing catalysts.

A purified and dried sample of complex **1** was selected for electrochemical analysis; DMF was selected as the solvent to avoid electrochemical interference in the window of interest. A three electrode cell was employed, consisting of a glassy carbon working electrode, platinum wire secondary electrode and a saturated calomel reference electrode (SCE). [n-Bu_4N][BF_4] was used as the supporting electrolyte and the test solution was isolated from the reference electrode using a bridge tube with a vycor fritt. Unless otherwise stated, all redox potentials are referenced to the ferrocenium/ferrocene (Fc^+/Fc) couple ($E_{1/2}$ +0.49V vs SCE) which was used as an internal standard; no compensation was applied for internal resistance.

The Pd_6 tiara shows the first reductive process at E_p^c -1.75 V vs Fc^+/Fc (*ca.* -1.25 V vs SCE). In contrast, for a hexanuclear nickel tiara [$Ni(SCH_2CH_2Ph)_2]_6$ the reductive process does not appear until -1.8 V vs SCE and for a comparable hexanuclear palladium tiara [$Pd(SCH_2CH_2Ph)_2]_6$ the reduction occurs at -1.64 V. This may indicate that the presence of the amide allows for the easier reduction of the complex. The first oxidative process occurs at E_p^a -0.29 V vs Fc^+/Fc (*ca.* +0.21 V vs SCE) in contrast to $Ni_6(PET)_{12}$ which shows an oxidation at +0.8 V vs SCE and $Pd_6(PET)_{12}$ which shows an oxidation at +1.25 V. Oxidation of the complex therefore occurs at less positive potentials similar to the reductive processes occurring at less negative potentials, suggesting that oxidation of the complex is likewise easier to accomplish than for either $Ni_6(PET)_{12}$ or $Pd_6(PET)_{12}$.

To examine the possibility that a palladium-sulfur complex could be used to reduce H^+ as nickel-sulfur tiara-like complexes have been shown to, a simple electrochemical experiment was set up to measure the change in current on addition of H^+ to a solution of **1**; the results of which are shown in *Figure 3.29*. Acetic acid (AcOH) was selected as the proton source to achieve comparison with $Ni_6(PET)_{12}$. A solution of the acid (0.2M) dissolved in DMF was added incrementally to the test solution of complex **1** with aliquots corresponding to 2 equivalents of acid per addition and the test solution was reduced to -1.9 V before returning to -0.5 V. On addition of the acid, the measured current was observed to increase, stabilising after ~ 14 eq. However, the onset of reduction was not observed to shift to either more positive or negative potentials, which may indicate that the metal centres do not undergo protonation during this process.

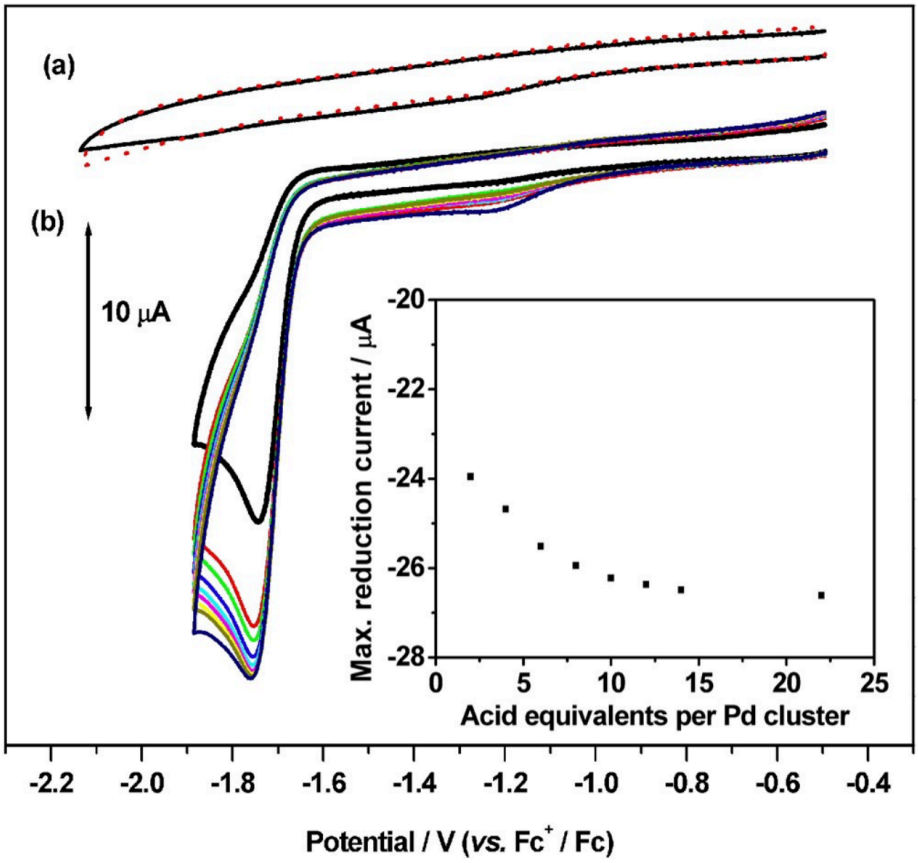


Figure 3.29: Cyclic voltammogram of a) [n-Bu_4N][BF_4] (0.2M) in DMF (solid black line) and with addition of AcOH (dotted red line); b) complex **1** in DMF (solid black line) and increasing concentration of AcOH up to 22 eq. Inset: plot of max. reduction current (μA) as a function of AcOH equivalents.

In comparison with $Ni_6(PET)_{12}$, the increase in reduction current is very modest; ~10μA for **1** when compared with ~60μA for $Ni_6(PET)_{12}$. In an attempt to elicit a stronger response to the addition of acid, the strength of the acid was increased via replacement of acetic acid (pKa = 4.76) with trifluoroacetic acid (TFA, pKa = 0.23). In the subsequent experiment, shown in *Figure 3.30*, the measured increase in current was much more significant and did not reach saturation until approximately 30 equivalents.

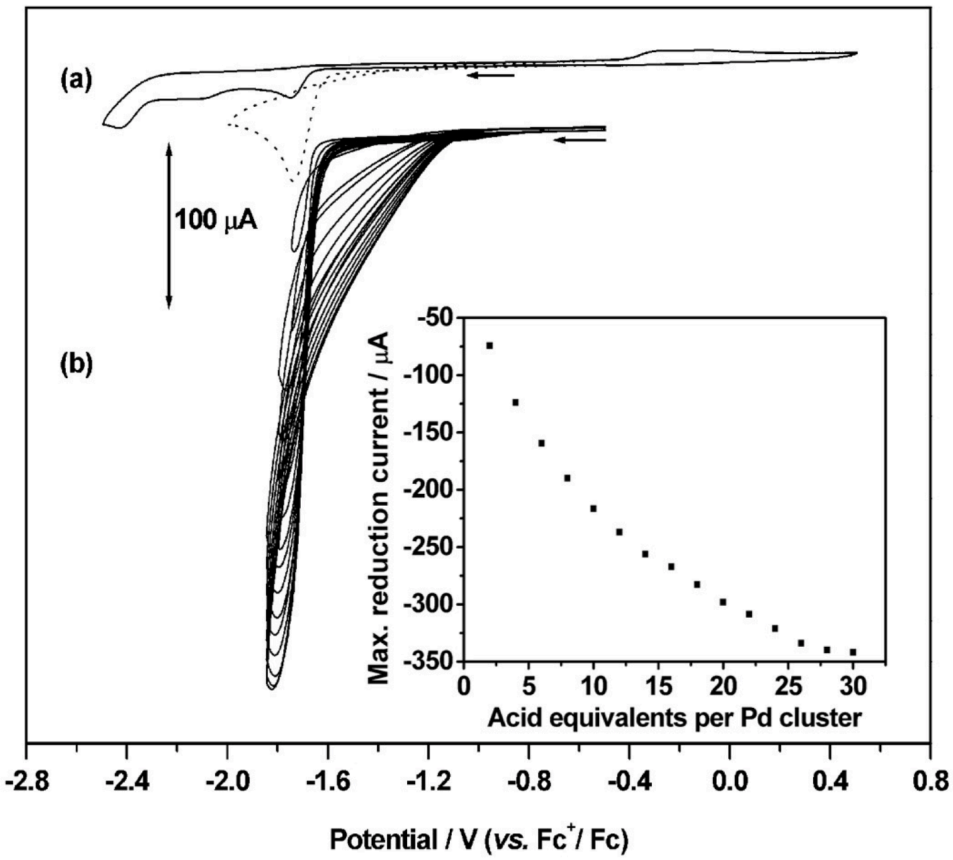


Figure 3.30: Cyclic voltammogram of a) Complex **1** with $[n\text{-}Bu_4N][BF_4]$ (0.2M) in DMF (solid black line) and in 2 eq. TFA (dotted line); b) complex **1** in DMF (solid black line) and increasing concentration of TFA up to 30 eq. Inset: plot of max. reduction current (μA) as a function of TFA equivalents.

The max. reduction current at saturation (~30 eq.) is over 300μA greater than that of **1** in DMF alone; a significant increase in the change in current when compared to the addition of acetic acid. Further to this, the onset of the reduction shifts to more positive potentials with

the increasing concentration of acid, though the position of the peak current does not likewise shift to significantly more positive potentials; this may indicate that protonation of the metal centres is occurring in the presence of trifluoroacetic acid, which was not observed for acetic acid. The peak continued to be observed even at high concentrations of acid, suggesting that the electrochemical process remained under diffusion control during the entire experiment.

Interestingly, even at the addition of just 2 equivalents of trifluoroacetic acid, the currents were observed to cross during the electrochemical experiment; with the return wave crossing the forward wave at the approximate onset of the reduction current peak. This phenomenon persisted with increasing concentrations of TFA even up to 30 equivalents. This was not observed for the complex in the presence of acetic acid, possibly due to the significantly lower currents measured. The nature of the current crossing was suspected to be arising due to a deposition of solid material upon the electrode, reducing its surface area and therefore reducing the current. Previous work done for $Ni_6(PET)_{12}$ included a rinse experiment wherein cyclic voltammetry was performed on a THF solution of the Ni complex (1mM) in the presence of acetic acid at saturation (approximately 22 equivalents). The electrode was then rinsed with THF and replaced into a fresh solution of all components aside from the complex, the results of which confirmed the absence of colloid formation on the electrode.

To examine the possibility that heterogeneous palladium products may be forming on the electrode surface, a similar rinse experiment was performed, the result of which is given in *Figure 3.31*. A solution of **1** and TFA (30 equivalents) was subjected to a reductive potential of -1.40 V vs SCE and the potential held for 10 minutes to allow for the build up of any particulate matter. Maintaining the inert atmosphere, the working electrode was then rinsed with fresh electrolyte solution and then placed into a fresh solution containing only the supporting electrolyte and TFA (30 equivalents) before the CV was re-recorded (see *Figure*

3.31, plot d)). Following this, the working electrode was removed and cleaned to remove any particulate matter and then replaced into the same solution and the CV re-recorded (see *Figure 3.31, plot e)*).

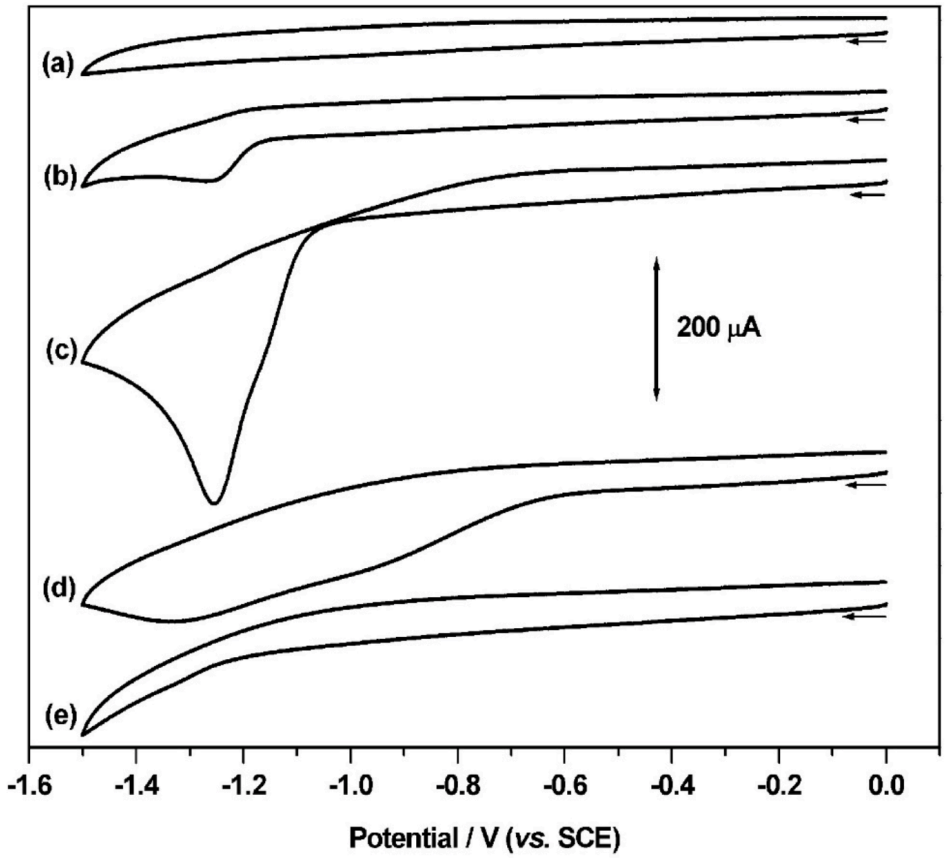


Figure 3.31: Cyclic voltammogram of a) [n-Bu_4N][BF_4] (0.2M)/ DMF; b) [n-Bu_4N][BF_4] (0.2M), **1** ($5.3E^{-6}$ M)/ DMF; c) [n-Bu_4N][BF_4] (0.2M), **1** ($5.3E^{-6}$ M), TFA ($1.7E^{-4}$ M)/ DMF; d) [n-Bu_4N][BF_4] (0.2M), TFA ($1.7E^{-4}$ M)/ DMF after initial rinse; e) [n-Bu_4N][BF_4] (0.2M), TFA ($1.7E^{-4}$ M)/ DMF after the working electrode was cleaned.

The results of the electrochemical rinse test suggest that there is some degree of deposition of material onto the electrode- likely in the form of heterogeneous palladium. However, the currents involved are fairly small, which suggests that the total contributions from the heterogeneous material to the large currents seen during the reduction of the palladium tiara-like complex are minor. However, the onset of reduction is again seen at less negative potentials, which may explain the same observation seen in the previous cyclic voltammetry experiments. The currents do not cross on the return wave, which is consistent with the

sample containing no further palladium complex to deposit onto the electrode. On cleaning the electrode to remove any built-up material and then returning it to the same solution, these small currents are no longer observed, giving a voltammogram that appears again similar to the original waves seen in *Figure 3.31 plot a)*.

In an attempt to determine whether or not these reduction currents corresponded to the reduction of protons to dihydrogen, the experiments were modified from cyclic voltammetric to coloumetric analysis. Bulk electrolysis was carried out of a solution of complex **1** in the presence of TFA using a reticulated vitreous carbon (RVC) electrode (80 ppi). A Pt/Rh gauze electrode was employed as the secondary electrode, which was separated from the working RVC electrode by a glass frit. The reference electrode employed again was the saturated calomel electrode, which was connected to the test solution by a bridge tube and placed in the centre of the working electrode. The solution was stirred vigorously during the bulk electrolysis. The potential applied was -1.40 V vs SCE for 6000s.

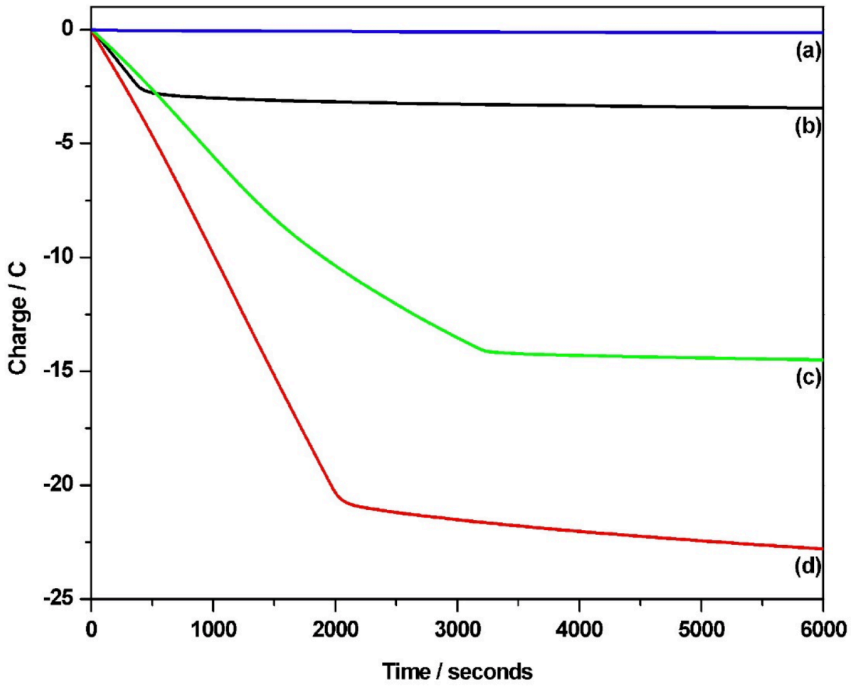


Figure 3.32: Charge / Time plot for a) [n-Bu_4N][BF_4] (0.2M)/ DMF; b) [n-Bu_4N][BF_4] (0.2M), **1** ($5.3E^{-6}$ M)/ DMF; c) [n-Bu_4N][BF_4] (0.2M), TFA ($1.7E^{-4}$ M)/ DMF; d) [n-Bu_4N][BF_4] (0.2M), **1** ($5.3E^{-6}$ M), TFA ($1.7E^{-4}$ M)/ DMF. All potentials were applied as -1.40 V vs SCE.

The results of the coloumetric analysis, shown in *Figure 3.32*, indicate the transfer of approximately 1.2 electrons per palladium centre, suggesting that the peak cathodic potential at 1.75 V vs Fc^{+}/Fc may be a one electron reduction. This would be consistent with the reported one electron reduction of Ni^{II} to Ni^{I} in $Ni_6(PET)_{12}$ at *ca.* -1.80 V vs SCE. The accumulation of charge was accompanied by a change in colour of the test solution from yellow to red-brown (see *Figure 3.33*), which persisted after the potential was removed and the solution exposed to air.

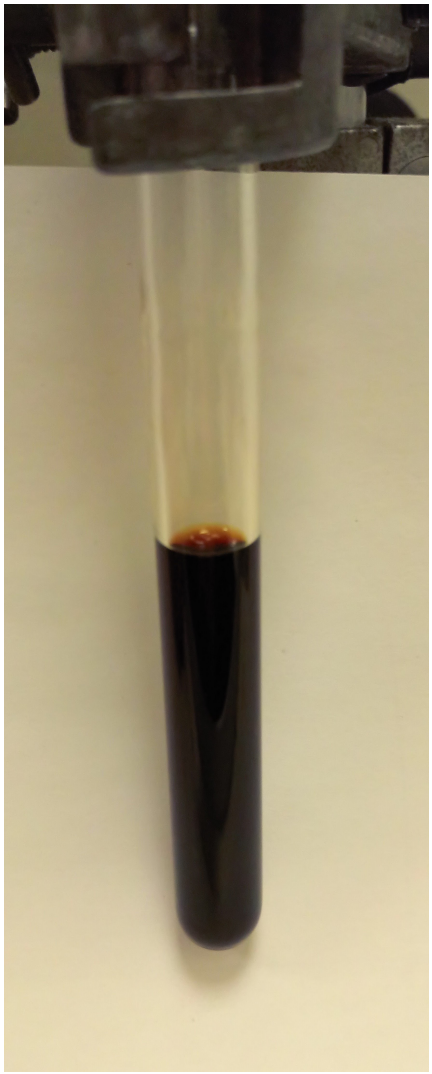


Figure 3.33: Dark brown-red colour observed on sustained reduction at -1.40 V vs SCE

It is worth noting that reduction of the acid is seen to occur even in the absence of complex **1** as shown by in *Figure 3.32 plot c)*. However, the rate of reduction, as measured by the accumulation of charge over time (Q/t) is reduced. The total charge accumulated in *Figure 3.32 plot d)* is sufficient to account for both reduction of the Pd clusters and complete reduction of the acid protons (assuming liberation of dihydrogen gas).

3.2.3.2 Dynamic Light Scattering (DLS)

The observed colour change from yellow to a deep red-brown during the bulk electrolysis of the complex occurred both in the presence and absence of acid, and could not immediately be explained by the electrochemical results. One possible explanation for the dark colouration could be due to the formation of palladium nanoparticles via the electrolysis; this would be consistent with the observation that heterogeneous palladium builds up on the working electrode when a potential of -1.40 V vs SCE is applied to the solution. While this is markedly different from the observation that $Ni_6(PET)_{12}$ was not seen to form such particles, palladium tiara-like complexes have already been shown to be precursor materials to nanoparticle formation. To ascertain whether or not the colour change resulted from the formation of nanoscale aggregates, the electrolysed sample of **1** was taken for Dynamic Light Scattering analysis.

Preserving the inert atmosphere via a glovebox, the samples was transferred to an airtight sealed cuvette and the analysis was performed. The results of the scattering experiment however suggested that the average size of the particles in the solution were of a micrometre scale, rather than nanoparticles. However, it remained uncertain whether this sizing measurement represented an accurate average of the particles in solution or if it was due to a small amount of larger contaminant molecules. Due to the Rayleigh approximation that $I \propto d^6$ where I is the intensity of the scattered light and d is the diameter of the scattering

particles, a 10x increase in particle results in a 1,000,000x increase in the light scattered. Therefore an exceedingly small proportion of large contaminant species can effectively "mask" the presence of smaller species in solution.

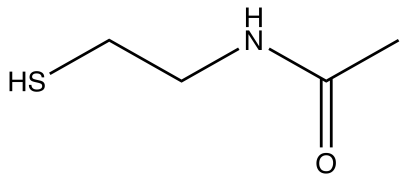


Figure 3.34: Structure of *N*-acetylcysteamine. The short chain of the ligand is thought to result in inefficient capping of the nanoparticles, resulting in aggregation.

The potential aggregation of palladium nanoparticles present into larger microparticles was not entirely unexpected however, given the size of the *N*-acetylcysteamine thiolate chain (see *Figure 3.34*) present in complex **1**. Ordinarily longer thiolate chains are often required to stabilise smaller nanoparticle structures and prevent aggregation into larger assemblies; in the example of the nanoparticles formed from $[Ni(S(CH_2)_{11}CH_3)_2]_6$ the long dodecanethiolate chain allows for nearly monodisperse ~2nm nanoparticles that show little aggregation.

In order to determine whether the large microparticles measured in the light scattering experiment were aggregated palladium particles or contaminants, the sample was analysed by Transmission Electron Microscopy (TEM).

3.2.3.3 Transmission Electron Microscopy (TEM)

By a 'drop-casting' method, a small quantity of the electrolysed sample was deposited onto a graphene oxide holey carbon film TEM grid and the excess was removed due to the low volatility of the DMF solvent. Imaging of the resultant grid revealed the deposition of nanoparticular species. The results of the TEM imaging are shown in *Figure 3.35* to *Figure 3.38*.

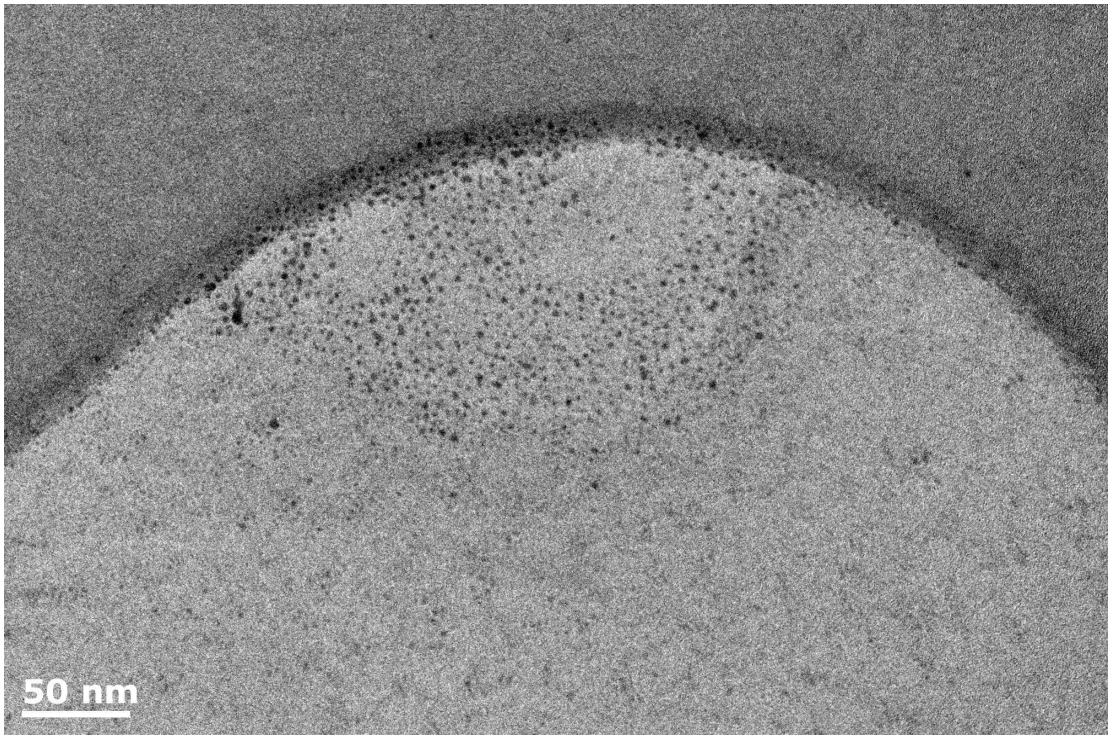


Figure 3.35: TEM image of electrolysed solution of **1**, showing nanoscale species. Scale bar = 50nm.

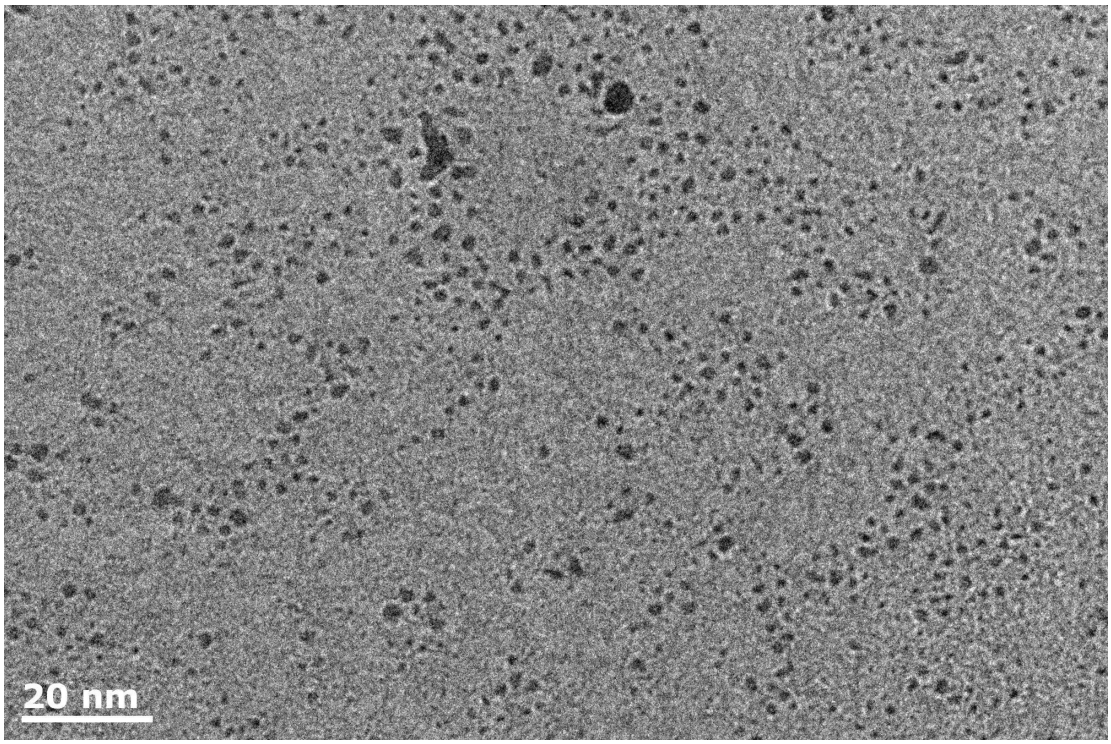


Figure 3.36: TEM image of electrolysed solution of **1**. Scale bar = 20 nm.

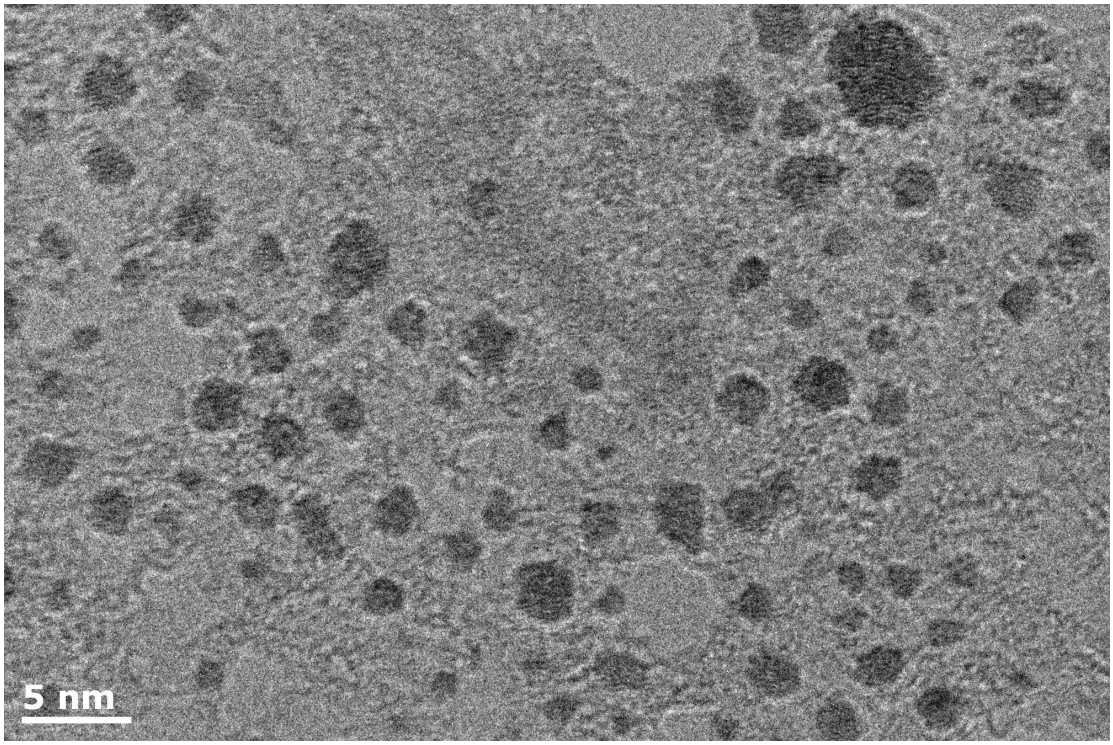


Figure 3.37: TEM image of electrolysed solution of **1**, showing mostly 1-2 nm particles. Scale bar = 5 nm.

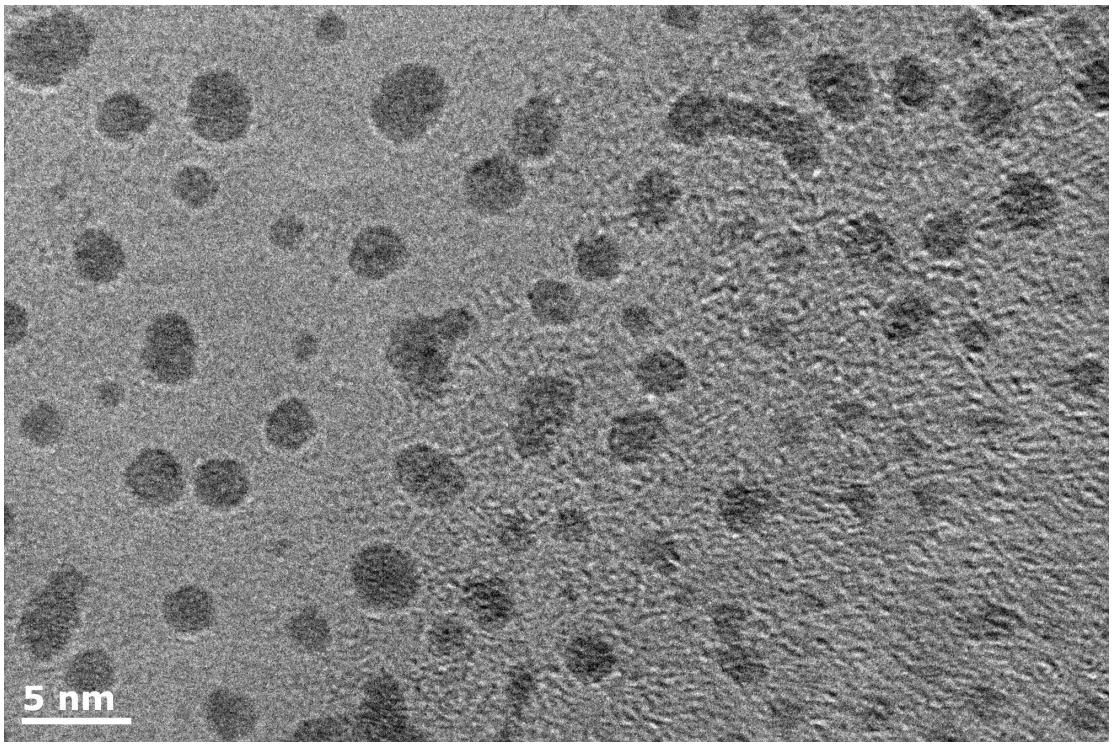


Figure 3.38: TEM image of electrolysed solution of **1**, showing mostly 2-4 nm particles. Scale bar = 5nm.

Viewing the particles at increased magnification indicates that they are not of a uniform size; while the largest are up to 5 nm in diameter, the smallest may well be lower than 1 nm across. Neither do they possess a uniform and regular geometry- while some are approximately spherical, others are elongated into oval or increasingly irregular shapes. However, the irregular distribution of sizes and shapes is expected and rational for the reasons outlined earlier concerning the inefficient capping of the nanoparticles by the short chain *N*-acetylcysteamine thiolate ligand.

Naturally, while the existence of the nanoparticles can be confirmed by the TEM imagery and the size and geometry of the particles can also be gauged, their composition cannot be likewise determined by simple microscopy techniques, and there remains the possibility that the particles are contaminants, possibly material from the RVC electrode utilised in the electrochemical experiments. Two techniques, High Angle Annular Dark Field Scanning Transmission Electron Microscopy (HAADF STEM) and Energy-Dispersive X-ray (EDX) spectroscopy were employed in order to confirm the composition of the particles.

The annular dark field scan was used first as qualitative analysis to examine the presence of heavy elements and confirm their localisation within the nanoparticles on the grid before running the EDX to quantify the elements present. The results, illustrated in *Figure 3.39*, showed bright spots of the image that corresponded to the areas where nanoparticles were present, indicating the presence of heavy elements within the particles.

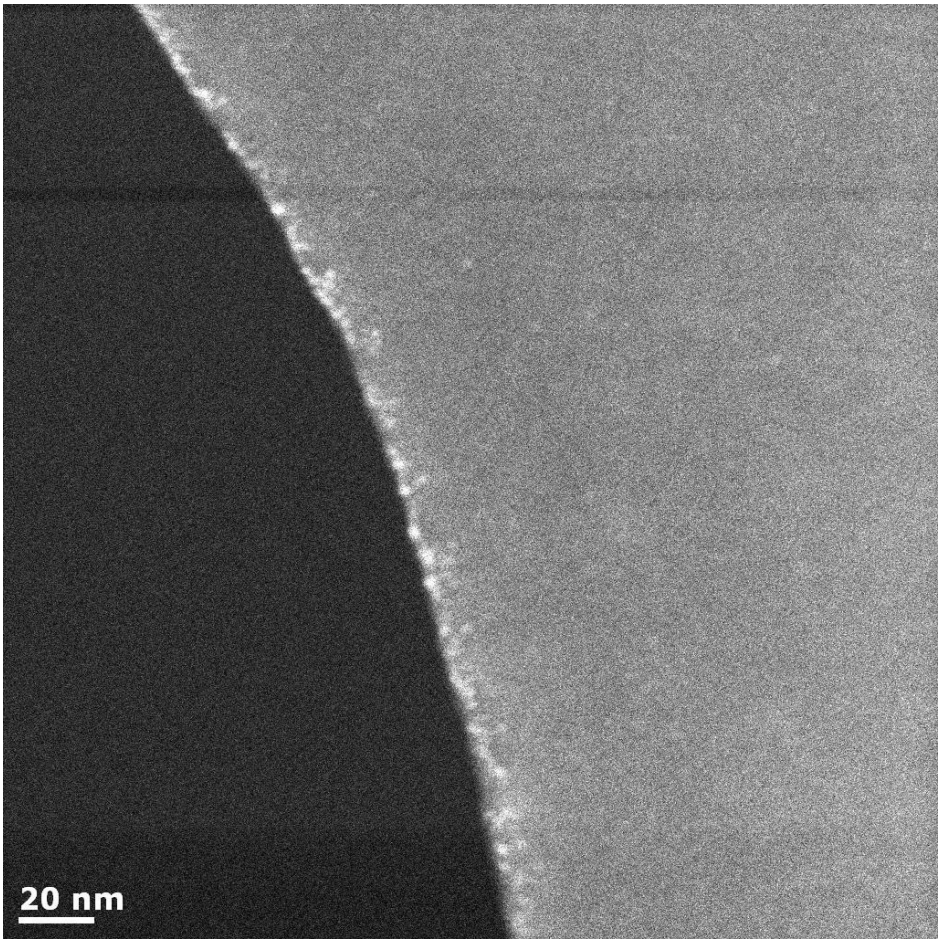


Figure 3.39: HAADF-STEM image showing white spots indicating presence of heavy elements in the nanoparticles. Scale bar = 20 nm.

While the annular dark field image shows the presence of heavy elements within the nanoparticles, the high Z atoms are relative to the background light elements such as carbon and oxygen from the graphene oxide grid, therefore EDX spectroscopy was employed as a more quantitative form of analysis to determine the precise nature of the heavy atoms, as well as the percentage composition.

Element	Weight (%)
C	86.01
O	6.06
F	1.12
Na	0.44
Si	1.74
P	0.02

S	0.12
Cl	0.04
K	0.04
Ca	0.04
Cr	0.01
Fe	0.01
Co	0.01
Cu	4.23
Pd	0.09
Au	0.02

Table 3.6: TEM-EDX results showing elemental composition by weight. Palladium returns approximately 0.1% of the composition.

The initial results of the EDX analysis, given in *Table 3.6*, suggested a very high proportion of carbon present in the sample along with oxygen, and only a very small (0.09%) palladium composition. However, the vast majority of elements detected by this method originate from either the graphene grid (eg. C, O) or the support holder (eg. Fe, Au). When the spectroscopy is repeated to subtract the support elements, a much higher proportion of palladium is returned. The result of the deconvolution is given below in *Table 3.7*.

Element	Weight (%)
F	58.61
Na	23.38
P	0.98
S	6.07
Cl	2.13
K	2.18
Ca	2.13
Pd	4.52

Table 3.7: TEM-EDX results after deconvolution. The high proportion of fluorine results from the supporting electrolyte and trifluroacetic acid. The palladium content originates from the tiara sample.

While the other metals detected previously (Fe, Co, Cr, Cu) originate from the support holder, the palladium detected in the sample could only arise from the sample itself. The high proportion of fluorine detected is likely to originate from the supporting electrolyte salts used

in the electrochemistry, along with traces of trifluoroacetic acid.

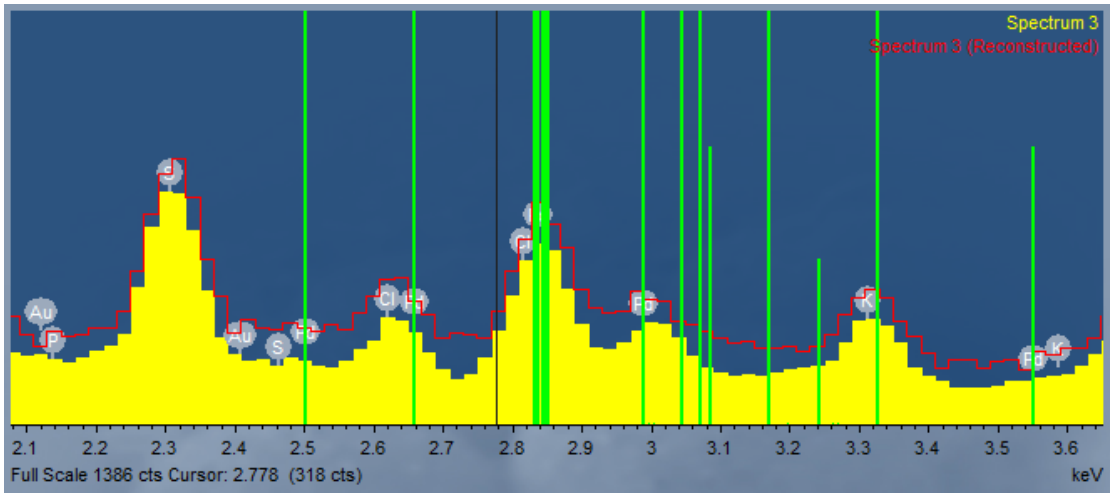


Figure 3.40: Excerpt from EDX spectrum of the nanoparticle dispersion. Green lines- predicted signals from palladium. Red outline- predicted spectrum of palladium-containing nanoparticles

The predicted and experimental EDX spectra (see *Figure 3.40*) for palladium-containing nanoparticles are in convincing agreement. It is probable therefore that complex **1** has the potential to act as a precursor material for the formation of nanoparticles that are formed electrolytically via the sustained reduction of the complex at -1.40 V vs SCE. It should be noted that the potentiostat struggled initially to apply the full voltage therefore some caution is advised in the interpretation of these results, however reduction of the complex to form nanoparticles may be feasible at lower potentials than those reported here.

3.2.4 Inclusion Complexes and Hirshfeld Surfaces

3.2.4.1 Tiara-like Inclusion Complexes and Host-Guest Chemistry

While the hexanuclear tiara-like complexes synthesised in this work are of an insufficient size to act as molecular hosts for a guest, complex **2** is an octanuclear tiara and therefore has the potential to entrap small molecules. A sample of **2** was purified by crystallisation before being dried extensively under vacuum to remove any trace of prior solvents or entrapped guests. This was then dissolved in methyl iodide to form a saturated solution and placed in a capped vial pierced with a needle. This was then placed into a larger vial half-filled with pentane and sealed. Crystal growth was observed after approximately one week but left for a further week to attain full growth, this yielded a small crop of deep red needles. Screening of a suitable crystal suggested a space group of P4/mnc; a tetragonal system of considerably higher symmetry than the original monoclinic space group of C2/c. Solution of the data confirmed this crystal system and revealed the structure illustrated in *Figure 3.41*.

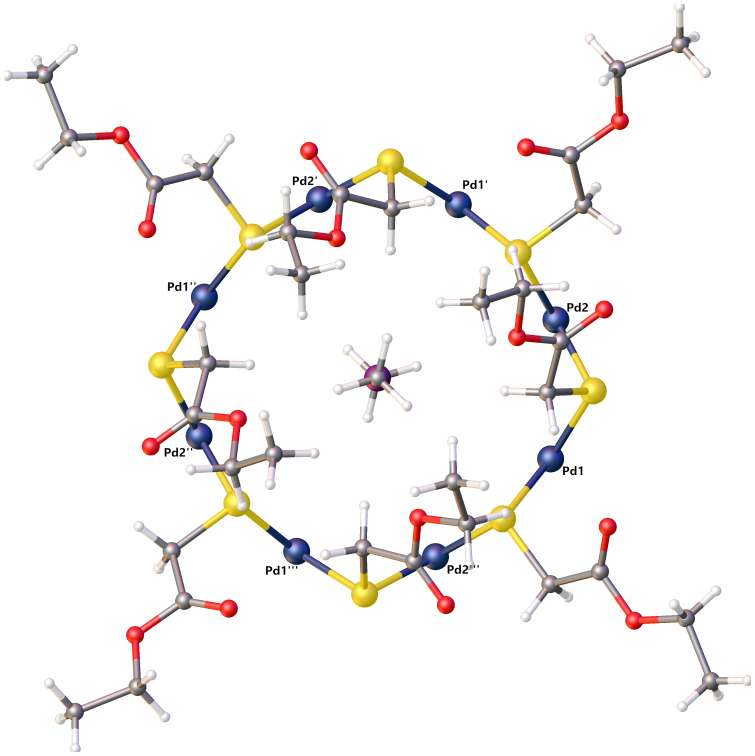


Figure 3.41: Crystal structure of **2** crystallised from methyl iodide. ' = 1-Y, +X, 1-Z. '' = 1-X, 1-Y, 1-Z. ''' = +Y, 1-X, 1-Z. Atom colours: Pd-dark blue, S-yellow, I- purple, C-grey, O-red, H-white.

The structure of the complex is considerably different from the original structure solution of **2** crystallised from chloroform, justifying the increase in cell symmetry. The geometry of the ring has distorted from the original octagonal shape to nearly square. This demonstrates the large degree of flexibility inherent in the framework of the complex, able to expand and contract to accommodate a guest molecule. This degree of distortion is unprecedented in tiara-like complexes, far above that of even the related complex $[Pd(SCH_2COOCH_3)_2]_8$, which showed reduced distortion on hosting a guest molecule (see *Figure 3.42*).

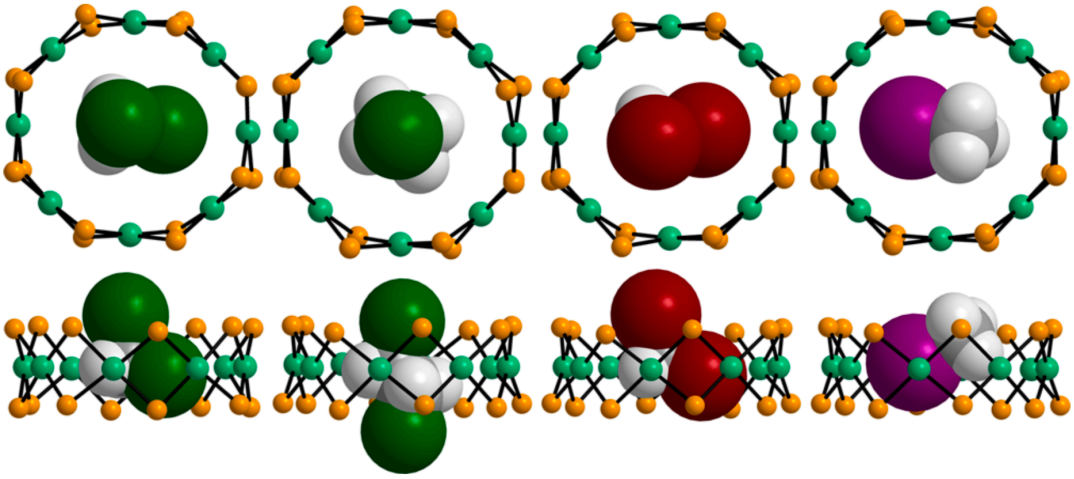


Figure 3.42: Previously reported host-guest structures for $[Pd(SCH_2COOCH_3)_2]_8$ on inclusion of (left to right): dichloromethane, 1,2-dichloroethane, dibromomethane, methyl iodide.[52]

Justification for the increased distortion seen in **2** over the methyl analog can be found when the central void of the complex is examined. As can be seen in *Figure 3.41*, within this crystal structure the central void is occupied by methyl iodide. However, in sharp contrast to $[CH_3I\subset Pd(SCH_2COOCH_3)_2]_8$ there exist two molecules of methyl iodide within the centre of the cavity and further solvent molecules exterior to the ring.

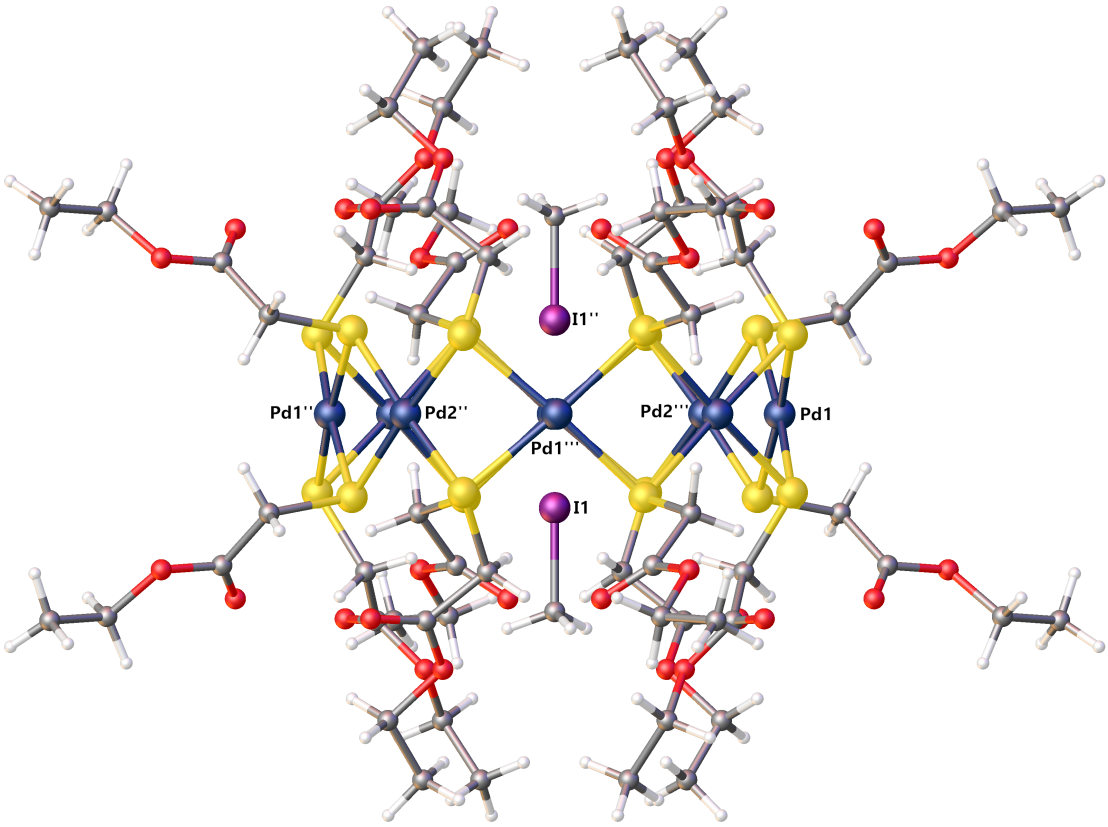


Figure 3.43: Crystal structure of **2** on inclusion of methyl iodide (side view). '' = 1-X, 1-Y, 1-Z. ''' = +Y, 1-X, 1-Z. Atom colours: Pd-dark blue, S-yellow, I- purple, C-grey, O-red, H-white.

As seen within *Figure 3.43*, the two molecules of methyl iodide within the ring appear to adopt a iodide-iodide facing configuration, separated by an I···I distance of 3.554 Å (> C-I···I 180.0°). This is shorter than the sum of the van der Waals radii of the iodine atoms (3.96 Å), indicating a weak interaction between the two molecules. The Pd···I distance ranges from 4.543 Å to 4.651 Å, suggesting no strong interaction between the solvents and the metal atoms. The Pd···Pd separation for adjacent palladium atoms on the 'side' of the square is 3.364 Å and 3.097 Å for adjacent palladium atoms on the 'corner'. The longest Pd···Pd separation for opposite metal atoms across the tiara is 8.363 Å.

The extended packing of the complex is shown below in *Figure 3.44*.

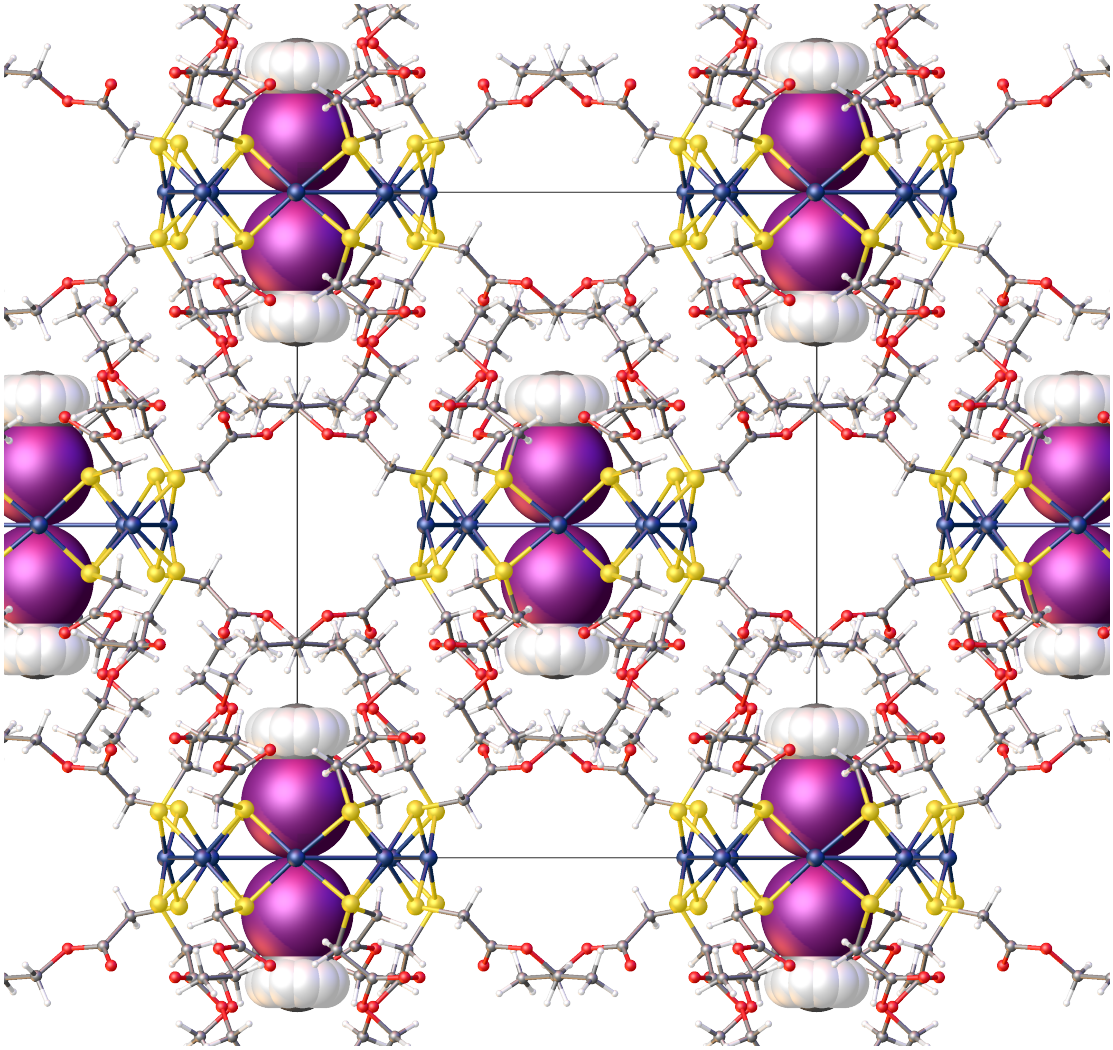


Figure 3.44: Packing of the complex within the unit cell (outlined by solid black lines). External solvents omitted. Internal solvents illustrated as spheres. Atom colours: Pd-dark blue, S-yellow, I-purple, C-grey, O-red, H-white.

The solvent molecules exhibit significant static and rotational disorder, but the occupancies were refined to give an approximation of 7 methyl iodides per tiara, equalling 14 solvent molecules per cell.

The solvent molecules exterior of the rings are shown within the lattice in *Figure 3.45*.

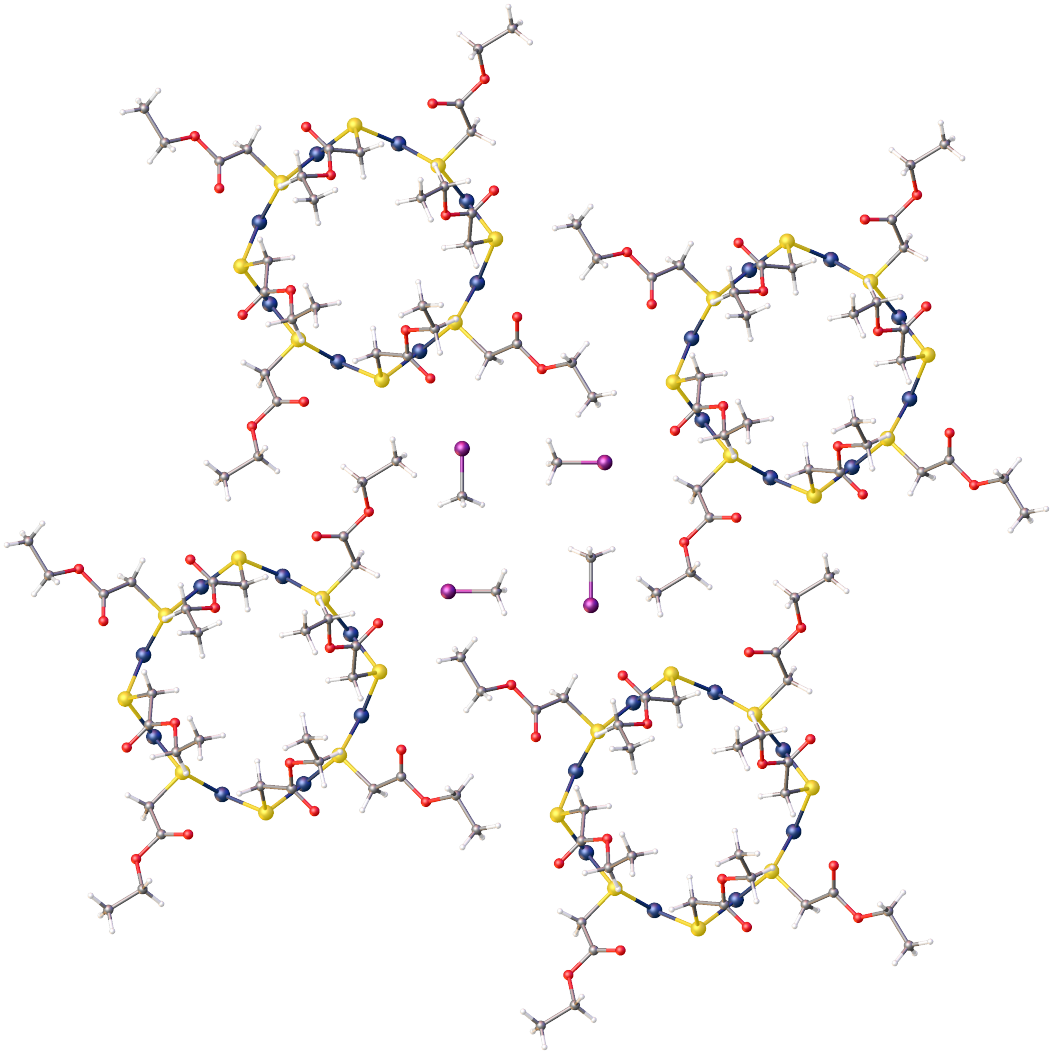


Figure 3.45: Positioning of methyl iodides between four adjacent molecules of **2**. Internal solvents omitted. Atom colours: Pd-dark blue, S-yellow, I- purple, C-grey, O-red, H-white.

3.2.4.2 Hirshfeld Surface Analysis

To better understand the non-covalent, supramolecular properties of the complexes synthesised in this work, of particular importance for complex **1** due to the extensive hydrogen bonding observed, Hirshfeld Surface Analysis was employed. The finalised crystallographic information files (CIFs) were processed by CrystalExplorer[57] in order to obtain a mapped molecular surface which was then interpreted. The Hirshfeld surface of **1** is shown in *Figure 3.46* and *Figure 3.47*.

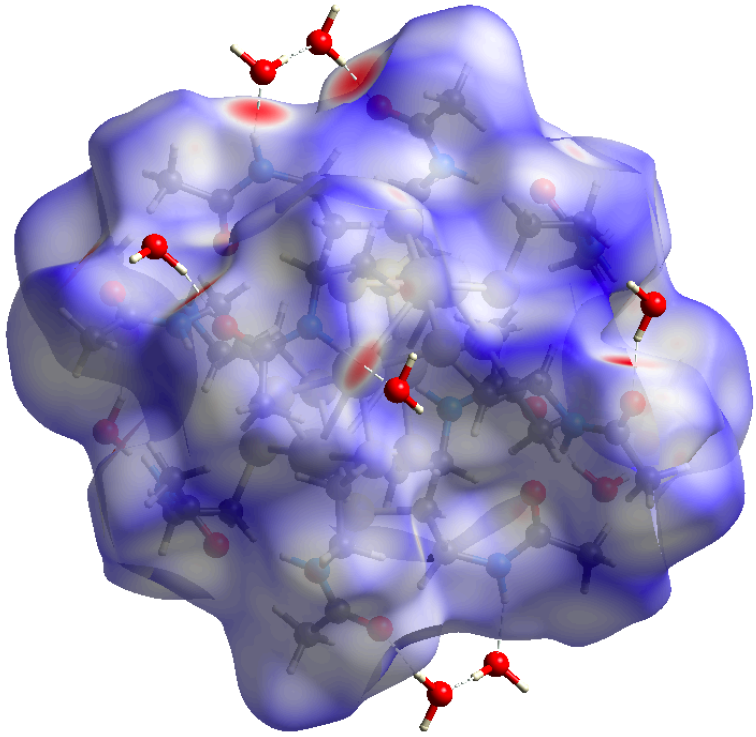


Figure 3.46: Hirshfeld d_{norm} surface of **1** showing hydrogen bonding to neighbouring water molecules. Atom colours: O-red, H-white.

The colour shown on the surface reports on the nature of the closest contact to the molecule; blue indicates a long distance over the sum of the van der Waals radii of the internal and external atoms (>0), white indicates a contact approximately equal to the sum of the van der Waals radii (=0) and red indicates contacts shorter than the sum of the spheres (<0). Within the crystalline state complex **1** forms a total of 10 hydrogen bonds to water molecules present in the lattice around the tiara. In addition, each complex forms a total of 4 hydrogen bonds to neighbouring tiara molecules via two donor moieties and two acceptor moieties. Therefore out of the possible 24 maximum hydrogen bonding sites within the complex, 14 are engaged in intermolecular bonds and only 10 bond intramolecularly.

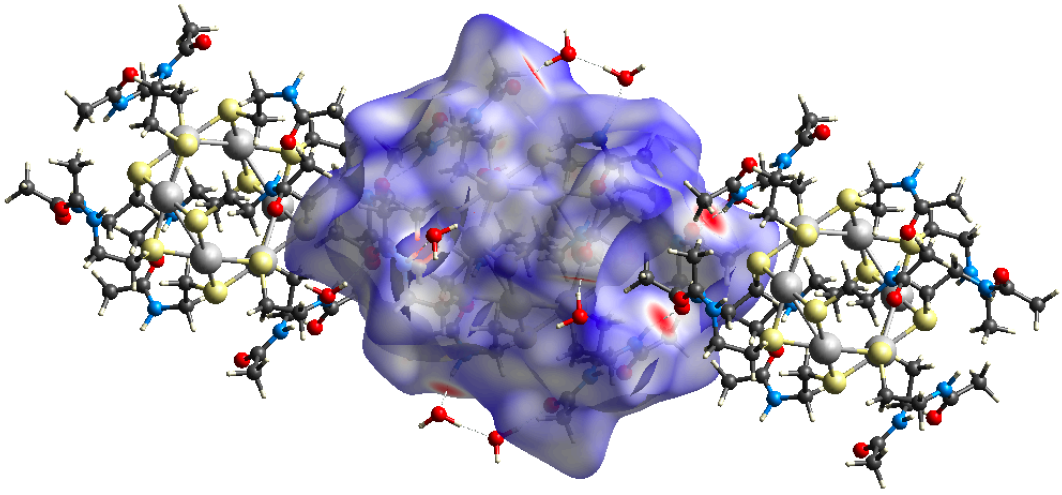


Figure 3.47: Close contacts (hydrogen bonds) between tiara-like complexes

The fingerprint diagram for complex **1**, given in *Figure 3.48*, shows characteristic peaks corresponding to these hydrogen bonding interactions.

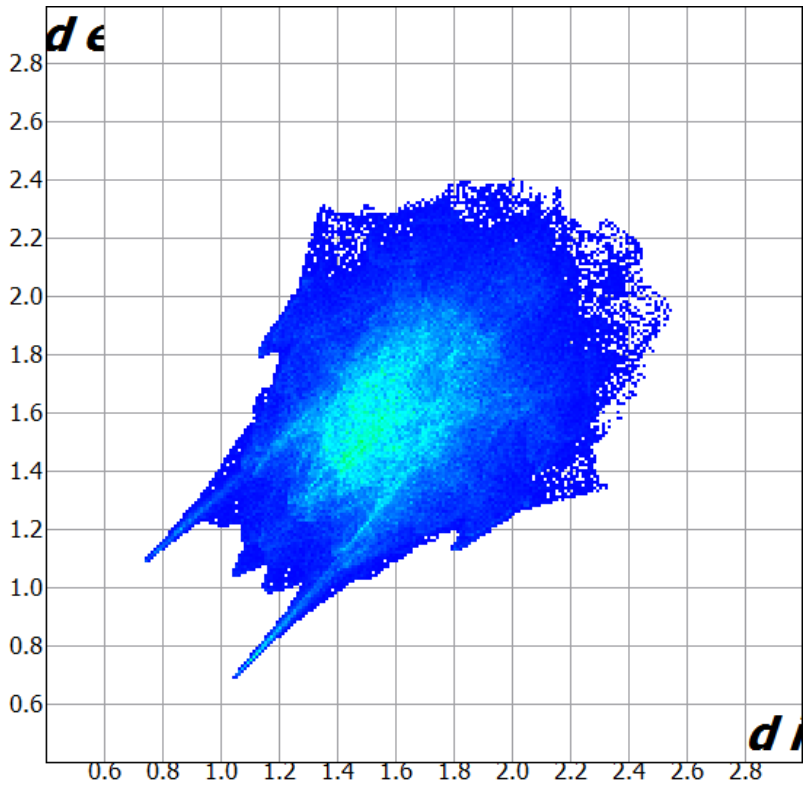


Figure 3.48: Full fingerprint diagram for **1**. The two sharp peaks at the lower left of the diagram correspond to the hydrogen-bonding interactions of the complex.

The two sharp peaks located at the lower left of the fingerprint plot represent these supramolecular interactions; the shape of which results from the strongly directional nature of the bonding. The lower peak ($d_i > d_e$) and upper peak ($d_e > d_i$) are representative of the hydrogen bond acceptors and hydrogen bond donors, respectively.

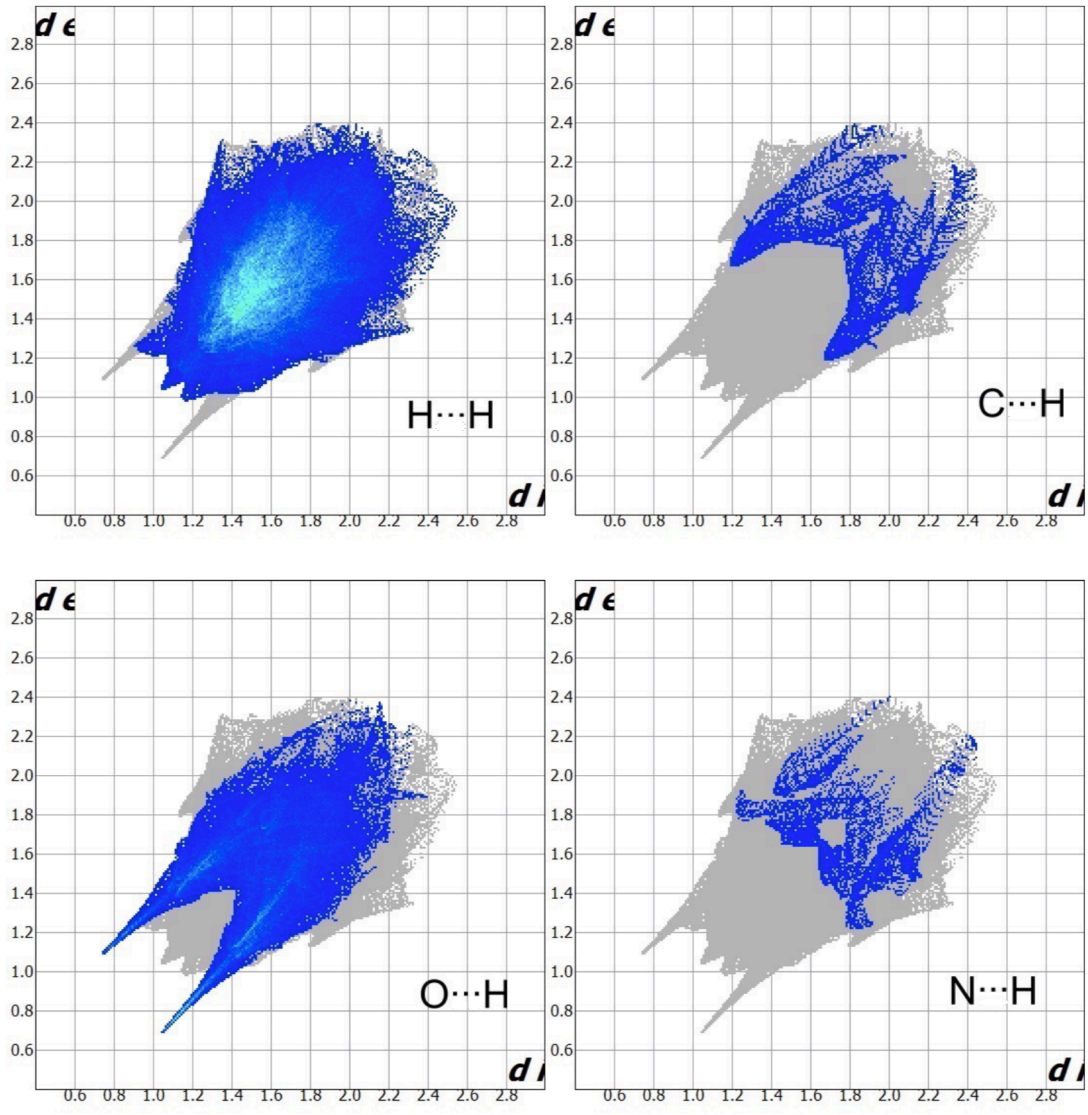


Figure 3.49: Fingerprint plots indicating interactions originating from H···H (67.9%), C···H (2.8%), O···H (22.2%) and N···H (2.0%) contacts.

From the fingerprint diagrams specific to certain atom interactions given in *Figure 3.49*, it can be seen that the H···H interactions make up the vast majority of the contacts from the

complex in the crystalline state (67.9%) and range from diffuse (high d_e, d_i) to closer, sharper contacts (low d_e, d_i), whereas the C···H and N···H contacts make up 2.8% and 2.0% of the fingerprint plot each. Interestingly, despite their proximity to the centre of the complex, the sulfur atoms are shown to have significant contacts with hydrogen atoms, as S···H contacts (see *Figure 3.50*) make up approximately 2.8% of the fingerprint plot.

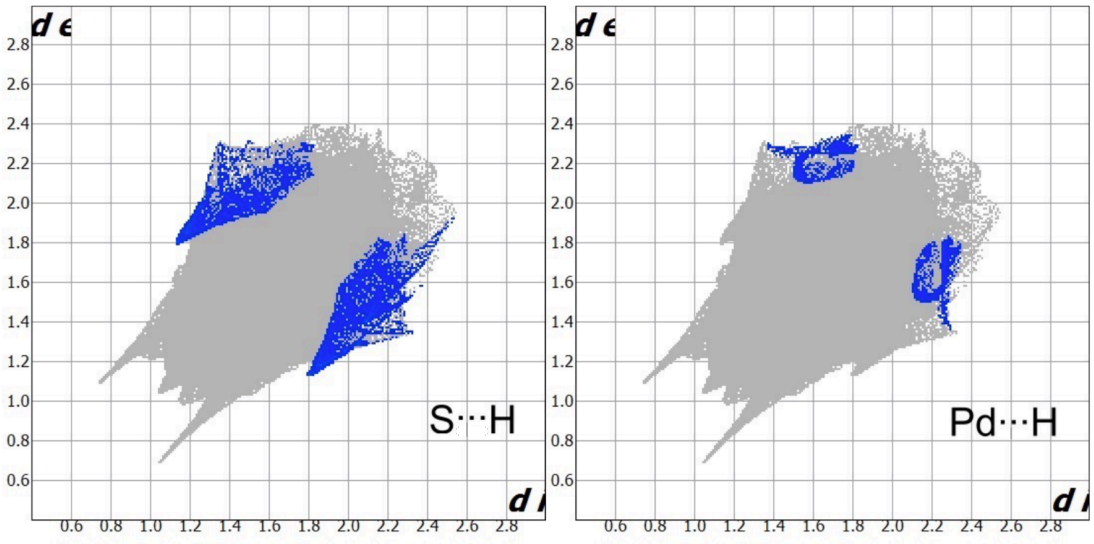


Figure 3.50: Fingerprint plots indicating interactions of S···H (2.8%) and Pd···H (0.8%).

The Pd···H interactions are measured at 0.8% of the overall fingerprint plot and show that the centre of the complex is not subsumed within a shell comprised of the ligand arms, but able to present, in a limited fashion, the palladium centres to the outside of the complex. This may suggest that the metals are more chemically accessible to external species than previously thought; which may affect factors such as protonation during electrochemical experiments, or chemical attack at the Pd-S ring. All other interactions, including C···C, C···N, C···O, N···N, N···O, O···O, Pd···Pd, Pd···C, Pd···N, Pd···O, S···C, S···S, S···Pd, S···N and S···O each make up 0.5% or less of the total fingerprint plot (< 3% in total) and are not thought to contribute significantly to the packing of the complex within the solid state.

In contrast, the Hirshfeld surface for complex **3** shows significant but expected differences

given the lack of hydrogen bonding capability. The surface is illustrated in *Figure 3.51*.

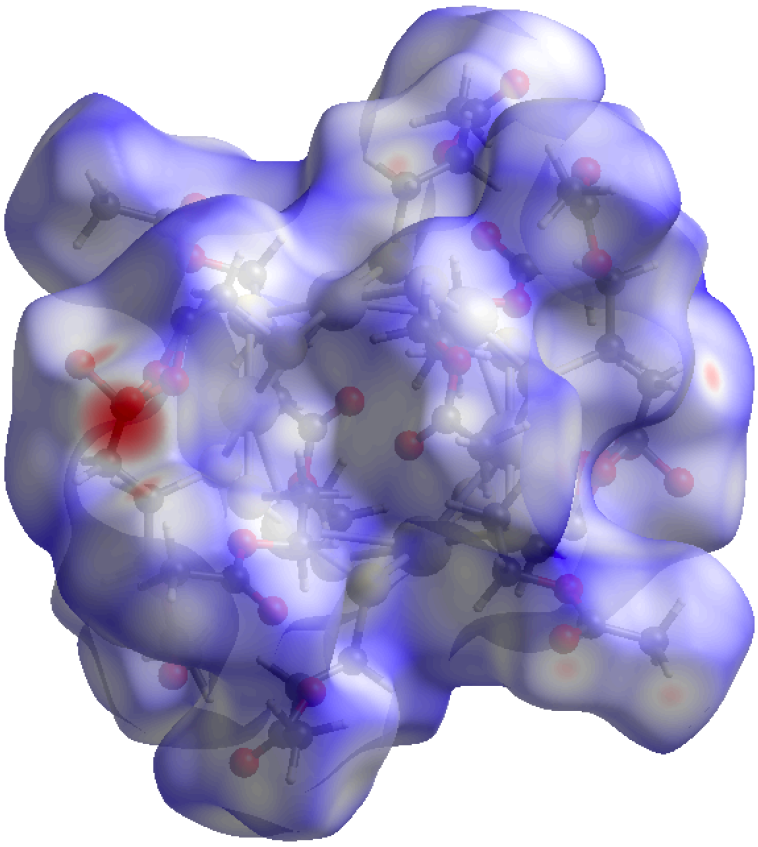


Figure 3.51: Hirshfeld d_{norm} surface of **3**.

There exist far fewer areas on the Hirshfeld surface where the closest contact is made at a distance shorter than the sum of the van der Waals spheres of the internal and external atom (coloured red). Notably, several of the short contacts just under the sum of the van der Waals spheres of the internal and external atoms (coloured white with small red centres) appear to occur at the terminal CH_3 groups of the thiolate arms. The ^1H NMR spectrum of **3** suggests that these protons are the most shielded in the complex, though due to the change in functional group from an amide to an ester, they are slightly less shielded than the corresponding CH_3 in complex **1**, potentially increasing the strength of C-H···O interactions.

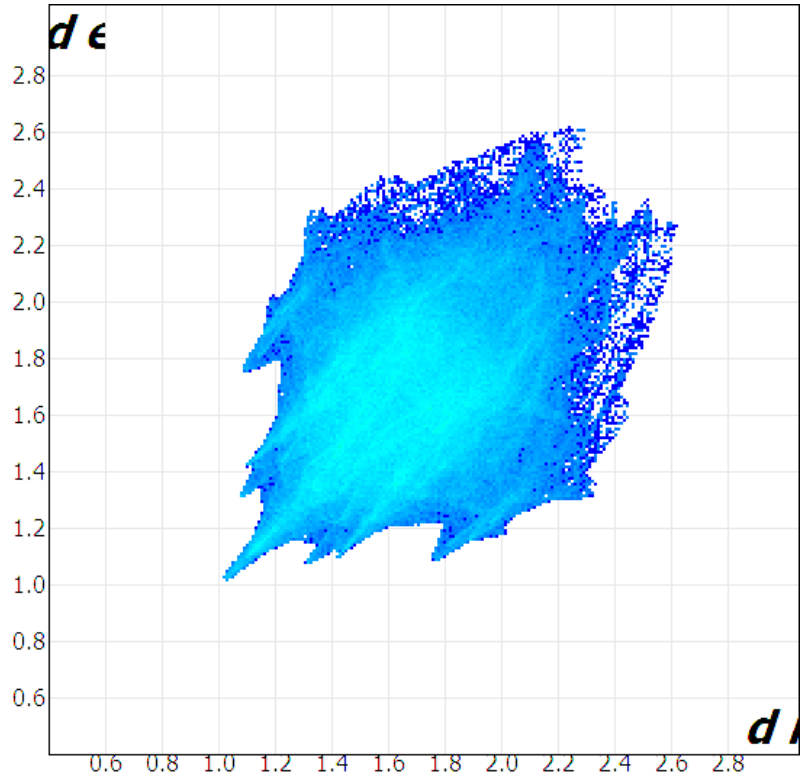


Figure 3.52: Full fingerprint diagram for **3**, showing reduced hydrogen-bonding interaction 'peaks' relative to **1**.

The fingerprint diagram, given above in *Figure 3.52*, bears a broadly similar profile to that of **1**; the principal difference being the lack of the two hydrogen bonding O···H spikes at the lower left of the spectrum. The H···H interactions have decreased from 67.9% of the fingerprint plot of **1** to 49.6% of the fingerprint plot of **3**; while the majority of these interactions remain diffuse, at the lower left portion of the plot some of these interactions have become sharp, more directional contacts reminiscent of the O···H peaks observed in the fingerprint plot for complex **1**; this may indicate weak C-H···O hydrogen bonds. This observation appears to confirm the earlier hypothesis that the change of functional group and the consequent deshielding of the CH_2 and CH_3 protons could strengthen interactions from these groups. This is particularly applicable to the β-CH_2 protons, as the chemical shifts in the ^{1}H NMR spectra are shifted downfield from 3.57 and 3.44 ppm in complex **1** to 4.39 and 4.29 ppm in complex **3**.

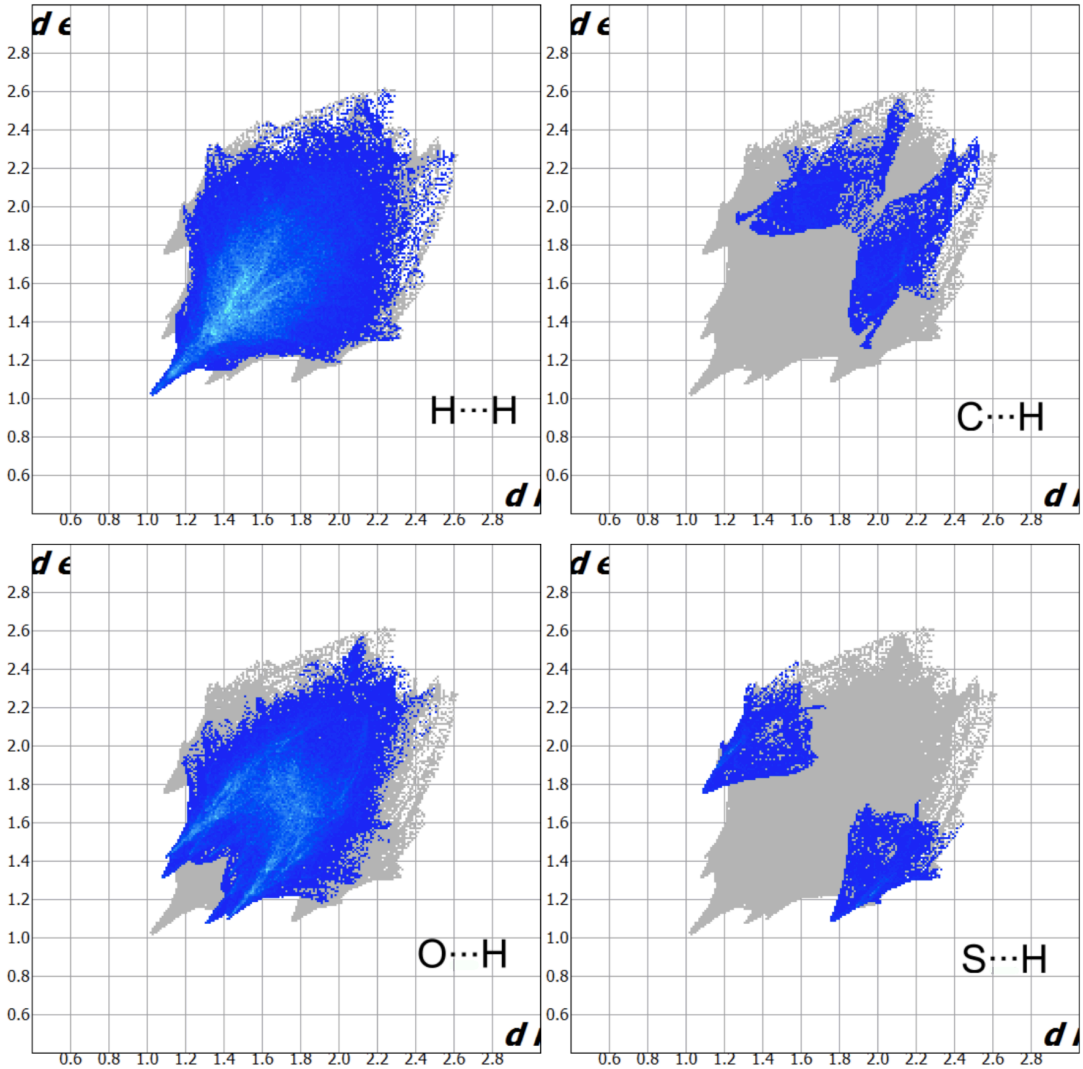


Figure 3.53: Fingerprint plots indicating interactions originating from H···H (49.6%), C···H (4.5%), O···H (36.2%), S···H (3.7%) contacts.

Additionally, the 'wings' corresponding to the S···H interactions (see *Figure 3.53*) also appear to have undergone a sharpening in the peaks, potentially representing stronger interactions. O···O and C···O interactions comprise 2.8% and 2.1% of the fingerprint plots respectively, Pd···H interactions are slightly increased to 1.1% of the fingerprint plot; all other interactions, including C···C, Pd···Pd, Pd···C, Pd···O, S···C, S···S, S···Pd and S···O comprise a negligible proportion of the fingerprint plot.

3.3 Conclusions

The spectroscopic properties of the tiara-like complexes in Chapter 2 have been explored at significant length. The 2D NMR studies, hitherto a sparse area of investigation, turned up interesting observations and properties about the complexes. The COSY data for **1** revealed a relatively long ranged scalar coupling not seen for the other complexes; this has been attributed to either the partial double bond character of the amide or a strong hydrogen bonding interaction holding the complex in a particular geometry for the long range coupling. NOESY and ROESY investigations into complex **2** suggested chemical exchange between the axial and equatorial ligands, indicating a fairly low barrier to inversion of the thiolate.

DOSY studies performed for complexes **1**, **2** and **6** suggest that the increase of nuclearity from a hexanuclear to an octanuclear complex leads to only a small increase in the hydrodynamic radius of the complex, resulting in only a small increase in the diffusion coefficient. This supports the earlier observation that the complexes are extremely difficult if not impossible to separate by size exclusion chromatography. However, the results of the DOSY analysis confirmed that each of the tiara solutions consisted of only a single component. Variable temperature experiments performed for complexes **1** and **2** agreed with previous experiments wherein the octanuclear complex undergoes asymmetric signal broadening, indicating dynamic movement of the ligand arms in and out of the centre of the ring, whereas hexanuclear complexes such as **1** do not show this behaviour.

A solution of **1** in DMF shows irreversible reduction when held at a potential of -1.40 V vs SCE accompanied by a colour change from yellow to red/brown. Coloumetric analysis indicates a transfer of approximately 1.2 electrons per metal centre, which may suggest reduction from Pd(II) to Pd(I). On the addition of acid to the experiment, the measured current increased; the magnitude of this increase was significantly higher for trifluoroacetic

acid than for acetic acid. A slight shift in the onset of reduction may indicate protonation of the metal centres. The currents were also observed to cross between the forward and backward cycles for the complex in the presence of TFA- a further rinse test performed on the electrode indicates the presence of heterogeneous deposits on the electrode but further experiments suggest that these particulates may only partially contribute to the reductive processes. Transmission Electron Microscopy analysis coupling with Energy-Dispersive X-ray spectroscopy of the reduced solution revealed the presence of palladium nanoparticles, indicating that **1** may act as a precursor to form nanoparticles via electrolysis.

On crystallisation from a solution of methyl iodide, complex **2** shows host-guest propensity, able to host two molecules of MeI within the cavity of the ring. This is accompanied by a radical change of geometry of the complex from octagonal to almost square, illustrating the flexibility of the framework. The inclusion of two solvent molecules within the tiara is unprecedented in previously reported literature, as only a single molecule has only been previously observed encapsulated within a tiara-like complex. This observation opens up potential new avenues of host-guest chemistry, including the performing of chemical reactions under confinement.

3.4 Experimental

3.4.1 Materials

Tiara-like complexes were synthesised according to the protocols outlined in Chapter 2.4. Other materials used in this section were obtained from commercial suppliers and used without further purification. Anhydrous DMF was obtained from Sigma-Aldrich and stored over 4Å molecular sieves before use.

3.4.2 Spectroscopic Methods

3.4.2.1 NMR Spectroscopy

2D NMR experiments were carried out using a Bruker AV(III)400HD with a BBFO smart probe. Chemical shifts are reported relative to the MeOD residual peak at 3.31ppm or the $CDCl_3$ residual peak at 7.26 ppm. DOSY experiments were performed using a 3mm NMR tube without convection compensation. Variable Temperature (VT) experiments were recorded by repeated acquisition of a ^1H spectrum at 10°C intervals.

3.4.2.2 Infra-red Spectroscopy

Infra-red spectra were obtained with a Bruker Tensor 27 FTIR spectrometer with an ATR attachment at room temperature.

3.4.2.3 UV-vis Spectroscopy

UV-vis absorption spectra were obtained using a Perkin-Elmer Lambda 25 spectrometer.

3.4.2.4 Electrochemistry

All electrochemical experiments were carried out with an Autolab PGSTAT20 potentiostat. A three electrode cell was employed, consisting of a glassy carbon working electrode, platinum

wire secondary electrode and a saturated calomel reference electrode (SCE). [n-Bu_4N][BF_4] was used as the supporting electrolyte and the test solution was isolated from the reference electrode using a bridge tube with a vycor fritt. Unless otherwise stated, all redox potentials are referenced to the ferrocenium/ferrocene (Fc^+/Fc) couple ($E_{1/2}$ +0.49V vs SCE) which was used as an internal standard; no compensation was applied for internal resistance.

For proton reduction experiments, solutions of either acetic or trifluoroacetic acid were added in small quantities amounting to 2 equivalents of acid to complex per addition.

For electrode rinsing experiments, a solution of **1** and trifluoroacetic acid (30 eq.) was held at a potential at the working electrode of -1.40 V vs SCE for 10 minutes. Maintaining the inert atmosphere, the solution was removed from the cell, the cell and electrodes were rinsed with a solution of the electrolyte in DMF, and the cell was then refilled with a solution containing only electrolyte and TFA (30 eq.) before the CV was re-recorded.

For bulk electrolysis experiments, a two compartment cell was introduced with Pt/Rh gauze electrode employed as the secondary electrode, which was separated from the working RVC electrode by a glass frit. The reference electrode employed again was the saturated calomel electrode, which was connected to the test solution by a bridge tube and placed in the centre of the working electrode. The solution was stirred vigorously during the bulk electrolysis. The potential applied was -1.40 V vs SCE for 6000s. A new electrode was applied for each new experiment to avoid build up of heterogeneous species on the electrode surface.

3.4.2.5 Dynamic Light Scattering

Dynamic Light Scattering measurements were performed using a Malvern Zetasizer Nano-ZS at room temperature.

3.4.2.6 Transmission Electron Microscopy and Energy-Dispersive X-ray Spectroscopy

An electrolysed solution of **1** in the experimental DMF solution was drop-cast onto a TEM grid (graphene oxide on holey carbon film obtained from EM Resolutions. TEM images were obtained using a JEOL 2100-F FEGTEM equipped with a Gatan Orius SC1000 camera. EDX spectroscopy was performed using an Oxford X-max 100 SDD.

3.4.2.7 Hirshfeld Surface Analysis

Molecular Hirshfeld Surfaces were generated by the program CrystalExplorer.[57]

3.4.2.8 Single Crystal X-ray Diffraction

Single crystal x-ray diffraction experiments were performed on an Oxford Diffraction SuperNova Duo Atlas diffractometer. Data was collected at 120K using monochromated Cu Kα radiation (λ = 1.54184 Å) and processed using CrysAlisPro.[58] Structures were solved using ShelXS via Direct Methods and refined by ShelXL[59] via a Least Squares method within Olex2.[60] Non-hydrogen atoms were refined anisotropically and hydrogen atoms placed at calculated positions.

Crystal Data for $C_{71}H_{133}I_7O_{32}Pd_8S_{16}$ (M =3751.23 g/mol): tetragonal, space group *P*4/mnc (no. 128), a = 16.8583(2) Å, c = 21.5805(3) Å, V = 6133.23(17) Å^3, Z = 2, T = 120(2) K, μ(CuKα) = 26.160 mm^{-1}, D_{calc} = 2.031 g/cm^3, 67149 reflections measured (6.654° ≤ 2Θ ≤ 149.734°), 3236 unique (R_{int} = 0.0717, R_{sigma} = 0.0174) which were used in all calculations. The final R_1 was 0.0545 (I > 2σ(I)) and *w*R_2 was 0.1489 (all data).

3.5 References

1. M. Frenkel, *J. Soc. Chem. Ind.*, London, 1910, **28**, 692.
2. J. Smidt, W. Hafner, R. Jira, J. Sedlmeier, R. Sieber, R. Rüttinger, and H. Kojer, *Angew. Chem.*,1959, **71**, 176-182.
3. Reinhard Jira, *Angew. Chem. Int. Ed.*, 2009, **48**, 9034–9037.
4. R. F. Heck, *J. Am. Chem. Soc.*, 1968, **90**, 5518.
5. R. F. Heck, *J. Am. Chem. Soc.*, 1968, **90**, 5526.
6. R. F. Heck, *J. Am. Chem. Soc.*, 1968, **90**, 5531.
7. R. F. Heck, *J. Am. Chem. Soc.*, 1968, **90**, 5535.
8. R. F. Heck, *J. Am. Chem. Soc.*, 1968, **90**, 5538.
9. R. F. Heck, *J. Am. Chem. Soc.*, 1968, **90**, 5542.
10. R. F. Heck, *J. Am. Chem. Soc.*, 1968, **90**, 5546.
11. R. F. Heck, *J. Am. Chem. Soc.*, 1969, **91**, 6707.
12. R. F. Heck and J. P. Nolley, *J. Org. Chem.*, 1972, **37**, 2320.
13. T. Mizoroki, K. Mori, and A. Ozaki, *Bull. Chem. Soc. Jap.*, 1971, **44**, 581.
14. B. K. Allam and K. N. Singh, *Synthesis*, 2011, 1125-1131.
15. L. Zhou, L. Wang, *Synthesis*, 2006, 2649-2652.
16. S. Li, Y. Lin, H. Xie, S. Zhang and J. Xu, *Org. Lett.*, 2006, **8**, 391-394.
17. E. A. B. Kantchev, G.-R. Peh, C. Zhang and J. Y. Ying, *Org. Lett.*, 2008, **10**, 3949-3952.
18. C. Wu and J. Zhou, *J. Am. Chem. Soc.*, 2014, **136**, 650-652.
19. B. Karimi and D. Enders, *Org. Lett.*, 2006, **8**, 1237-1240.
20. E.-I. Negishi and S. Baba, *Chem. Commun.*, 1976, 596.
21. S. Baba and E.-I. Negishi, *J. Am. Chem. Soc.*, 1976, **98**, 6729-6731.
22. E.-I. Negishi, A. O. King, and N. Okukado, *J. Org. Chem.*, 1977, **42**, 1821.
23. A. O. King, N. Okukado, and E.-I. Negishi, *Chem. Commun.*, 1977, 683.
24. N. Miyaura, K. Yamada, and A. Suzuki, *Tetrahedron Lett.*, 1979, **20**, 3437.
25. N. Miyaura and A. Suzuki, *J. Chem. Soc. Chem. Commun.*, 1979, 866.
26. L. E. Overman, M. J. Brown, S. F. McCann, *Org. Synth.* 1990, **68**, 182.
27. Y. Wang and Y. Xia, *Nano Letters*, 2004, **4** (10), 2047–2050.
28. I. Khan, K. Saeed and I. Khan, *Arabian J. Chem.*, 2017, In Press.
29. S. Zeng, K.-T. Yong, I. Roy, X.-Q. Dinh, X. Yu and F. Luan, *Plasmonics*, 2011, **6** (3), 491-506.
30. W. A. de Heer, *Rev. Mod. Phys.*, 1993, **65**, 611.
31. E. C. Dreaden, A. M. Alkilany, X. Huang, C. J. Murphy and M. A. El-Sayed, *Chem. Soc. Rev.*, 2012, **41**, 2740-2779.

32. C. N. R. Rao, G. U. Kulkarni, P. J. Thomas and P. P. Edwards, *Chem. Soc. Rev.*, 2000, **29**, 27-35.
33. S. Link and M. A. El-Sayed, *J. Phys. Chem. B*, 1999, **103**, 4212-4217.
34. S. K. Ghosh, S. Nath, S. Kundu, K. Esumi and T. Pal, *J. Phys. Chem. B*, 2004, **108** (37), 13963-13971.
35. M. Faraday, *Philos. Trans. R. Soc.*, London, 1857, **147**, 145.
36. M. S. Chen and D. W. Goodman, *Science*, 2004, **306**, 252-255.
37. M. Valden, X. Lai and D. W. Goodman, *Science*, 1998, **281**, 1647-1650.
38. I. X. Green, W. Tang, M. Neurock and J. T. Yates, *Science*, 2011, **333**, 736-739.
39. Z. Li and Q. Xu, *Acc. Chem. Res.*, 2017, **50** (6), 1449-1458.
40. F. P. Zamborini, S. M. Gross, R. W. Murray, *Langmuir*, 2001, **17**, 481-488.
41. B. Veisz and Z. Kiraly, *Langmuir*, 2003, **19**, 4817-4824.
42. M. Brust, M. Walker, D. Bethell, D. J. Schiffrin and R. Whyman, *J. Chem. Soc. Chem. Commun.*, 1994, **7**, 801-802.
43. M. Brust, J. Fink, D. Bethell, D. J. Schiffrin and C. Kiely, *J. Chem. Soc. Chem. Commun.*, 1995, **16**, 1655-1656.
44. Z. Yang, A. B. Smetana, C. M. Sorensen and K. J. Klabunde, *Inorg. Chem.*, 2007, **46**, 2427-2431.
45. Z. Yang, K. J. Klabunde and C. M. Sorensen, *J. Phys. Chem. C*, 2007, **111**, 18143-18147.
46. V. P. Ananikov, N. V. Orlov, I. P. Beletskaya, V. N. Khrustalev, M. Y. Antipin and T. V. Timofeeva, *J. Am. Chem. Soc.*, 2007, **129**, 7252-7253.
47. P. Woodward, L. F. Dahl, E. W. Abel and B. C. Crosse, *J. Am. Chem. Soc.*, 1965, **87**, 5251.
48. I. G. Dance, M. L. Scudder and R. Secomb, *Inorg. Chem.*, 1985, **24**, 1201.
49. S. A. Ivanov, M. A. Kozee, W. A. Merrill, S. Agarwal and L. F. Dahl, *Dalton Trans.*, 2002, 4105-4115.
50. C. Zhang, S. Takada, M. Kölzer, T. Matsumoto and K. Tatsumi, *Angew. Chem. Int. Ed.*, 2006, **45**, 3768-3772.
51. C. Zhang, T. Matsumoto, M. Samoc, S. Petrie, S. Meng, T. C. Corkery, R. Stranger, J. Zhang, M. G. Humphrey and K. Tatsumi, *Angew. Chem. Int. Ed.*, 2010, **49**, 4209-4212.
52. Y. Yamashina, Y. Kataoka and Y. Ura, *Inorg. Chem.*, 2014, **53**, 3558-3567.
53. P. Alemany and R. Hoffmann, *J. Am. Chem. Soc.*, 1993, **115**, 8290-8297.
54. R. Angamuthu, H. Kooijman, M. Lutz, A. L. Spek and E. Bouwman, *Dalton Trans.*, 2007, 4641-4643.
55. Q. Chen, S. Liu and J. Zubieta, *Inorg. Chem.*, 1989, **28**, 4433.
56. Q. Chen, S. Liu and J. Zubieta, *Angew. Chem. Int. Ed. Engl.*, 1988, 27.

57. M. J. Turner, J. J. McKinnon, S. K. Wolff, D. J. Grimwood, P. R. Spackman, D. Jayatilaka and M. A. Spackman, CrystalExplorer 17, 2017, University of Western Australia.
58. CrysAlisPro, 2013, Agilent Technologies UK Ltd. Oxford, UK.
59. G. Sheldrick, *Acta Crystallogr. A*, 2008, **64**, 112-122.
60. O. V. Dolomanov, L. J. Bourhis, R. J. Gildea, J. A. K. Howard and H. Puschmann, *J. Appl. Cryst.*, 2009, **42**, 339-341.

Chapter 4

Heteronuclear and Non-Palladium Tiara-like Complexes

4.1 Introduction

4.1.1 Metalloproteins and Metalloenzymes

4.1.1.1 Occurrence of Metals Within Biological Systems

It has been estimated that half of all proteins require a metal cofactor in order to function efficiently.[1-3] These metal-containing proteins, or metalloproteins, are therefore a hugely important factor in our own physiology as well as that of plant and microbial life, and have been a huge area of study since the first discovery of a protein to contain metal, myoglobin- which at the same time was also the first protein to have its structure elucidated by x-ray crystallography.[4]

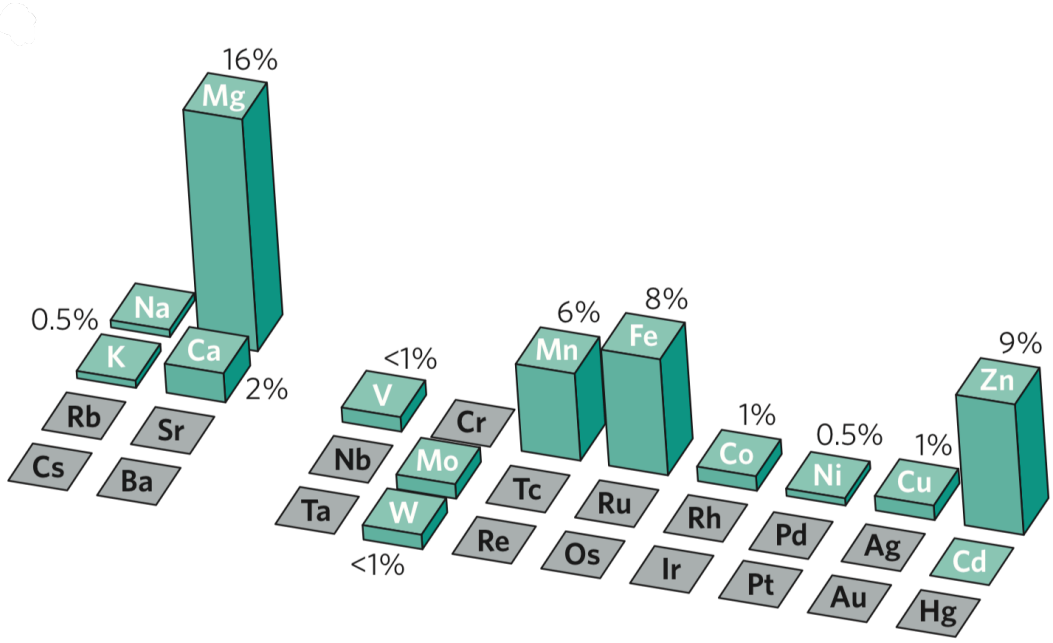


Figure 4.1: Metals utilised in biology for metalloenzyme cofactors.[2] The height of each column represents the proportion of known structures using that element. The column for cadmium represents a single known structure.[5]

All of the metals that exist in nature however, not all are found in living organisms as metal cofactors in proteins. In general, the first row transition metals (see *Figure 4.1*) are more readily observed than the second and third rows in addition to the biologically well-known alkali

metal and alkaline earth metal electrolytes: sodium, potassium, magnesium and calcium.

Magnesium, in addition to being vital as the free ion in eukaryotic cells to many metabolic activities,[6] is also the most common metal cofactor for metalloenzymes making up approximately 16% of known metalloproteins[2] and 41% of the Metal-MACie (Mechanism, Annotation and Classification in Enzymes) database.[7] Many enzymes involved in metabolic cycles such as the citric cycle and glycolytic cycle are dependent on magnesium for their operation,[8] where the divalent Mg^{2+} ion is thought to bind to protein substrates and coordinate water molecules.[9-11]

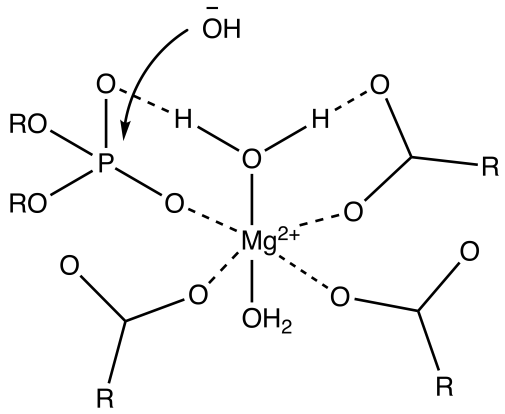


Figure 4.2: Binding of Mg^{2+} within certain metalloenzymes. R groups represent the remainder of the protein *via* glutamate and/or aspartate residues.

In these metalloenzymes the magnesium is not catalytically active but instead regulates the active site through a network of hydrogen bonding interactions, an example of this is illustrated in *Figure 4.2*. This is achieved by the small ionic radius and high charge density of the Mg^{2+} cation relative to transition metals and other alkaline earth metals such as calcium leading to preferential binding of solvent molecules rather than bulkier ligands.[8] The role of the magnesium is therefore three-fold, firstly acting as a template for the reaction, electrostatic stabilisation of transitional species and Lewis acid catalysis.[8] Magnesium is also utilised in the structure of chlorophyll, the structure of which is given in *Figure 4.3*. Chlorophyll is

ubiquitously found in plant species and is used to transform solar energy into chemical energy via photosynthesis.[12]

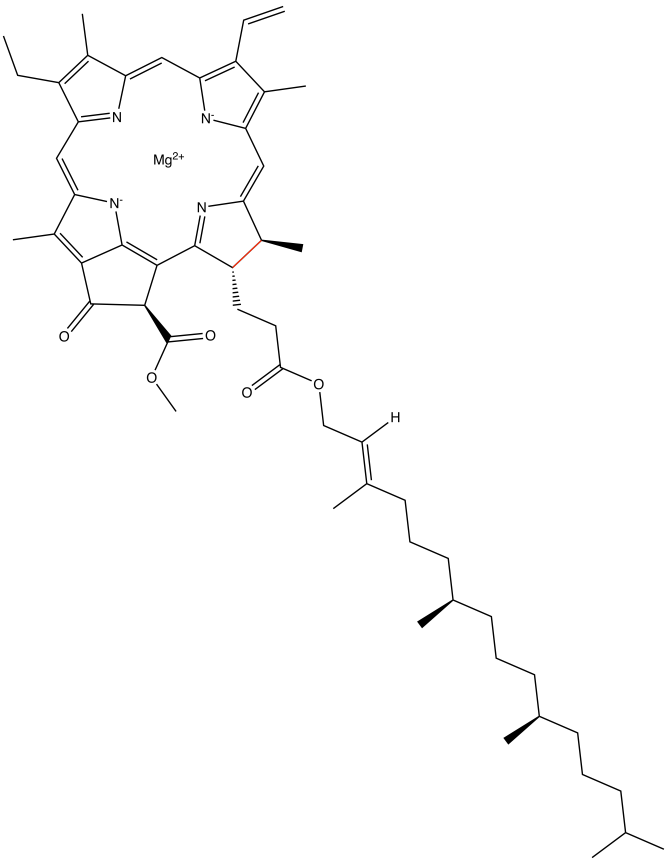


Figure 4.3: Structure of chlorophyll a. The bond in red, located at the lower right area of the ring, indicates the bond that would be oxidised in a porphyrin.

The coordination of magnesium is vital to the role of chlorophyll by alteration of the electronic properties to tune the absorption profile of the photosystems; the removal of magnesium from the ring results in the transformation of the molecule to pheophytin, which possesses UV/vis absorptions at different wavelengths.[13,14]

Chlorophyll is included within the chlorin class of molecules, related to porphyrins but slightly reduced, with the replacement of a double bond to a single bond from the porphyrin to chlorin. This difference is illustrated in *Figure 4.3* by the highlighting of the bond in question.

Porphyrins are important biological molecules in their own right, and often coordinate zinc or iron to perform their roles- these metals are the next most common metal cofactors in biology after magnesium, at 9% and 8% respectively. Iron, while possibly most famous for its use as oxygen transport and storage in the porphyrins haemoglobin and myoglobin, is also catalytically useful in the hydrogenase class of biological enzymes.

4.1.1.2 Hydrogenases

Hydrogenases catalyse a simple redox reaction, that of the reduction of two protons and two electrons to dihydrogen, and vice versa- it is possible for these enzymes to perform their reaction in reverse as necessary.[15,16] Originally the hydrogenases were divided into two classes, [FeFe]-hydrogenases and [NiFe]-hydrogenases before a third category of metal-free hydrogenases were included; these were later renamed to the [Fe]-hydrogenases as they lack a metal-sulfur cluster core but retain an iron atom within the structure.[17-19]

The active sites of the [FeFe]-hydrogenases and the [NiFe]-hydrogenases are given in *Figure 4.4*; they are similar in structure, both being coordinated by the inorganic ligands CN^- and CO along with bridging sulfides. Each active site has a single vacant coordination site on one of the two metal atoms. Beyond the active site in both enzyme classes there exist a number of cubane [Fe-S] clusters that facilitate the transfer of electrons into the protein.

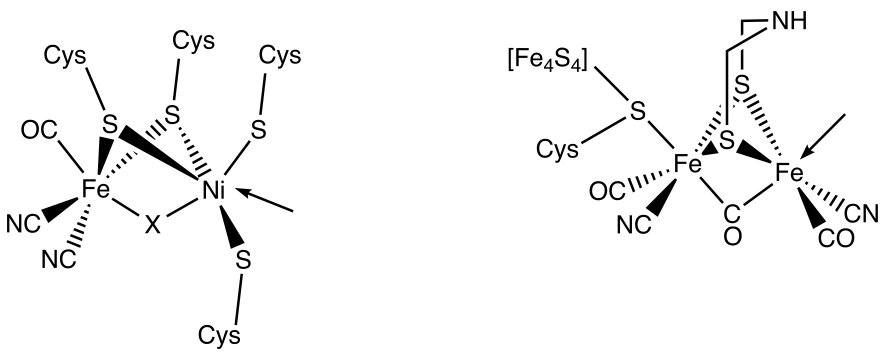


Figure 4.4: Structures of the active sites of [NiFe]-hydrogenases (left) and [FeFe]-hydrogenases (right). The arrows represent the vacant coordination site. X may represent O^{2-}, OH^-, OH_2, SO or H^-.

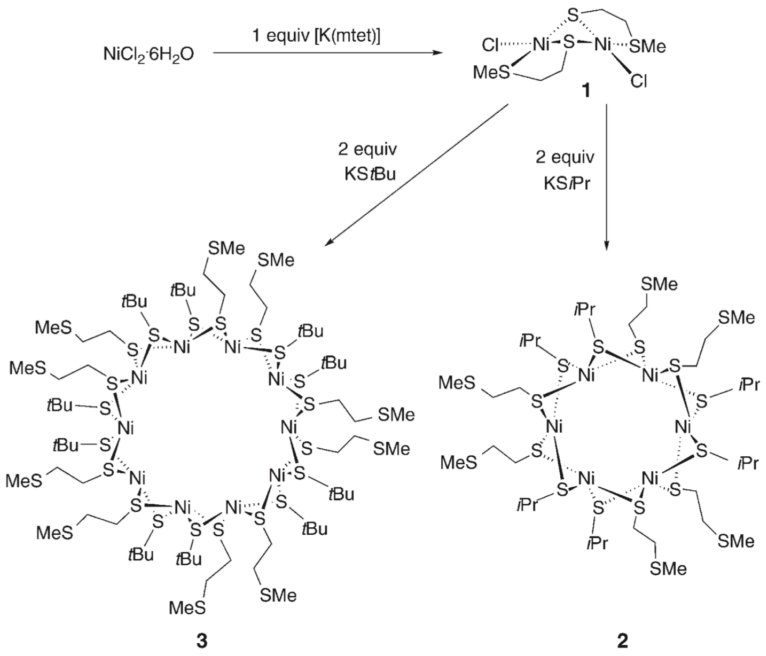
In general, while both classes of hydrogenase are capable of H_2 production via an input of energy and the consumption of H_2 to output energy, the [NiFe]-hydrogenases are more commonly oriented towards the latter purpose while the [FeFe]-hydrogenases are predominantly dihydrogen producers, shown to be capable of production of 10^4 molecules of H_2 per second at room temperature.[20,21] Due to these properties, there is great interest in developing functional dihydrogen-producing catalysts that are efficient at operating at mild conditions. Sulfide-bridged metal centres are currently being investigated as artificial structural mimics of these hydrogenase active sites, and in the case of the [NiFe]-hydrogenases the presence of a mixed metal centre is important to its function as a catalyst.

4.1.2 Mixed Ligand Tiara-like Complexes

The study of the tiara-like complexes to date has focused on variability stemming from the replacement of the thiolate SR group to create new complexes. The vast majority of tiara-like complexes use nickel as the metal and utilise a single thiolate ligand bridging the metal centres. Recently, several groups have reported new tiara-like complexes incorporating multiple different thiolate ligands into the tiara core by several methods, introducing a novel form of modification to the study of these compounds.

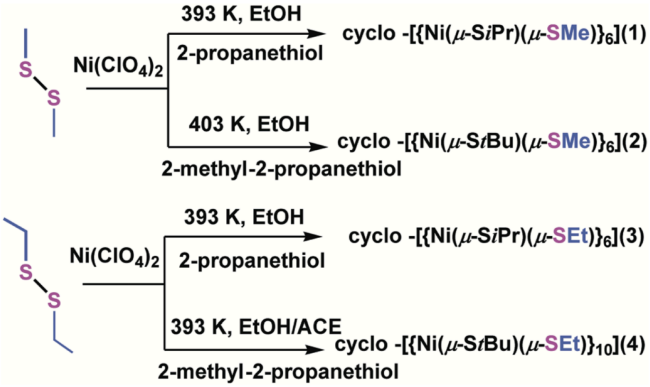
The first such reported complexes were $[Ni(\mu\text{-S}i\text{Pr})(\mu\text{-mtet})]_6$ and $[Ni(\mu\text{-S}t\text{Bu})(\mu\text{-mtet})]_{10}$, reported in 2006, where mtet = 2-methylthioethanethiolate.[22] The synthesis of these complexes is given in *Scheme 4.1* and was accomplished by introducing the ligands in a stepwise fashion to the metal; reaction of the nickel precursor salt with one equivalent of mtet resulted in the formation of $[NiCl(\mu\text{-mtet})]_2$. Following its isolation, this intermediate could be treated with two equivalents of either K(S*i*Pr) or K(S*t*Bu) to afford the hexanuclear or decanuclear tiara respectively. The resulting complexes form a structure wherein each

$[Ni(SR)_2]$ subunit comprises instead $[Ni(SR^1)(SR^2)]$ such that one ligand adopts the axial position and the other adopts the equatorial position; this minimises the steric repulsion between the bulky isopropyl or tertbutyl groups.



Scheme 4.1: Formation of $[Ni(\mu\text{-}S\textit{i}Pr)(\mu\text{-mtet})]_6$ (2) and $[Ni(\mu\text{-}S\textit{t}Bu)(\mu\text{-mtet})]_{10}$ (3).[22]

This was followed up in 2010 with the publication of the structures of the related complexes $[Ni(\mu\text{-}StBu)(\mu\text{-etet})]_{12}$, where etet = 2-ethylthioethanethiolate, $[Ni(\mu\text{-}S\textit{t}Bu)(\mu\text{-pyet})]_{10}$, where pyet = 2-(2-mercaptoethyl)pyridine, and $[Ni(\mu\text{-}S\textit{t}Bu)(\mu\text{-atet})]_{10}$, where atet = 2-aminoethanethiol.[23] In 2012, it was shown that mixed ligand tiaras could also be formed *in situ* by solvothermal synthesis (see *Scheme 4.2*). The formation of the complexes $[Ni(\mu\text{-}S\textit{i}Pr)(\mu\text{-}SMe)]_6$, $[Ni(\mu\text{-}S\textit{t}Bu)(\mu\text{-}SMe)]_6$, $[Ni(\mu\text{-}S\textit{i}Pr)(\mu\text{-}SEt)]_6$ and $[Ni(\mu\text{-}S\textit{t}Bu)(\mu\text{-}SEt)]_{10}$ was achieved by the cleavage of a disulfide bond by the high temperature of the reaction.[24]



Scheme 4.2: Solvothermal synthesis of mixed ligand tiara-like complexes. ACE = acetone[24].

This was then followed up with the publication of the related structures $[Ni(\mu\text{-EDT})]_5$, $[Ni(\mu\text{-S}i\text{Pe})_2]_6$, $[Ni_6(\mu\text{-S}t\text{Bu})_4(\mu\text{-EDT})_4]$, $[Ni_6(\mu\text{-S}t\text{Bu})_4(\mu\text{-PDT})_4]$, $[Ni_6(\mu\text{-SPh})_4(\mu\text{-EDT})_4]$ and $[Ni_6(\mu\text{-SPh})_4(\mu\text{-PDT})_4]$, where S*i*Pe = isopentylthiol, EDT = 1,2-ethanedithiol, PDT = 1,3-propanedithiol.[25] These structures, the latter two of which are shown in *Figure 4.5*, are interesting due to firstly the acquisition of the unusual pentanuclear tiara but also due to the presence of a bidentate dithiol ligand.

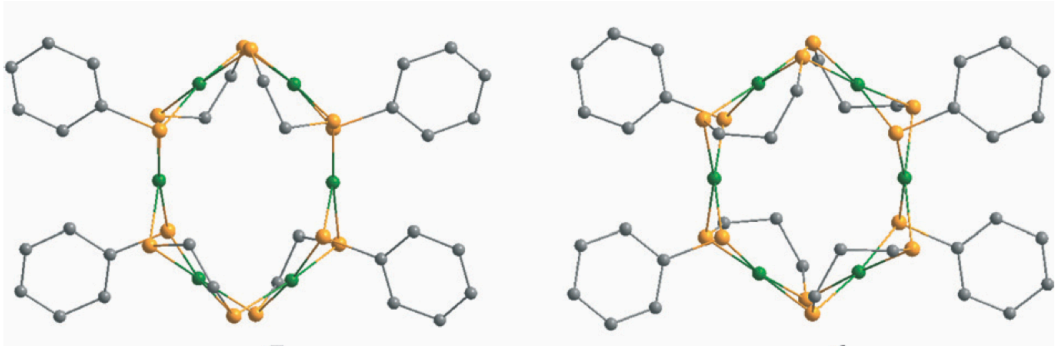


Figure 4.5: Structures of $[Ni_6(\mu\text{-SPh})_4(\mu\text{-EDT})_4]$ (left) and $[Ni_6(\mu\text{-SPh})_4(\mu\text{-PDT})_4]$ (right).[25]

These multiligand tiara-like complexes represent a promising new avenue for investigation into these compounds, as they bear a stronger degree of similarity to the active sites of metal-sulfur containing enzymes such as the hydrogenases. Further advances in this area could lead to the development of enzyme structural mimics for catalytic applications.

4.2 Results and Discussion

4.2.1 A Nickel Analog Tiara-like Complex

4.2.1.1 Synthesis of Ni MMP

The main focus of this work has been the investigation of the contribution of the ligand on determining the nuclearity of a tiara-like complex. To a lesser extent, the role of the solvent has also been investigated. However, thus far there have been few studies investigating the contribution from the metal used to the process of the self-assembly of the complex. This is quite unsurprising, however, when the number of possible metals used in the formation of these complexes is severely limited. The vast majority of structures reported between the years of 1965 and the present day have used nickel as the complex metal and palladium has been gaining in popularity in recent years. Platinum, the third Group 10 metal, has only appeared twice with the first report as recently as 2015.

There have been a few instances in previously reported literature wherein the same ligand has been used to form both a nickel-containing and a palladium-containing structure. However, the complexes have invariably been synthesised by different teams, and no great comparison has been made of the properties. *Table 4.1* summarises tiara-like complexes previously synthesised for nickel and palladium that incorporate the same ligand.

Thiolate Ligand	Nickel	Palladium
SCH_2CH_3	1965[26]	2001[27]
$SCH_2CH_2CH_3$	1992[28]	1968[29]
SPh	2002[30]	2009[31]
SCH_2CH_2Ph	2013[32]	2015[33]
SCH_2CH_2OH	1970[34]	2013[35]

Table 4.1: Tiara-like complexes containing common thiolates for both nickel and palladium and year of first reporting.

With the success in the synthesis of a number of previously unreported palladium-containing tiara-like complexes, it was decided to investigate the effect that the replacement of the metal had in the resultant formation of the complex, and examine whether or not nickel or platinum may influence the formation of a tiara-like complex of a greater (or lesser) nuclearity.

The ligand that was chosen for the experiment was methyl 3-mercaptopropionate (MMP) that was used to create complex **6** (see *Figure 4.6*). This was selected due to the observation that both signals corresponding to both hexanuclear and octanuclear tiaras had previously appeared in the MALDI mass spectrum for Pd MMP; it was therefore anticipated that even a small effect of the metal may be observable by simply comparing the relative abundance of the resultant mass spectrometry signals, or potentially by the isolation of a pure complex of a nuclearity other than six. Other factors, such as the contribution of the solvent, were assumed to be negligible for this ligand, in contrast to the synthesis of Pd NAC, which was expected to have a significant effect from the solvent.

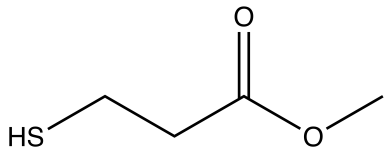


Figure 4.6: Chemical structure of methyl 3-mercaptopropionate (MMP).

The synthesis of the tiara-like complex was performed in similar conditions to that of the original Pd MMP, **6**. A dark red-brown solution was obtained which was worked up via normal protocols. Purification of the product was accomplished by crystallisation via a vapour diffusion of pentane into a saturated chloroform solution to yield deep red crystals of $[Ni(MMP)_2]_6$ (**7**).

The ^1H NMR spectrum of **7**, given in *Figure 4.7*, was expected to resemble that of **6** given the

identical ligand makeup of the complex with any small differences attributable to the nickel composition rather than palladium. However, the obtained spectrum differed significantly; instead of the expected two singlets and four triplets, instead were obtained two singlets, two triplets and a multiplet. This was attributed to a possible roofing effect that was observable to a lesser degree within the spectrum of **6**.

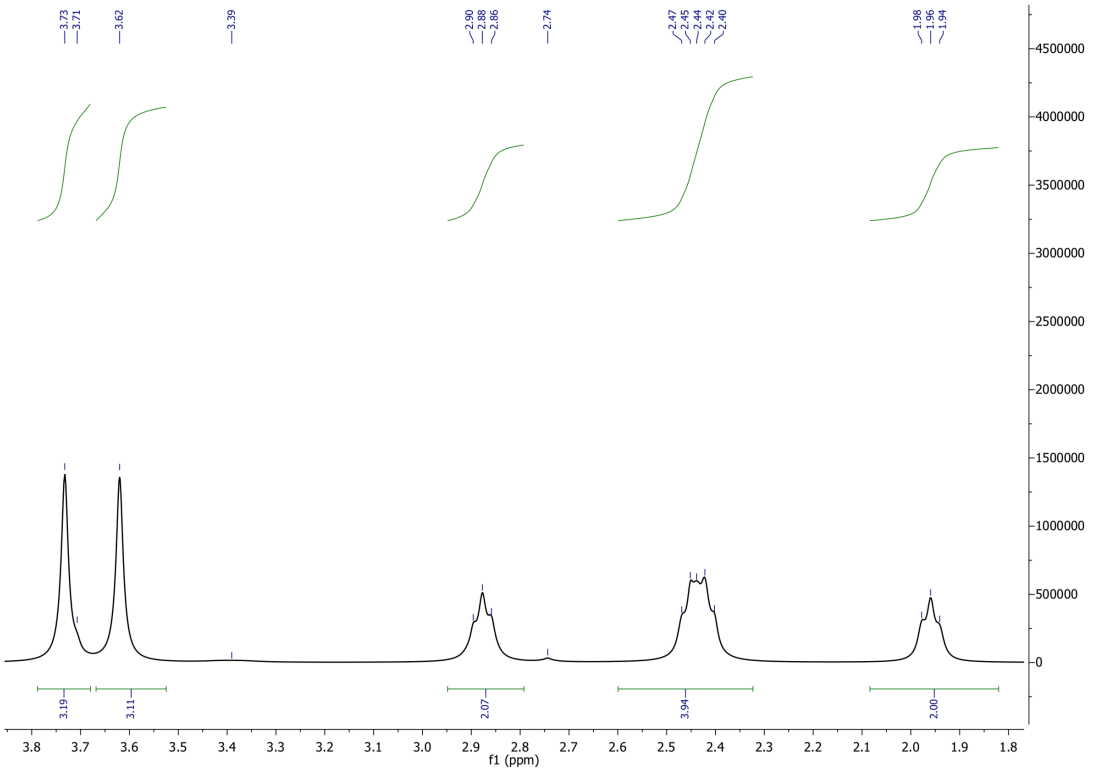


Figure 4.7: ^{1}H NMR spectrum from 1.8 ppm to 3.8 ppm of **7**. Solvent: chloroform-d, 16 scans.

4.2.1.2 Crystallography

A suitable single crystal was selected and taken for XRD analysis. Screening of the crystal suggested a space group of *P*-1, a common space group for tiara-like complexes previously synthesised but significantly lower symmetry than was obtained for the previously synthesised palladium analog **6**. Solution and refinement of the data confirmed the formation of the nickel analog of **6**, $[Ni(MMP)_2]_6$ (**7**), the crystal structure of which is shown in *Figure 4.8* and *Figure 4.9*.

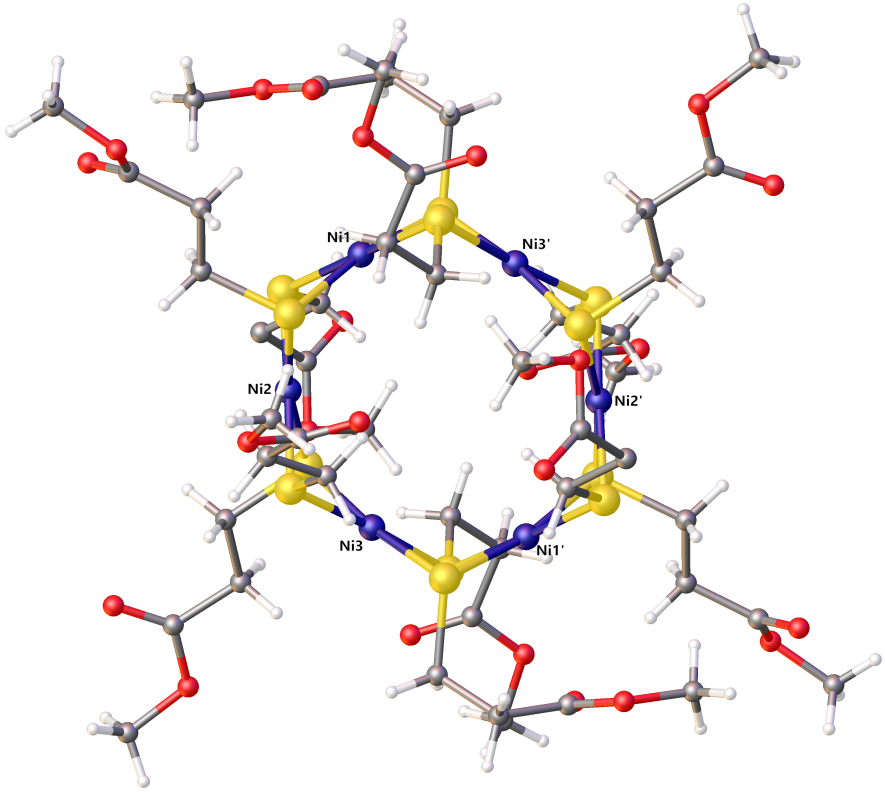


Figure 4.8: Crystal structure of **7** (top view). ' = 1-X, 1-Y, 1-Z. Atom colours: Ni-dark blue, S-yellow, C-grey, O-red, H-white.

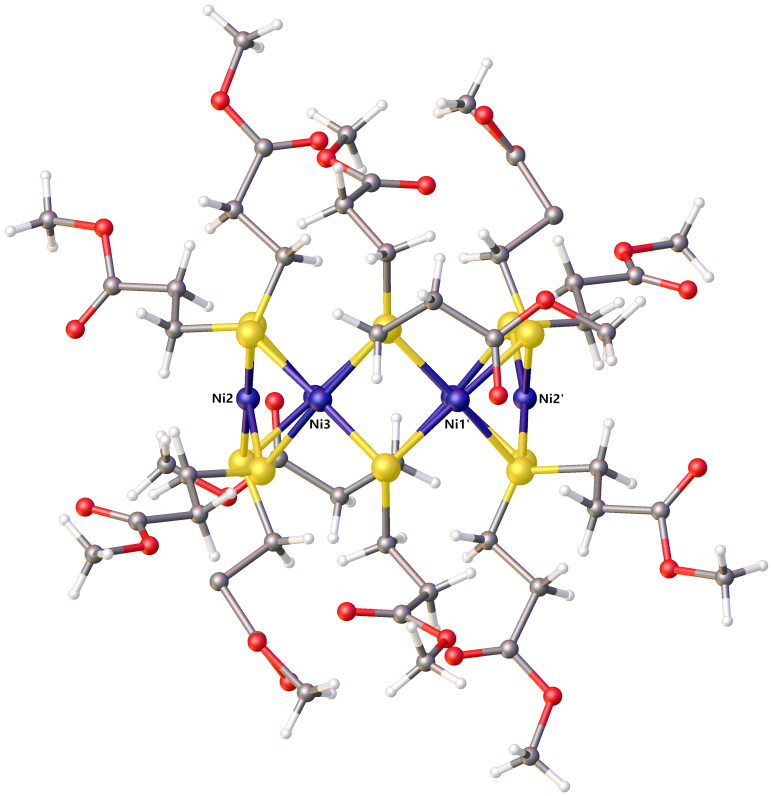


Figure 4.9: Crystal structure of **7** (side view). ' = 1-X, 1-Y, 1-Z. Atom colours: Ni-dark blue, S-yellow, C-grey, O-red, H-white.

As expected, the complex is almost structurally identical to that of **6**; crystallisation of **7** into a lower symmetry space group may be due to the differing bond angles and lengths for Ni-S over Pd-S. As noted in the crystal structure analysis of **6** in *Chapter 2.2.7.3*, the internal dimensions for **6** gives > Pd-Pd-Pd angles of exactly 120° to give an idealised symmetrical hexagon, whereas for **7** the > Ni-Ni-Ni angles are 114.6°, 120.8° and 124.6°, leading to significant distortion and adoption of a lower symmetry space group. Interestingly, this fits the earlier observation that for nickel and palladium tiara-like complexes containing ethyl thioglycolate, the palladium tiara (**2**) adopts a higher symmetry space group (*C* 2/c) than the nickel equivalent (*P*-1) (see *Chapter 2.2.3.3*).

As expected, the IR spectrum of **7**, given in *Figure 4.10*, is almost exactly identical to that of **6**. It conserves the C-H stretch at 2951 cm^{-1} and the C=O stretch occurs at 1726 cm^{-1} (1724 cm^{-1} for **6**). A broad absorption is noted at 3360 cm^{-1}; this is most likely due to water present in the compound mixture and unlikely to represent any bonds present within the true structure.

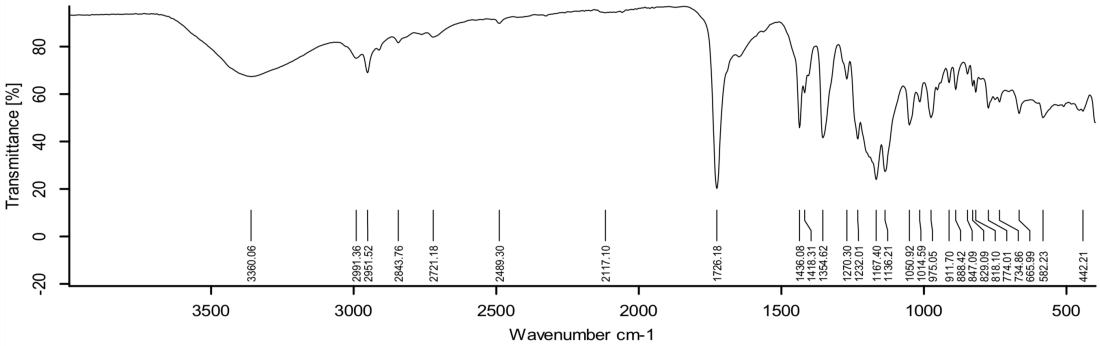


Figure 4.10: ATR-IR spectrum from 4000 cm^{-1} to 400 cm^{-1} of **7**, showing good similarity to the palladium equivalent **6**. The broad absorption at 3360 cm^{-1} may result from water in the sample.

The UV spectrum of **7**, given in *Figure 4.11*, retains the absorption maxima of its palladium analog, having sharp absorbance peaks at 267.83 nm (272.94 nm for **6**) and 407.92 nm

(412.95 nm for **6**). However, the nickel tiara also shows a strong absorbance at 335.22 nm and a weaker absorbance at 544.10 nm. These additional absorbances, covering the high energy purple to yellow region of the visible light spectrum, result in the complex developing a dark red colouration in solution, in contrast to the palladium analog, which lacks these absorbances and therefore appears to be a lighter yellow-orange in colour.

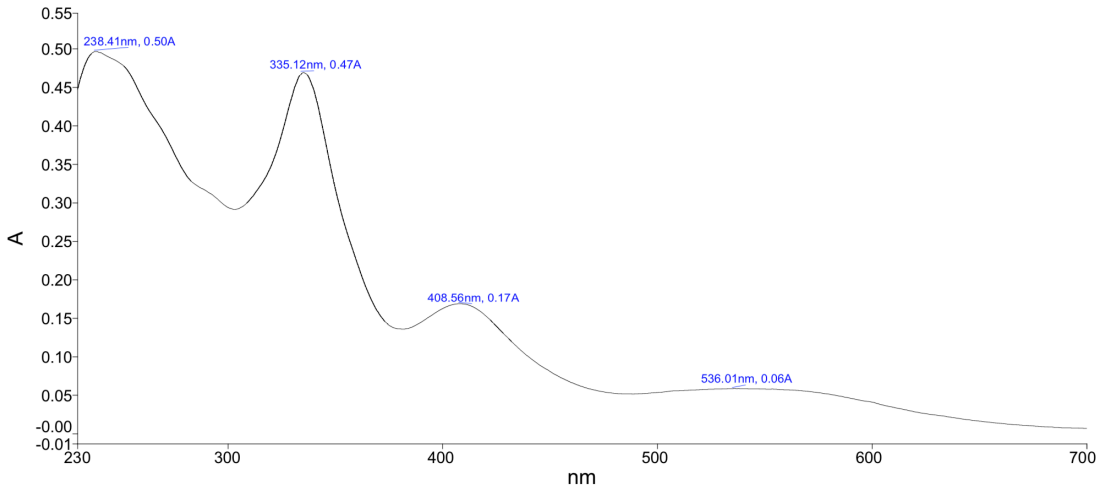


Figure 4.11: UV/vis spectrum from 230 - 700 nm of **7**. The absorbance at 536 nm absorbs UV light in the orange region of the spectrum, resulting in a red-brown colouration compared to **6**.

The extinction coefficients calculated for **7** are presented in *Table 4.2*.

λ (nm)	ε	ε / PdS_2
536.01	4,680	780
408.56	13,250	2,210
335.12	36,640	6,110
238.41	38,980	6,500

Table 4.2: UV/vis maxima and extinction coefficients for **7**

The calculated extinction coefficients, while intense, are reduced when compared to the palladium complex **6** due to the different transitions present for Ni-S and Pd-S. The combined spectra for both nickel and palladium complexes are illustrated below in *Figure 4.12*.

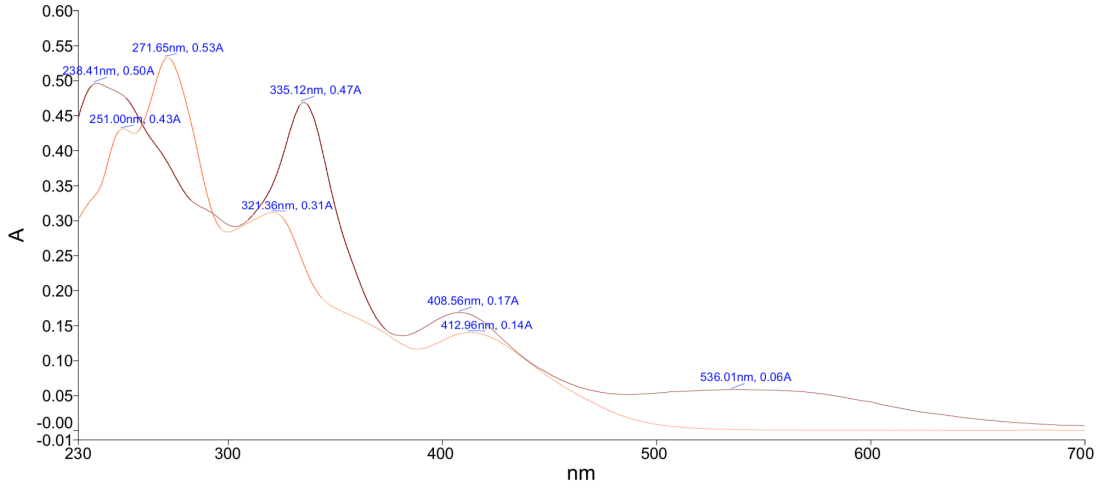
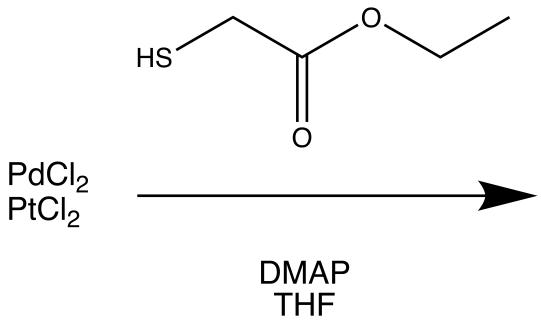


Figure 4.12: Combined UV/vis spectrafrom 230 - 700 nm for **6** and **7** . Red = **6**, orange = **7**.

4.2.2 Pd/Pt Heteronuclear Tiara-like Complexes

4.2.2.1 Heteronuclear Isomers and Purification

The first attempted heteronuclear complexes to be synthesised were designed to incorporate both palladium and platinum within the ring. This combination was selected due to the high levels of similarity between the two metals, as both share very similar physical and chemical properties, including the solubility of the respective metal (II) chloride starting materials. It was therefore hypothesised that the two metals would react with the thiol ligand at reasonably equivalent rates, resulting in a larger proportion of complexes formed from both metals.



Scheme 4.3: Proposed synthesis of mixed Pd/Pt tiaras by combining a 1 : 1 : 4 : 4 ratio of Pd : Pt : thiol : base.

The synthesis of the proposed heteronuclear complex was performed by using a 1 : 1 : 4 : 4 ratio of palladium : platinum : thiol : base (see *Scheme 4.3*). The thiol chosen was ethyl thioglycolate (ETG) given the previous success of methyl thioglycolate (MTG) at forming both a palladium-containing and a platinum-containing tiara-like complex separately.[36] The disadvantage arising from the use of this thiol was that the product formed in each case for palladium and platinum separately was the octanuclear tiara, potentially leading to the formation of a greater number of products. Unless the reaction selectively formed a single product, perhaps resulting from a particularly favourable arrangement of the metals within the ring, it was likely that the end result of the synthesis would be a statistical mix of products containing various ratios of palladium to platinum.

For a hexanuclear complex, the potential products are $[Pd_nPt_{6-n}(SR)_2]$, where $0 \leq n \leq 6$, allowing for a total of 7 possible products, whereas an octanuclear mixed tiara would give products $[Pd_nPt_{8-n}(SR)_2]$, where $0 \leq n \leq 8$, allowing for 9 products. In addition to isomerism derived from the ratio of the metals incorporated into the complexes, further isomerism results from the arrangement of the metals within the ring.

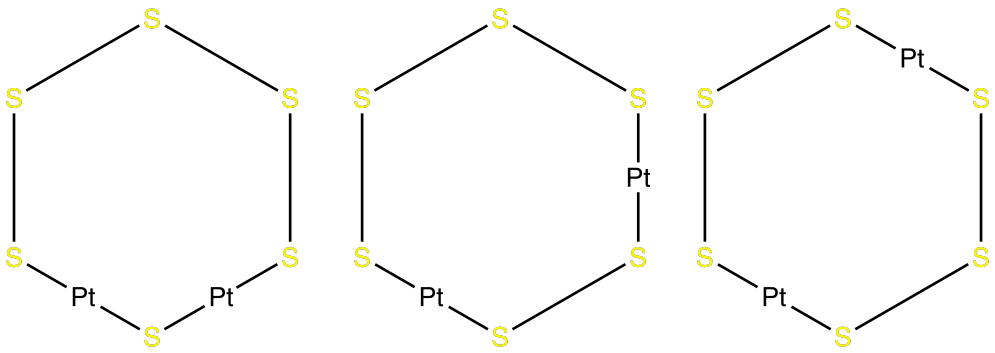


Figure 4.13: Simplified isomers possible for hexanuclear n = 4

For a hexanuclear tiara, four of the products (where n = 0, 1, 5 or 6) have only a single possible unique arrangement of the metals, whereas the other three potential products (where n = 2, 3 or 4) each have three unique arrangements, bringing the total number of potential products up to 13 possible isomers. Similarly in an octanuclear complex, four of the products where n = 0, 1, 7 or 8 have only a single isomer, but the other five have a varying number, 4 for n = 2 or 6, 5 for n = 3 or 5 and 8 for n = 4, resulting in a total of 30 unique possible isomers formed in the reaction.

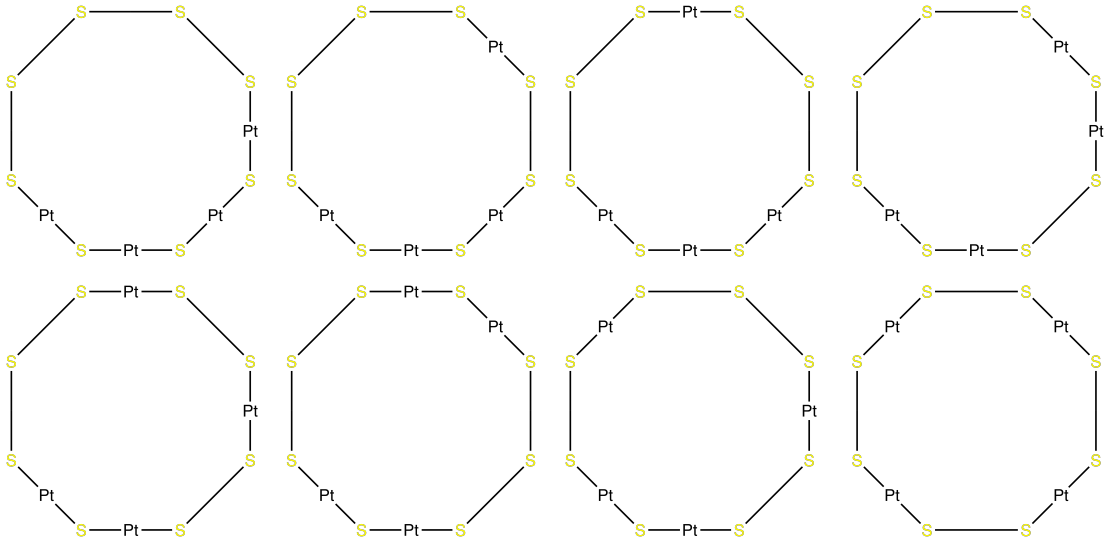


Figure 4.14: Simplified isomers possible for octanuclear n = 4.

Therefore the total number of theoretical products formed from the simultaneous reaction of palladium and platinum chlorides more than doubles from 13 to 30 on proceeding from a hexanuclear to an octanuclear tiara-like complex. Additionally, the separation of these complexes was predicted to be an even greater challenge than that of the previous separations described in *Chapter 2* due to the high similarity of palladium and platinum. Although there is an increase in the molecular weight of the complex on replacement of palladium with platinum, the dimensions of the complex remain the same, rendering size-exclusion chromatography ineffective at separating the isomers. Further to this, the isomers resulting from the arrangement of the metals with the same value of *n* are identical in molecular weight and spatial dimensions, heightening the difficulty of any separation to purify a single isomer.

However, in the example of $[Pd(MTG)_2]_8$ and $[Pt(MTG)_2]_8$, which can be considered to be isomers of $[Pd_nPt_{8-n}(SR)_2]$ where n = 8 for the former and n = 0 for the latter, the crystal structures of the two complexes showed that they adopt different conformations in the crystalline state.[36] The differences within the geometries of the two complexes may render them incompatible of co-crystallising, making it possible that the mixed isomers could be purified by crystallisation.

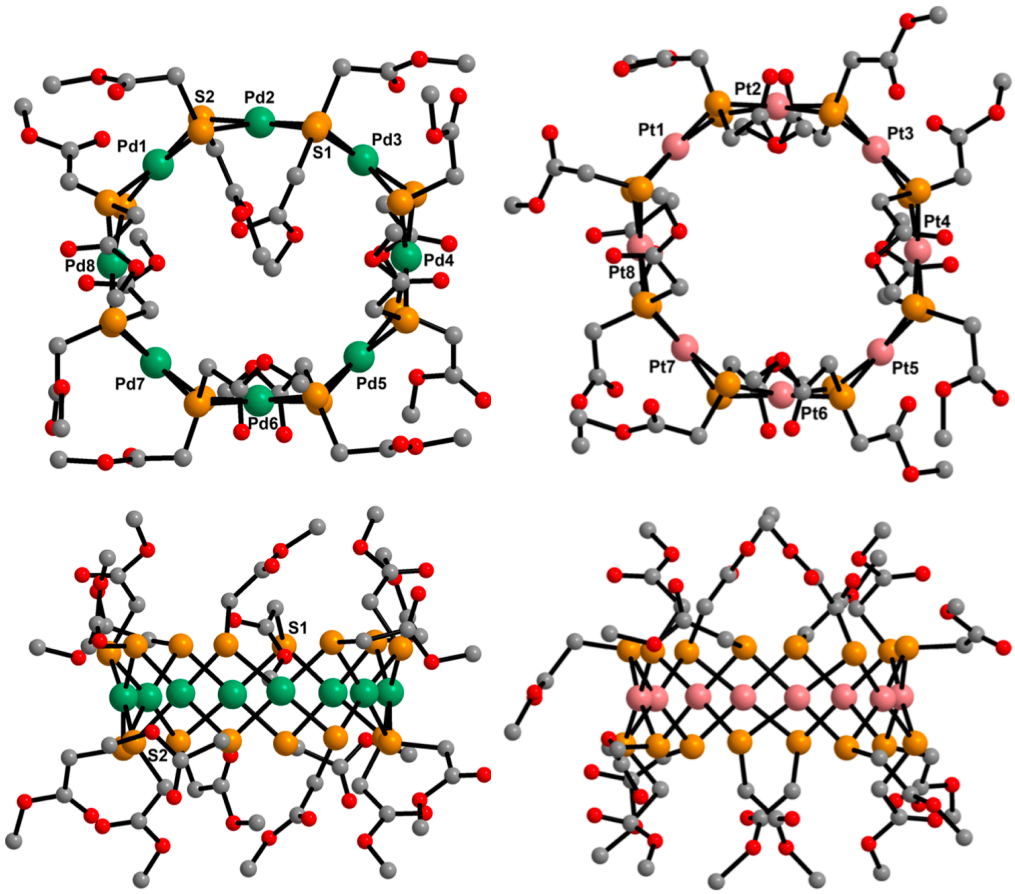


Figure 4.15: Previously synthesised complexes $[Pd(MTG)_2]_8$ (left) and $[Pt(MTG)_2]_8$ (right).[36]

With a potential solution for the purification problem outlined, it was decided to proceed with the proposed synthesis of the mixed-metal tiara-like complexes, with any resultant complexes to be purified by crystallisation.

4.2.2.2 Synthesis of mixed Pd / Pt Complexes

The initial attempt to synthesise mixed palladium-platinum tiaras was performed by mixing one equivalent each of both $PdCl_2$ and $PtCl_2$ into a solution of ethyl thioglycolate (4 equivalents) and *N*, *N*-DIEA (4 equivalents) in n-propanol at room temperature. A cloudy brown precipitate resulted on the addition of the metals but no product was observed at the end of the reaction time. Allowing the reaction to continue overnight yielded a small quantity of yellow-orange precipitate following work-up. However, no signals in the MALDI mass

spectrum could be assigned to mixed tiaras with the principal signal showing overwhelming abundance of $[Pd(ETG)_2]_8$.

Repetition of the reaction procedure via methods outlined by Yamashina *et al.* suggested a change of the reaction solvent from n-propanol to methanol and elevation of the experiment temperature to 70°C as per their original reported synthesis of $[Pt(MTG)_2]_8$. All other conditions and reagents were kept constant. In contrast to the previous experiment, a dark red solution was observed rather than a cloudy brown precipitate. The reaction was continued overnight, after which time it was cooled to afford an orange-red precipitate which was filtered. A MALDI mass spectrum, given in *Figure 4.16* of the powder revealed the acquisition of mixed palladium-platinum tiara-like complexes.

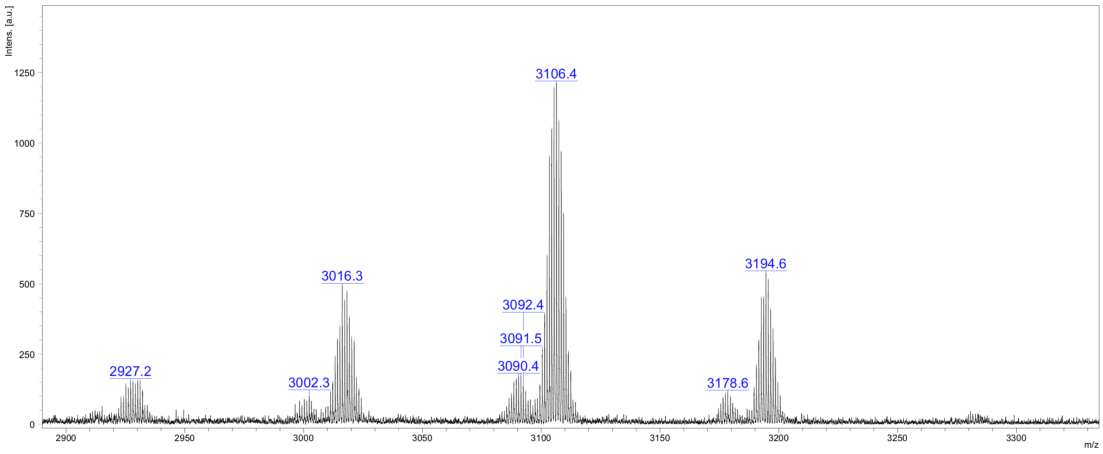


Figure 4.16: MALDI-ToF mass spectrum from 2000 m/z to 3400 m/z showing mixed palladium-platinum tiara-like complexes $Pd_6Pt_2(ETG)_{16}$ (2930.3 m/z, $[M+H]^+$, calc. 2930.6), $Pd_5Pt_3(ETG)_{16}$ (3019.3, $[M+H]^+$, calc. 3019.7 m/z), $Pd_4Pt_4(ETG)_{16}$ (3108.5, $[M+H]^+$, calc. 3108.7 m/z), $Pd_3Pt_5(ETG)_{16}$ (3197.5, $[M+H]^+$, calc. 3197.8 m/z). Matrix: DCTB, Mode: Positive.

Analysis of the signals obtained from the spectrum show peaks corresponding to complexes of the formula $[Pd_nPt_{8-n}(ETG)_{16}]$, where $2 \leq n \leq 6$, i.e. tiara-like complexes of the Pd : Pt ratios 6 : 2 (2927.2 m/z), 5 : 3 (3016.3 m/z), 4 : 4 (3106.4 m/z), and 3 : 5 (3194.6 m/z). As expected, the most abundant signal within the mass spectrum corresponds to the complex containing the 1 : 1 ratio of the two metals given the equal stoichiometry of the starting

reagents. The 3 : 5 and 5 : 3 signals are present in relatively large and similar intensity, however the 2 : 6 is of far higher intensity than the corresponding 6 : 2, which is almost non-existent within the spectrum. Tiara-like complexes of the ratios 6 : 0 and 0 : 6, i.e. homonuclear tiaras, were not observed within the spectrum, neither were the complexes of the ratios 1 : 5 and 5 : 1, most likely due to the lower probability of a single growing tiara-like chain encountering successive metals of the same element. Therefore, it appears that the reaction products adopt a statistical result, wherein a growing tiara oligomer chain has an equal probability of encountering, and reacting with, either a palladium monomer or a platinum monomer. The observed ratio of products does support the hypothesis that the palladium and platinum reagents react at roughly equivalent rates within the reaction; as weighted products towards homonuclear tiaras (6 : 0 and 0 : 6) would be expected to be observed at a greater abundance if the metal monomers reacted at different rates.

Crystallisation of the tiara mixture resulted in orange block crystals which were screened for single crystal x-ray diffraction analysis, which suggested a space group of $P2_1/n$, a marked difference from the space group of *F*dd2 for $[Pd(MTG)_2]_8$ and *P*-1 for $[Pt(MTG)_2]_8$, suggesting a different composition to both. The structure was solved, however refinement proved difficult. The solution indicated a tiara core distorted from the octagonal geometry of **2**, as shown in *Figure 4.17*.

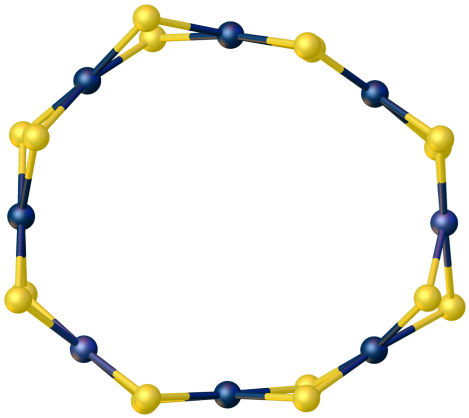


Figure 4.17: Distorted tiara core observed in the crystal structure. Ligands omitted for clarity. Atom colours: Pd-dark blue, S-yellow.

It was thought that the challenge in attempting refinement to convergence resulted from the crystallisation of multiple isomers within the crystal lattice with small differences in bond lengths and angles to show average values. Further, due to the significant probability discussed previously that isomerism in the complexes could also result from the arrangement of the metals within the ring, averaging of the isomers present in the lattice into a single statistical structure would render it impossible to identify any single isomers crystallographically. It was therefore surmised that no definitive conclusions could be drawn from further analysis of the crystal structure, and the refinement did not progress any further due to this and difficulty in achieving convergence.

Despite this setback, it was of interest to examine whether or not the initial statistical mixture of tiara-like complexes could be influenced by a change in the stoichiometry of the starting reagents, as a 1 : 1 ratio of metals resulted in a predominantly 1 : 1 ratio product complex. A change in the starting materials from a 1 : 1 ratio of Pd : Pt to a 3 : 1 ratio was used and methyl thioglycolate was used in place of ethyl thioglycolate due to circumstance; this was not expected to have a significant effect on the distribution. Differences were seen within the mass spectrometry analysis of the crude product. The mass spectrum from the reaction is given in *Figure 4.18*.

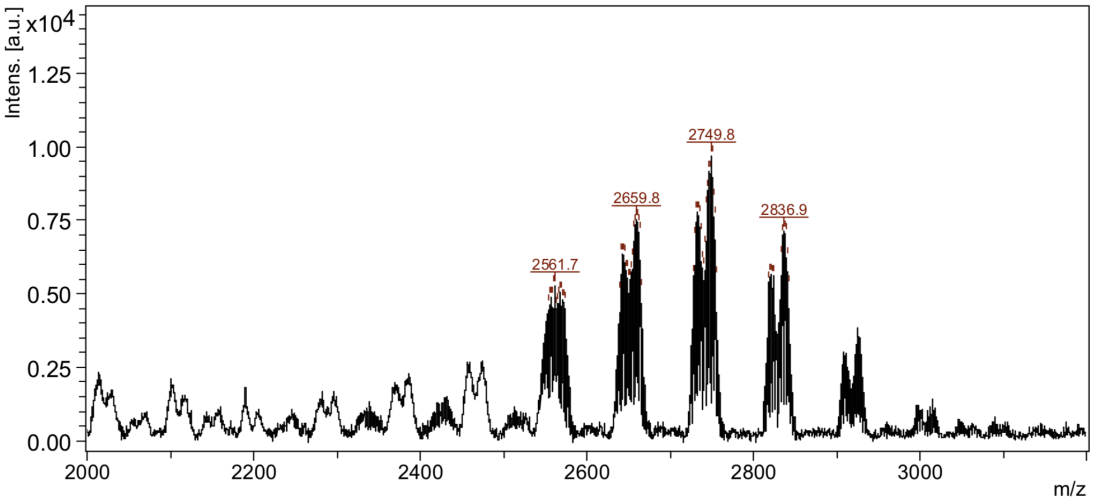


Figure 4.18: MALDI-ToF mass spectrum from 2400 m/z to 3100 m/z of the 3 : 1 crude mixture of Pd : Pt, showing $Pd_8(MTG)_{16}$ (2566.7 m/z, $[M+K]^+$, calc. 2566.2 m/z), $Pd_7Pt_1(MTG)_{16}$ (2655.8 m/z, $[M+K]^+$, calc. 2655.3), $Pd_6Pt_2(MTG)_{16}$ (2744.8 m/z, $[M+K]^+$, calc. 2744.3), $Pd_5Pt_3(MTG)_{16}$ (2833.9 m/z, $[M+K]^+$, calc. 2833.4) and $Pd_4Pt_4(MTG)_{16}$ (2922.9 m/z, $[M+K]^+$, calc. 2922.5). Matrix: DCTB, Mode: Positive.

Analysis of the resulting spectrum suggested that the primary product of the reaction the expected product, $[Pd_6Pt_2(MTG)_{16}]$, i.e. a tiara-like complex containing the 6 : 2 (or simplified, the 3 : 1) ratio of metals. The range of products extends from the homonuclear palladium tiara (i.e. ratio 8 : 0) to the 5 : 3 complex; no complexes containing a higher ratio of platinum were observed. Despite again obtaining a mixture of products, the observation that the product most likely to be present in the highest abundance was the complex containing the same ratio of metals as present in the starting reagents, was a promising result, and a further experiment was designed to examine whether a predominantly platinum-containing tiara could be obtained by the same method. The same reaction was repeated with modification of the starting ratio of metals to a Pd : Pt ratio of 1 : 7.

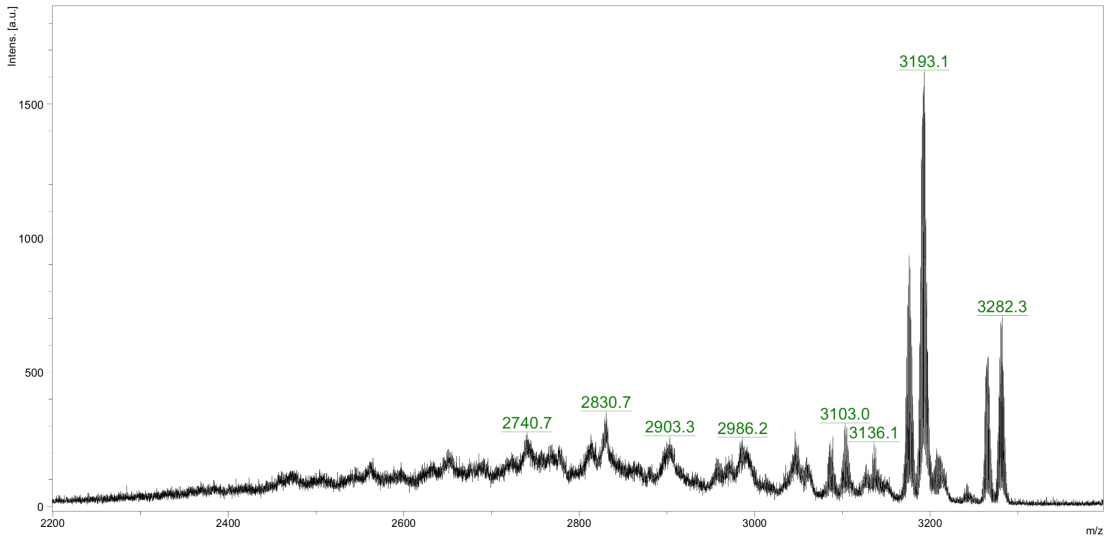


Figure 4.19: MALDI-ToF mass spectrum from 2200 m/z to 3400 m/z of the 1 : 7 Pd : Pt mixture showing $Pd_3Pt_5(ETG)_{16}$ (3197.2 m/z, $[M+H]^+$, calc. 3197.8) and $Pd_2Pt_6(ETG)_{16}$ (3286.3 m/z, [M+H]+, calc. 3286.9).

The mass spectrum (see *Figure 4.19*) indicated that the predominant product was likely to be the tiara-like complex containing a 3 : 5 ratio of Pd : Pt. This was somewhat unexpected, as the anticipated primary product had been expected to be the 1 : 7 complex. Other unusual features noted in the spectrum were the lack of complexes containing a ratio of platinum higher than 2 : 6, as homonuclear platinum tiaras had been expected to form in the reaction. However, despite the presence of signals corresponding to tiara-like complexes containing a greater proportion of palladium, the difference in intensity of the primary product and the remainder of the complexes was significantly greater for the 3 : 5 complex. To examine whether this product could be separated by crystallisation, single crystals were grown from a saturated chloroform solution over a few weeks. Screening of a suitable crystal suggested a space group of *P*-1, similar to that of the homonuclear platinum octanuclear tiara. However, due to the continuing difficulties in achieving convergence due to either poor data quality or unresolvable errors due to the isomerisation, refinement was not completed. The solved structure of the tiara core is given in *Figure 4.20*.

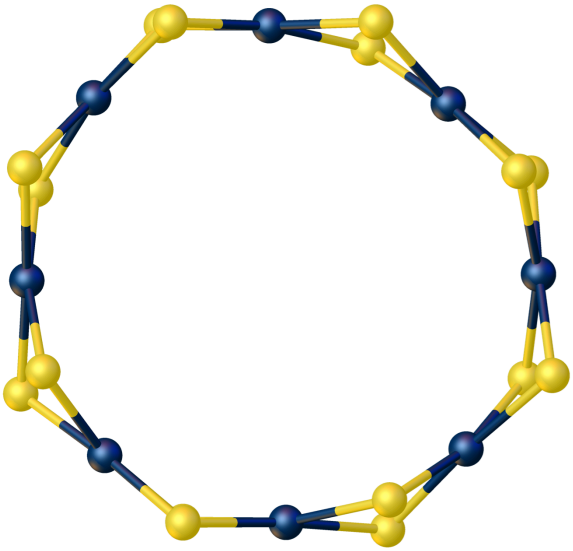


Figure 4.20: Tiara core observed in the crystal structure. Ligands omitted for clarity. Atom colours: Pd-dark blue, S-yellow.

The initial sizing of the unit cell suggested similar, but not identical values to that of the homonuclear platinum tiara-like complex.[36] A table of unit cell dimensions for the homonuclear platinum tiara-like complex, a series of inclusion complexes reported by Yamashina *et al.* and the cell screened for the crystals grown from the crude reaction mixture of the primary 3 : 5 tiara product, is given in *Table 4.3*.

	Pt	. CH_2Cl_2	. $ClCH_2CH_2Cl$	. CH_2Br_2	(3 : 5)
Space group	*P*-1	*P*-1	*P*-1	*P*-1	*P*-1
a/Å	14.8597(8)	14.972(5)	14.874(5)	15.009(5)	14.7907(3)
b/Å	15.0719(7)	15.233(5)	15.160(5)	15.279(5)	15.0567(2)
c/Å	21.3777(10)	21.264(5)	20.963(7)	21.271(5)	20.8262(4)
α/°	103.3212(11)	102.981(5)	102.418(4)	103.088(5)	102.567(1)
β/°	97.069(2)	98.033(5)	97.522(8)	97.974(5)	97.360(2)
γ/°	101.2611(15)	102.249(5)	101.807(3)	102.537(5)	101.920(1)
V/$Å^3$	4497.9(4)	4528(2)	4442(2)	4546(2)	4355.93(14)
Z	2	2	2	2	2

Table 4.3: Comparison of unit cell dimensions for platinum-containing tiara-like complexes. From left to right: $[Pt(MTG)_2]_8$, inclusion complexes with dichloromethane, 1,2-dichloroethane, dibromomethane and crude mixture of 3 : 5 heteronuclear palladium : platinum tiara.

The results obtained for the attempted heteronuclear tiara are very similar to those reported for the homonuclear platinum tiara-like complex and related inclusion complexes. All adopt the *P*-1 space group with similar unit cell axes and Z = 2. In contrast, for the homonuclear palladium analog of this complex, $[Pd(MTG)_2]_8$, the structure of the emptied complex and the structures of all inclusion complexes reported were solved in the space group *F*dd2. Comparison of the mixed tiara product obtained here with the reported data for homonuclear palladium and platinum complexes therefore suggests a predominantly platinum composition of the crystals grown from the mixed complexes.

While purification of these heteronuclear tiara-like complexes has yet to be reliably demonstrated, due in most part to the extreme difficulties presented by the isomerisation of the complexes outlined at the beginning of this chapter, this work has demonstrated that it is possible to synthesise such complexes and even to an extent influence the composition of the resultant tiaras by modifying the conditions of the reaction. Further research into potential separation or purification of a mixture of tiara-like complexes is needed.

4.3 Conclusions

A nickel analog of the palladium methyl 3-mercaptopropionate (Pd MMP, **6**) tiara-like complex described in *Chapter 2* has been synthesised and characterised, with comparative properties. The core of the tiara is significantly distorted on replacement of the palladium atoms with nickel such that the internal angles of the nickel tiara adopt the values of > Ni-Ni-Ni 114.6°, 120.8° and 124.6° which result in the adoption of a lower symmetry space group of *P*-1 from *R*-3 for the palladium tiara.

The IR spectrum shows good agreement with the palladium analog tiara **6** with no inconsistencies between the two sets of data. In contrast, the UV data shows a significant change; two additional maxima at 335 and 554 nm result in a strong absorbance across the high energy visible light spectrum, resulting in a deep red colouration. These differences are thought to arise from the energetically lower lying 3d electron orbitals for nickel allowing for different transitions to the comparatively higher energy 4d orbitals for the palladium tiaras.

Mixed metal palladium / platinum tiara-like complexes have also been shown to exist experimentally by mass spectrometry when a suspension of palladium chloride and platinum chloride is treated with the thiol methyl thioglycolate. When the metals are combined with a ratio of 1:1, the resulting spectrum shows a distribution of products corresponding to $[Pd_nPt_{8-n}(SR)_2]$, where $2 \leq n \leq 6$. The major product within the spectrum is the 1:1 complex, of which there are eight possible structural isomers. No homonuclear tiara-like complexes (n = 0 or n = 8, $[Pd(SCH_2COOCH_3)_2]_8$ and $[Pt(SCH_2COOCH_3)_2]_8$) were detected, suggesting that the distribution of products follows a statistical pattern wherein the growing tiara chain has an equal probability of encountering a palladium or a platinum reactive centre and indicating that both metals react at a similar rate. Two crystal structures of the products were solved but refinement to convergence proved challenging, most likely due to the number of unique

isomers present. Nevertheless, the rough data suggested a high degree of disorder within the tiara core, which is consistent with the isomerisation.

When the ratio of starting components is altered, the distribution of products is likewise altered. Changing of the ratio to 3:1 palladium : platinum resulted in the major product within the mass spectrum becoming the 3:1 complex, indicating that the products obtained can be modified by the changing of the reaction conditions. Homonuclear palladium tiara-like complexes were also observed at this stage. A ratio of starting materials at 1:7 however gave the majority of product as the 3 : 5 tiara with no homonuclear platinum tiara-like complexes observed. Crystallisation of the reaction products suggested a unit cell similar, but not identical to the homonuclear tiara-like complex reported in the literature,[36] supporting the high platinum content of the mass spectrum.

The results of these syntheses may further corroborate the theory that these complexes are stable once formed and do not form an equilibrium between interconverting sizes in solution. In a stability experiment, heating of a homonuclear palladium tiara-like complex in a solution of platinum chloride showed no acquisition of mixed complexes by mass spectrometry.

4.4 Experimental

4.4.1 Materials

All reagents were purchased from commercial suppliers (Sigma-Aldrich or VWR international) and used without further purification. All solvents were degassed by bubbling through N_2 for at least 10 minutes prior to use.

4.4.2 Spectroscopic Methods

4.4.2.1 NMR Spectroscopy

^{1}H NMR experiments were recorded using a Bruker AV(III)400. Chemical shifts are reported relative to the $CDCl_3$ residual peak at 7.26 ppm. For ^{1}H spectroscopy, splitting patterns are described in brackets after the chemical shift (s=singlet, t=triplet, q=quartet, bs=broad singlet, m=multiplet), followed by the number of protons and the proton assignation.

4.4.2.2 Single Crystal X-ray Diffraction

The data was collected on a XtaLAB Pro: Kappa single diffractometer. Data was collected at 120K using monochromated CuKα radiation (λ = 1.54184 Å) and processed using CrysAlisPro.[37] Structures were solved by ShelXT using Intrinsic Phasing and refined by ShelXL[38] via a Least Squares method within Olex2.[39] Non-hydrogen atoms were refined anisotropically and hydrogen atoms placed at calculated positions.

4.4.2.3 Mass Spectrometry

MALDI-ToF mass spectra were recorded with a Bruker Ultraflex III mass spectrometer. Trans-2-[3-(4-tert-butylphenyl)-2-methyl-2-propenylidene]-malononitrile was used as the matrix and sodium trifluoroacetate was used as a cationising agent where necessary.

4.4.3 Synthesis of Tiara-like Complexes

*4.4.3.1 Synthesis of Ni MMP (**7**)*

$NiCl_2.6H_2O$ (100 mg, 0.42 mmol) was added to 5ml methanol and stirred to dissolution. To this solution was added sequentially *N,N*-diisopropylethyl amine (146 µl, 0.84 mmol) and methyl 3-mercaptopropionate (93 µl, 0.84 mmol). Upon addition of the thiol, an immediate colour change from light green to deep red/brown was observed. The solution was stirred continuously for 4 hours before removal of the solvent. The sticky deeply coloured red-brown product was dissolved in CH_2Cl_2 before being washed with NaOH (0.1M), brine and dried over magnesium sulfate. Single crystals for characterisation were grown by vapour diffusion of pentane into a saturated chloroform solution. ^{1}H NMR (400MHz, $CDCl_3$) δ 3.73 (s, 3H, CH_3), 3.62 (s, 3H, CH_3), 2.88 (t, 2H, α-CH_2), 2.44 (m, 4H, α-CH_2, β-CH_2), 1.96 (t, 2H, β-CH_2). MS MALDI (+) ($CHCl_3$, DCTB/MeCN) m/z 1805.0 $[M+Na]^+$.

4.4.3.2 General Method for synthesis of mixed Pd/Pt Tiara-like Complexes

Mixed Pd/Pt tiara-like complexes were synthesised according to a general procedure. To a solution of *N,N*-diisopropylethyl amine and methyl thioglycolate in methanol at 70°C, $PdCl_2$ and $PtCl_2$ were simultaneously added and the mixture stirred under reflux overnight. After removal of the solvent, the resultant brown solids were washed with NaOH (0.1M), brine and dried over magnesium sulfate.

4.4.3.3 Attempted synthesis of 1:1 Pd/Pt Tiara-like Complexes

The general procedure was followed using *N,N*-diisopropylethyl amine (195 µl, 1.12 mmol), methyl thioglycolate (100 µl, 1.12 mmol), $PdCl_2$ (50 mg, 0.28 mmol), and $PtCl_2$ (75 mg, 0.28 mmol) in methanol (10 ml).

4.4.3.4 Attempted synthesis of 3:1 Pd/Pt Tiara-like Complexes

The general procedure was followed using *N*,*N*-diisopropylethyl amine (195 µl, 1.12 mmol), methyl thioglycolate (100 µl, 1.12 mmol), $PdCl_2$ (74 mg, 0.42 mmol), and $PtCl_2$ (37 mg, 0.14 mmol) in methanol (10 ml).

4.4.3.5 Attempted synthesis of 1:7 Pd/Pt Tiara-like Complexes

The general procedure was followed using *N*,*N*-diisopropylethyl amine (390 µl, 2.24 mmol), methyl thioglycolate (200 µl, 2.24 mmol), $PdCl_2$ (25 mg, 0.14 mmol), and $PtCl_2$ (262 mg, 0.98 mmol) in methanol (20 ml).

4.4.4 Crystallographic data

4.4.4.1 Crystal data for ***7***

Single crystals suitable for XRD analysis were grown by slow diffusion of pentane into a saturated chloroform solution.

Crystal Data for $C_{48}H_{80}Ni_6O_{24}S_{12}$ (M =1778.10 g/mol): triclinic, space group *P*-1 (no. 2), a = 10.97710(10) Å, b = 11.88400(10) Å, c = 15.30520(10) Å, α = 106.5090(10)°, β = 101.8710(10)°, γ = 101.2830(10)°, V = 1803.33(3) $Å^3$, Z = 1, T = 120(2) K, μ(CuKα) = 5.538 mm^{-1}, D_{calc} = 1.637 g/cm^3, 19148 reflections measured (8.06° ≤ 2Θ ≤ 154.756°), 7349 unique (R_{int} = 0.0185, R_{sigma} = 0.0135) which were used in all calculations. The final R_1 was 0.0362 ($I > 2\sigma(I)$) and wR_2 was 0.0965 (all data).

4.5 References

1. J. Finkelstein, *Nature*, 2009, **460**, 813.
2. K. J. Waldron, J. C. Rutherford, D. Ford and N. J. Robinson, *Nature*, 2009, **460**, 823-830.
3. A. J. Thomson and H. B. Gray, *Curr. Opin. Chem. Biol.*, 1998, **2**, 155-158.
4. M. G. Rossmann, *Protein Sci.*, 1994, **3** (10), 1731-1733.
5. T. W. Lane, M. A. Saito, G. N. George, I. J. Pickering, R. C. Prince and F. M. Morel, *Nature*, 2005, **435**, 42.
6. F. I. Wolf, A. Torsello, S. Fasanella and A. Cittadini, *Mol. Aspects Med.*, 2003, **24**, 11-26.
7. C. Andreini, I. Bertini, G. Cavallaro, G. L. Holliday and J. M. Thornton, *Bioinformatics*, 2009 **25**, 2088-2089.
8. J. A. Cowan, *BioMetals*, 2002, **15** (3), 225-235.
9. J. A. Cowan, *Chem. Rev.*, 1998, **98** (3), 1067-1088.
10. J. A. Cowan, *Inorg. Chem.*, 1991, **30**, 2740-2747.
11. J. A. Cowan, *Inorg. Chim. Acta*, **275-276**, 24-27.
12. B. Kräutler and P. Matile, *Acc. Chem. Res.*, 1999, **32**, 35-43.
13. R. Livingstone, R. Pariser, L. Thompson and A. Weller, *J. Am. Chem. Soc.*, 1953, **75** (12), 3025-3026.
14. V. V. Klimov, *Photosynth. Res.*, 2003, **76**, 247-253.
15. W. Lubitz, H. Ogata, O. Rüdiger and E. Reijerse, *Chem. Rev.*, 2014, **114**, 4081-4148.
16. P. M. Vignais and B. Billoud, *Chem. Rev.*, 2007, **107**, 4206-4272.
17. S. Shima and R. K. Thauer, *Chem. Rec.*, 2007, **7**, 37-46.
18. P. M. Vignais, B. Billoud and J. Meyer, *FEMS Microbiol. Rev.*, 2001, **25**, 455-501.
19. J. C. Fontecilla-Camps, A. Volbeda, C. Cavazza and Y. Nicolet, *Chem. Rev.*, 2007, **107**, 4273-4303.
20. R. Cammack, *Nature*, 1999, **397**, 214-215.
21. E. C. Hatchikian, N. Forget, V. M. Fernańdez, R. Williams and R. Cammack, *Eur. J. Biochem.*, 1992, **209**, 357-365.
22. C. Zhang, S. Takada, M. Kölzer, T. Matsumoto and K. Tatsumi, *Angew. Chem. Int. Ed.*, 2006, **45**, 3768-3772.
23. C. Zhang, T. Matsumoto, M. Samoc, S. Petrie, S. Meng, T. C. Corkery, R. Stranger, J. Zhang, M. G. Humphrey and K. Tatsumi, *Angew. Chem. Int. Ed.*, 2010, **49**, 4209-4212.
24. C. Tan, M. Jin, X. Ma, Q. Zhu, Y. Huang, Y. Wang, S. Hu, T. Sheng and X. Wu, *Dalton Trans.*, 2012, **41**, 8472-8476.

25. C. Tan, M. Jin, H. Zhang, S. Hu, T. Sheng and X. Wu, *CrystEngComm*, 2015, **17**, 5110-5115.
26. P. Woodward, L. F. Dahl, E. W. Abel and B. C. Crosse, *J. Am. Chem. Soc.*, 1965, **87**, 5251-5253.
27. A. I. Stash, T. I. Perepelkova, Y. G. Noskov, T. M. Buslaeva and I. P. Romm, *Russ. J. Coord. Chem.*, 2001, **27**, 585-590.
28. M. Kriege and G. Henkel, *Z. Naturforsch. B*, 1987, **42**, 1121-1128.
29. N. G. Kunchur, *Acta Crystallogr. B.*, 1968, **24**, 1623-1633.
30. S. A. Ivanov, M. A. Kozee, M. W. Alex, S. Agarwal and L. F. Dahl, *J. Chem. Soc. Dalton Trans.*, 2002, 4105-4115.
31. A. I. Stash, V. V. Levashova, S. A. Lebedev, Y. G. Hoskov, A. A. Mal'kov and I. P. Romm, *Russ. J. Coord. Chem.*, 2009, **35**, 136-141.
32. H. N. Kagalwala, E. Gottlieb, G. Li, T. Li, R. Jin and S. Bernhard. *Inorg. Chem.*, 2013, **52**, 9094-9101.
33. J. Chen, L. Liu, L. Weng, Y. Lin, L. Liao, C. Wang, J. Yang and Z. Wu, *Sci. Rep.*, 2015, **5**, 16628-16635.
34. R. O. Gould and M. M. Harding, *J. Chem. Soc. A.,* 1970, 875-881.
35. K. T. Mahmudov, X. I. Hasanov, A. M. Maharramov, A. N. Azizova, K. Q. Ragimov, R. K. Askerov, A. N. Kopylovich, Z. Ma and A. J. L. Pombeiro, *Inorg. Chem. Comm.*, 2013, **29**, 37-39.
36. Y. Yamashina, Y. Kataoka and Y. Ura, *Inorg. Chem.*, 2014, **53**, 3558-3567.
37. CrysAlisPro, 2013, Agilent Technologies UK Ltd. Oxford, UK.
38. G. Sheldrick, *Acta Crystallogr. A*, 2008, **64**, 112-122.
39. O. V. Dolomanov, L. J. Bourhis, R. J. Gildea, J. A. K. Howard and H. Puschmann, *J. Appl. Cryst.*, 2009, **42**, 339-341.

Chapter 5

Conclusions and Future Work

5.1 Conclusions

5.1.1 General Summary of Thesis

Tiara-like complexes are perhaps the quintessential class of metal-thiolate complexes; composed of generally at least six [MS_4] metal centres, they possess very little extraneous composition. Their organic make-up arises from the remainder of the thiolate ligands attached to the central core, which possess a very high potential for modification and customisation to either tune the electronic properties of the inorganic metal thiolate or to provide additional functionalisation beyond the original scope of the complex.

The primary objective of this work was to investigate the self-assembly of the complexes with specific attention to the factors influencing the size or nuclearity of the resultant tiara. This was accomplished in *Chapter 2* by the synthesis of several previously unknown palladium tiara-like complexes incorporating the ligands *N*-acetylcysteamine (compound **1**, Pd NAC), ethyl thioglycolate (compound **2**, Pd ETG), 2-mercaptoethyl acetate (compound **3**, Pd MEA) and methyl 3-mercaptopropionate (compound **6**, Pd MMP). These ligands, differing only in the structural arrangement of their constituent atoms between **2**, **3** and **6**, or the nature of the functional group between **1** and **3**, gave significantly different outcomes from the complex formation reactions. It was found that the structural rearrangement of the ligands favoured formation of octanuclear complexes when the carbonyl oxygen (C=O) was located on the second (beta) carbon from the thiol sulfur, whereas hexanuclear complexes were synthesised when the carbonyl oxygen was located on the gamma or delta carbon atoms.

Figure 6.1 shows the general structure of the thiol ligands used in this work with the placement of carbonyls for each ligand.

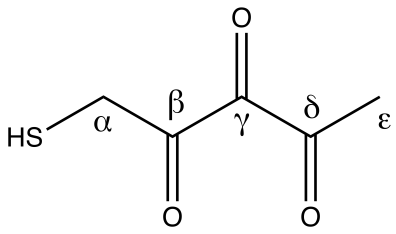


Figure 6.1: General structure of thiol ligands used in this work, with illustrated β - C=O (for ethyl thioglycolate, complex **2**), γ - C=O (for methyl 3-mercaptopropionate, complex **6**) and δ - C=O (for 2-mercaptoethyl acetate, complex **3**).

The reasons for this change of selectivity on isomerisation of the thiol ligand are theorised to be steric in nature rather than for electronic effects of the carbonyl on the sulfur donor. Placement of the carbonyl on the β-carbon allows for optimal occupation of the central void by the thiolate ligand arm, stabilising the larger octanuclear structure over the hexanuclear. Relocation of the carbonyl further down the ligand backbone to either the γ- or δ- carbons renders the ligand arm too sterically hindered to provide stabilisation of the larger void present in octanuclear complexes.

Further to these effects, replacement of the ester functionality to an amide was found to make the formation of the complex solvent-dependent, with smaller hexanuclear complexes being favoured during synthesis in aprotic solvents such as THF, whereas a progressively increased ratio of larger ring products including octanuclear and nonanuclear was seen to be formed in the MALDI-MS of tiara-like complexes synthesised using n-propanol, ethanol or methanol as the reaction solvent. These effects are thought to arise via the self-association of the thiolate ligand during the complex assembly process, resulting in shorter reaction times as the growing tiara chain terminates rapidly. The presence of protic solvent molecules in a huge excess, able to compete for hydrogen bonding sites during the self-assembly, effectively masks this intramolecular association and potentially stabilises the intermediate polymer chains, allowing them to reach a greater length before termination. Methanol, being the solvent of the smallest

molecular size, is thought to be able to cluster more effectively around the polymer chain and therefore provides the greatest amount of shielding.

The properties of the complexes, as well as further spectroscopic investigations, were discussed in *Chapter 3*. A COSY experiment of complex **1** showed a relatively long-ranged scalar coupling over five bonds, which could either be due to the partial double bond character of the amide or a result of a particular conformation of the molecule in solution, which would provide some evidence for the presence of hydrogen bonding interactions in the solution phases as well as the solid state crystalline phase. DOSY calculations suggest that only a very small decrease in the diffusion coefficient occurs on proceeding from a hexanuclear to an octanuclear tiara ($4.195E^{-10}$ m^2/s for the hexanuclear complex **6** vs. $4.108E^{-10}$ m^2/s for the octanuclear complex **2**). This suggests that the overall diameter of tiara-like complexes does not significantly increase from hexanuclear to octanuclear tiaras, and this difference is expected to be even smaller between complexes of greater nuclearity. The DOSY measurements also indicated single-component systems, illustrating that the complexes are stable and do not interconvert between ring sizes in the solution phase.

Electrochemical reductions of complex **1** provide evidence for proton reduction and the formation of nanoparticles, which are remarkably well protected against aggregation into microparticular species despite the small nature of the thiolate ligand believed to cap the surfaces. EDX analysis of the particles confirms the palladium composition, and the hydrogen bonding capability of the ligand may bestow interesting physical or chemical properties on the resultant nanoparticles, making them species of interest in catalysis or supramolecular chemistry. Finally, complex **2** showed propensity toward host-guest chemistry, able to incorporate two molecules of methyl iodide into its central void, making it the first tiara-like complex recorded to accommodate two guest molecules, opening up interesting avenues in

chemical entrapment with potential applications for reaction confinement.

Other tiara-like complexes have been discussed in *Chapter 4*, beginning with a nickel variant **7** of the palladium complex **6** described in *Chapter 2*, and the properties of the two are compared therein. While the structures are vastly similar, small differences arise from the change from palladium to nickel and the variation in electronic properties is quite pronounced. Structurally, the incorporation of nickel within the tiara distorts the bonding away from the perfect hexagonal geometry of **6**, therefore crystallising into the lower symmetry space group *P*-1 rather than *R*-3. Within this chapter are also described a series of reactions designed to synthesise tiara-like complexes containing two different types of metal, palladium and platinum. It was seen that the resultant distribution of tiara complexes was found to vary on alteration of the ratio of starting components, leading to acquisition of different primary products. These heteronuclear tiaras were observed to have greatly distorted metal-thiolate cores, possibly allowing for an eventual separation based on crystallography or high performance shape distinction.

5.1.2 Future Work

The primary difficulties encountered in this work have been the separation and purification of individual isomers of the tiara-like complexes synthesised. This is equally true for the nuclearity (size-based) isomers of **1** that were described in *Chapter 2* and the elemental isomers of the Pd/Pt tiaras described in *Chapter 4*. There is a general lack of protocol available within the scientific literature to purify tiara-like complexes, with only a few unique procedures described.[1-3]

A potential resolution to surpass this issue is the employment of advanced size exclusion chromatrography using high performance beads to facilitate separation of isomeric mixtures of complexes. Complete separation, and therefore purification, of all isomers in a mixture would allow each of them to be studied separately and their properties compared. Additionally, this would allow for the precise ratio of products obtained from the reaction to be quantified and yields calculated for each isomer. This would allow for a more accurate analysis of the distribution of products obtained from the reaction of *N*-acetylcysteamine with palladium chloride in protic solvents. Further, the effects of factors such as temperature, base and concentration (which are believed to have a small or occasionally negligble effect) on the distribution and yield of the products could more easily be investigated.

The formation of palladium nanoparticles by electrochemical means should be investigated more thoroughly along with an in-depth study of the nanoparticles themselves. It is possible that the reductive effects observed in the voltammetry experiments may be attributable to the *in situ* generated nanoparticles rather than the parent tiara complexes themselves. If the *N*-acetylcysteamine ligands cap the surfaces of the nanoparticles, their hydrogen bonding capability may lead to interesting nanoscale supramolecular effects.

Expanding the family of tiara-like complexes synthesised in *Chapter 2* to the other members of the Group 10 metals for comparison would also be a worthwhile investigation. Platinum in particular has been relatively unexplored in the study of tiara-like complexes[4] and additional successes thereof would be of greater significance than additional nickel complexes, which are the most widespread within the scientific literature already.[3]

Ultimately, it is hoped that the end result of this work will allow some control over the nuclearity of tiara-like complexes, as well-designed complexes with expected and reliable nuclearity will be of value to research groups attempting to exploit the many interesting properties of these complexes. Supramolecular and host-guest chemistry more than other areas will benefit from tiara-like complexes with easily obtainable high nuclearities such as ten or greater, and the inclusion of guest molecules other than solvents will be of huge advantage to the nanoscale chemist. As ring-shaped molecules, tiara-like complexes have a great potential for use in supramolecular assemblies such as catenanes and rotaxanes, as described in *Chapter 1*. However, it is likely that development of larger rings is an obstacle that must be overcome before their use in interlocked structures is reported. Nevertheless, the diverse and chemically interesting properties of the tiara-like complexes will only be of greater interest when interlocked with other functional molecules in supramolecular structures.

5.2 References

1. J. Chen, L. Liu, L. Weng, Y. Lin, L. Liao, C. Wang, J. Yang and Z. Wu, *Sci. Rep.*, 2015, **5**, 16628.
2. C. Tan, M. Jin, H. Zhang, S. Hu, T. Sheng and X. Wu, *CrystEngComm*, 2015, **17**, 5110-5115.
3. C. Zhang, T. Matsumoto, M. Samoc, S. Petrie, S. Meng, T. C. Corkery, R. Stranger, J. Zhang, M. G. Humphrey and K. Tatsumi, *Angew. Chem. Int. Ed.*, 2010, **49**, 4209-4212.
4. Y. Yamashina, Y. Kataoka and Y. Ura, *Inorg. Chem.*, 2014, **53**, 3558-3567.

Appendices

Appendix I: Standard Stench Protocols

A1.1 Working Procedure for Noxious Compounds

Several of the thiol compounds utilised in this work readily volatilise to elicit strong, pungent odours at very low concentrations in air. Low molecular weight thiols are particularly noxious and the threshold for detection can be as low as ca. 10 parts per billion. To prevent release of these odours during the course of these reactions, it was necessary to develop containment procedures for efficient isolation of the apparatus contents.

A simple sealing of the reaction vials was considered but disregarded early. The need for a continuous flow of inert gas over the reaction mixture and the requirement for refluxing solvent in several experiments precluded any closed system from safe operation due to pressure concerns. However, normal anoxic procedures were deemed insufficient to contain the sulfurous odour when the system was subjected to the flow of inert gas resulting in a constant stream of volatile thiol vapour leaking from the reaction flask.

A modification of the standard oxygen-free gas technique was decided upon that could be applied to almost all reactions involving odorous thiols. A 50ml two-necked flask was fitted with an air-tight suba seal through which a metal needle could be inserted and connected to the nitrogen inlet. To the other neck was fitted the condenser if required, or a simple gas adapter if elevated temperatures were not required. Where a condenser was required the gas adapter was fitted to the top. The adapter was then connected to a dreschel bottle containing a solution of concentrated bleach, through which the gas outlet from the reaction could be bubbled through. This setup was designed to minimise release of pungent thiol and was

efficient under low gas flow.

A complete degassing of the reaction space and solvent was generally performed under high gas flow rates prior to the addition of the thiol, after which point the flow of nitrogen was limited to avoid forcing excess vapour from the reaction flask. A very low rate of nitrogen flow was continued over the course of reactions to maximise odour neutralisation.

Typically reactions would be completed with either excess thiol remaining within the reaction mixture and/or contamination of the glassware with vaporised thiol. Excess thiol is often removed by evaporation under reduced pressure within literature reports but this suffers drawbacks of further contamination of the equipment used to perform the procedure. During the course of this work, it was discovered that dissolution of the entirety of the crude reaction material in an organic phase non-miscible with water followed by repeated washings with sodium hydroxide was effective at removing the majority of the excess thiol. This procedure was effective for most compounds with the main exception of **1**, however the lack of odour associated with *N*-acetylcysteamine rendered such procedures unnecessary.

Decontamination of the reaction apparatus, including glassware, suba seals and magnetic stirrers was achieved by immersion of the contaminated items in a solution of concentrated bleach to oxidise the thiols to non-odorous sulfates and ordinary dish soap to act as a surfactant. These were normally left for a period of at least 24 hours in order to achieve complete decontamination. Following removal from this solution, all items were rinsed thoroughly with water before being cleaned by normal methods.

Appendix II: Analytical Techniques

A2.1 Introduction

All of the techniques described in this work are the product of many years of development and refinement, and to completely elaborate on their origins and working processes would require a lengthy discussion. However for the purposes of this thesis, a brief overview of each should suffice to introduce them.

A2.2 Techniques

A2.2.1 2-Dimensional Nuclear Magnetic Resonance Spectroscopy[1,2]

A2.2.1.1 Introduction to 2D NMR

2D NMR was originally put forward in a research paper by Richard Ernst inspired by a lecture delivered by Jean Jeener.[3] As its name suggests, it differs from 1D NMR by the addition of a second axis to the data output spectrum. This is often generated as a result of some form of time parameter due to the way that 2D data is obtained. The basic sequence in 2D NMR is to excite the nuclei of interest in a similar manner to 1D NMR in the 'preparation period', however the sample is then allowed a period during which time spin precession is allowed to evolve, hence the introduction of an 'evolution time', also noted as t_1, before being subjected to further radio frequency pulses. This period is denoted as the 'mixing time' and usually comprises some form of magnetisation transfer from one nucleus to a second. In the case of COSY experiments, this is by scalar coupling through chemical bonds and in NOESY or ROESY experiments magnetisation is transferred through space by the Nuclear Overhauser Effect. This then leads into the 'detection time', or t_2, during which time the Free Induction Decay (FID) is measured. The FID is then Fourier Transformed twice (also called Two Dimensional FT) and the NMR experiment is repeated with a change in the

evolution time. This normally results in some change to the FID and so this is recorded. The experiment is repeated a number of times to allow for a significant number of variations in t_1 before the data is plotted as a 2D spectrum of two frequencies, f_1 and f_2. f_1 in most cases comprises the 1D spectrum and is plotted as normal, and f_2 represents the change in FID corresponding to the change in t_1.[3,4] An example pulse sequence for 2D NMR is given in *Figure A2.1* and an example spectrum is given in *Figure A2.2*.

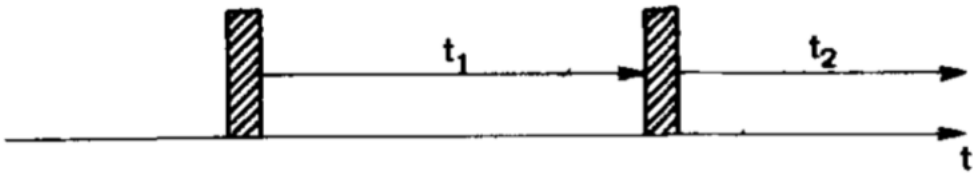


Figure A2.1: Example pulse sequence for a 2D NMR experiment. The first block represents the preparation period, followed by t_1 (evolution time), the second block represents mixing time, last followed by t_2 (detection time).[3]

The discovery and development of 2D NMR allowed for the unravelling of complicated spectra with chemical shifts too close in frequency to be analysed in one dimension. The structures of natural products too convoluted to be deciphered by 1D NMR could now be solved, pushing forward modern drug development. Hence, the Nobel Prize for Chemistry in the year 1991 was awarded to Professor Richard R. Ernst for his work on FT and 2D NMR.

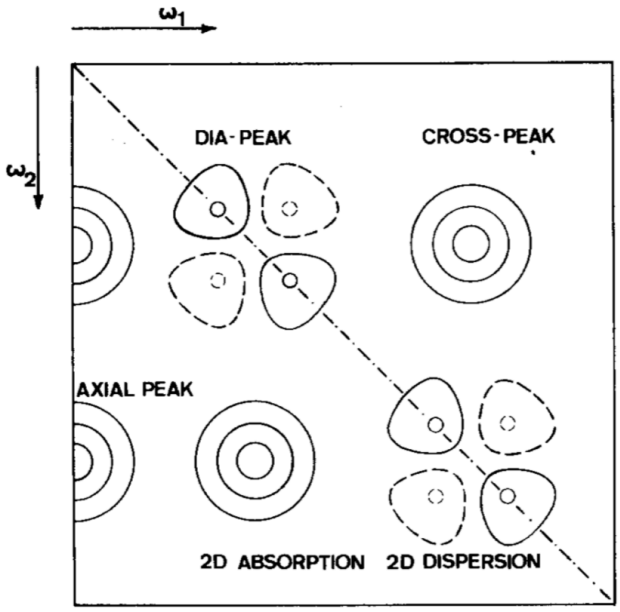


Figure A2.2: Example of the features of a 2D NMR spectrum. The two axes of the spectrum indicate the two frequency domains and the additional 2D information is given by the cross-peaks between different 1D signals.[3]

A2.2.1.2 Correlation Spectroscopy

^{1}H-^{1}H COSY (see *Figure A2.3*) is one of the most commonly used 2D experiments to the modern NMR chemist. The principle involves transfer of magnetisation from particular proton nuclei to neighbouring protons. The employment of the second pulse in the ^{1}H NMR experiment leads to various transitions between the population states of all mutually-coupled nuclei. This results in a modulation of the signal which is detectable, allowing for the recognition of all coupling partners.

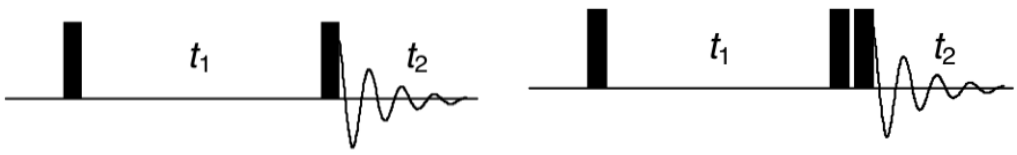


Figure A2.3: Pulse sequences for COSY (left) and DQF COSY (right).

The information gained by the COSY experiment is displayed within the 2D spectrum as in *Figure A2.4* wherein the presence of cross-peaks represents coupling between the protons

indicated by the 1D ^{1}H NMR spectrum.

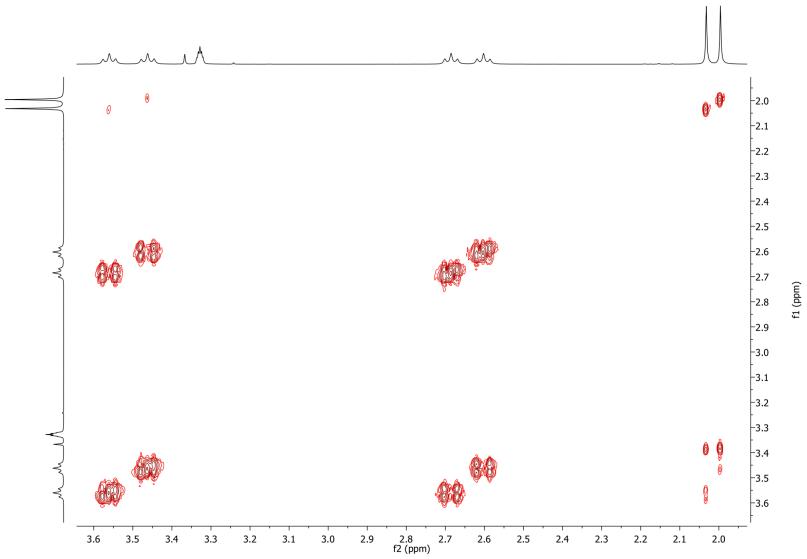


Figure A2.4: Example COSY spectrum taken from *Chapter 3.2.1*. The cross-peaks, red contours off the diagonal, indicate coupling between protons.

COSY spectra can be obtained for nuclei other than ^{1}H, such as ^{19}F and ^{13}C. The low sensitivity and abundance of the latter however normally requires for ^{13}C labelled samples.

A2.2.1.3 Nuclear Overhauser Effect Spectroscopy and Rotating-frame Overhauser Effect Spectroscopy

The NOESY and ROESY experiments are a form of spectroscopy that allows for the recognition of protons that are adjacent in space (up to approx. 4-5 Å), rather than close together within the molecule as for the COSY experiment. The origin of the Nuclear Overhauser Effect (NOE) arises from the interaction of the nuclei dipoles. If the A transition illustrated within *Figure A2.5* is irradiated then saturation occurs between the αα and the βα levels and the αβ and ββ levels. Spin-lattice relaxation following the double quantum ω2 pathway of the A nucleus from β to α also involves a transition of an X nucleus from β to α, therefore increasing the population density of A.

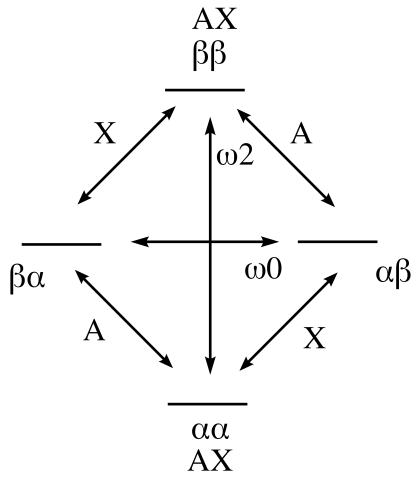


Figure A2.5: Energy states for a two-spin system of protons A and X in proximity showing the zero and double quantum pathways ω0 and ω2.

In contrast, the zero quantum ω0 pathway involves a transition of the X nucleus from α to β, thereby decreasing the population density of A. The former is a positive NOE while the latter is a negative NOE. The positive effect increases the intensity of the signal of the X proton within the spectrum while the negative effect results in a decrease in intensity. The ω2 pathway predominates in smaller molecules with a faster molecular tumbling rate leading to the observation of positive NOEs whereas the ω0 pathway is the major relaxation pathway in macromolecules with a slower tumbling rate, leading to the observation of negative NOEs. If the ω0 and ω2 pathways are operating at a similar rate then the population of X is being increased and decreased at the same time, reducing the magnitude of the NOE; the closer the rates of relaxation, the more the NOE tends to zero.

In summary, small molecules will show positive NOEs and large molecules will show negative NOEs. Molecules around a certain size, depending on solvent viscosity, will not show NOEs due to the competing pathways. This is most common for molecules between 1000 and 3000 Da. In this case, the ROESY experiment may be employed. Due to the introduction of a 'spin lock', the cross polarisation occurs between transverse magnetisation components rather than the longitudinal components for the NOESY experiment. The pulse sequence is similar to

that of the TOCSY sequence, which may lead to the acquisition of artefacts in the spectrum.

A2.2.1.4 Diffusion Ordered Spectroscopy

The DOSY technique allows the analytical chemist to determine the rate at which the molecules of interest are diffusing through the solvent. This may be linked to the molecular weight of the molecule via the Stokes-Einstein equation:[5]

$$D = \frac{kT}{6\pi\eta R} \quad (1)$$

Where D is the diffusion coefficient, k is the Boltzmann constant, T is the temperature in Kelvin, η is the solvent viscosity and R is the hydrodynamic radius of the molecule. This may be related to the molecular weight by the following equation:[6]

$$R_{\mathrm{H}} = \sqrt[3]{\frac{3M}{4\pi\rho N_{\mathrm{A}}}} \quad (2)$$

Where R_H is the hydrodynamic radius, M is the molecular weight of the compound, ρ is the density of the species and N_A is Avogadro's number. However, this approximation loses accuracy as the shape of the molecule departs from the spherical ideal. Nevertheless it remains a good estimate of molecular weight even for irregularly shaped molecules provided accurate data.

The DOSY experiment is performed by utilising a gradient to spatially 'tag' the location of molecules within the NMR tube before allowing them to move during the diffusion time (Δ, also called 'big delta'). The greater the diffusion of the molecules, the less refocused the signal will be during the refocusing of a later pulse after the diffusion time. This attenuation in signal can be quantised to determine the diffusion coefficient as smaller molecules will diffuse more rapidly and therefore give a larger loss of signal. The strength of the gradient used is given the

term δ (also called 'little delta'), and the two 'deltas' determine the loss of signal. These parameters are freely alterable and are often optimised in order to give 95% signal loss for the most accurate determination of the diffusion coefficient.

The diffusion measurement may be adversely affected by the presence of convection currents within the sample tube that lead to inaccurate measurements. This may be addressed by utilising sample tubes of a smaller diameter such as 3mm when compared to the standard 5mm NMR tubes or selecting a solvent of higher viscosity such as DMSO. Also available are specialised pulse sequences that are capable of performing adjustments to compensate for convection currents.

DOSY experiments may be displayed as 2D spectra of the 1D NMR spectrum plotted against the diffusion coefficient D; this is most useful when comparing multiple species within the same solution. For the experiments detailed in this work it is more useful to plot the decrease in the gradient G over the datapoints and fit the data, as a linear fit indicates the single component system diffusing at a single rate whereas a curved fit indicates the presence of multiple diffusing species.

A2.2.2 Electrochemistry[7]

The history of electrochemistry can be traced back many years to the pioneering work of Michael Faraday, and has myriad uses and applications that are beyond the scope of this work. This thesis is mainly concerned with the simple practice of utilising electrical energy to drive redox transformations. In general, chemical species are capable of oxidation or reduction, being the loss or gain of electrons respectively to either change oxidation state or alternatively form radical species.

A2.2.2.1 Cyclic Voltammetry

In an electrochemical cell, a compound of interest, the analyte, is subjected to either a positive or negative potential. This is most commonly achieved by the use of three electrodes, which comprise the working electrode, counter electrode and the reference electrode. The working electrode applies the potential to the cell and facilitates the transfer of electrons to or from the sample. The counter electrode completes the circuit, balancing the charge of the cell. Finally, the reference electrode is uninvolved with the redox process, simply monitoring the working potential of the cell. These electrodes are placed in contact with the analyte. In this work, all experiments were carried out in DMF solution. To facilitate the transfer of charge, a supporting electrolyte is normally added such as [n-Bu_4N][BF_4]. Finally, an internal standard may be used to reference the electrode potentials, a common choice is ferrocene as the ferrocene/ferrocenium couple is well-understood.[8] Ferrocene is robust, largely soluble in many solvents and oxidises reversibly at the accessible potential of +0.49V vs SCE.

The cell being assembled, a ramping potential is applied to it and the resulting current is measured with an ammeter. Once a set potential has been reached, the potential is reversed, typically to the same potential with the opposite sign before returning to zero. This step may be omitted if only one of the oxidation or reduction processes is to be examined. The peaks obtained give a large degree of information about the electrochemical processes of the analyte. A reversible process will show a return wave whereas an irreversible process will not; the degree of reversibility may be judged from the symmetry of the forward and return waves. Cyclic voltammetry samples the thin diffusion layer proximal to the electrode while not disturbing the bulk solution, and is typically limited by the speed with which the analyte diffuses to the electrode surface; this results in a peak current that is proportional to the square root of the scan rate; it is common practice to repeat cyclic voltammetry experiments with varying scan rates to examine this.

A2.2.2.2 Coloumetry

The coloumetric experiment, or properly potentiostatic coloumetry experiment, is similar to the cylic voltammetry experiment. The principal difference arises from the application of the potential. As the name suggests, instead of sweeping the potential, a set potential is applied and held to the electrochemical cell. Then, instead of measuring the peak current, the total current is measured and the charge imparted onto the system is calculated. Typically this is performed for a lengthy period of time sufficient to oxidise or reduce all of the analyte, indicated by the lowering to zero of the current as the initial electrolyte is consumed. This experiment uses an electrode with a far greater surface area than the CV experiment; the CV electrodes are generally made as small as possible to minimise resistance while coloumetry is performed with high surface area electrodes to quicken the redox of the solution and shorten the experiment time, further the solution is normally stirred in contrast to the CV experiment with an unagitated solution. Analysis of the total charge imparted on the system allows for the calculation of the number of electrons imparted per molecule of analyte.

If the redox process applied to the analyte results in a chemical transformation, the product of the electrochemical experiment may be stable while the cell remains sealed, allowing for the performing of chemical analysis on the solution such as NMR, IR and UV.

A2.2.3 Hirshfeld Surface Analysis

A2.2.3.1 Hirshfeld Surfaces

Hirshfeld surfaces are a form of molecular surface analysis that are extremely useful in assaying the intermolecular forces between molecules in a crystal, first introduced in 1997.[9] The surface is constructed by partioning the space within the crystal structure into separate

regions wherein the electron density of the molecule of interest (promolecule), $\rho_{promolecule}(\boldsymbol{r})$, is dominating over the electron density of the remainder of the crystal (procrystal), $\rho_{procrystal}(\boldsymbol{r})$. A weight function can therefore be defined using the former value as the numerator and the latter as denominator to give $w(\boldsymbol{r})$. The Hirshfeld surface is then defined as the region wherein $w(\boldsymbol{r}) = 0.5$.[10]

This provides two values: d_i, the distance from the surface to the nearest internal atom (i.e. an atom of the promolecule) and d_e, the distance from the surface to the closest external atom (i.e. an atom of the procrystal).[11] These can then be used to map the surface to show close interactions. However, this approach does not take into account the van der Waals radii of the atoms involved, therefore these values are usually converted into d_{norm}, which corrects these results to give a normalised set of values.[12] This surface can then be represented on the promolecule chromatically, with blue interactions indicating contacts greater than the sum of the van der Waals radii of the internal and external atom, white surface indicating contacts approximately equal to the sum and red surface areas showing interactions shorter than the sum.

An example Hirshfeld surface for 2-chloro-4-nitrobenzoic acid is given in *Figure A2.6*.

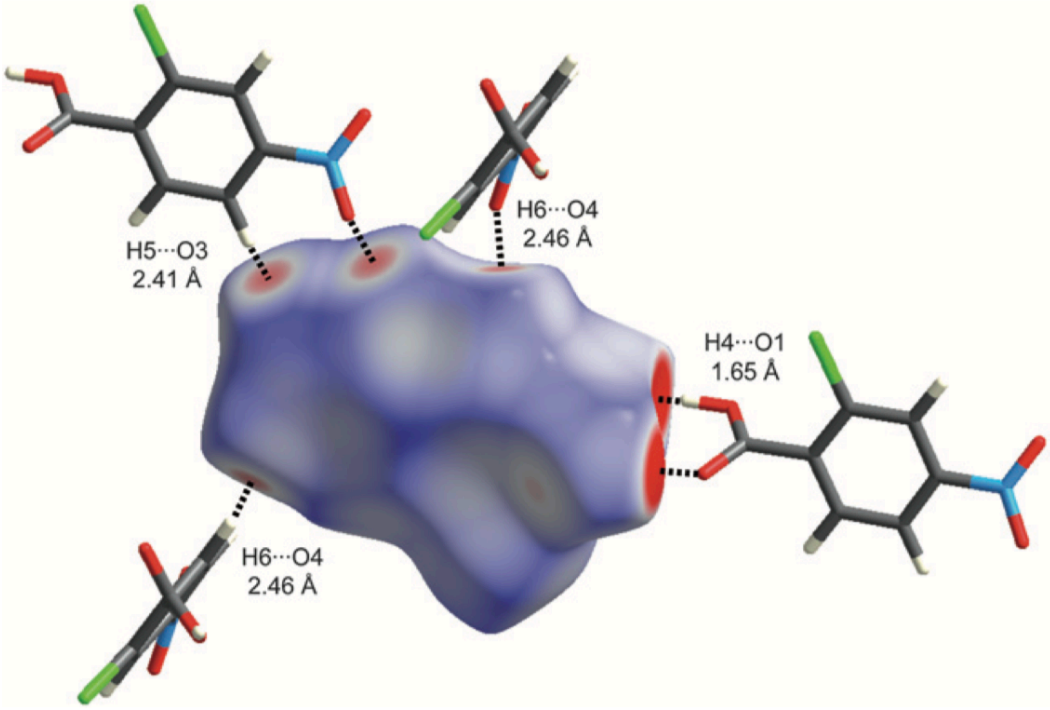


Figure A2.6: Example Hirshfeld surface for 2-chloro-4-nitrobenzoic acid (form I), d_{norm} mapped. Neighbouring molecules making close contacts are shown along with the nature of the interaction and the distance.[10] Atom colours: grey = carbon, green = chlorine, blue = nitrogen, red = oxygen, white = hydrogen.

A2.2.3.2 Fingerprint Diagrams

For ease of interpretation, Hirshfeld surfaces can also be represented by a 2D histogram known as a fingerprint diagram.[13] Each unique (d_i, d_e) pair is grouped in a small area of 0.01 Å and represented on the plot; these can then be coloured to represent the number of interactions within that area or 'bin'.[10] In contrast to the graphical Hirshfeld surface, the colours used are blue to green and through to red, where blue represents only a relative few interactions and red indicates the most interactions in that (d_i, d_e) bin.[14] An important aspect of these diagrams is that they possess a rough mirrored symmetry over the $d_i = d_e$ diagonal similar to COSY spectra.

An example fingerprint diagram for 2-chloro-4-nitrobenzoic acid is given in *Figure A2.7*.

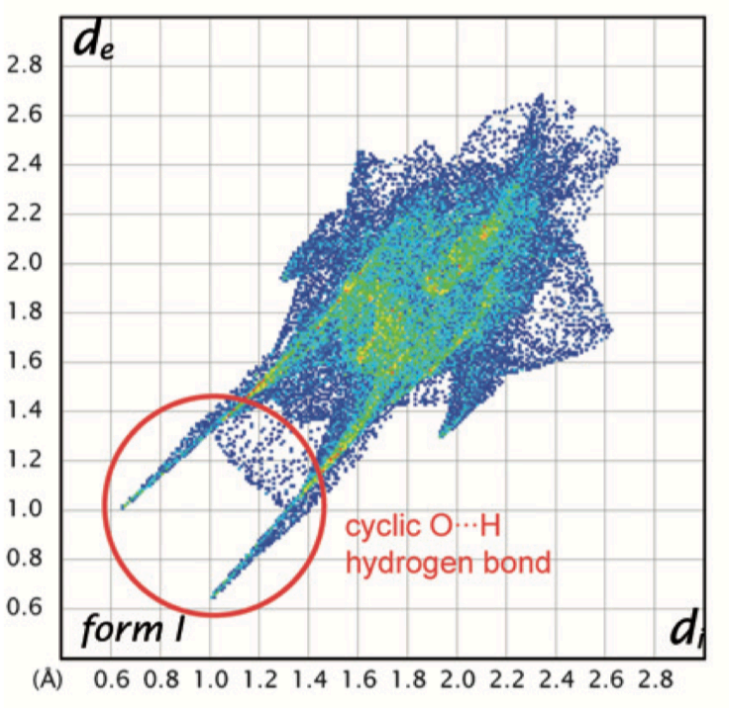


Figure A2.7: Example fingerprint plot for 2-chloro-4-nitrobenzoic acid (form I). Encircled are the (d_i,d_e) 'spikes' that are indicative of hydrogen bonding interactions.[10]

Points on a fingerprint diagram towards the lower left (small d_i, d_e) represent close interactions and points toward the upper right (high d_i, d_e) show longer ranged interactions. As expected therefore, very close contacts such as hydrogen bonds tend to appear at the lower left of the fingerprint plots and often appear as conspicuous 'spikes' within an otherwise round and diffuse plot,[10] making their identification easier. Fingerprint plots of a promolecule are very sensitive to the surrounding molecules in a crystal structure, thereby rendering them extremely useful in comparing crystals of polymorphic structures[15] or high-pressure structures.[16] Much as their name suggests, each fingerprint plot is practically unique, even to the same molecule in different polymorphs or forms. This can be seen in *Figure A2.8*, where different molecules of 2-chloro-4-nitrobenzoic acid in the same crystal form show different fingerprint diagrams.

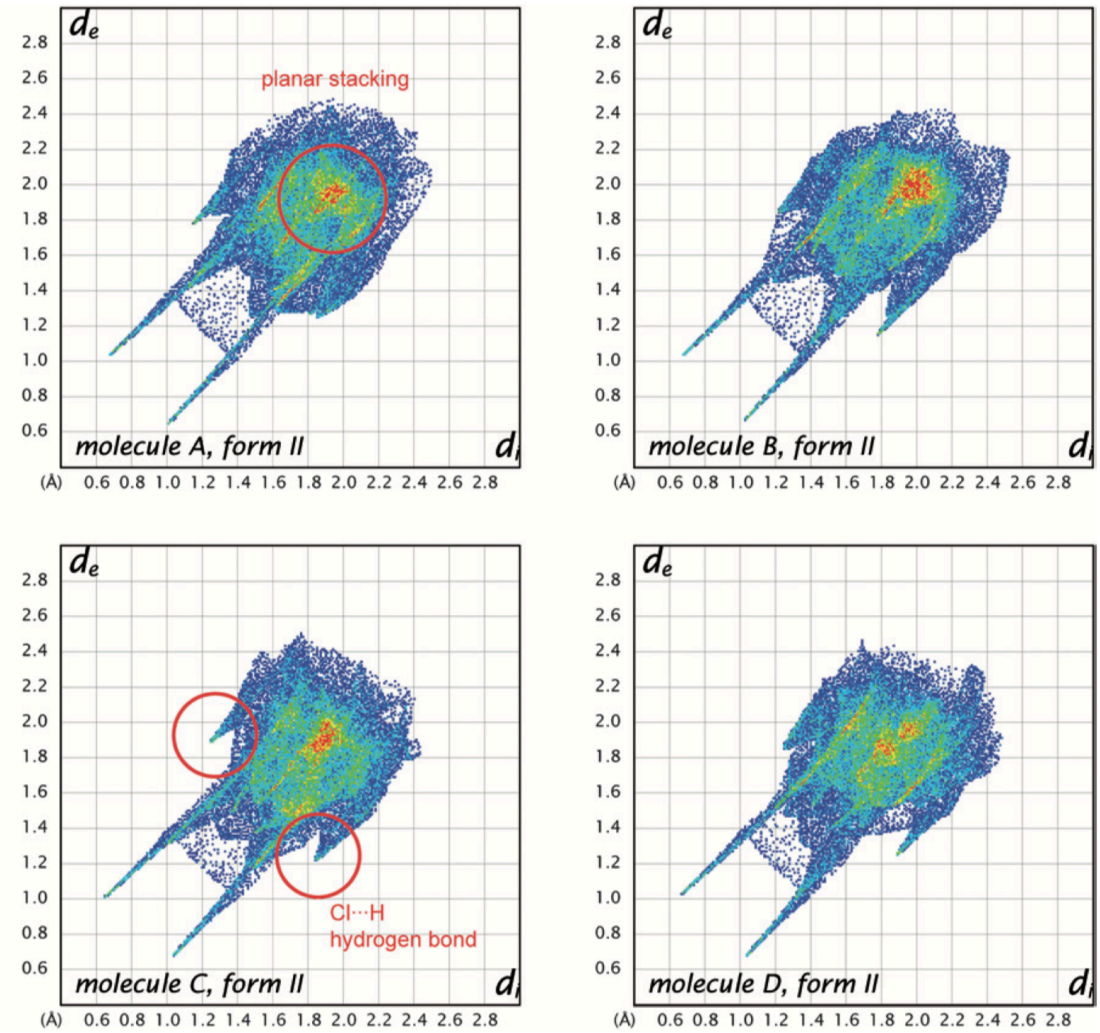


Figure A2.8: Comparison of the fingerprint plots for the four molecules of 2-chloro-4-nitrobenzoic acid (form II). Some key features, such as the planar stacking and Cl···H hydrogen bonding interactions have been highlighted.[10]

All Hirshfeld surfaces used in this work, including fingerprint diagrams, were processed and generated by the program CrystalExplorer.[17]

A2.2.4 Infra-red Spectroscopy

Chemical bonds are not static, rigid entities but in a state of constant movement and vibration. The energies of this vibration generally falls in a range approximately equal to that of electromagnetic radiation in the infra-red region of approximately 2500 nm to 25,000 nm. A photon travelling at a particular frequency may therefore interact with a chemical bond

vibrating with the same frequency and be absorbed. This absorption may be detected as a drop in intensity of a infra-red source beam compared to a reference beam or background sample, also known as 'transmittance'. IR spectra are therefore displayed as a plot of the frequency against the transmittance. For convenience, wavenumbers (cm^{-1}) are often used instead of wavelength (nm), such that 2500 nm is equal to 4000 cm^{-1} and 25,000 nm is equal to 400 cm^{-1}. Stronger, shorter bonds such as O-H bonds are generally excited at higher wavenumbers (ca. 3600 cm^{-1}) corresponding to higher energy photons and weaker, longer bonds such as C-X, where X is a halide, at lower wavenumbers (ca. 700 cm^{-1}) corresponding to lower energy photons.

IR spectra may be obtained for pure solids, liquids and gases, along with solution phase samples. Due to absorption of IR frequencies by the solvent, chlorinated solvents such as $CHCl_3$ and DCM are often employed, as the narrow carbonyl absorption windows of solvents such as acetone or DMSO mean that sample peaks may be obscured by the overwhelming solvent absorption.

All spectra collected in this work were obtained via Attenuated Total Reflection (ATR) IR spectroscopy, a solid phase technique wherein a crystalline sample of the sample of interest is placed between an 'anvil' and a small diamond crystal. The IR beam is directed into the crystal where total internal reflection allows a small degree of penetration into the crystal before the beam exits the crystal onto a detector.

A2.2.5 Size Exclusion Chromatography[18]

Size-Exclusion Chromatography (SEC) is a purification technique wherein impure mixtures of compounds are separated according to their molecular weights or sizes, in contrast to silica gel chromatography where separation is due to differences in solubility. The primary targets

for this technique tend towards larger molecules such as proteins and polymers. Often, particularly for polymers, the molecules to be separated are identical in composition but differ in the size, making this technique particularly attractive for mixtures of tiara-like complexes that are composed of the same ligand but have multiple nuclearities. A low resolution purification of a protein is given below in *Figure A2.9*.

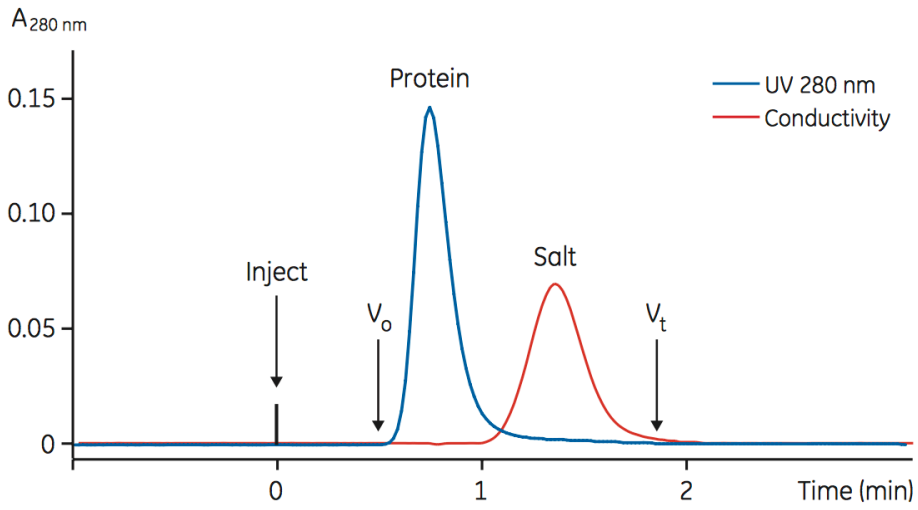


Figure A2.9: Low resolution purification of a protein sample (desalting), showing separation of the target protein from the salt contaminant. The spectrum plots UV absorbance against time.

Much like silica gel chromatography, SEC involves a stationary phase and a mobile phase in operation. The stationary phase consists of porous beads containing channels that are packed into a long column; these beads are often stored dry and require swelling in the mobile phase. Mobile phases can either be aqueous, most commonly utilised for separation of proteins and polypeptides, or organic, in which case the technique is often referred to as gel-permeation chromatography (GPC).

For aqueous mobile phases, the stationary phase usually consists of sugar and starch-based cross-linked polymers. Organic mobile phases in gel permeation chromatography are normally solvents such as THF or toluene. Short chain alcohols such as methanol do not swell the beads effectively and the beads tend to float in chlorinated solvents due to their high

density, making packing difficult. This nominally limits the choices of organic solvents that can be selected as a mobile phase; usage of chloroform and dichloromethane is possible but requires a pre-swelling of the beads and packing in another solvent such as THF followed by careful replacement of the solvent.

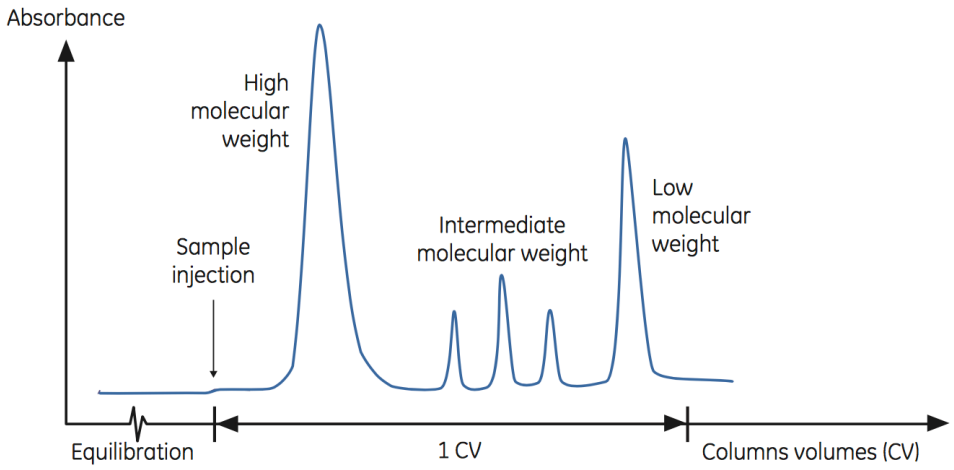


Figure A2.10: High resolution separation of multiple compounds. High molecular weight molecules elute quickly from the column, followed by lower molecular weight species.

The premise of the technique is that the sample(s) to be purified are dissolved in the mobile phase and eluted through the column containing the stationary phase. As the molecules travel through the beads in the stationary phase, larger molecules that have a radius greater than that of the channels will pass around the beads and elute quickly. This is shown by the separation plot in *Figure A2.10*. Molecules that are smaller than the radius of the channels will pass into the beads and have a greater retention time, therefore eluting more slowly (see *Figure A2.11*).

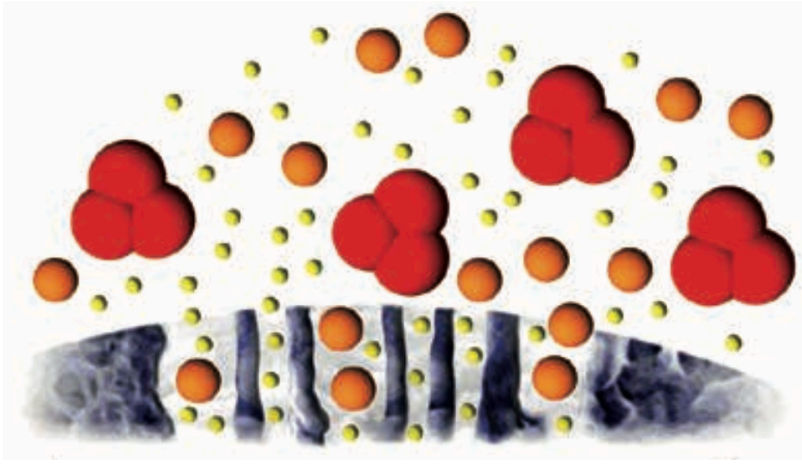


Figure A2.11: Entrapment of smaller compounds (yellow and orange) within the beads. Larger molecules (coloured red) are not entrapped by the beads and so elute quickly.

There are several advantages to the use of this technique. Firstly, the beads are reusable; after performing the separation the column can be cleaned by rinsing through with additional solvent. This is of particular use when the stationary phase is fixed within the column for high throughput separations. Secondly, unlike in silica gel chromatography, the solubility or polarity of the compounds does not affect the rate at which the compounds elute through the column. Thus, compounds of similar polarities but different sizes, such as polymers, can be separated by this method.

A2.2.6 Transmission Electron Microscope

Ordinary microscopes operate by focusing visible light reflected from a sample through lens to be detected by the eye, and are capable of resolving small objects in higher resolution than the human eye unaided. However, there is a limit to the size of the objects that can be resolved by visible light due to the wavelength of the photon waves. The wavelength of visible light ranges from approximately 400 to 700 nm and thus smaller objects, such as molecules, are unable to resolved by conventional microscopes. However, usage of waves with a shorter wavelength bypass this restraint. In the year 1939 the first commercial transmission electron microscope was developed.

The principle of the electron microscope is generally similar to that of the optical microscope. High energy electrons are generated by a source and accelerated and focussed onto the sample to be investigated, which is prepared as a thin slice. The electron travel through the sample and are then magnified by a lens onto a detector plate. Due to the scattering and dispersion of the electrons by the sample, the resultant beam can be formed into an image capable of resolving the nanometre scale.

A2.2.7 Energy-Dispersive X-ray Spectroscopy

Energy-dispersive x-ray spectroscopy operates as a form of elemental analysis allowing for the composition of a sample to be quantified. It requires a high-energy electron source, and is often therefore combined with a TEM or SEM (scanning electron microscope). When an electron interacts with a sample, it may cause ejection of a core-shell electron in a similar manner as Electron Impact ionisation. This hole is then occupied by a higher energy electron which migrates to the lower energy level. The energy difference between the two levels is resolved by the emission of x-ray radiation equal to the energy gap between the two levels. Each element has unique energy signatures of this process, such that the identification of the atom is possible if the x-ray radiation is detected. This process is illustrated by *Figure A2.12*.

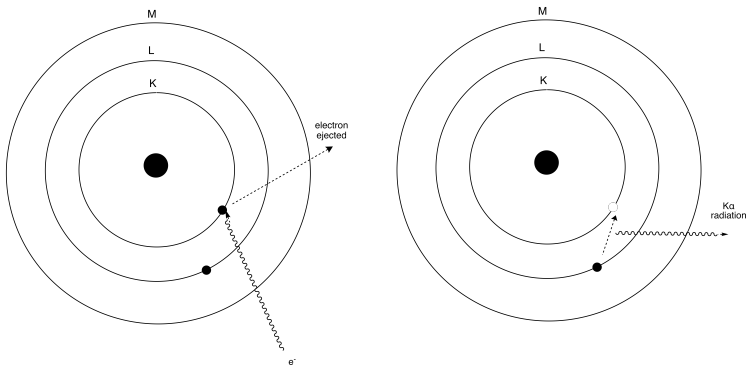


Figure A2.12: Principle of EDX spectroscopy. A core electron is ejected by an incoming high-energy electron, leaving a hole. This is then filled by a higher energy electron, resulting in the emission of an x-ray photon.

A2.2.8 UV/Visible Spectroscopy

UV/vis spectroscopy carries similarities to that of IR spectroscopy, but deals with far higher energy electromagnetic waves in the visible spectrum extending into the ultraviolet region. The photons of these energies, instead of interacting with the chemical bonds of the molecule are instead of a wavelength suited to interacting directly with the electrons of the constituent atoms. If a photon with an energy equal to a spectrally allowed electron transition in the sample molecule interacts with that sample, it may be absorbed to initiate that transition, resulting in the promotion of an electron to a higher energy level. Like IR spectroscopy, that absorption may be detected as the drop of intensity of a source beam when compared to a reference beam. By scanning the sample with a varying wavelength beam, a spectrum may be plotted of the absorption against the wavelength. In general the region of interest occurs between 200 and 1100 nm, containing the whole visible light spectrum (from ca. 400 nm to 700 nm) and extending slightly into the ultraviolet (< 400 nm) and IR (> 700 nm) regions.

By knowing the path length (l) of the sample, the concentration (c) of a sample of interest and measuring the absorbance (A) of the peak maxima, molar extinction coefficients (ε) may be calculated which allow the strength of the transition to be gauged and compared via the Beer-Lambert Law:

$$A = \varepsilon c l \qquad (3)$$

This form of spectroscopy is most commonly used for transition metal complexes due to their often intense colours resulting from *d* electron transitions, however certain organic compounds, especially conjugated systems, may also be strongly absorbing in the visible region.

A2.2.9 X-ray Diffraction[19,20]

A substance in the crystalline state is comprised of itself within an infinitely repeating three-dimensional lattice with regular symmetry, which may include translation, rotation and reflection. The repeating structure is defined by the unit cell, which is chosen to simplify the representation of the lattice. In general the choice of unit cell often has many possible options but is chosen to maximise symmetry where possible or otherwise shorten the sides and obtain angles close to 90°. The sides of the unit cell are given by the dimensions *a*, *b* and *c* (measured in angstroms, Å) and the angles between them are given the designations α, β and γ such that α is the angle between *b* and *c*, β is the angle between *a* and *c* and γ is the angle between *a* and *b*. The unit cell is also defined by its volume, measured in $Å^3$.

In 1914 Max von Laue was awarded the Nobel Prize in Physics for his discovery that x-rays could be diffracted by a crystal. However, unless the x-rays are in phase when diffracted by the crystal, the destructive interference reduces the intensity of the resultant waves. W. H. Bragg and W. L. Bragg, a father and son team, then showed that for waves scattered by planes separated by a distance *d*, the lower beam travels an extra distance of 2dsinθ. For both waves to remain in phase with each other, this distance must be equal to an integer value of the wavelength of the wave, or the mismatching phase will result in destructive interference. This gave rise to Bragg's Law:

$$n\lambda = 2d\sin\theta \quad (4)$$

Where n is an integer, λ is the wavelength of the x-ray beam, d is the spacing between the planes and θ is the angle between the plane and the incident ray (see *Figure A2.13*). For their work, W. H. Bragg and W. L. Bragg shared the 1915 Nobel Prize in Physics.

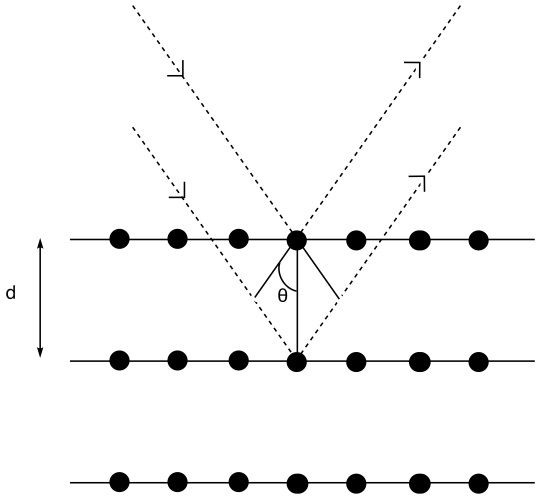


Figure A2.13: Illustration of Bragg's Law. For the two waves scattered by planes separated by distance *d*, the extra length of the path travelled by the lower wave is 2dsinθ.

This diffraction of x-ray by the electrons within the atoms of the molecules of the crystal lattice then produces a diffraction pattern on a detector that is placed in proximity to the crystal. However, while the intensities of the x-ray waves may be recorded by the detector, the relative phases of the waves are lost, making the determination of the crystal structure non-trivial. This is known as the Phase Problem, and new methods for tackling it continue to be developed. Early approaches to this issue were to include a heavy atom such as a transition metal such as mercury. The diffracting power of an atom increases with the atomic number due to the greater electron density surrounding the atom, meaning that the most intense x-ray diffraction peaks could be assigned to that atom, and the remainder of the structure solved from this. In general, the solving process today has become a mathematical solution by relying on probability relationships known as Direct Methods. The structures are then refined by Least Squares, wherein the calculated phases are compared to the observed phases (actually used are the amplitudes $|F_o|$ and $|F_c|$) and repeated many times to give best agreement between the two. The final measure of agreement between the two values is given by the residual or R value, defined as:

$$R1 = \frac{\Sigma | |F_o| - |F_c| |}{\Sigma |F_o|} \qquad (5)$$

The end result of this solution-refinement process is a completed crystal structure, with the positions of all non-hydrogen atoms located and often displayed as ellipsoids due to the anisotropy of the vibrating atoms. These are normally calculated such that a 50% probability of locating the electron density of the atoms is within the ellipsoid (see *Figure A2.14*). Hydrogen atoms are treated differently due to that with only a single electron, hydrogen atoms are very weakly diffracting. Therefore hydrogen atoms are normally placed at calculated positions according to the secondary bonding atom, using standard bond lengths and angles. If a definite determination of the hydrogen atoms is required, samples may be submitted to neutron diffraction instead, a related technique wherein neutrons are scattered by the atomic nucleus rather than the electron cloud, giving higher sensitivity to lighter elements such as hydrogen.

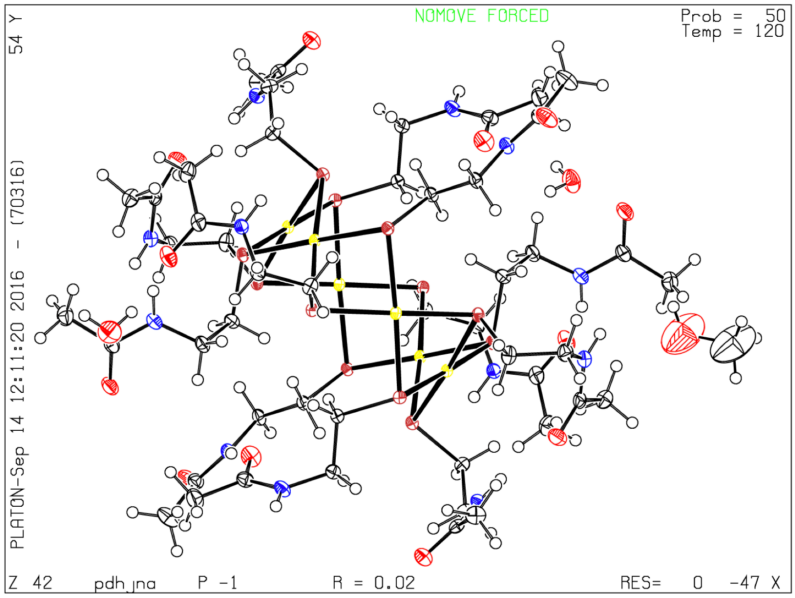


Figure A2.14: Example ORTEP diagram of **1**. Ellipsoids are shown at the 50% probability level. Atom colours: Pd-yellow, S-dark red, C-white (ellipsoids), O-light red, N-blue, H-white (circles).

A2.3 References

1. H. Günther, *NMR Spectroscopy: Basic Principles, Concepts, and Applications in Chemistry*, Wiley-VCH, Germany, 2013.
2. H Friebolin, *Basic One- And Two-Dimensional NMR Spectroscopy*, Wiley-VCH, Germany, 2011.
3. W. P. Aue, E. Bartholdi and R. R. Ernst, *J. Chem. Phys.*, 1976, **64**, 2229-2246.
4. "Press Release: The 1991 Nobel Prize in Chemistry". Nobelprize.org. Nobel Media AB 2014. Web. 15 Feb 2018.
5. R. Evans, Z. Deng, A. K. Rogerson, A. S. McLachlan, J. J. Richards, M. Nilsson and G. A. Morris, *Angew. Chem.*, 2013, **125**, 3281-3284.
6. S. Floquet, S. Brun, J.-F. Lemonnier, M. Henry, M.-A. Delsuc, Y. Prigent, E. Cadot and F. Taulelle, *J. Am. Chem. Soc.*, 2009, **131**, 17254-17259.
7. R. Holze, *Experimental Electrochemistry: A Laboratory Textbook*, Wiley-VCH, Germany, 2009.
8. G. Gritzner and J. Kuta, *Pure Appl. Chem.*, 1984, **56**, 4, 461-466.
9. M. A. Spackman and P. G. Byrom, *Chem. Phys. Lett.*, 1997, **267**, 215-220.
10. M. A. Spackman and D. Jayatilaka, *CrystEngComm*, 2009, **11**, 19-32.
11. J. J. McKinnon, M. A. Spackman and A. S. Mitchell, *Acta Cryst. B*, 2004, **60**, 627-668.
12. J. J. McKinnon, A. S. Mitchell and M. A. Spackman, *Chem. – Eur. J.*, 1998, **4**, 2136-2141.
13. M. A. Spackman and J. J. McKinnon, *CrystEngComm*, 2002, **4**, 378-392.
14. J.J. McKinnon, D. Jayatilaka and M.A. Spackman, *Chem. Commun.*, 2007, 3814-3816.
15. J. J. McKinnon, F. P. A. Fabbiani and M. A. Spackman, *Cryst. Growth Des.*, 2007, **7**, 755-769.
16. S. A. Moggach, S. Parsons and P. A. Wood, *Crystallogr. Rev.*, 2008, **14**, 143-184.
17. M. J. Turner, J. J. McKinnon, S. K. Wolff, D. J. Grimwood, P. R. Spackman, D. Jayatilaka and M. A. Spackman, CrystalExplorer 17, 2017, University of Western Australia.
18. GE Healthcare, *Size Exclusion Chromatography: Principles and Methods*, UK, 2014.
19. W. Clegg, *X-Ray Crystallography*, Oxford Chemistry Primers, United Kingdom, 2015.
20. D. W. Bennett, *Understanding Single Crystal X-Ray Crystallography*, Wiley-VCH, Germany, 2010.